Investigation on Thermal Barrier Coating and Thermal Behaviour at High Temperature

By

Siwen Ding, *BEng, MSc*

A thesis submitted to the
University of Nottingham
for the degree of
Doctor of Philoscophy

Supervisor: Prof. Yuying Yan
Co-supervisor: Prof. John Billingham, Dr. Simon Lawes, Dr Xianghui Hou
November, 2016

Abstract

The oxidation behaviour of diffusion and overlay coating, manufactured by pack cementation and high velocity oxygen fuel (HVOF) techniques, was studied under isothermal condition at a temperature of 1100 °C for up to 500 hours. Detailed analysis on oxide thickness coupled with cross section microstructure observation was carried out. The results shown sub-parabolic oxide growth for all samples.

To simulate a real operating condition for the thermal barrier coating (TBC) system, high temperature oxy-acetylene flame based burner rig was designed, manufactured and calibrated. A maximum surface temperature of 1400 °C detected by a single wavelength pryormeter with a 700 °C through sample thickness thermal gradient was achieved. A TBC system in which the ceramic top layer deposited by air plasma spray (APS) technique was tested under such condition. Several damage/failure types were identified in comparison with samples tested under isothermal loading.

A novel physical based mathematical moving boundary problem model ultilizing asymptotic analysis that predicts the growth of the oxide layer on a binary bond coat system was proposed. The governing equations were discretized and solved numerically using finite difference and Newton's iteration method respectively. Numerical results obtained from this model had shown a good qualitative agreement from comparison with the experimental studies.

Acknowledgements

I would like to take this opportunity to thank the project sponsor and the Department of Mechanical, Materials and Manufacturing for the financial support during this project.

I am gradefully to my supervisor Prof. Y. Y. Yan for the encouragement and guidance that he has offered.

I would like to thank Prof. J. Billingham for the guidance in mathematical modelling.

I would also like to thank Dr S. Lawes for the support of burner rig design, especially on the insights of Labview programming.

I would like to thank Dr X. H. Hou for the experimental support.

I would like to thank Dr L. Y. Qian for his help on roughness measurement and sample preparation.

I would like to express my appreciation to Mr R. Screaton and Mr J Hinchliffe for the assistance throughout the coating and burner rig manufacturing process.

Last but not least, I am extremely grateful to my wife, Ms N. Y. Tang, her unconditional encouragement and support during the difficult times has made this thesis possible.

Glossary

-cycle	number of thermal cycles
-pass	number of coating passes that control the thickness of the top coat
MCrAlY	bond coat type where M stands for nickel or cobalt
P-1,2…	pack cementation sample number
AP-1,2…	above the pack cementation sample number
NP-P-1,2…	nickel plated pack cementation sample number

Abbreviations

TET	turbine entry temperature
NOx	nitrogen oxides
TBC	thermal barrier coating
BC	bond coat
TC	top coat
TGO	thermally grown oxide
YSZ	yittria stabilized zirconia
APS	air plasma spraying
EBPVD	electron beam physical vapour deposition
HVOF	high velocity oxygen fuel
VPS	vacuum plasma spraying
LPPS	low pressure plasma spraying
NiAl	nickel aluminum
NiCrAl	nickel chromium aluminum
$(Al,Cr)_2O_3$	chromia oxide
wt%	weight percentage
at%	atomic percentage
CMAS	calcium magnesium aluminosilicate
HTHC	high temperature hot corrosion
LTHC	low temperature hot corrosion
SEM	scanning electron microscopy
EDS	energy dispersive x-ray
XRD	x-ray diffraction
FPGA	field programmable gate array
I/O	input/output
AI/AO	analogue input/analogue output
DSUB	D subminiature

VI	virtual instrument
OZ	outer zone
Secondary-OZ	secondary outer zone
IDZ	inter-diffusion zone

Nomenclature

Ni	nickel
Co	cobalt
Cr	chromium
Al	aluminum
Y	yttrium
Hf	hafnium
NiO	nickel oxide
γ	gamma
γ'	gamma prime
δ	delta
θ	theta
α	alpha
α	dimensionless constant within the boundary condition (Chapter 7)
β	beta
$\sigma_{residual}$	residual stress
E_{TC}	top coat Young's modulus
$\Delta\alpha_{TC}$	difference in coefficient of thermal expansion
ΔT	temperature drop
U_{TC}	top coat stored energy
H_{TC}	top coat thickness
ρ	mass density
μ	viscosity
P	pressure
cp	specific heat
$\dot{q}$	rate of internal heat generation
G_k	turbulent kinetic energy

Y_m	fluctuating dilation
α_k	inverse effective Prandtl number
α_ε	inverse effective Prandtl number
Δy_e	experimentally measured oxide thickness
k_β	calculated oxidation rate constant from experiment data
t_e	oxidation time
n_e	calculated power law exponent from experiment data
Ω	volume per atom
C^A	concentration of aluminum atom
C^B	concentration of nickel atom
c	specified atom concentration
c_i	initial concentration
coa	oxygen atmospheric concentration
$\underline{N}^A$	net flux of aluminum
$\underline{J}^A$	diffusion flux of aluminum
$\underline{J}^B$	diffusion flux of nickel
$\underline{J}$	total flux
K	gas constant
k_e	experimental rate constant
k_n	numerical rate constant
T	absolute temperature
ϕ	thermodynamic factor
D^A	diffusivity of aluminum
D^B	diffusivity of nickel
D^o	diffusivity of oxygen
$\underline{v}^{(1)}$	marker velocity in alloy region
$\underline{V}^{(1)}$	interface velocity
$v^{(2)}$	internal velocity in oxide region
c_o	oxygen concentration

$\rho^{(1)}$	density of aluminum
$\rho^{(2)}$	density of oxide
y_1	oxide lower boundary
y_2	oxide upper boundary
$\bar{y}$	dimensionless oxide thickness
$\bar{t}$	dimensionless time
$\bar{V}$	dimensionless interfacial velocity
$\bar{p}$	dimensionless pressure
$\bar{D}$	dimensionless diffusivity
$\bar{D}^{oa}$	dimensionless oxygen diffusivity
$\bar{c}_o$	dimensionless oxygen concentration
$\bar{v}^{(2)}$	dimensionless internal velocity
n_e	experimental exponent
n_n	numerical exponent

Chapter 1 - Introduction

Chapter 2 - Literature Review

Chapter 3 - Experimental Methodology and Procedures

Chapter 4 - Burner Rig Deisgn Development and Calibration

Chapter 5 - Microstructure Characterization

Chapter 6 - Oxidation Test Results

Chapter 7 - Mathematical Modelling of the Oxidation of Binary β-phase Nickel aluminium Alloys

Chapter 8 - Discussion

Chapter 1

Introduction

1.1 - Background and Motivation

For aero engine manufacturers, increase in thermal efficiency for gas turbine engines is always the primary requirement in the industry. From the gas turbine process, known as Brayton cycle, Figure 1, thermal efficiency is mainly determined by the turbine entry temperature (TET). As operating temperature increases in the high pressure turbine section, Figure 2, pollutant produced from combustion process such as nitrogen oxides NOx can also have an enormous impact on the environment. Therefore, this has led to the rapid development of appropriate turbine cooling technique and advanced protective coating systems in order for turbine structure to maintain the integrity under high temperature. Apart from the widely adopted film cooling technique which employs small holes in turbine component to release internal coolant onto the turbine surface. Another most applied technique to further improve temperature gradient on the turbine is the use of thermal barrier coating (TBC); this technique not only offers thermal protection but also significantly improves the turbine life.

Conventional TBC consists of three layers of coating in which the bottom layer and top layer have a thickness of 30 μm to 100 μm bond coat (BC) and 120 μm to 200 μm top coats (TC) respectively, as shown in Figure 3. The metallic bond coat normally made of MCrAlY provides oxidation protection as well as a better chemical bond between top coat and substrate. Yittria stabilized Zirconia with ZrO_3-8%$Y2O_3$ is commonly used as the ceramic top coat which acts as a thermal insulator and has the ability to lower the substrate temperature.

These layers are normally applied either by Air Plasma Spraying (APS) [1] or the Electron Beam Physical Vapour Deposition (EB-PVD) [2]. Top coat that is applied by APS gives the isotropic mechanical behaviour; this is due to randomly deposited material grains. In contrast, top coat applied by EB-PVD has different mechanical behaviours and properties; this is due to the fact that the columnar grain structure is produced which results in material anisotropy. Depending on the coating deposition process, the top coat can be designed to offer certain resistance against strain induced cracking and delamination. It is essential that by incorporating micro cracks and porosity in the material, a certain level of strain tolerant within the top coat can be achieved [3]. As the oxygen penetrates through the top coat, the third layer, namely, thermally grown oxide (TGO) layer forms as the bond coat oxidizes. The oxidation takes place while the component is in operation at high temperature, the aluminium diffuses outwards from the bond coat, at the same time, the oxygen diffuses inwards; ultimately, the reaction between alumina and oxygen forms new oxide which also acts as an oxidation barrier preventing the oxygen to penetrate further through the coating. Therefore, the life of the substrate is heavily relied on the basis of oxidation resistance offered by the coatings. However, the study of thermally grown oxide layer is proving to be challenging, due to the growth of TGO layer and creep deformation of the bond coat, the interface morphology of the TGO layer with adjacent layers (BC and TC) keeps evolving during the life of the TBC [4].

For aero turbine engines, TBCs are normally subjected to thermo mechanical fatigue, which is caused by the mismatch between each layer in the coating system. It is not surprising to realize that in TBC system, each individual layer is much stronger than the two interfaces (TC/TGO and BC/TGO); hence the degradation of the interface toughness is proportional to the thermal exposure time [5]. As a result, TBCs are susceptible to delamination, also known as spallation, which occurs along the TGO interfaces [3]. Explicitly speaking, the TBC system is subjected to critical thermal/mechanical load while in operation, which causes the spallation to occur. The term ‘spallation’ is often referred to as the detachment of the TC, the mechanisms behind spallation depend on the loading condition as well as geometrical and material properties; it is worth noting that among those parameters, the interface thermo-mechanical properties and morphological features with adjacent layers are the prominent factors that contribute to the failure in TBC system. The process of spallation can be seen as follows [6]: a) interfaces imperfection causes nucleation of cracks;

b) crack propagation driven by the oxidation stresses; c) spallation under cooling through a process known as large scale buckling which occurs when the critical delamination length has exceeded. Some detailed studies of buckling initiation; propagation and coalescence for this type of failure mechanism have been studied by a number of researchers [7-10].

The present study is aimed to investigate the oxidation behaviour of diffusion and overlay coating systems. Results from experiments and numerical simulation are presented with respect to the followings,

- Microstructure investigation of diffusion and overlay coating, manufactured by pack cementation and HVOF techniques, under isothermal condition.
- Design, manufacture and calibrate a high flame temperature testing rig using a single wavelength pyrometer in order to assess the flame thermal cycling behavior and high temperature oxidation resistance of the thermal barrier coating system deposited by APS technique.
- Develop a novel physical based mathematical model that ultilizes asymptotic analysis in order to predict the oxide growth of the coating system.

This thesis consists of 9 Chapters. Literature review is presented in Chapter 2. The experimental methods used and manufacturing procedures throughout the project is detailed in Chapter 3. The design, manufacturing and calibration of the flame burner rig is presented in Chapter 4. Microstructure of as-coated diffuion and overlay coating system is presented in Chpater 5. The investigation of microstructure developments of diffusion coating and overlay coating are presented in Chapter 6. The effect of post surface treatment on oxide roughness and oxide growth of overlay coating, as well as failure observation from flame thermal cycling results is also included in Chapter 6. The construction of mathematical model and numerical results are presented in Chapter 7 followed by discussion, conclusion and future work, which are presented in Chapter 8 and 9 respectively.

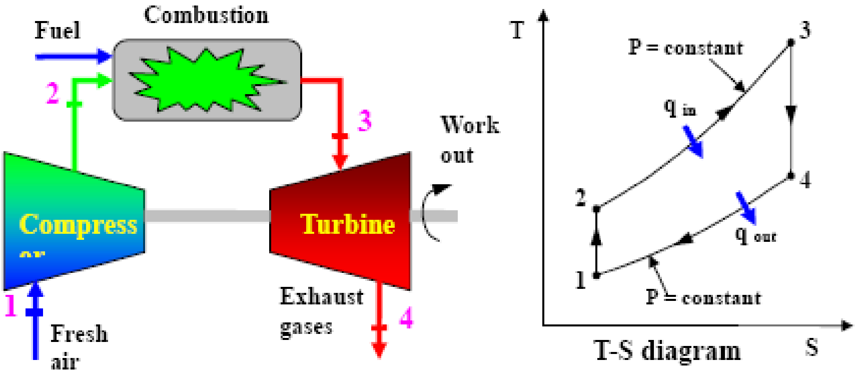

Figure 1– Schematic and T-S plot showing the Brayton cycle [11].

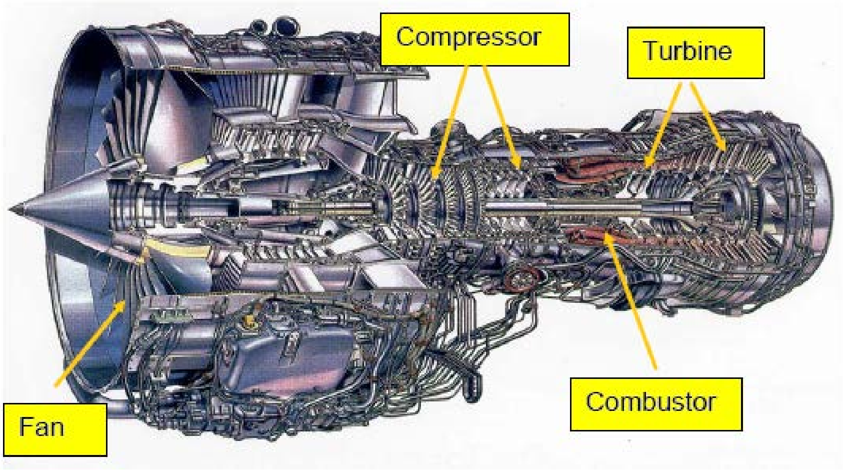

Figure 2– Image showing a gas turbine jet engine [12].

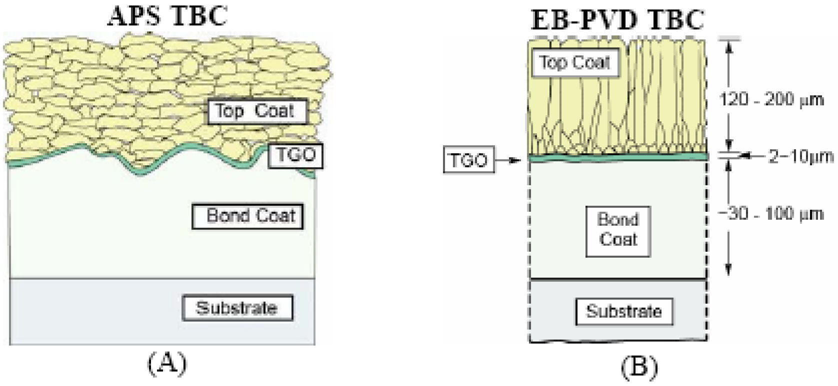

Figure 3- A) Air plasma spray TBC B) Electron-beam physical vapor deposition TBC [13].

Chpater 2

Literature Review

2.1 - State of the Art

2.1.1 - Conventional TBC system and Their Thermo-Mechanical Properties

Superalloy Substrate

In the modern aero engine, high pressure turbine blades operates in the condition where good combined properties such as high temperature strength, oxidation and creep resistance and stiffness are required from the alloy. It is therefore, for the past few decades, nickel based super-alloy has been the preferred choice of substrate material for gas turbine blades. Complex stress development, such as high centrifugal stress and bending stress, can impose on the blade due to the high rotating speed and high pressure operating environment. Furthermore, TBC system life cycles are heavily depended on the Young's modulus, thermal expansion and conductivity of the substrate. In addition, the high temperature creep and fatigue behaviour also contributes towards the coating damage evolution.

A nickel based single crystal super-alloy normally consists up to 12 additional elements (Co, Cr, Mo, W, Ta, Al, Ti, Fe, C, Re, Hf) in order to improve overall performance depending on varying factors, such as, the type of fuel usage, the construction of the engine, operation cycles and environment. The evolution chart of super-alloys in terms of temperature, manufacturing techniques and chemical compositions is shown in Figure 4 [14]. It can be seen from the chart that as the alloy manufacturing techniques gets more and more advanced, a significant improvement on high temperature creep has been made possible. The advantage of single crystal alloy over other conventional polycrystal alloys is that most of solutes of grain boundary strengthening are removed. Thus, this results in an increase of melting temperature up to 1250°C.

However, diffusion of certain elements at high temperature may occur at the interface between the bond coat and substrate. Therefore the inter-diffusion phenomenon can ultimately have a profound influence on the failure of TBC system.

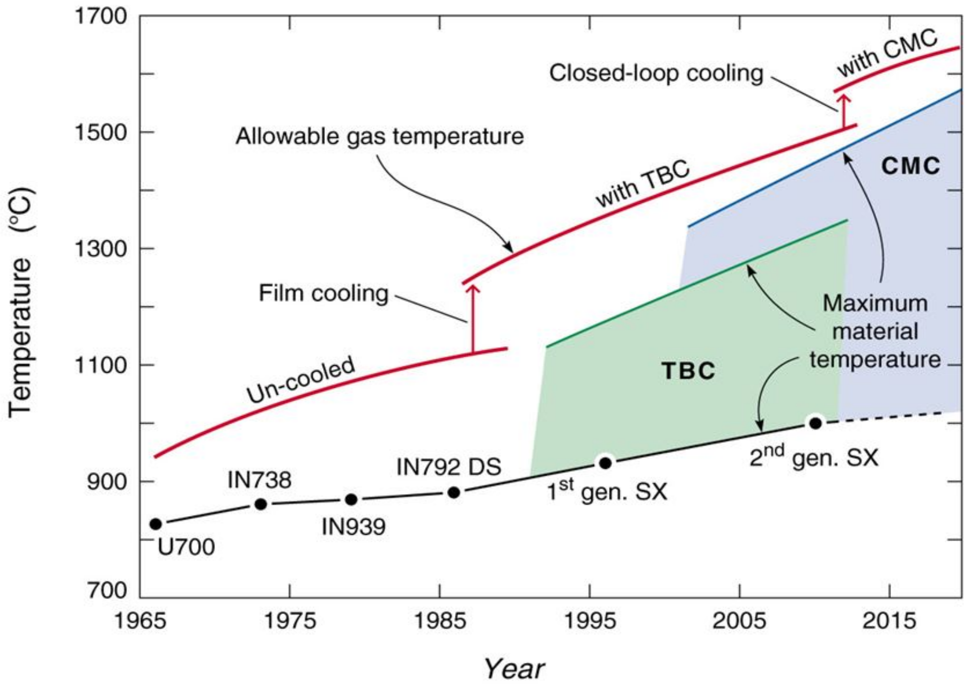

Figure 4 – Evolution chart of superalloy [14].

Bond Coat

As the name suggests, this metallic layer provides an improvement on the adhesion strength between thermal barrier coating (top coat) and the substrate. It also compensates the thermal expansion misfit between coatings layers and plays an important role of offering a certain level of protection to the substrate from thermal oxidation and corrosion. Currently, type of bond coat has been categorised into two group [15, 16], they are, single phase $\beta - \mathrm{NiAl}$ with

Pt in solid solution and two phase MCrAlY (where M = Co, Ni or Co/Ni) with elements in γ/γ' phases.

Single phase $\beta - \text{NiAl}$ with Pt in solid solution – this type of bond coat is normally produced using electroplating technique in which a thin layer of Pt is deposited onto the substrate surface aluminized using another technique called, chemical vapour deposition. The usefulness of Pt in (Pt,Ni)Al bond coats is that it renders the coating to be more sulphur tolerant and to prevent delamination at the thermally grown oxide and bond coat interface [17].

Two phase MCrAlY with elements in γ/γ' phases – this type of bond coat can be produced by several techniques, such as, vacuum plasma spraying (VPS), low pressure plasma spraying (LPPS), air plasma spraying (APS), high velocity oxygen fuel (HVOF) and last but not the least, electron beam physical vapour deposition (EBPVD). VPS and LPPS permit denser and more oxidation resistant coating than APS. Some of the techniques will be described in detail in the next section. For bond coat composition of MCrAlY where M can be the element of Ni or Co. Typical key elements of contents are shown in Table 1.

Table 1 – key elements contents [16]

Main Element Contents	
	wt%
Ni	45~50
Co	10~30
Cr	15~22
Al	8~12
Y	0.2~0.5

The bond coat in general has the elastic behaviour at ambient but also has the tendency to yield and creep at the elevated temperature. This phenomenon is in contrast to TGO in which the highest stresses occur at ambient and the strength decreases significantly at high temperature. Literatures wrote by [18, 19] have shown that the yielding of bond coat can be predicted not only around the stress hotspots along the imperfections but also in a much larger scale. Strictly speaking, bond coat has the intriguing evolution of properties as it provides aluminium for the formation of TGO, during this process, the composition of bond coat changes with time, known as phase transformation of grains, hence, individual grains or average properties of grains can be modelled to allow the transformation to take place [20].

Ceramic Top Coat

The ceramic top coat is the outermost layer for the TBC system, and is in direct contact with the extremely hot gas from combustion chamber. The main functionality of this layer is to prevent the substrate from melting and allowing the operating temperature to be increased by 100 to 200°C, hence, through thickness thermal gradient between hot gas and super-alloy substrate can be improved. There are certain criteria for which the top coat must meet, they are [21],

- Low thermal conductivity.
- High melting point.
- Appreciable high thermal expansion coefficient that matches with the super-alloy substrate.
- Stability of phases from ambient temperature to operating temperature.
- High toughness to improve life cycles.
- Good erosion resistance preventing from foreign object damage.
- Thermodynamically stable with alumina oxide and bond coat.

At the present, the most commonly used top coat material is the 6-8wt% Yttria Stabilized Zirconia, typically known as YSZ. This type of ceramic material which meets the above requirements was first approved by [22] in late 70s.

However, the misfit of thermal expansion coefficient between the top coat and substrate is still in existence [23]. Therefore, in order to prevent the failure caused by this misfit, Young’s modulus of this insulating oxide layer has to be effectively controlled within the range not greater than 50GPa [24]. This is because that under high temperature YSZ creep causes the stress in the material to relax and eventually, upon cooling, residual stress occurs due to misfit of thermal expansion. Let's assume that the YSZ is fully dense and has a modulus of 200 GPa and Poisson's ratio of 0.2, with a typical temperature drop of 1100°C the residual stress can be calculated as -0.8 GPa from the expression

$$\sigma_{residual} = \frac{E_{TC}\Delta\alpha_{TC}\Delta T}{1-v_{TC}}, \tag{1}$$

where E_{TC} is the top coat Young's modulus, $\Delta\alpha_{TC}$ is the difference in coefficient of thermal expansion between top coat and substrate, ΔT is the temperature drop and v_{TC} is the Possion's ratio of top coat. Moreover, based on the value from above, the stored energy per unit area for the top coat for a given thickness of 100µm can be obtained as 160 J/m^2 from the expression

$$U_{TC} = \frac{\sigma_{residual}^2 H_{TC}}{2E_{TC}}, \tag{2}$$

Where H_{TC} is the thickness. However, for the typical 6-8%YSZ top coat, the mode I toughness is roughly 45 J/m^2 [25], therefore, it is obvious that the stored energy obtained from above is much greater than the typical toughness of the top coat, the consequence by having a large stored energy is that the top coat would fail. To avoid the problem, deposition techniques, such as EBPVD, have been developed in order to produce less dense microstructure of top coat, thus, enabling the Young's modulus of top coat to be reduced to a reasonable level [26].

Thermally Grown Oxide

The thermally grown oxide is a layer mainly consists of Al_2O_3 which forms between the bond coat and top coat. This TGO layer grows when the coating system is under elevated temperature and due to its impermeability to oxygen this layer also acts as an oxidation barrier preventing bond coat/substrate from being oxidised further. Hence, the TGO layer plays a very important role towards the TBC lifetime [6]. The growth of the TGO layer is mainly controlled by the inward diffusion of oxygen through the top coat [27-29] and outward diffusion of aluminium from the bond coat. The TGO growth will be described in detail in section 2.2. However, it is worth noting that as α-Al_2O_3 layer grows, a small amount of compressive stress develops [30, 31]. Similar to the top coat, the misfit of thermal expansion with adjacent layer causes the compressive stress to increase upon cooling. It has been reported [32] that at ambient temperature the residual stress of the TGO layer can reach to -4 GPa. Although the TGO thickness is relatively thin, from equation 2, it can be seen the stored energy per unit area is large. Hence, the failure at the TGO/bond coat interface is potentially increased. Figure 5 illustrates the energy release rate for delamination as a function of TGO thickness along the interface.

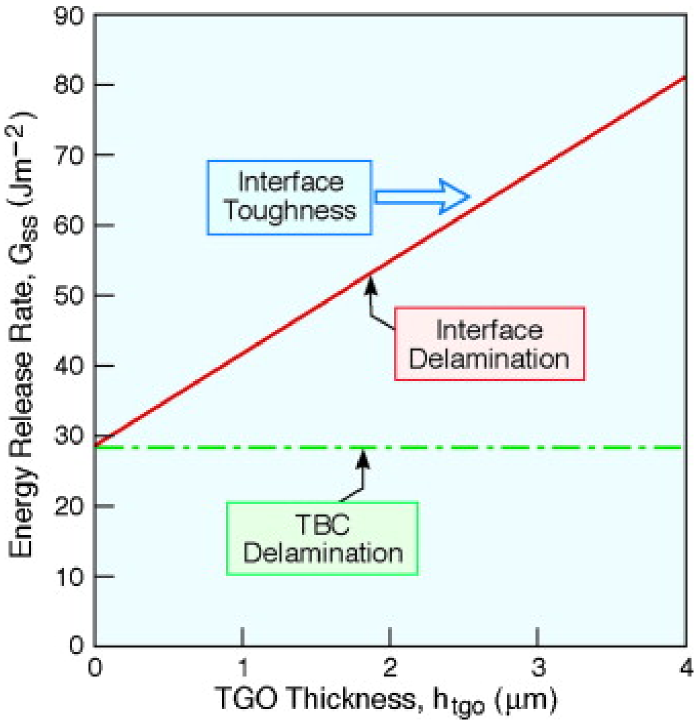

Figure 5 - The plot showing the energy release rate for delamination as a function of TGO thickness [23].

2.1.2 - Coating Process Technique

Air Plasma Spray (APS)

In this relatively cheaper coating process, solid coating powders are injected through an injection tube into the high temperature plasma flame during which the melted particles are propelled to the substrate surface by electrostatic field. The molten droplets then spread out onto the substrate and solidifies to form a deposit as coatings, Figure 6 (a) [33]. In the coating layers produced by air plasma spray, formation of splat pores as the direct result from impingement of the droplets on the substrate. The orientation of these pores along with micro-cracks are parallel to the metallic interface, Figure 6 (b) [33].

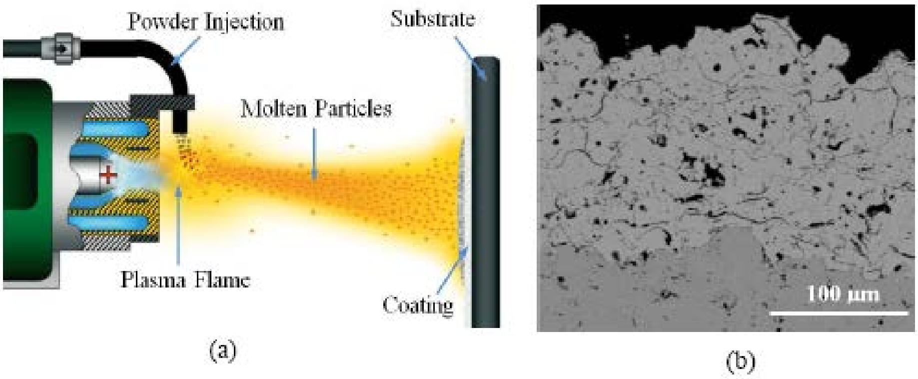

Figure 6 – (a) Schematic showing APS process and (b) Microstructure of a typical APS coating [33].

It has been demonstrated by [34] that the pore volume fraction has a significant effect on the thermal conductivity in the top coat layer, Figure 7. It can be seen that as the porosity level increases, the thermal conductivity will decrease. This is due to the fact that the amount of pores preventing through thickness heat flow resulting the top layer to have a low thermal conductivity. Moreover, low elastic modulus and high strain tolerance are also directly related to the high level of porosity in the coating [35-38].

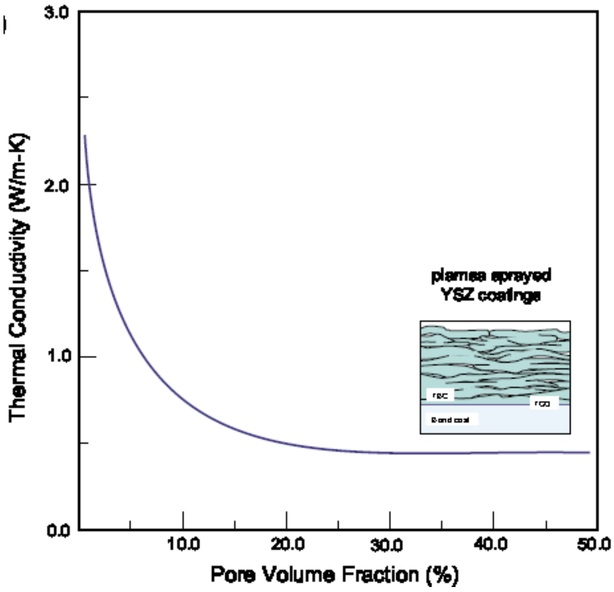

Figure 7 – The reduction of thermal conductivity is effectively dictated by the level of porosity in the APS coating [34].

However, the thermal expansion coefficient misfit between top coat layer and substrate leads to the initiation of existing micro-cracks and causes cracks to propagate which significantly limits the spallation life of the APS coating. It is therefore, such coating technique is often applied for less frequent thermal cycling applications, i.e. land based power generation turbines.

Electron Beam Physical Vapor Deposition (EBPVD)

In this relatively more expensive coating process, the electron beam which transforms the high kinetic energy of electrons into thermal energy is used to melt and evaporate the coating material. The coating on the surface of the substrate is subsequently formed by vapour condensation, Figure 8. The whole coating process takes place under a vacuum condition; however, a small amount of oxygen is required for the stoichiometric composition of the top coat. Here, this oxygen exposure permits the early formation of thermally grown oxide with a thickness usually less than 0.5μm. For complex geometry such as turbine blades, homogeneous thickness is achieved by replacing the components onto a rotating platform. Unlike the APS coating process, the top coating layer produced by EBPVD has a columnar structure with fine porosity in each columns and separation of each columns at high temperature gives more strain tolerance to the TBC. Hence, thermal expansion stress misfit can be effectively compensated [39], Figure 9. Thermal conductivity can be reduced due to intercolumnar pores in each column structure but still relatively higher than that of APS produced coating. Advantages and disadvantages have been summarised in Table 2 shown below [40].

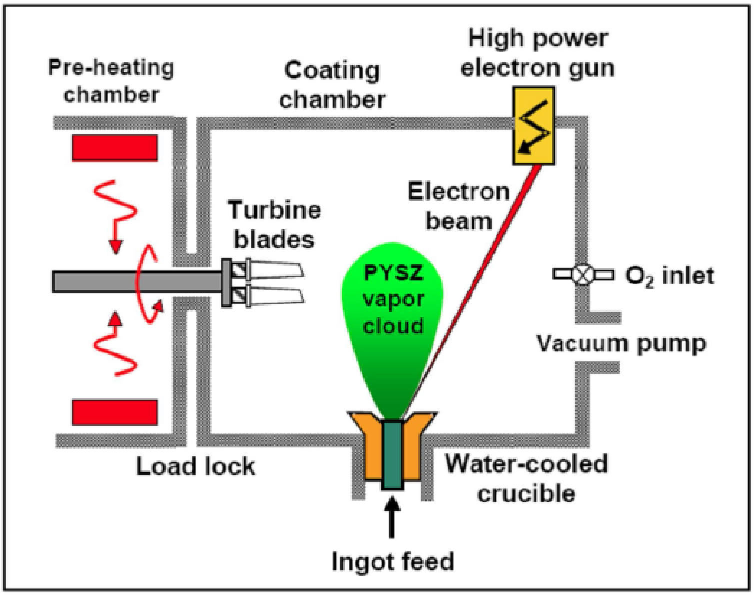

Figure 8 – Schematic showing the EBPVD coating process [41].

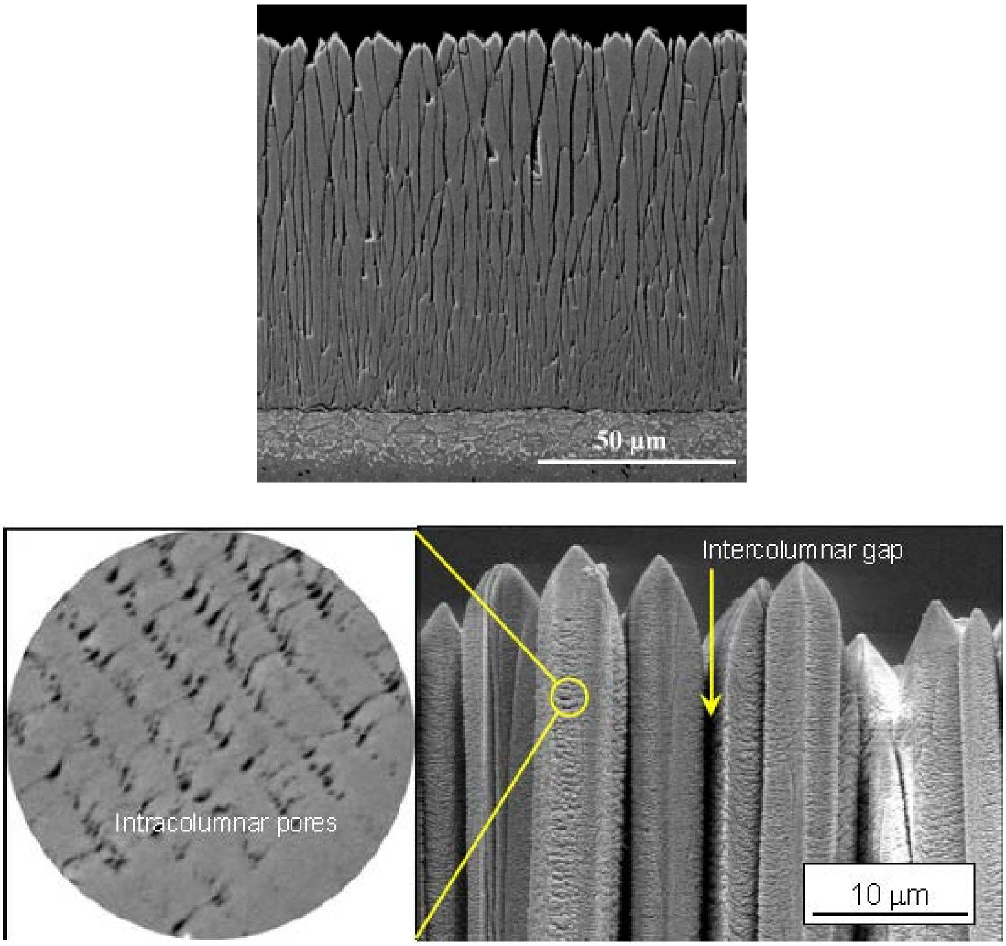

Figure 9 – Microstructure showing the column structure with porosity produced by EBPVD [41].

Table 2 – Comparison between APS and EBPVD coating process [40].

	Plasma Spraying	*EB-PVD*
Structure	Lamellar	Columnar
Surface finish	Good, but needs extra polishing	Excellent
Bondcoat roughness	Grit blasted (10µm)	Smooth (1µm)
Bonding mechanism	Mechanical	Chemical
Typical ceramic thickness	0.2-3mm	0.1-0.3mm
Cooling hole closure	Poor	Excellent
Large part predicable	Favourable	Little closure
Investment cost (%)	100	100-400
Parts per charge	1	1-10

2.2 - High Temperature Degradation Mechanism of TBCs

2.2.1 - Oxidation

Assuming that in the absence of liquid (water), while a metal is under direct contact with oxygen, oxidation of metal at high temperature would seem inevitable which also could result in material loss and major components failure during service. Therefore, for application such as gas turbines, it is crucial to efficiently prevent and control oxidation at high temperature. In the following texts, the basic understanding of alloy oxidation will be described.

Understanding of Alloy Oxidation

Initially, oxidation takes place as oxygen atoms are being adsorbed onto the alloy surface [42]. Subsequently, reaction between oxygen and alloy at the surface is taken place to form a thin layer of oxide film, this phenomenon can be written as,

$$aM + \left(\frac{b}{2}\right)O_2 = M_aO_b. \tag{3}$$

The formation of the oxide can be affected by many ways, such as surface impurities and orientation; crystal defects as well as the purity of source hot gas [43]. According to Wagner theory [44] an insulation barrier starts to emerge as the process oxide scale is being formed, thus, the migration of ions and electrons is required for this process to take place. Moreover, as the result, solid-state diffusion of cation and anion through the oxide scale must take place for allowing further oxidation to be happening. The sequence for which oxide growth on the alloy surface can be described as follows [45],

1. Oxygen is being continuously adsorbed onto the existing oxide which formed on the alloy surface
2. The atoms of oxygen that is being adsorbed on the alloy surface begins to transfer through the oxide
3. The oxygen that is being adsorbed starts to transport through oxide

4. Reaction starts to occur on the metal surface. Vacancy in the alloy lattice is created as alloy atoms are being diffused into oxide.
5. Extinction of cation vacancies begins as the result of climbing of interfacial dislocation at the oxide and alloy interface

Therefore, it is important to realise that the oxide growth location is predefined by the species of diffusion elements [43], such process is illustrated in Figure 10 from which the transport of cation is defined if cation diffusion dominates as oxide is being formed at the oxide and oxygen interface; whereby the transport of anion is defined if anion diffusion is the dominating factor.

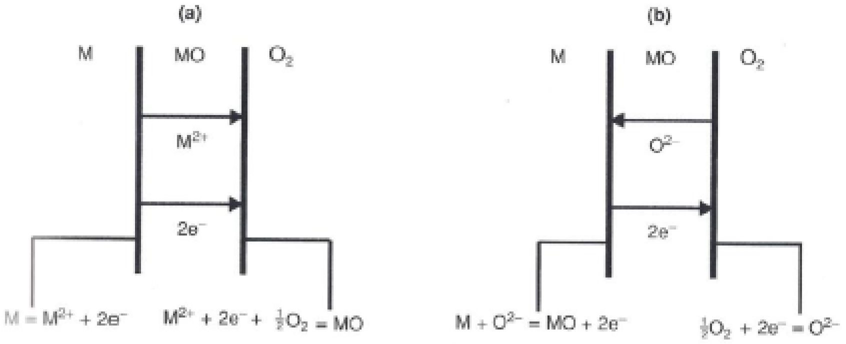

Figure 10 – Schematic showing cation and anion transport during oxidation of alloy. a) transport of cation dominates; b) anion transport dominates. [43]

Several driving forces such as concentration gradient; pressure; electrical filed; stresses and temperature can cause this diffusion process to occur in a solid alloy[42]. All these factors can be described as chemical potential gradients in a given solid. Furthermore, pre-existing defects in the solid layer (i.e. oxide) initiates the diffusion of elements, so the path of lattice diffusion or bulk diffusion goes through lattice defects, whereas the path for surface diffusion is through the line and surface defects which is often regarded as grain boundaries or dislocation between grains.

2.2.2 - The Growth of TGO

It has been understood in the previous section that oxide layer can be formed and grown while the alloy is exposed in air. For a thermal barrier coating system, the growth of oxide (i.e. thermally grown oxide TGO) at the bond coat and top coat interface is very important due to its oxidation resistance capability to the overall thermal barrier coating system. It is worth noting that a thin layer (<1μm) of TGO is formed during manufacturing of the bond coat. Once the coating is exposed into the environment, the thickness of this layer starts to grow and can reach to a critical value of 7μm [46]. However, in the study done by [47], the critical thickness of TGO was measured to be 12μm prior to spallation.

Experimentalists [48] observed the oxide was formed on the surface as well as in the sub-surface of the Ni-Cr-Al alloy at the temperature range between 1000-1200˚C under normal atmospheric environment. Further remarks were made by suggesting that in order for the α-Al_2O_3 oxide to offer any sort of protection from oxidation over 1000˚C, 3-6 wt% of Al are required in the alloy. The exact concentration percentage is highly depended on the chromium content in the alloy.

As describe in previous section 2.1.1, nickel based super-alloy is commonly used for applications such as gas turbines and it has higher aluminium content which is favourable to produce Al_2O_3 oxide at elevated temperature. However, at the same time, the downside of having higher content of aluminium is that the mechanical properties at high temperature are reduced, such as fracture toughness and ductility. It is, therefore, essential to apply additional coatings which described in section 2.1.1 to assist the development of α-Al_2O_3.

Consumption of aluminium at high temperature in the bond coat/substrate layer results in formation of α-Al_2O_3 in the TGO layer. However, this desired phase of oxide is transformed from other phases, the sequence is as follows [49],

$$\gamma - \boldsymbol{Al_2O_3} \quad \text{->} \quad \boldsymbol{\delta - Al_2O_3} \quad \text{->} \quad \boldsymbol{\theta - Al_2O_3} \quad \text{->} \quad \boldsymbol{\alpha - Al_2O_3}$$

The phase transformation usually takes place during the actual operating temperature in excess of 1000˚C.

Bond coat oxidation under high temperature can be described with three distinct stages [50] and [51] demonstrated the relationship between TGO kinetics and stability under high temperature exposure. Figure 11 illustrates the oxidation kinetics between coated and uncoated alloy at each stage. First, a transient stage in which all species of oxide is formed simultaneously. Second, a steady state stage allows the oxide growth and formation into stable phase which is α-Al_2O_3. Third, a breakaway stage results in spallation where oxide fails completely and losses its protection to the alloy.

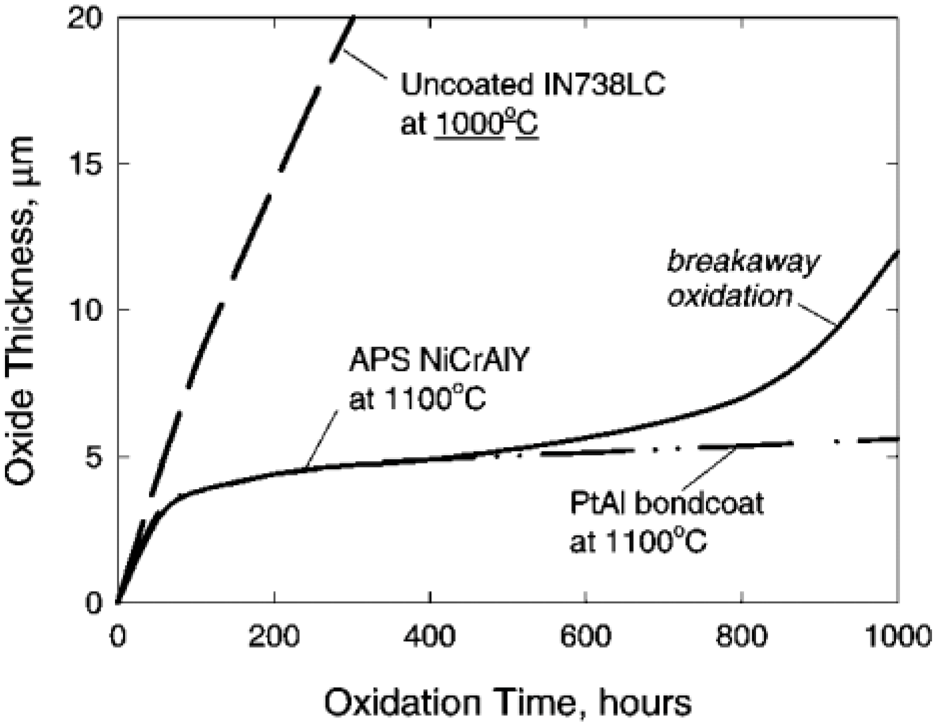

Figure 11 – Comparison of oxidation kinetics between coated and uncoated alloy in terms of oxide scale thickness and time [51].

Transient stage – this is the initial stage of oxidation where the metastable oxides (γ-Al_2O_3, δ-Al_2O_3, θ-Al_2O_3) dominance the growth. [52] studied the transitional growth of oxide which is exposed to a fixed temperature of 900˚C. The first sight of θ-Al_2O_3 was found after 16 hours exposure and mixed form oxide of α-Al_2O_3 with θ-Al_2O_3 was identified after 135 hours. The same mixture formation of oxide was also observed at a slightly higher temperature of 950˚C after 60 hours. It was concluded from this investigation that metastable oxides are hard to find and phase transition takes place fairly quickly as exposure temperature increases.

Steady state stage – after the initial transition stage of oxidation, the Al oxidizing species dominate growth of TGO which forms a continues layer becomes more stabilized as reflected in Figure 11. At turbine engine operating temperature, the only existence of oxide is in form of α-Al_2O_3 which is the most stable phase of oxide. The development of oxide during this steady stage depends on the super-alloy substrate composition; oxidation environment and temperature [53]. Based on the β-phase NiAl the high temperature oxidation transformation diagram of oxide, as shown in Figure 12, was developed by [54]. It can be seen from the schematic diagram that stable α-Al_2O_3 starts to emerge from other unstable transit phases at uppermost temperature range after long period of exposure. The rate at which oxide grows changes from being interface controlled to diffusion controlled as a continuous layer of oxide is formed in the steady state stage. The expression of this diffusion controlled oxidation is as followed,

$$h_{TGO} = h_i + kt^{1/n} \ with \ n = 2, 3, \tag{4}$$

where h_{TGO} is the oxide thickness which also can be defined as $weight\ gain \big/ oxidised\ area$, h_i is the initial oxide thickness formed during transient stage, k is the constant and t is the time under which the coating is exposed to. In majority of cases, the oxidation growth is regarded as parabolic when $n = 2$ [55]. However, from the experimental study done by [56] has shown that the depletion of Al from the bond coat layer (NiCrAl) can lead to a change of the growth kinetics from parabolic to sub-parabolic ($n = 3$) after a prolonged exposure time of 1000 hours at 1100˚C. Number of other studies [51, 57, 58] has also observed such change in oxide growth kinetic on other substrate material systems, such as (FeCrAl), in recent years.

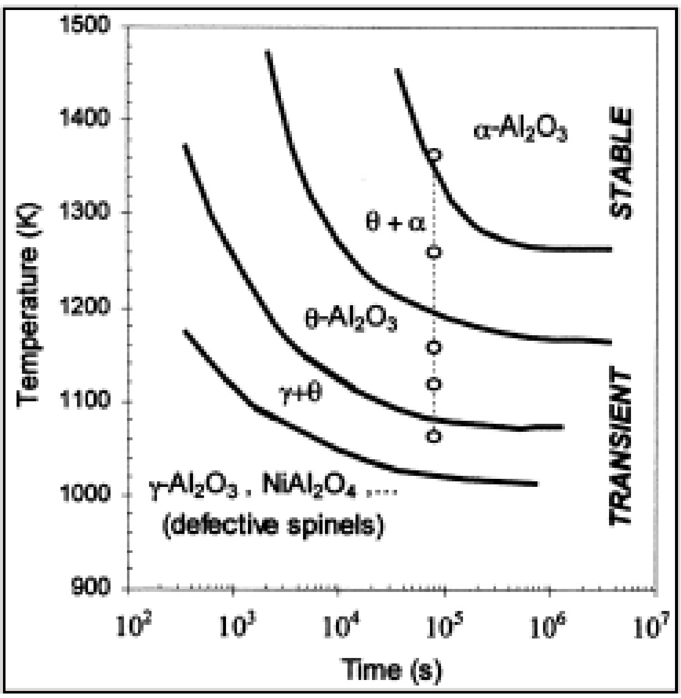

Figure 12 – Oxidation transformation diagram [54].

Internal and External Oxidation

For a Ni based super-alloy in particular, external oxidation provides real protection to the alloy system and the amount of Al in the alloy promotes the growth of oxide. However, at the same time, the internal oxidation can take place when the diffusion of oxygen is faster than the diffusion of aluminium at the surface. In other words, protective oxide layer cannot be formed sufficiently as the aluminium oxidize internally with oxygen before it reaches or diffuses to the surface of the alloy. Figure 13 shows the difference between internal and external oxidation schematically.

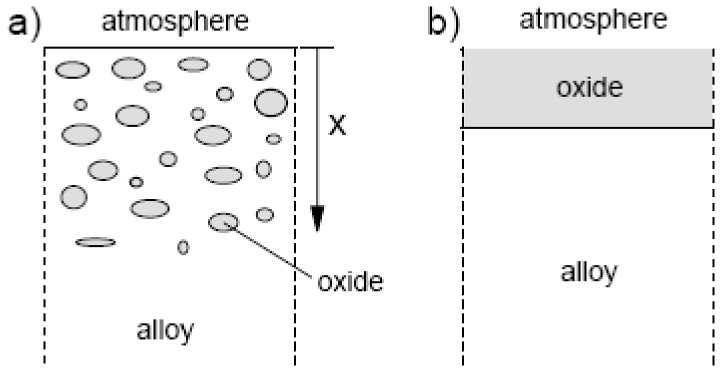

Figure 13 – a) internal oxidation in which Al oxides with oxygen below the surface. b) external oxidation which forms a protection layer [59].

It will of course be undesirable if internal oxidation dominates the oxide layer forming process. A shift from internal oxidation to external oxidation must be needed in order for the alloy to have any protections from the oxide layer. The literature done by [59] suggested an equation for which the thickness of the internal oxide layer can be expressed as,

$$x = \left(\frac{2N_o D_o t}{vN_m} \right)^{1/2}, \qquad (5)$$

where N_o is the oxygen mole fraction near the surface of the alloy, D_o is the diffusion coefficient of oxygen in the alloy, t is the time, v is the ratio of metal/oxygen atoms in the oxide which is formed internally and N_m is the mole fraction of aluminium in the oxide. It can be seen from above equation (5) that the thickness of internally oxidised layer is inversely proportional to the mole fraction of aluminium. This suggests that ultimately the shift from internal to external oxidation will occur as the internal oxide layer decreases with increase of mole fraction of aluminium. [60] reported that at least 17wt% of aluminium are needed in order for the shift to happen for NiAl super-alloy system.

This value, however, seems rather high. One way of getting the amount of aluminium to drop down to a reasonable level would be to add other elements, such as chromium [61]. As this reactive element forms chromia which acts as getter for trace amounts of oxygen and enables the diffusion of oxygen to slow down, thus, internal oxidation can also be retained. Figure 14 shows the type of oxide for the NiCrAl system at 1000˚C, it can be seen that in order to ensure Al_2O_3 growth in such system, an approximately 35 at% of aluminium is required. However, this value can be reduced significantly to 12 at% with a 5 at% additional element of chromium.

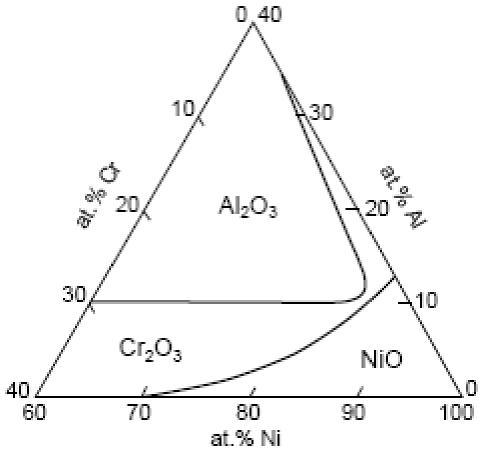

Figure 14 – Oxides for NiCrAl system at 1000˚C [62].

So far, we've been focusing on the oxide that forms under steady state stage at the bond coat and thermally grown oxide interface. For a complete thermal barrier coating system, other oxides can form due to elements reactions from bond coat and top coat. Literature from [63] reported that mixed oxides in form of, chromia oxide $(Al,Cr)_2O_3$; spinel oxide $Ni(Al,Cr)_2O_4$ and nickel oxide (NiO) are formed very early under high temperature exposure and continues to grow as temperature increases to about 1200˚C.

2.2.3 - Effect of Creep on Stress Development

Plastic and Visco-plastic Behaviour

Freborg [64] investigated the stress development of an APS TBC system in which the thermal cycling, i.e. oxidation as well as TC and BC creep have been introduced into a finite element model. The results indicated that TC and BC creep has the prominent effect on the tensile and compressive stress generated at BC peak, off peak and valley positions respectively. Oxidation, on the other hand, causes the stress transition to occur in which at peak and off peak location the stress changes from tensile to compressive and vice versa at valley location. The author concluded that the size of the tensile region increases with the increase of TGO thickness. It is, therefore, crack growth can be effectively controlled by linking early generated cracks near peak region due to tensile region at the valley. As a result, combination action of oxidation and creep are the factors that lead to crack progression and spallation. However, other factors, such as sintering phase changes in the TC, BC and TGO layer should be considered for a better understanding of the failure mechanism.

Cheng [65] studied the thermal/residual stress response from non-flat interface PVD samples by considering nonlinear plastic behaviour of the TGC/BC interface. It was found that the effective plastic strain, which could lead to fatigue cracks in BC is highly concentrated at the tip of the TGO/BC interface cavity after cool down. The author concluded the literature by stating that the stresses obtained from the elastic analysis is higher than that of elastic-plastic analysis. In other words, elastic calculations overestimate the stresses in the TBC systems, thus it is not an ideal procedure for calculating stresses for an interface which has the wavy form. Furthermore, an irregular interface is one of the contributors to large localized tensile stress to occur in the TGO layer in radial direction.

2.3 - Failure of TBCs

A typical overhaul life span for the TBC system in a modern jet engine sits between 10000 and 20000 hours equivalent to 2000 to 4000 thermal cycles [12]. In recent years, many experimental [66, 67], numerical [68] and analytical studies [69] have been carried out to assist understanding of the mechanisms which cause failure for the TBC system. Many factors that influence the lifetime of a TBC system have since been identified as depended on the operating temperature, oxidation exposure time and total number of thermal cycles. Due to the complex nature TBC system, each individual layer has its own unique thermal and mechanical properties; hence multiple combinations of failure mechanisms can occur simultaneously. Some of the key mechanisms have been summarised by [6], Figure 15.

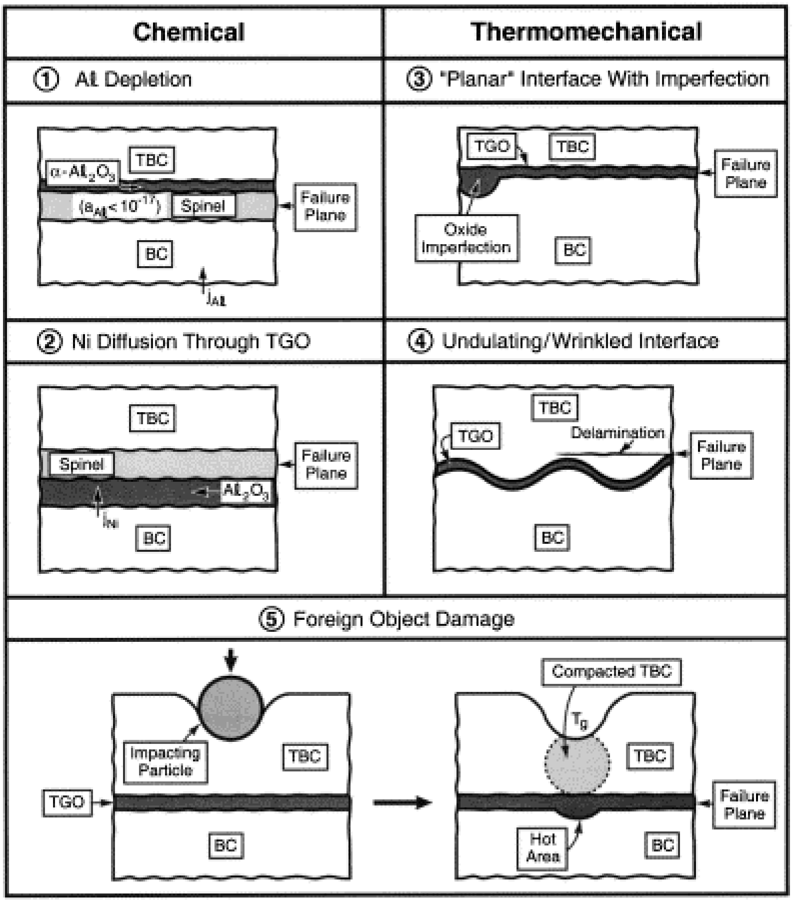

Figure 15 – Schematic illustrates some of the key failure mechanism for TBC system [6]

2.3.1 - Aluminium Depletion

TBC system failure caused by depletion of aluminium from the bond coat was investigated by [70]. As the bond coat gets oxidised, the content of aluminium decreases in the bond coat as the depletion takes place at the TGO/BC interface. This process mainly results in the formation of less desirable oxide and allows oxygen to diffuse much faster to create localised oxidation zones [71]. Furthermore, as the aluminium depletion continues, compressive residual stress which is proportional to the TGO thickness can reach to its highest level at ambient temperature [19]. Ultimately, failure is likely to occur at the interface where the phase transformation (from aluminium rich ductile β-phase to more stiffer and brittle γ-phase) normally takes place [67].

2.3.2 - Top Coat Sintering

Sintering of ceramic top coat takes place when the coated component undergoes substantial high temperature exposure [72]. For EBPVD manufactured top coat, the morphology of the columnar microstructure changes depending on the surface on which the ceramic coating is coated. If the surface is flat, the columnar structure stay upright and parallel to one another, all columns are sintered together and the microstructure stability remain unchallenged, so that crack initiation can be prevented with no phase transformation at 1400°C for 135 hours [73]. If, however the surface is not flat, potential necking formation, and clusters of each individual columns are sintered together to form localised densification region. Furthermore, it has been reported [41] that number of necks (contact region) along the length of the column structure effectively dictate the sintering force. Figure 16 illustrates necking formation between each column. The consequence of top coat sintering can result in

- Lose of strain tolerance due to increase in stiffness upon necking formation [74];
- Localized densification leads to an increase in thermal conductivity as well as rumpling upon thermal cycling [75];
- Paving an easier path for crack propagation when damages are caused by foreign object [76].

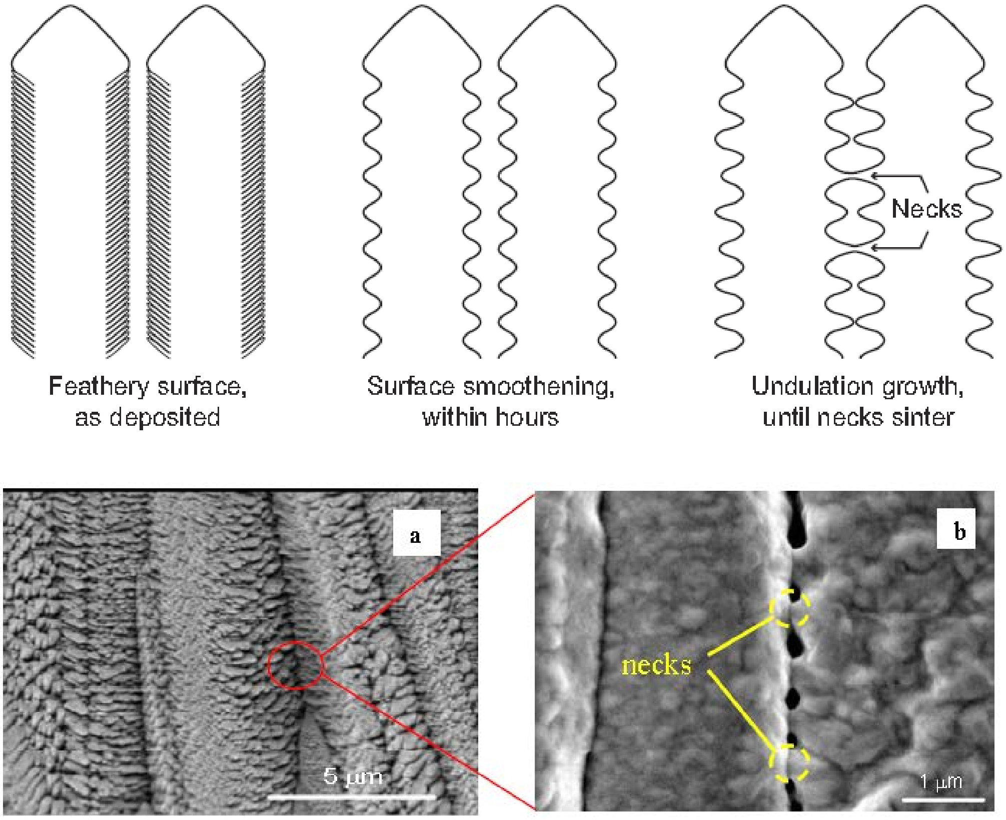

Figure 16 – Schematic illustration on necking formation when top coat undergoes high temperature sintering. At first, the initial feathery structure starts to smooth. As the exposure gets prolonged, surface undulation growth creates necks which form localised densification region. The microstructure images reveal the true morphology of necking [73, 77].

2.3.3 - Rumpling

After thermal cycling, roughening of bond coat surface is called rumpling. This phenomenon is often regarded as one of the mechanisms which lead to reduction of TBC system life. Not all bond coats have this phenomenon, it has been reported that apart from NiCoCrAlY alloyed bond coat, surface roughening has occurred for MCrAlY and Pt aluminide bondcoats [78]. Different presumption that focuses on the stress development initiated by the misfit of thermal expansion coefficient may have been the cause of rumpling. Other researcher may have argued that the phenomenon of rumpling is caused by the bond coat volume expansion as the result of martensitic transformation at each thermal cycle [79]. Furthermore, the author also pointed out that the coating thickness is inversely proportional to the undulation amplitude.

Bond coat experiences plastic deformation during cooling period in each thermal cycle [80, 81], this makes the undulation amplitudes to increase in the TGO layer. This growth in amplitude has been confirmed by the in plane compressive stress that develops in the TGO layer during cooling [82, 83]. TBC system is considered to be failed as the roughness of TGO layer reaches to a critical/unstable point where cracks in top coat layer start to grow and lead to delamination at the TC/TGO interface [6]. Experimental work done by [84] investigated further on the true cause of rumpling. They found that the reason for rumpling to occur not only because of thermal expansion coefficient misfit between layers or the volume changes due to martensitic transformation in the bond coat, but also due to inter-diffusion between bond coat and substrate.

2.3.4 - Foreign Object Damage

This type of damage is usually caused by the foreign objects that are sucked into the engine during operation (mainly during take-off), often known as Bird-Strike [85]. Once entered the engine, size of fragmental pieces of these objects can be very small (50 to 500μm). The impact velocity on the TBC system depends on the size of the object. [86] demonstrated that for smaller pieces the velocity can reach to 170 m/s, whereas for larger piece the impact velocity is reduced down to 10 m/s. The damage caused by the impact of foreign objects generally result in localized compression damage to the top coat, leading to plasticity deformation and densification at impact zone. Ultimately, thermal insulation capability of the top coat is compromised and through thickness kink bands development leads to interfacial delamination of top coat, Figure 17 [86].

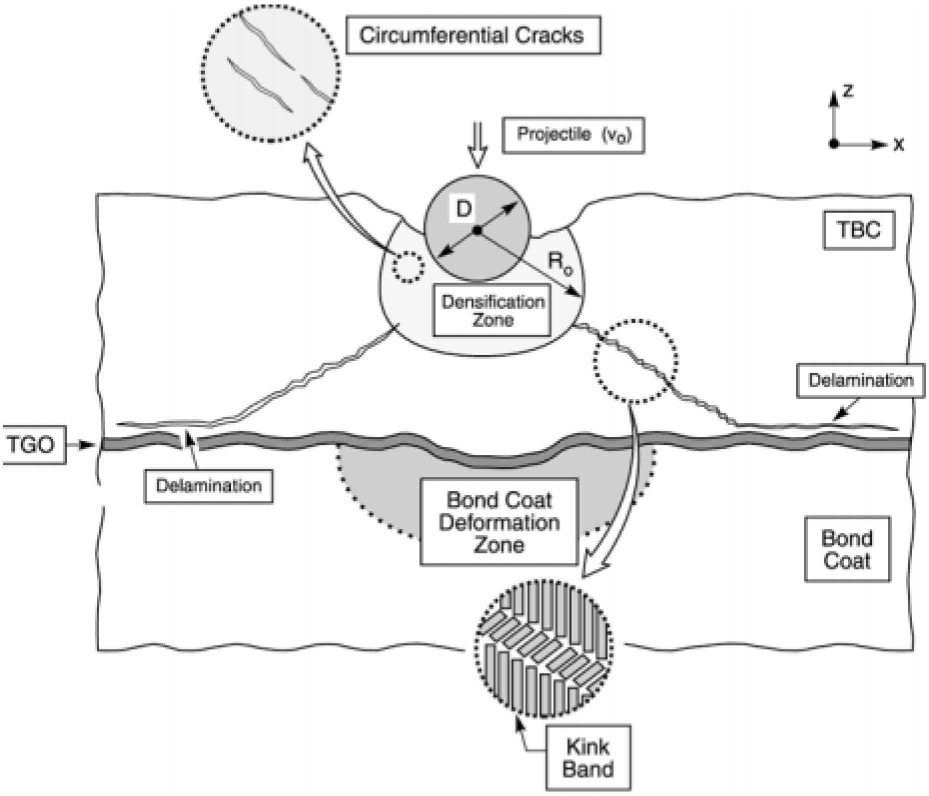

Figure 17 – Schematic illustrates the foreign object damage development [86].

2.3.5 - Erosion of APS and EBPVD Coating

The erosion damage somewhat differs from foreign object damage, purely due to the fact that the size of impact object is much smaller (less than 5μm) and impact zone is more evenly distributed along the coating. These imperfections at the top coat surface will lead to gradually degrading the overall performance of the TBC system [76]. Erosion-corrosion also has major role in the failure of TBC system. Depending on the coating technique, the erosion rate of EB-PVD coatings does not appear to be affected by the increasing in temperature, whereas for APS coating, a rapid increase in erosion rate with increase in temperature from 600-800˚C [87]. The author summaries the erosion rate of TBC system under various conditions shown in Table 3.

Table 3 – Erosion rate of TBC under various testing conditions [88].

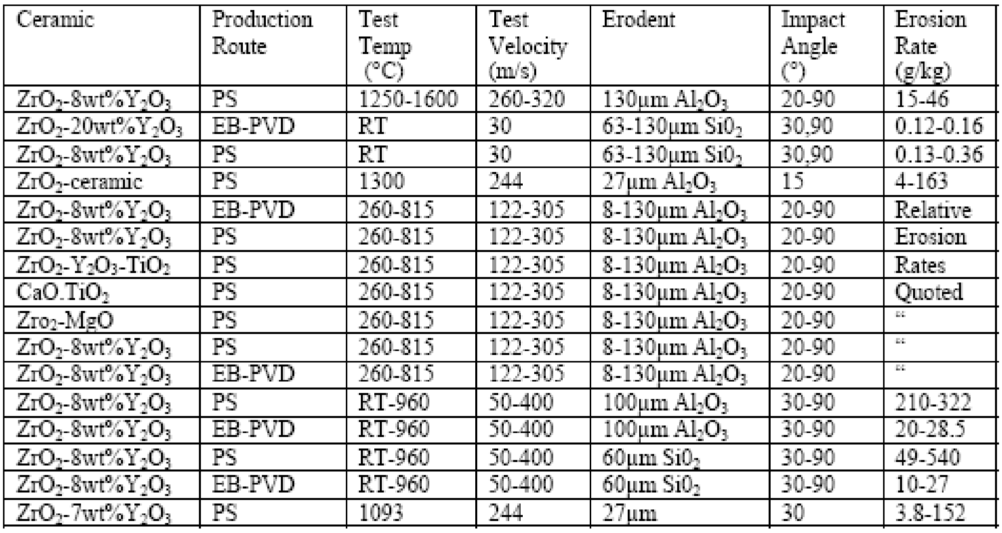

Ceramic	Production Route	Test Temp (°C)	Test Velocity (m/s)	Erodent	Impact Angle (°)	Erosion Rate (g/kg)
ZrO_2-8wt%Y_2O_3	PS	1250-1600	260-320	130µm Al_2O_3	20-90	15-46
ZrO_2-20wt%Y_2O_3	EB-PVD	RT	30	63-130µm $Si0_2$	30,90	0.12-0.16
ZrO_2-8wt%Y_2O_3	PS	RT	30	63-130µm $Si0_2$	30,90	0.13-0.36
ZrO_2-ceramic	PS	1300	244	27µm Al_2O_3	15	4-163
ZrO_2-8wt%Y_2O_3	EB-PVD	260-815	122-305	8-130µm Al_2O_3	20-90	Relative
ZrO_2-8wt%Y_2O_3	PS	260-815	122-305	8-130µm Al_2O_3	20-90	Erosion
ZrO_2-Y_2O_3-TiO_2	PS	260-815	122-305	8-130µm Al_2O_3	20-90	Rates
CaO.TiO_2	PS	260-815	122-305	8-130µm Al_2O_3	20-90	Quoted
Zro_2-MgO	PS	260-815	122-305	8-130µm Al_2O_3	20-90	"
ZrO_2-8wt%Y_2O_3	PS	260-815	122-305	8-130µm Al_2O_3	20-90	"
ZrO_2-8wt%Y_2O_3	EB-PVD	260-815	122-305	8-130µm Al_2O_3	20-90	"
ZrO_2-8wt%Y_2O_3	PS	RT-960	50-400	100µm Al_2O_3	30-90	210-322
ZrO_2-8wt%Y_2O_3	EB-PVD	RT-960	50-400	100µm Al_2O_3	30-90	20-28.5
ZrO_2-8wt%Y_2O_3	PS	RT-960	50-400	60µm $Si0_2$	30-90	49-540
ZrO_2-8wt%Y_2O_3	EB-PVD	RT-960	50-400	60µm $Si0_2$	30-90	10-27
ZrO_2-7wt%Y_2O_3	PS	1093	244	27µm	30	3.8-152

2.4 - Test Methods

During actual operation environment, TBC system on the turbine blade will endure several internal and external degradation mechanisms or attacks [89], Figure 18 illustrates some of key damage sources to the turbine coatings. The topic of hot corrosion in the aviation industry did not receive much of an attention until the Vietnam conflict in which the gas turbine engines of military aircraft suffered severe corrosion when operating over seawater. Before the true recognition of hot corrosion mechanism, the initial understanding of failed parts often indicated sulfides of nickel and chromium, the cause of failure from inspection was named as sulfidation. The purpose of this section is to review some of the fundamental knowledge of hot corrosion and appropriate testing methods, i.e. burner rig testing.

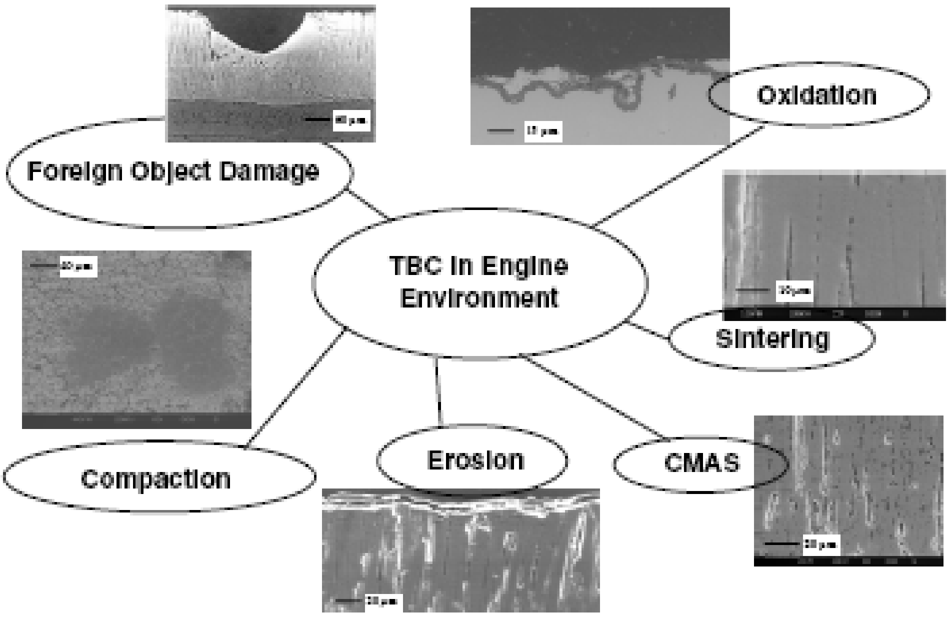

Figure 18 – Schematic illustrates the possible damage sources to TBCs in operation[89]

2.4.1 - Definition of Hot Corrosion

The accelerated oxidation induced from the thin layer of fused salt contamination at elevated temperature is defined as hot corrosion [90]. Fused contaminants result from low fuels quality contain impurities such as Na and V all of which can produce Na_2SO_4, NaCl and V_2O_5 salt on the surface of the turbine blade. Such compound and oxide can react with YSZ and cause phase transformation[1] during cooling [91] , thus have the tendency to damage the protective oxide surface. Furthermore, attack from calcium-magnesium-aluminosilicate (CMAS) deposits can also result in reduction of strain tolerance and lead to premature failure of the coating.

Type of Hot Corrosion

Two types of hot corrosion exist, namely, Type I High Temperature Hot Corrosion (HTHC) ranging from 850 to 950˚C [92] or higher and Type II Low Temperature Hot Corrosion (LTHC) ranging from 650 to 800˚C [93]. At elevated temperature, hot corrosion starts to occur in which the deposit is in liquid state or in solid state and melts into liquid state due to reaction with the environment. Parameters such as alloy composition; thermo-mechanical condition; contaminant composition; flux rate; temperature cycles; gas velocity and composition and erosion process can have the effect on the development of the type of hot corrosion [90].

2.4.2 - Hot Corrosion Test Method

Various test methods have been reported and used to study hot corrosion [94], such as high pressure high velocity burner rigs; atmospheric pressure simulation rigs and high atmospheric pressure and low velocity burner rigs; as well as numerous versions of electrochemical; crucible and furnace tests. Although high pressure high velocity burner rigs can simulate all aspect of the engine accurately, high installation, operating and maintenance costs severely hindered the use of such facility. While the simpler laboratory furnace and crucible tests have been shown the lag of ability to simulate realiably the

---

[1] Transformation of tetragonal or cubic zirconia to monoclinic phase.

corrosion product morphologies found in operating turbines [95]. The first laboratory test method known as immersion testing and cannot be considered reliable to simulate the true gas turbine environment [96]. For the purpose of studying corrosion mechanism, the salt coated method is well established in the academia field. However, for engine manufacturers, realising the full potential of relative alloy performance and simulating the gas turbine environment can be crucial towards the design of TBCs, thus atmospheric pressure simulation and high (Mach 0.3-1.0) and low (Mach 0.1-0.3) velocity burner rig test is recognised as the most suitable laboratory testing method to date. The Mach number is the ratio between object moving speed through a fluid and the local speed of sound.

2.4.3 - Burner Rig

This type of testing system is shown in Figure 19 [97]. Highly flammable gases are fed through tubes through a burner which produces a high temperature flame. In addition, sea salt solution or dust particles can be injected through an injection system which mounted near the burner head.

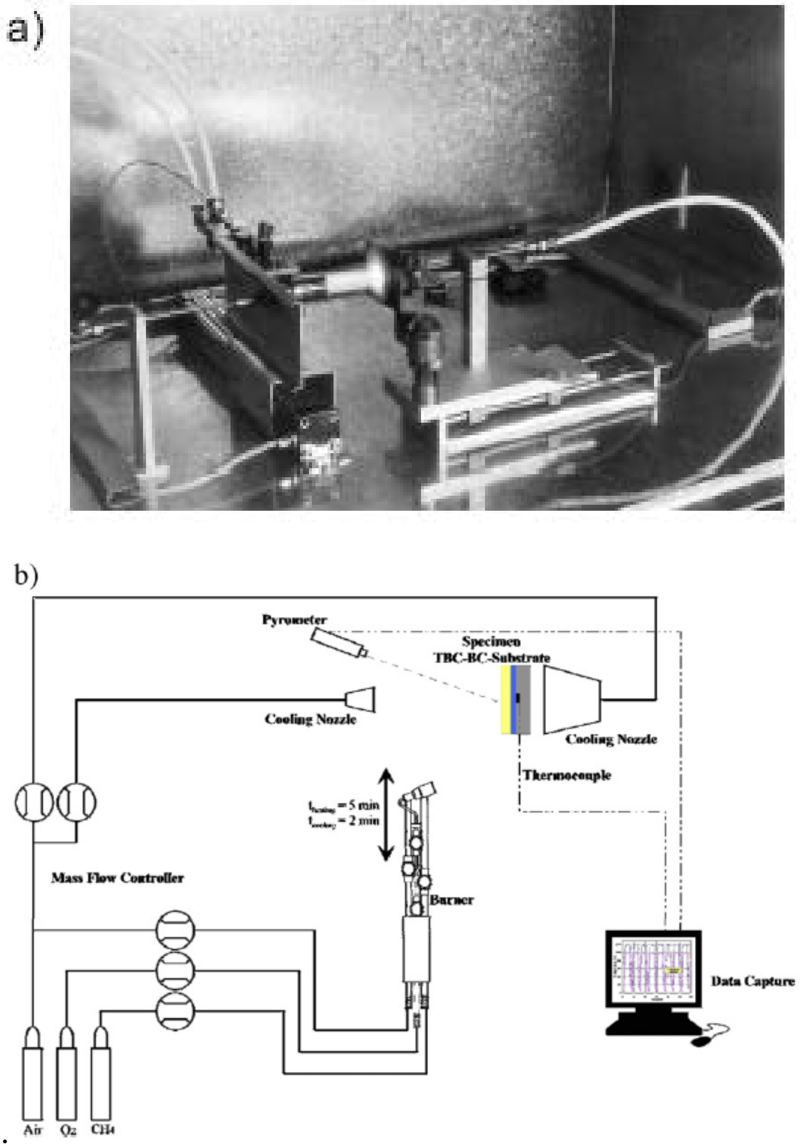

Figure 19 – a) actual testing rig during operation, b) schematic illustrates the setup of the rig system [97].

From this setup, the movement of the burner is controlled by the compressed air driven slide. During the heating stage, the burner is positioned right in front of the sample. Back cooling facility is used during both heating and cooling stage to the sample (at uncoated side) in order to create a temperature gradient. Figure 20 shows burner rig testing temperature curve [98].

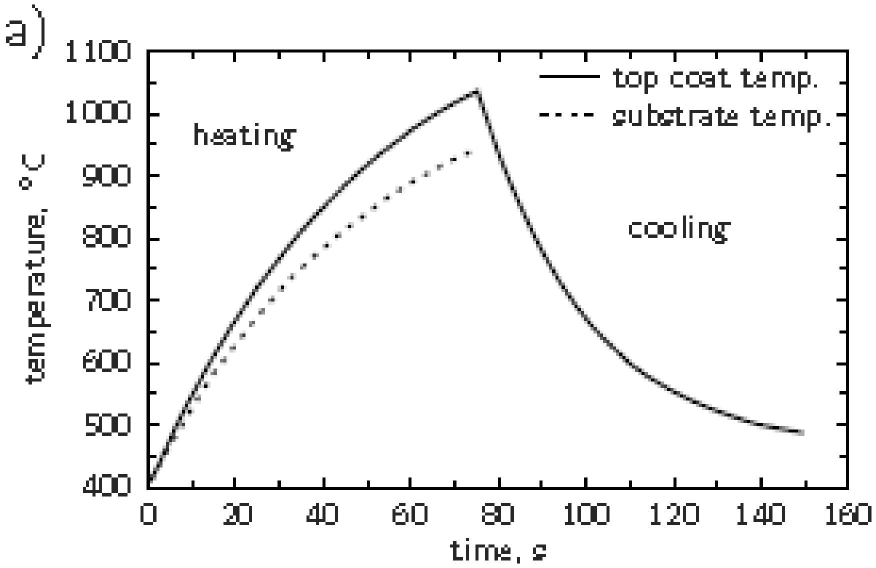

Figure 20 – Burner rig thermal cycles temperature curve [98].

Rig Operating Condition

Ideally, it would be desirable to control deposition rate directly in order to simulate the exact operating environment for the turbine blades. However, due to the complexities of such controlled operation, it is not possible to direct control of deposition rates on the specimens. However, it has been observed in the literature [95] that the deposition rate depends upon the contaminant flux rate (CFR) in the combustion gas, thus the corrosion rates are dependent upon the CFR. The calculation of contaminant flux rate can be found in the literature [94].

According to [95], burner rig CFRs are selected on the basis that the corrosion product morphology achieved in the rig within the desired testing time is similar to that of the blades taken from actual operating engine. Therefore, a wide range of rig operating conditions are to be considered. Table 4 shows some of the typical operating conditions for some high and low velocity rigs.

Table 4 – Burner rig operating conditions giving deposition and sodium mass flux rates [95].

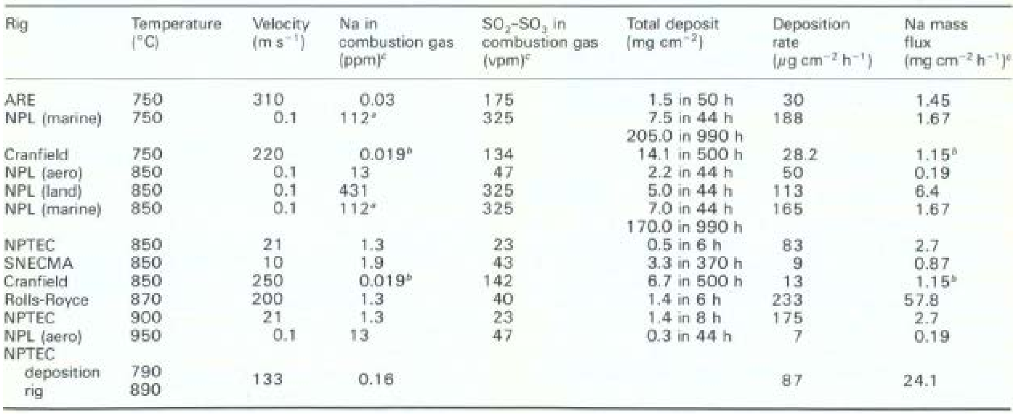

Rig	Temperature (°C)	Velocity (m s^{-1})	Na in combustion gas (ppm)[c]	SO_2–SO_3 in combustion gas (vpm)[c]	Total deposit (mg cm^{-2})	Deposition rate (μg cm^{-2} h^{-1})	Na mass flux (mg cm^{-2} h^{-1})[c]
ARE	750	310	0.03	175	1.5 in 50 h	30	1.45
NPL (marine)	750	0.1	112[a]	325	7.5 in 44 h 205.0 in 990 h	188	1.67
Cranfield	750	220	0.019[b]	134	14.1 in 500 h	28.2	1.15[b]
NPL (aero)	850	0.1	13	47	2.2 in 44 h	50	0.19
NPL (land)	850	0.1	431	325	5.0 in 44 h	113	6.4
NPL (marine)	850	0.1	112[a]	325	7.0 in 44 h 170.0 in 990 h	165	1.67
NPTEC	850	21	1.3	23	0.5 in 6 h	83	2.7
SNECMA	850	10	1.9	43	3.3 in 370 h	9	0.87
Cranfield	850	250	0.019[b]	142	6.7 in 500 h	13	1.15[b]
Rolls-Royce	870	200	1.3	40	1.4 in 6 h	233	57.8
NPTEC	900	21	1.3	23	1.4 in 8 h	175	2.7
NPL (aero)	950	0.1	13	47	0.3 in 44 h	7	0.19
NPTEC deposition rig	790 890	133	0.16			87	24.1

Standardisation of Hot-(salt) Corrosion Test

In the literature done by [94], the author recommended a guideline for such test in the burner rigs. Two international round robin tests have been completed [99] by ASTM in 1970 and Versailles Project on Advanced Materials and Standard VAMAS. The following text will summarise the standardisation in brief.

- Test Temperature – 700-900˚C ±10˚C (This temperature has been increased since)
- Duration – 500hours. Shorter duration should be between 100-300hours. Below 100h may not be valid. (the duration needs to be modified to suit temperature)
- Test cycle – specimens should be cycled from the test temperature to room temperature at once every 10hours i.e. 50 cycles per 500hours test duration with a maximum of 100 cycles per 500hour test.
- Fuel – ASTM D1655 Jet A for low air/fuel ratio.
- Sea salt additions – ASTM D1141-75.
- Reference Materials
  - Alloy – IN738LC and Rene 80
  - Coating – Aluminized coating system, i.e. NiAl or PtAl
- Pin Geometries
- Assessment of deposition rate
- Assessment of deposit chemistry
- Assessment of corrosion
  - Visual inspection
  - Mass change measurement (optional)
  - Assessment of corrosion product chemistry
  - Measurement of section loss

Geometry of the Specimen

It was noted from the code of practice [100] that the size and shape of test specimens may be governed by the type and form of material available. Three basic shapes of specimen can be used, shown in Figure 21.

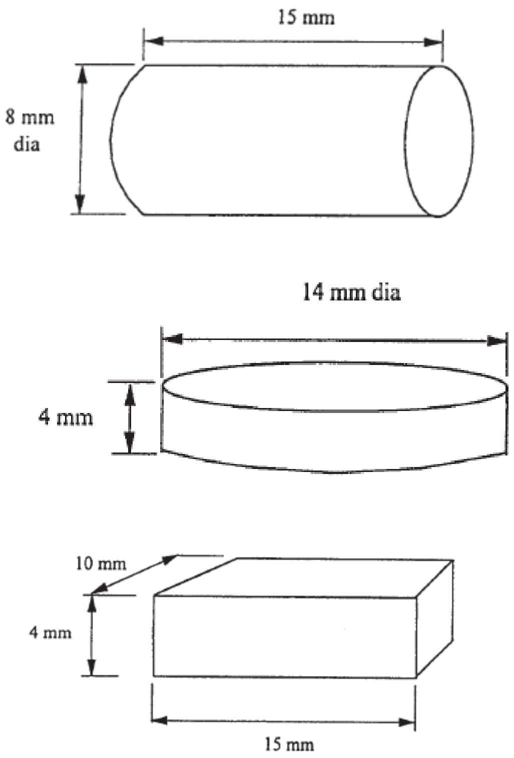

Figure 21 – Types of corrosion test specimen as recommended in the guideline [99].

However, for more specific corrosion testing applications, such as, thermal barrier coating, the size of specimen may vary. From the literature done by [101], the author used a round shaped specimen, Figure 22. The sample is flat in the middle and has round edges. A notch is machined around the whole outer edge of the sample so that sample holder can be locked without generating large contact forces, this can be considered as an advantage due to extensive heat transfer.

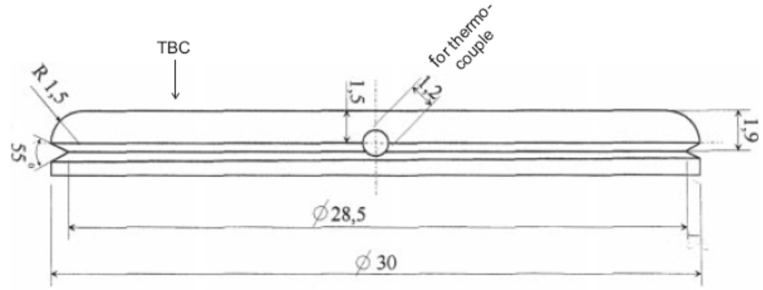

Figure 22 – Specific sample geometry showing the configuration [97]

2.4.4 - Thermal Fatigue

Due to the misfit of thermal expansion coefficient between the substrate/bond coat/top coats, stresses are generated in the overall TBC system after each thermal cycle. In the previous section, one of the mostly adopted thermal cycling tests, burner rig test has been introduced. Another popular test method which will be described next is thermal cycling fatigue test uses a cyclic furnace facility.

In contrast to burner rig testing, the samples that are tested in cyclic furnace move in and out between high and low temperature zones, Figure 23. Such testing method has less heating intensity compared with direct flame heating and due to lack of back cooling to the sample, through thickness temperature gradient within the testing piece appears to be less apparent during heating process. In addition, high temperature dwell time appears to be longer than burner rig test, Figure 24.

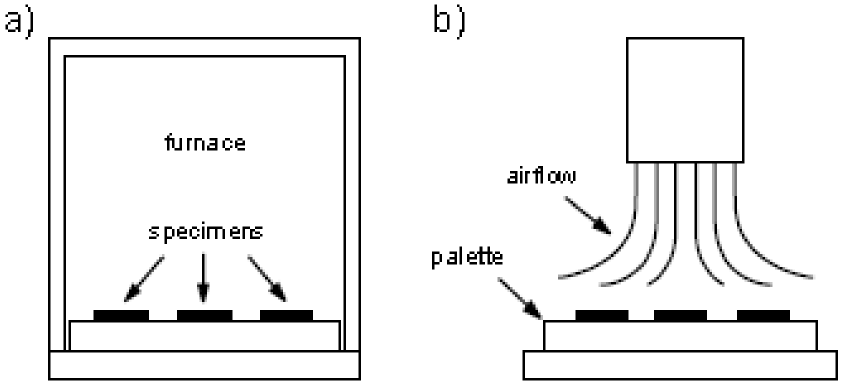

Figure 23 – Schematic illustrates a) high temperature stage, b) compressed air cooling stage [98].

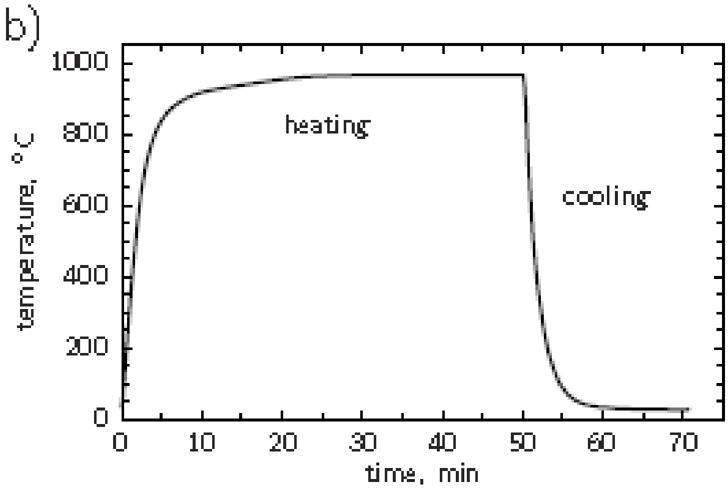

Figure 24 – Temperature curve from a cyclic furnace [98].

2.5 - Life Prediction Modelling of TBCs

Early days of the development of life prediction models for thermal barrier coating systems are mainly empirically based on and driven by the fitting model parameters to data generated under thermo mechanical fatigue testing, i.e. burner-rig tests [102]. Perhaps the simplest way of predicting TBC service life is to correlate the spallation life with thermal exposure time and number of cycles. In the literature done by Meier [103] proposed a life prediction model that is based on the maximum in plane TGO layer tensile strain and TGO formation for both APS and PVD TBCs. However, the construction of the model seems to be questionable as the TGO layer is under compressive strain. A life prediction model was developed by Chan et al. [104] for PVD TBCs that is based on coating degradation mechanisms including oxidation; spallation and aluminium depletion in the bond coat. Many factors influence the life of TBC systems; it is however, not an easy task to predict the failure. Generally speaking, maximum operating temperature can be seen as a critical factor for predicting TBC life. Yanar [105] demonstrated that failure of TBC occurs under 45 minutes cyclic heating at 1100 °C and 1200 °C after 1200 cycles and 120 cycles respectively. This result shows that the model developed by the author is sensitive and capable to predict the TBC failure at various designated operating temperatures. The accuracy of life prediction of TBCs can be challenging due to scattering of data even among identically processed specimens. Initial coating process defects and microstructure variability are the major influence factors. It is unavoidable that randomly distributed flaws do exist within the TC; the scatter in fracture strength may be caused by the severity and location of these flaws [106]. The following text will give some insights on models that have been built based on the stress distribution between individual layers and diffusion of elements.

2.5.1 - Stress Distribution Modelling

The stress evolution and deformation for each individual layer in the TBC system can be predicted through appropriate calculations by the commercial available finite element software. Mechanical failures in the TGO and adjacent coating layers caused by the external loading during service (at high temperature stage); temperature differences through materials after thermal cycles due to mismatch of thermal expansion coefficient and oxide formation can be predicted using the method of total strain superposition, Figure 25. Martena [107] reported that failures result from the strain relief in the top coat after the total strain reaches a certain critical value.

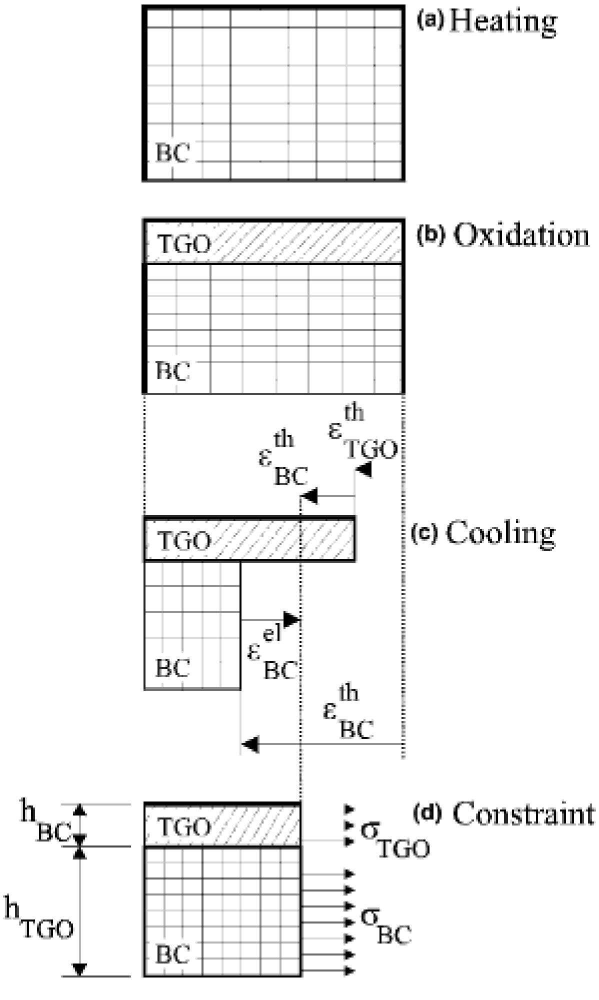

Figure 25 – Schematic illustrates the stress field upon formation of thermal grown oxide [107]. a) heating bond coat sample without oxide; b) oxide forming; c) cooling stage with bond coat and oxide layer free to shrink; d) stress occours when constraint is applied.

A methodology based on stress evolution measurement for predicting the life of EBPVD TBC system have been developed by Busso [108]. In his analysis, the model is constructed by integrating the quantified TBC system damage, so that the damage measurements related to the roughness upon each thermal cycles can be achieved. Then the life of the TBC system can be predicted by extracting the data from finite element analysis from which the key relationship between the accumulations of localised stress at the interface over time can be obtained. However, this over simplified finite element model is thought to be inaccurate due to the fact that uneven growth of thermally grown oxide is excluded in the analysis, Figure 26.

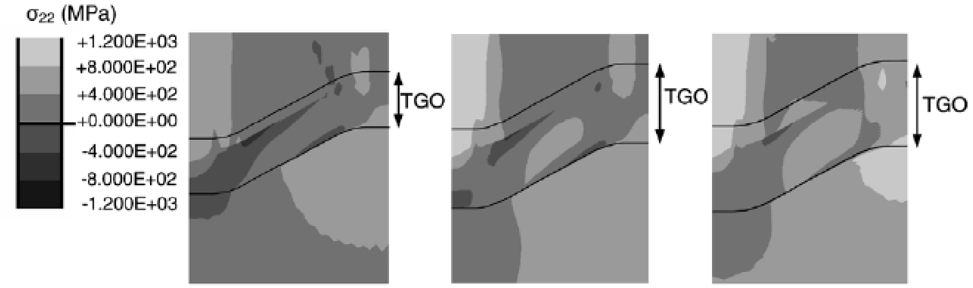

Figure 26 – Out of plane stress generated at TGO interface during cooling down period from 1000°C to ambient temperature for 61, 167 and 241 hours [108].

2.5.2 - Elemental Diffusion Model

The life of TBC system can be influenced by the rate and mechanism of depletion of aluminium from the bond coat. Numerical models demonstrated by [109, 110] have highlighted the TGO growth mechanisms caused by the transport diffusion of certain elements through the top coat and bond coat layer in the TBC system, Figure 27 a). These models also have the capability of predicting the consumption of essential elements within TBC system Figure 27 b).

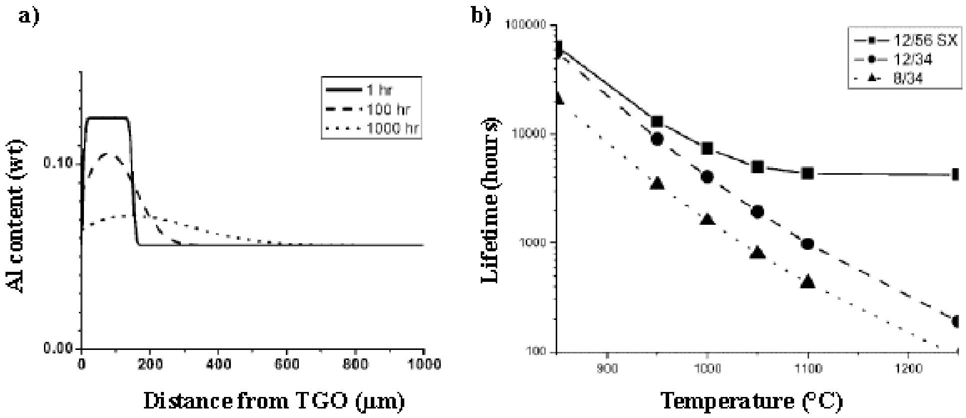

Figure 27 – a) Plot showing bond coat aluminium diffusion leads to TGO growth; b) Plot showing the life of the TBC system due to depletion of aluminium from the bond coat with internal oxidation at a temperature range between 850°C to 1250°C [109].

2.6 Conclusion

In this chapter, a number of papers have been reviewed covering the work carried out over the past decade or so, if not longer, in terms of the recognition of the important role of the conventional three-layer thermal barrier coating system applied to modern single-crystal turbine engine blade, and high temperature degradation and failure of thermal barrier coatings. The three-layer system, namely, bond coat (BC); top ceramic coat (TC) and thermally grown oxide (TGO), each layer has its unique functional contribution towards the overall coating system. To date, The advantage of single crystal alloy over other conventional polycrystal alloy is that most of solutes of grain boundary strengthening are removed, this results in an increase of melting temperature up to 1250˚C. However, with increase of thermal efficiency from the modern jet engines, the turbine entry temperature, known as TET, can result in significant damage to the uncoated turbine blade. Therefore, the coating system offers thermal protection (improving through thickness thermal gradient) to the metallic substrate material as well as improving the overall lifespan of the turbine itself.

Oxidation of BC and the process of TGO growth is a primary focus on high temperature degradation mechanism of TBCs. Consumption of aluminium at high temperature from bond coat and substrate layer results in the formation of α-Al2O3 which is the most stable phase of oxide in TGO layer. As the TGO layer grows, the interface between BC and TC layer with the TGO layer is sequentially formed. This leads to three distinct stages of BC oxidation, namely, a transient stage in which all species of oxide are formed simultaneously; followed by the steady state stage where formation of most stable phase of oxide takes place and finally the breakaway stage results in spallation and the coating system is considered to have lost its protection to the metallic substrate.

Due to the complex nature TBC system, each individual layer has its own unique thermal and mechanical properties; hence multiple combinations of failure mechanisms can occur simultaneously. Some of the key failure mechanisms such as aluminium depletion, top ceramic coat sintering, rumpling of bond coat, damage induced by foreign object as well as erosion of coatings are reviewed. Among all of failure mechanisms, top coat spallation and TGO instability caused by the rumpling of the bond coat are said to be the major ones. From the perspective of experimental work, burner rig testing is proven to be the most relevant and reliable testing method.

Due to the complexity of flame control process, mass flow controller needs to be included in the system in order to control the flame temperature and cooling rate at the back of the sample. Furthermore, thermocouples will also be included with Labview software to be used to give an overall control of the whole burner rig system. The testing procedure should follow the international test standard, however, due to the laboratory limitation; the detailed procedure will need to be altered. The analysis of the cross-sectional tested sample will be carried out by using SEM; EDX and XRD. This would allow us to further understand how the TGO layer behaves under different test conditions and how the morphology change dependent on the different materials. In addition, interface rampling amplitude will be measured in order to carry out comparison work with the numerical results obtained from the model.

The main focus of the mathematical model is to develop a simplified model through asymptotic analysis based upon the small amplitude of the surface roughness relative to the thickness of the conventional TBC. By reducing the geometrical complexity of the problem it will be possible to investigate how the rates and sizes of the various physical processes affect the outcome without using computationally expensive methods. This work involves

- Formulate full partial differential equation model for the system.
- Determine the critical processes using dimensional analysis.
- Formulate reduced model using asymptotic methods.
- Determine appropriate solution strategy.
- Comparison with previous numerical and experimental results.
- Model refinement.

Such approach will be able to deliver a simplified model of this complex system, increased understanding of the interaction of the various factors that affect the outcome, and novel ideas for modifications of TBCs to increase their expected lifetime.

References

1. Chen, L., Yttria-stabilized zirconia thermal barrier coatings—a review. Surface Review and Letters, 2006. 13(05): p. 535-544.
2. Leyens, C., et al. R&D status and needs for improved EB-PVD thermal barrier coating performance. in MATERIALS RESEARCH SOCIETY SYMPOSIUM PROCEEDINGS. 2000. Cambridge Univ Press.
3. Wright, P. and A. Evans, Mechanisms governing the performance of thermal barrier coatings. Current Opinion in Solid State and Materials Science, 1999. 4(3): p. 255-265.
4. Tolpygo, V., D. Clarke, and K. Murphy, Oxidation-induced failure of EB-PVD thermal barrier coatings. Surface and Coatings Technology, 2001. 146: p. 124-131.
5. Tolpygo, V.K., D. Clarke, and K. Murphy, Evaluation of interface degradation during cyclic oxidation of EB-PVD thermal barrier coatings and correlation with TGO luminescence. Surface and Coatings Technology, 2004. 188: p. 62-70.
6. Evans, A.G., et al., Mechanisms controlling the durability of thermal barrier coatings. Progress in materials science, 2001. 46(5): p. 505-553.
7. He, M., A. Evans, and J. Hutchinson, Effects of morphology on the decohesion of compressed thin films. Materials Science and Engineering: A, 1998. 245(2): p. 168-181.
8. Hutchinson, J. and Z. Suo, Mixed mode cracking in layered materials. Advances in applied mechanics, 1992. 29(63): p. 191.
9. Evans, A., M. He, and J. Hutchinson, Effect of interface undulations on the thermal fatigue of thin films and scales on metal substrates. Acta materialia, 1997. 45(9): p. 3543-3554.
10. Choi, S.R., J.W. Hutchinson, and A. Evans, Delamination of multilayer thermal barrier coatings. Mechanics of materials, 1999. 31(7): p. 431-447.
11. Stöver, D. and C. Funke, Directions of the development of thermal barrier coatings in energy applications. Journal of Materials Processing Technology, 1999. 92: p. 195-202.
12. Stolle, R., Conventional and advanced coatings for turbine airfoils. MTU Aero Engines, D-80995 München http://www. mtu. de/en/technologies/engineering_news/conventional_and_advanced_coati ngs. pdf.(Accesed in May).
13. Karlsson, A.M., Modelling Failures of Thermal Barrier Coatings. Key Engineering Materials, 2007. 333: p. 155-166.
14. Wadley Research Group. University of Virginia.
15. Goward, G., Progress in coatings for gas turbine airfoils. Surface and Coatings Technology, 1998. 108: p. 73-79.
16. Levi, C.G., Emerging materials and processes for thermal barrier systems. Current Opinion in Solid State and Materials Science, 2004. 8(1): p. 77-91.
17. Haynes, J., et al., Influence of sulfur, platinum, and hafnium on the oxidation behavior of CVD NiAl bond coatings. Oxidation of metals, 2002. 58(5-6): p. 513-544.
18. Shi, J., S. Darzens, and A.M. Karlsson, Aspects of the morphological evolution in thermal barrier coatings and the intrinsic thermal mismatch therein. Materials Science and Engineering: A, 2005. 392(1): p. 301-312.
19. Rabiei, A. and A. Evans, Failure mechanisms associated with the thermally grown oxide in plasma-sprayed thermal barrier coatings. Acta materialia, 2000. 48(15): p. 3963-3976.

20. Darzens, S. and A.M. Karlsson, On the microstructural development in platinum-modified nickel-aluminide bond coats. Surface and Coatings Technology, 2004. 177: p. 108-112.
21. Cernuschi, F., et al., Thermal diffusivity/microstructure relationship in Y-PSZ thermal barrier coatings. Journal of thermal spray technology, 1999. 8(1): p. 102-109.
22. Stecura, S., Effects of compositional changes on the performance of a thermal barrier coating system. 1979.
23. Evans, A., D. Clarke, and C. Levi, The influence of oxides on the performance of advanced gas turbines. Journal of the European Ceramic Society, 2008. 28(7): p. 1405-1419.
24. Johnson, C., et al., Relationships between residual stress, microstructure and mechanical properties of electron beam–physical vapor deposition thermal barrier coatings. Surface and Coatings Technology, 1998. 108: p. 80-85.
25. Mercer, C., et al., On a ferroelastic mechanism governing the toughness of metastable tetragonal-prime (t′) yttria-stabilized zirconia. Proceedings of the Royal Society A: Mathematical, Physical and Engineering Science, 2007. 463(2081): p. 1393-1408.
26. Strangman, T.E., Thermal barrier coatings for turbine airfoils. Thin Solid Films, 1985. 127(1): p. 93-106.
27. Hesnawi, A., et al., Isothermal oxidation behaviour of EB-PVD MCrAlY bond coat. Vacuum, 2007. 81(8): p. 947-952.
28. Lee, C., et al., Phase transformation and bond coat oxidation behavior of plasma-sprayed zirconia thermal barrier coating. Surface and Coatings Technology, 2000. 124(1): p. 1-12.
29. Naumenko, D., et al., Failure mechanisms of thermal barrier coatings on MCrAlY-type bondcoats associated with the formation of the thermally grown oxide. Journal of materials science, 2009. 44(7): p. 1687-1703.
30. Reddy, A., et al., In situ study of oxidation-induced growth strains in a model NiCrAlY bond-coat alloy. Oxidation of metals, 2007. 67(3-4): p. 153-177.
31. Heuer, A., et al., The effect of surface orientation on oxidation-induced growth strains in single crystal NiAl: An in situ synchrotron study. Scripta materialia, 2006. 54(11): p. 1907-1912.
32. Gong, X.-Y. and D. Clarke, On the measurement of strain in coatings formed on a wrinkled elastic substrate. Oxidation of metals, 1998. 50(5-6): p. 355-376.
33. Toscano, J., et al., Parameters affecting TGO growth and adherence on MCrAlY-bond coats for TBC's. Surface and Coatings Technology, 2006. 201(7): p. 3906-3910.
34. Brindley, W.J. and R.A. Miller, Thermal barrier coating evaluation needs, 1990, National Aeronautics and Space Administration, Cleveland, OH (USA). Lewis Research Center.
35. Cruse, T.A., B. Johnsen, and A. Nagy, Mechanical properties testing and results for thermal barrier coatings. Journal of thermal spray technology, 1997. 6(1): p. 57-66.
36. Siebert, B., et al., Changes in porosity and Young’s Modulus due to sintering of plasma sprayed thermal barrier coatings. Journal of Materials Processing Technology, 1999. 92: p. 217-223.
37. Zhu, D. and R.A. Miller, Thermal conductivity and elastic modulus evolution of thermal barrier coatings under high heat flux conditions. Journal of thermal spray technology, 2000. 9(2): p. 175-180.
38. Basu, D., C. Funke, and R. Steinbrech, Effect of heat treatment on elastic properties of separated thermal barrier coatings. Journal of materials research, 1999. 14(12): p. 4643-4650.

39. Unal, O., T.E. Mitchell, and A.H. Heuer, Microstructures of Y2O3-Stabilized ZrO2 Electron Beam-Physical Vapor Deposition Coatings on Ni-Base Superalloys. Journal of the American Ceramic Society, 1994. 77(4): p. 984-992.
40. Kaysser, W., et al. Processing, characterisation and testing of EB-PVD thermal barrier coatings. in AGARD Structures and Materials Panel Meeting on Thermal Barrier Coatings, AGARD R-823, AGARD (Advisory Group for Aerospace Research and Development), Aalborg, Denmark. 1998.
41. Flores Renteria, A., A small-angle scattering analysis of the influence of manufacture and thermal induced morphological changes on the thermal conductivity of EB-PVD PYSZ Thermal Barrier Coatings, 2007, Universitätsbibliothek.
42. Kofstad, P., High-temperature oxidation of metals. Vol. 584. 1966: Wiley New York.
43. Birks, N., G.H. Meier, and F.S. Pettit, Introduction to the high temperature oxidation of metals2006: Cambridge University Press.
44. Wagner, C. and J.H. Westbrook, Thermodynamics of alloys. Vol. 19. 1952: Addison-Wesley Reading, MA.
45. Pieraggi, B. Fundamental aspects of reactions at the metal/scale interface during scaling. in Materials Science Forum. 1997. Trans Tech Publ.
46. Ranjbar-Far, M., J. Absi, and G. Mariaux, Finite Element Modeling of the Different Failure Mechanisms of a Plasma Sprayed Thermal Barrier Coatings System. Journal of thermal spray technology, 2012. 21(6): p. 1234-1244.
47. Wu, F., et al., Thermally grown oxide growth behavior and spallation lives of solution precursor plasma spray thermal barrier coatings. Surface and Coatings Technology, 2008. 202(9): p. 1628-1635.
48. Giggins, C. and F. Pettit, Oxidation of Ni-Cr-Al Alloys Between 1000° and 1200° C. Journal of the Electrochemical Society, 1971. 118(11): p. 1782-1790.
49. Klumpes, R., et al., The influence of chromium on the Oxidation of β-NiAl at 1000° C. Materials and Corrosion, 1996. 47(11): p. 619-624.
50. Hindam, H. and D. Whittle, Microstructure, adhesion and growth kinetics of protective scales on metals and alloys. Oxidation of metals, 1982. 18(5-6): p. 245-284.
51. Evans, H. and M. Taylor, Oxidation of high-temperature coatings. Proceedings of the Institution of Mechanical Engineers, Part G: Journal of Aerospace Engineering, 2006. 220(1): p. 1-10.
52. Brumm, M. and H. Grabke, The oxidation behaviour of NiAl-I. Phase transformations in the alumina scale during oxidation of NiAl and NiAl-Cr alloys. Corrosion Science, 1992. 33(11): p. 1677-1690.
53. Gleeson, B., Thermal barrier coatings for aeroengine applications. Journal of propulsion and power, 2006. 22(2): p. 375-383.
54. Grabke, H., Oxidation of NiAl and FeAl. Intermetallics, 1999. 7(10): p. 1153-1158.
55. Wagner, C. and K. Gruenewald, CONTRIBUTION TO THE THEORY OF THE TARNISHING PROCESS. 3, 1966, DTIC Document.
56. Niranatlumpong, P., C. Ponton, and H. Evans, The failure of protective oxides on plasma-sprayed NiCrAlY overlay coatings. Oxidation of metals, 2000. 53(3-4): p. 241-258.
57. Quadakkers, W., et al., Growth rates of alumina scales on Fe–Cr–Al alloys. Oxidation of metals, 2004. 61(1-2): p. 17-37.
58. Naumenko, D., et al., Correlation between the microstructure, growth mechanism, and growth kinetics of alumina scales on a FeCrAlY alloy. Metallurgical and Materials Transactions A, 2007. 38(12): p. 2974-2983.

59. Davis, J.R., Heat-resistant materials; Asm International.1997. USA
60. Sims, C.T., N.S. Stoloff, and W.C. Hagel, Superalloys II. 1987. USA
61. Wagner, C., Passivity and inhibition during the oxidation of metals at elevated temperatures. Corrosion Science, 1965. 5(11): p. 751-764.
62. Wallwork, G. and A. Hed, Some limiting factors in the use of alloys at high temperatures. Oxidation of metals, 1971. 3(2): p. 171-184.
63. Chen, W., et al., Oxidation and crack nucleation/growth in an air-plasma-sprayed thermal barrier coating with NiCrAlY bond coat. Surface and Coatings Technology, 2005. 197(1): p. 109-115.
64. Freborg, A., et al., Modeling oxidation induced stresses in thermal barrier coatings. Materials Science and Engineering: A, 1998. 245(2): p. 182-190.
65. Cheng, J., et al., Thermal/residual stress in an electron beam physical vapor deposited thermal barrier coating system. Acta materialia, 1998. 46(16): p. 5839-5850.
66. Echsler, H., et al., Cracking in and around the thermally grown oxide in thermal barrier coatings: A comparison of isothermal and cyclic oxidation. Journal of materials science, 2006. 41(4): p. 1047-1058.
67. Lau, H., et al., Influence of bondcoat pre-treatment and surface topology on the lifetime of EB-PVD TBCs. Surface and Coatings Technology, 2003. 165(3): p. 217-223.
68. Ambrico, J., M. Begley, and E. Jordan, Stress and shape evolution of irregularities in oxide films on elastic–plastic substrates due to thermal cycling and film growth. Acta materialia, 2001. 49(9): p. 1577-1588.
69. He, M., J. Hutchinson, and A. Evans, Simulation of stresses and delamination in a plasma-sprayed thermal barrier system upon thermal cycling. Materials Science and Engineering: A, 2003. 345(1): p. 172-178.
70. Shillington, E. and D. Clarke, Spalling failure of a thermal barrier coating associated with aluminum depletion in the bond-coat. Acta materialia, 1999. 47(4): p. 1297-1305.
71. Spitsberg, I., D. Mumm, and A. Evans, On the failure mechanisms of thermal barrier coatings with diffusion aluminide bond coatings. Materials Science and Engineering: A, 2005. 394(1): p. 176-191.
72. Busso, E., et al., A mechanistic study of oxidation-induced degradation in a plasma-sprayed thermal barrier coating system.: Part I: model formulation. Acta materialia, 2001. 49(9): p. 1515-1528.
73. Lughi, V., V.K. Tolpygo, and D.R. Clarke, Microstructural aspects of the sintering of thermal barrier coatings. Materials Science and Engineering: A, 2004. 368(1): p. 212-221.
74. Busso, E.P. and Z.Q. Qian, A mechanistic study of microcracking in transversely isotropic ceramic–metal systems. Acta materialia, 2006. 54(2): p. 325-338.
75. Yanar, N., F. Pettit, and G. Meier, Failure characteristics during cyclic oxidation of yttria stabilized zirconia thermal barrier coatings deposited via electron beam physical vapor deposition on platinum aluminide and on NiCoCrAlY bond coats with processing modifications for improved performances. Metallurgical and Materials Transactions A, 2006. 37(5): p. 1563-1580.
76. Wellman, R. and J. Nicholls, Erosion, corrosion and erosion–corrosion of EB PVD thermal barrier coatings. Tribology International, 2008. 41(7): p. 657-662.
77. Clarke, D. and C. Levi, Materials design for the next generation thermal barrier coatings. Annual Review of Materials Research, 2003. 33(1): p. 383-417.

78. Hemker, K., B. Mendis, and C. Eberl, Characterizing the microstructure and mechanical behavior of a two-phase NiCoCrAlY bond coat for thermal barrier systems. Materials Science and Engineering: A, 2008. 483: p. 727-730.
79. Tolpygo, V.K. and D. Clarke, Rumpling induced by thermal cycling of an overlay coating: the effect of coating thickness. Acta materialia, 2004. 52(3): p. 615-621.
80. Balint, D. and J. Hutchinson, An analytical model of rumpling in thermal barrier coatings. Journal of the Mechanics and Physics of Solids, 2005. 53(4): p. 949-973.
81. Tolpygo, V.K. and D. Clarke, On the rumpling mechanism in nickel-aluminide coatings: Part II: characterization of surface undulations and bond coat swelling. Acta materialia, 2004. 52(17): p. 5129-5141.
82. Karlsson, A.M., J. Hutchinson, and A. Evans, A fundamental model of cyclic instabilities in thermal barrier systems. Journal of the Mechanics and Physics of Solids, 2002. 50(8): p. 1565-1589.
83. Pan, D., et al., Evolution of a diffusion aluminide bond coat for thermal barrier coatings during thermal cycling. Acta materialia, 2003. 51(8): p. 2205-2217.
84. Tolpygo, V.K. and D. Clarke, On the rumpling mechanism in nickel-aluminide coatings: Part I: an experimental assessment. Acta materialia, 2004. 52(17): p. 5115-5127.
85. Allan, J.R., The costs of bird strikes and bird strike prevention. 2000.
86. Chen, X., et al., Foreign object damage in a thermal barrier system: mechanisms and simulations. Materials Science and Engineering: A, 2003. 352(1): p. 221-231.
87. Richard Wellman, J.R.N., A Mechanism for the Erosion of EB-PVD TBCS. Materials Science Forum, 2001. 369-372: p. 531.
88. Wellman, R. and J.R. Nicholls. A mechanism for the erosion of EB PVD TBCs. in Materials Science Forum. 2001. Trans Tech Publ.
89. Wellman, R. and J. Nicholls, A review of the erosion of thermal barrier coatings. Journal of Physics D: Applied Physics, 2007. 40(16): p. R293.
90. Eliaz, N., G. Shemesh, and R.M. Latanision, Hot corrosion in gas turbine components. Engineering Failure Analysis, 2002. 9(1): p. 31-43.
91. Gurrappa, I., Thermal Barrier Coatings for Hot Corrosion Resistance of CM 247 LC Superalloy. Journal of Materials Science Letters, 1998. 17(15): p. 1267-1269.
92. Hancock, P., Vanadic and chloride attack of superalloys. Materials Science and Technology, 1987. 3(7): p. 536-544.
93. Stringer, J., High-temperature corrosion of superalloys. Materials Science and Technology, 1987. 3(7): p. 482-493.
94. Saunders, S. and J. Nicholls, The Need for a Standard Procedure in Hot-Salt Corrosion Testing. Guidelines for Hot-Salt Corrosion Burner Rig Tests. High Temp. Technol., 1989. 7(4): p. 232-235.
95. Saunders, S.R.J. and J.R. Nicholls, Hot salt corrosion test procedures and coating evaluation. Thin Solid Films, 1984. 119(3): p. 247-269.
96. Lai, G.Y., Hot Corrosion in Gas Turbines, in High Temperature Corrosion and Materials Application2007, ASM International. p. 249-258.
97. Steinke, T., et al., A novel test approach for plasma-sprayed coatings tested simultaneously under CMAS and thermal gradient cycling conditions. Surface and Coatings Technology, 2010. 205(7): p. 2287-2295.
98. Liu, Y., C. Persson, and J. Wigren, Experimental and numerical life prediction of thermally cycled thermal barrier coatings. Journal of thermal spray technology, 2004. 13(3): p. 415-424.

99. Nicholls, J.R. and M.J. Bennett, Cyclic oxidationguidelines for test standardisation, aimed at the assessment of service behaviour. Materials at High Temperatures, 2000. 17(3): p. 413-428.
100. Meadowcroft, D.B., Code of practice for discontinuous corrosion testing in high temperature gaseous atmospheres. 1997. 251-254(2): p. 973-978.
101. Traeger, F., et al., Thermal Cycling Setup for Testing Thermal Barrier Coatings. Advanced Engineering Materials, 2003. 5(6): p. 429-432.
102. Busso, E., J. Lin, and S. Sakurai, A mechanistic study of oxidation-induced degradation in a plasma-sprayed thermal barrier coating system.: Part II: Life prediction model. Acta materialia, 2001. 49(9): p. 1529-1536.
103. Meier, S.M., K. Sheffler, and D. Nissley, Thermal barrier coating life prediction model development, phase 2. Final report, 1991, Pratt and Whitney Aircraft, East Hartford, CT (United States).
104. Chan, K.S., N.S. Cheruvu, and G.R. Leverant, Coating life prediction for combustion turbine blades. Journal of engineering for gas turbines and power, 1999. 121(3): p. 484-488.
105. Yanar, N., et al., The effects of high temperature exposure on the durability of thermal barrier coatings. Key Engineering Materials, 2001. 197: p. 145-164.
106. Nemeth, N.N., et al., Durability evaluation of ceramic components using CARES/LIFE. Netherlands. June 13-16. 1994.
107. Martena, M., et al., Modelling of TBC system failure: Stress distribution as a function of TGO thickness and thermal expansion mismatch. Engineering Failure Analysis, 2006. 13(3): p. 409-426.
108. Busso, E.P., et al., A physics-based life prediction methodology for thermal barrier coating systems. Acta materialia, 2007. 55(5): p. 1491-1503.
109. Renusch, D., M. Schorr, and M. Schütze, The role that bond coat depletion of aluminum has on the lifetime of APS-TBC under oxidizing conditions. Materials and Corrosion, 2008. 59(7): p. 547-555.
110. Nesbitt, J.A., Numerical modeling of high-temperature corrosion Processes. Oxidation of metals, 1995. 44(1-2): p. 309-338.

Chapter 3

Experimental Methodology and Procedures

In this chapter details of specimen preparation will be provided along with microstructure analysis techniques used and the oxidation setup for all sample sets. Two types of coating methods were employed in the present work, namely, diffusion coating and thermal spray coating. The first part of this chapter focuses on the manufacturing process of aluminide diffusion coating, the second part gives the detail of thermal spray coating and the final part highlights the techniques for microstructure studies and measurement of oxide scale.

3.1 Substrate Specification

Aluminzed beta phase (NiAl) coating was produced on nickel based super alloy (Mar-M-246) and pure Ni which was electroplated on top of M-246. Mar-M-247 was used for thermal spray coating samples. Substrate without Ni plating samples were cut into 2mm thick discs from a 20mm in diameter round alloy rod. In order to improve the utilization of limited base material resources, substrate samples that require Ni plating were cut into 4 quarter pieces from the disc using ATM Brillant 220, cutting machine with a BUEHLER AcuThin Abrasive Cut-off wheel, cutting speed was held at 0.005 m/s so that the damage of the sample during cutting can be minimised. All substrate samples were ultrasonically cleaned with acetone. Detailed alloy composition is given in Table 3.1. Substrate size is summerised in Table 3.2.

Table 3.1 - Alloy composition.

Elements (wt. %)	C	Cr	Ni	Co	Mo	W	Ta	Ti	Al	B	Zr	Hf	Nb
Mar-M-246	0.15	9	Bal.	10	2.5	10	1.5	1.5	5.5	0.015	0.05	-	1
Mar-M-247	0.16	8.2	Bal.	10	0.6	10	3	1	5.5	0.015	0.05	1.5	-
Pure Ni	-	-	Bal.	-	-	-	-	-	-	-	-	-	-

Table 3.2 – Substrate geometry.

	Diameter, mm	**Thickness, mm**
Mar-M-246	20	2
Mar-M-247	20	5

3.2 Diffusion Coatings

It is generally accepted that diffusion coatings are formed by outward diffusion of nickel or inward diffusion of aluminium. The direction of nickel or aluminium diffuses depending on how thermodynamical and kinematical properties are applied during aluminisation process [1]. For outward diffusion coating, aluminium activity at the surface is low and with nickel diffuses outwards from the substrate, the β-phase NiAl layer grows on the original surface. Study [2] shown that the diffusivity of nickel is faster than that of aluminium with a maximum aluminium content limited to 51 at%. In contrast, for inward diffusion coating, aluminium activity at the surface is high, aluminium is diffused into the substrate γ-Ni/γ'Ni_3Al matrix and transformed into δ-Ni_2Al_3. As indicated in the phase diagram in Figure 3.1 [3], the diffusivity of nickel is almost zero compared with aluminium. β-phase NiAl layer is formed during heat treatment as nickel diffuses outwards from the substrate during which δ-Ni_2Al_3 phase is transformed into β-phase NiAl.

However, due to the slow diffusion of alloy element from the substrate, such as Tungsten(W), Molybdenum (Mo), Tantaium (Ta) etc, the coating matrix will be less clean and these elements may appear in precipitates and in the solid solution. To demonstrate and combat such problem, a set number of specimens were aluminised with and without a layer of pure nickel which was deposited on the alloy surface and the procedure is described in the following sections.

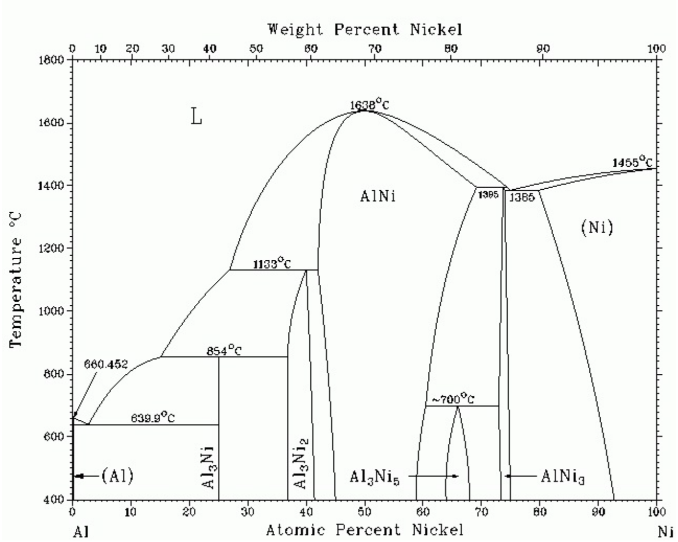

Figure 3.1 – NiAl phase diagram [3].

3.2.1 Electrodeposition of Nickel

In order to carry out aluminization on a pure nickel substrate condition, one of the most convenient and cost effective options would be to adapt metal electrodeposition of pure nickel in which M-246 alloy was used as target material. In general, electrodeposition process involves dissolution of metal, in this case pure nickel source, from an electrode (anode) into a solution that contains ions of the same metal. An electric discharge of that metal ion would attach to an electrode surface (cathode) in the solution by a passage of a continuous electric current along the solution. Electric current is created when a potential is applied between the electrodes and both electrodes, anode and cathode, are charged positively and negatively respectively. Then, positive metal ions in the solution would move towards the negatively charged cathode and vise versa. Figure 3.2 illustrates the electrochemical process schematically.

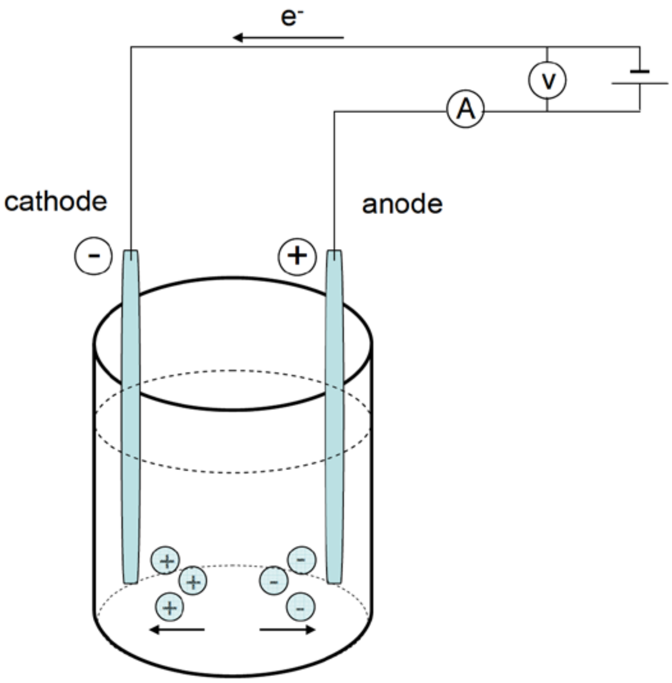

Figure 3.2 – Schematic of electrochemical process – [4]

3.3.2 Plating Procedures

Nickel sulphate, nickel chloride and boric acid granules were dissolved in a 1000 mL deionized water tank to be used as the electrolyte (plating solution). The pH level of the solution was checked periodically by using an OAKTON® pH meter and kept between 4 – 4.7. Prior to the nickel plating, 60 ml of electrolyte was filled in a 100 ml beaker and electrolyte temperature which was kept at 32 °C by a heat plate in a water tank. Same amount of electrolyte was also used for alumina particles plating process, additional alumina particles with concentration of 100 g/l were added to the solution and were ultrasonically agitated for 10 minutes prior to the plating process. The electrical current setting is dependent on the size of target material, Table 3.3 shows the calculated electrical current based on the current flux of 120 mA/in^2 (0.186 mA/mm^2) in this study. The electrolyte was mechanically agitated during the plating process.

In order to achieve a meaningful thickness of nickel during the plating process, three different timeframes were used, they are, 20, 40 and 60 minutes. Two groups of plated samples were subsequently created, the first group of samples is designed to experimentally study the boundary displacement in relation to the marker displacement, hence, alumina particles which act as markers were embedded in the plated nickel layer and they are the ones with 20 and 40 minutes. The second group of samples is designed to only have a pure nickel layer on top of existing substrate. Table 3.4 shows the relation of each sample group with corresponding timeframe.

Tabel 3.3 - Calculated electrical current based on the current flux of 120 mA/in^2 (0.186 mA/mm^2)

Sample	Sample area, mm^2	Electrical Current, mA
Full disc	754.0	140.2
Half disc	417.0	77.6
Quarter Disc	228.5	42.5

Table 3.4 – Nickel plating timeframe.

Group	Plating Duration, mins	Alumina Particles
1	20	With
	40	Without
2	60	Without

3.2.3 Aluminization

To carry out the aluminization process, a customized environmental controlled CARBOLITE® tube furnace was used. A horitontal alumina tube with custom designed seals in which argon gas is allowed to flow into the tube to create a protective atmosphere during heating and cooling process was created. In order to make sure easy access and protection of the rubber seal, the 85 mm in diameter and 120 mm in length aluminium tube was inserted into the furnace with attachable seals and cooling coil on both ends. Furthermore, argon gas flow was controlled at 0.5 SLPM by a OMEGA® gas flow meter and heating rate was controlled at 8 °C/min. To ensure direct leaking observation of the system during the coating process, the outlet gas tube was submerged in a water container, during normal operation gas bubble should appear throughout the process. All aluminized samples were heat treated under high vacuum (10^{-6} mbar) at 1100 ℃ prior to oxidation.

3.2.3.1 Pack and Above the Pack Process

As stated in previous chapters, there are number of coating processes to provide alloy surface protection. The selection of each of the processes depends on the design and application. Therefore, the coating technique used in this study, in which beta-phase coating is the stepping stone towards understanding of the mathematical modelling, were solely focused on pack and above the pack process, as illustrated in Figure 3.3 & 3.4. In pack process, the sample is embedded in the cement pack. In above the pack process, the sample is held above the cement pack by a tray. The cement pack once heated, it generates halide vapors which can effectively be plumbed on to the sample surface. Table 3.5, 3.6 and 3.7 reflect the aluminizing parameters used for producing the beta-phase coating on nickel based alloy, pure nickel and pure nickel with particles respectively.

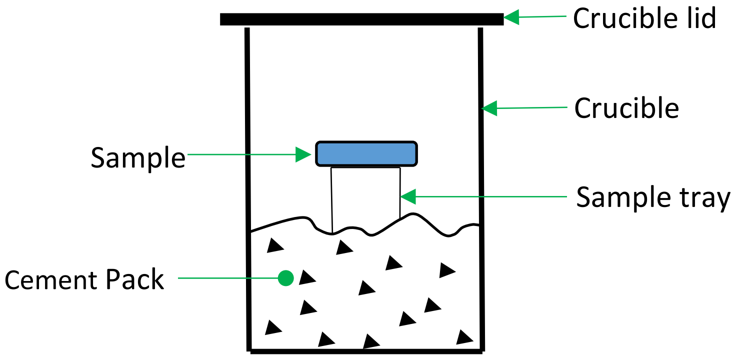

Figure 3.3 –Schematic of Above-the-pack process setup.

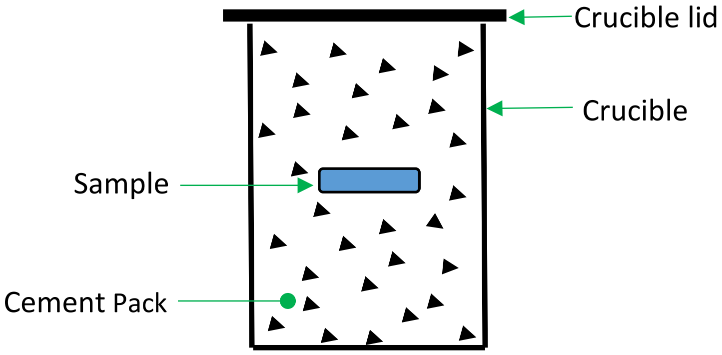

Figure 3.4 – Schematic of pack process setup.

Pack Activity

The cemetation pack contained three powders, they are, aluminium oxide powder acts as inert constituent, pure aluminium powder acts as source and ammonium chloride powder acts as activator. Due to the significance of diffusional nickel and aluminium species, although pack mixture was consistent for all aluminiztion processes, aluminium source was varied from low to high with the activator weight percentage kept the same at 3%.

Nickel Base Alloy

High and low activity pack were utilized for all the aluminization procedures during the manufacturing of beta phase coating. According to Table 3.5, sample P-1 to P-10 were manufactured using Pack technique where pack activity was varied from low (2%) to high (12.5%) respectively. In terms of temperature, lower activity pack generates lower vapor pressure of the aluminium halide species, hence, higher temperature (1050 ℃) was used for some of the low activity packs. However, such temperature was also used on high activity packs. Sample AP-1 to AP-8 were manufactured using Above the Pack technique where pack activity was also varied from low and high respectively. However, differ to Pack technique, temperature was kept at 1050 ℃ for all samples.

Pure Nickel

As seen from Table 3.6, for Above the Pack process, low activity pack with high temperature (HTLA) was used for sample NP-AP-1 & 2, whereas relative high activity pack with low temperature (LTHA) was used for sample NP-AP-3 to 5 with exception of sample NP-AP-3 where high temperature was applied. In contrast, high activity pack with low temperature was used for all Pack technique samples. Only high activity pack was used for samples, Par-1 & Par-2, that have aluminium oxide particles embedded within the aluminizied coatings, as shown in Table 3.7.

Table 3.5 – Aluminized sample group without nickel plating.

Sample ID	Aluminum Powder, wt%	Aluminum Oxide, wt%	Ammonium Chloride, wt%	Temperature, ℃	Dwell Time, hour	Vaccume Heat Treatment Temperature, ℃	Dwell Time, hour	Coating Technique
P-1	2	95	3	1000	2	1100	2	Pack
P-2	4	93	3	800	4	1100	4	Pack
P-3	4	93	3	1000	2	1100	1	Pack
P-4	6	91	3	1050	2	1100	2	Pack
P-5	8	89	3	800	4	1100	4	Pack
P-6	8	89	3	1000	2	1100	1	Pack
P-7	8	89	3	1050	2	1100	2	Pack
P-8	10	87	3	1050	2	1100	2	Pack
P-9	12.5	84.5	3	1050	2	1100	2	Pack
P-10	15	82	3	1050	2	1100	2	Pack
AP-1	6	91	3	1050	2	1100	2	Above Pack
AP-2	8	89	3	1050	2	1100	2	Above Pack
AP-3	10	87	3	1050	2	1100	2	Above Pack
AP-4	12.5	84.5	3	1050	2	1100	1	Above Pack
AP-5	12.5	84.5	3	1050	2	1100	2	Above Pack
AP-6	12.5	84.5	3	1050	4	1100	4	Above Pack
AP-7	15	82	3	1050	2	1100	2	Above Pack
AP-8	15	82	3	1050	4	1100	4	Above Pack

Table 3.6 - Aluminized sample group with nickel plating.

Sample ID	Ni Plating Duration, mins	Aluminum Powder, wt%	Aluminum Oxide, wt%	Ammonium Chloride, wt%	Temp, ℃	Dwell Time, hour	Vaccume Heat Treatment Temperature, ℃	Dwell Time, hour	Coating Technique
NP-AP-1	10 / post	8	89	3	1050	2	1100	2	Above Pack
NP-AP-2	20 / prior	8	89	3	1050	2	1100	2	Above Pack
NP-AP-3	20 / post	25	73	3	1050	2	1100	1	Above Pack
NP-AP-4	60 / prior	25	73	3	800	4	1100	4	Above Pack
NP-AP-5	60 / prior	50	47	3	800	4	1100	4	Above Pack
NP-P-1	20 / post	12.5	84.5	3	800	2	1100	2	Pack
NP-P-2	60 / prior	12.5	84.5	3	800	4	1100	4	Pack
NP-P-3	60 / prior	25	73	3	800	4	1100	4	Pack
NP-P-4	60 / prior	50	47	3	800	4	1100	4	Pack

Table 3.7 – Aluminized sample group with particles

Sample ID	Ni Plating with Particles, mins	Ni Plating Duration, mins	Aluminum Powder, wt%	Aluminum Oxide, wt%	Ammonium Chloride, wt%	Temp, ° C	Dwell Time, hour	Vaccume Heat Treatment Temperature, ° C	Dwell Time, hour	Coating Technique
Par-1	20	60 / prior	25	73	3	800	4	1100	4	Pack
Par-2	20	60 / prior	50	47	3	800	4	1100	4	Pack

3.3 Overlay Coating

For high temperature applications there are two main groups of coatings, namely, diffusion coatings and overlay coatings. For the purpose of comparison, both coating systems were considered in present work. Unlike diffusion coatings, deposition of overlay coatings involves less amount of interaction with the substrate and coating thickness can be more predictable and controlled. Commercially available Ni191-4, Ni-528 gas atomized nickel based MCrAlY powder from Praxair and Diamalloy 4008NS gas atomized Ni5Al powder from Oerlikon were considered. The chemical composition of each power (Table 3.8) was provided by the manufacturer and the sampling method is in accordance to ASTM B215.

Table 3.8 – Chemical compostion of bond coat powder Ni191-4, Ni-528 and Diamalloy 4008NS.

	Elements, wt%				
	Ni	Co	Cr	Al	Y
Ni191-4	Bal.	20.64	17.72	13.01	0.57
Ni-528	Bal.	-	17.8	6	-
Diamalloy 4008NS	Bal.	-	-	5.5	-

3.3.1 High Velocity Oxygen Fuel (HVOF) spraying

MCrAlY overlay coating was deposited onto Mar-M-247 bare alloy surface from a commercial Metallisation® MetJet III HVOF system, as shown in Figure 3.5. Stainless steel was also used as substrate for free standing coating purposes, the detachement of the coating will be addressed in later sections. For this system, kerosene and nitrogen were used as fuel and carrier gas respectively. The flow ratio of fuel, carrier gas and oxygen were adjusted during spray, as shown in Table 3.9. After ignition, hot gases are produced from this specific mixture of fuel and oxygen in the combustion chamber. At the same time, coating powders are injected downstream along the passage of the hot gases in the nozzle before exit. The MetJet gun is fixed on a robotic arm which only has one axis (vertical) movement in relation to the target spray sample. The travel distance of the traverse unit is programmed in accordance to the height of the sample. Therefore, the thickness is controlled by the number of passes in which one complete up and down moving cycle is regarded as one pass. Samples were mounted on a carousel which has constant roational speed of 70 rpm, as shown in Figure 3.6. Compressed air was used to cool the samples during and after the sparying.

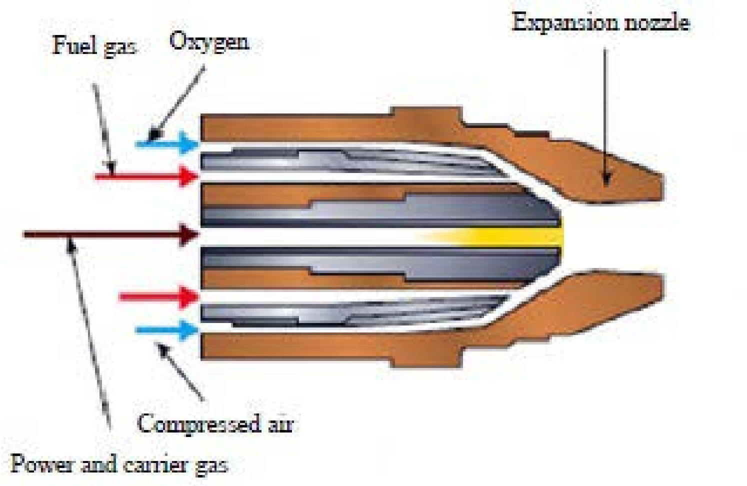

Figure 3.5 – Schematic of HVOF MetJet III gun [5].

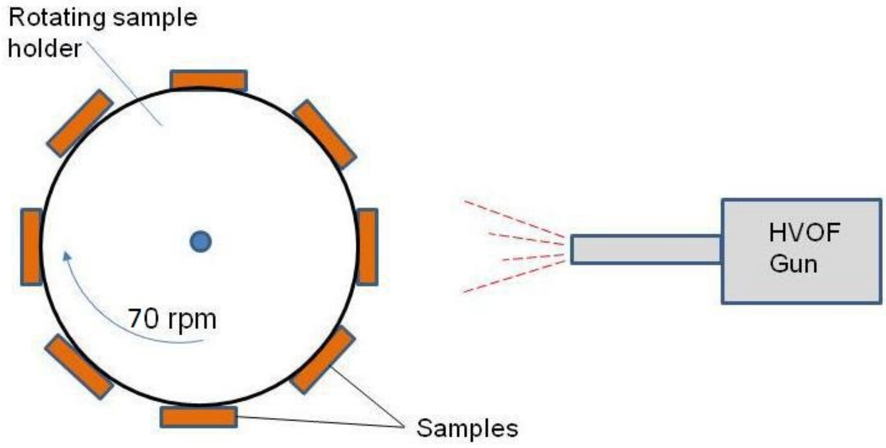

Figure 3.6 – A top view of the HVOF spraying setup arrangement [6].

Table 3.9 – HVOF spray parameters for powder Ni-191-4, Ni-528 and Dimalloy 4008NS.

Spray Parameter	Ni-191-4 & Ni-528
Spray distance, mm	356
Carrier gas flow rate, l/min	6
Oxygen flow rate, l/min	920
Kerosene flow rate, ml,min	475
Powder Feed rate, g/min	186

3.3.2 Free Standing Coating

Upon the completion of the spraying process, Ni-191-4 HVOF coatings were mechanically detached from the substrate, as illustrate in Figure 3.7. It is important to note that in order to detach the coating by bending the substrate, sandblasting was not applied to the stainless steel substrate prior to the coating process.

Figure 3.7 – Ni-191-4 coating detachement from the substrate [6].

3.3.3 Air Plasma Spray (APS)

8% Y_2O_3-doped ZrO_2 ceramic powder (Al-1075) from Praxair was used for deposition of top coat layer on top of the overlay bond coat by the APS coating method. Figure 3.8 illustrates the commercially available TAFA SG-100 plasma torch that was used in the present work. For this system, argon hydrogen plasma gas mixture (Ar-H_2) was used for fuel gases and Ar was used as carrier gas. APS spray parameter is given in Table 3.10. As illustrate in previous section, samples were mounted and thickness control was applied in a exactly manner with the HVOF process.

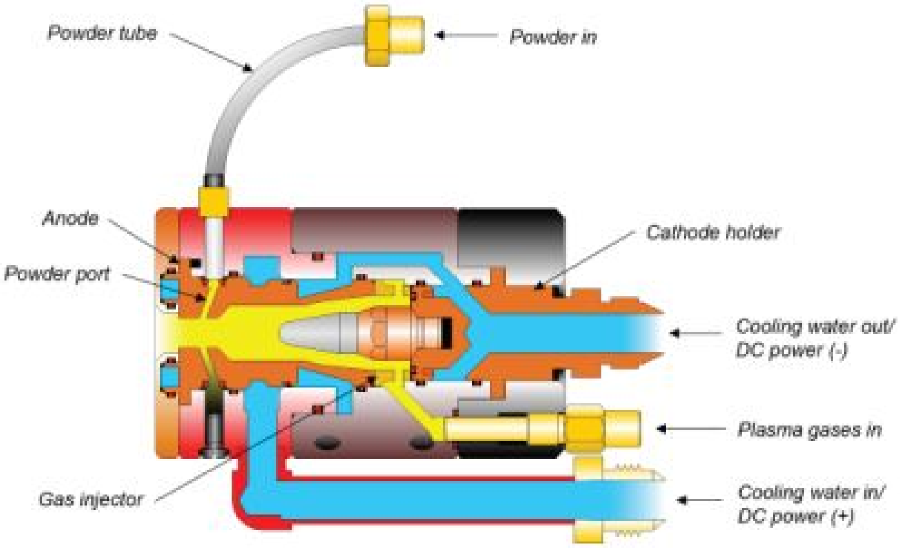

Figure 3.8 – Schematic configuration of a TAFA SG-100 plasma gun [7].

Table 3.10 – APS spray process for powder Al-1075.

Spray Parameter	Al-1075
Spray distance, mm	90
Carrier gas pressure, psi	40
Primary gas pressure, psi	34
Hydrogen gas pressure, psi	12

3.4 Thermal testing methods

The behavior of the diffusion coating, overlay coating and thermal barrier coating system were studied by adapting two most commonly known thermal testing methods: isothermal and flame rig or burner rig tests. The detail design development and calibration of oxyacetylene flame rig used in this work will be addressed in Chapter 4. Table 3.11 shows the overview of the test scheme. Details of the oxidation test equipment and test conditions are given thereafter.

Table 3.11 – Thermal testing scheme for each coating system.

Coating System	**Bond Coat Type**	**Thermal Testing Method**	
		Isothermal	**Flame Rig**
Diffusion coating	NiAl	✓	✗
Overlay coating	Ni-191-4	✓	✗
	Ni-528	✓	✗
	Dimalloy 4008NS	✓	✗
TBC system	Ni-191-4	✓	✓

3.4.1 Isothermal test

A Carbolite HTF 17/5 chamber furnace was used for all the samples. A equipment image taken from the OEM website is given in Figure 3.9. Temperature up ramping rate and down ramping rate was 8 °C/min and 15°C/min respectively. A universal maximum temperature of 1100 °C was applied. Dwell time at the elevated temperature was varied across the coating system, the sequence of oxidation duration is given in Table 3.12.

Table 3.12 – Isotheraml oxidation test plan.

Coating System	**Bond Coat Type**	**Isothermal Oxidation Duration, hr**										
		0.25	**0.5**	**0.75**	**1**	**2**	**3**	**24**	**50**	**100**	**200**	**500**
Diffusion Coating	NiAl	✓	✓	✓	✓	✓	✓	✓	✓	✓	✓	✓
Overlay Coating	Ni-191-4	×	×	×	✓	✓	✓	✓	✓	✓	✓	✓
	Ni-528	×	×	×	×	×	×	✓	✓	✓	✓	×
	4008 NS	×	×	×	×	×	×	✓	✓	✓	✓	×

Figure 3.9 – Isothermal testing furnace.

3.4.2 Flame rig test

The equipment used for this test will be addressed in detail in Chapter 4. Thermal cycling tests were carried out with a special designed flame rig. Only the TBC system was tested under a maximum temperature of 1400 °C. In brief, high temperature oxy-acetylene flame via a welding torch was used as the heating source. Sample surface, middle and back temperature measurements were achieved by means of pyrometer and thermocouples. In order to simulate the near realistic coating operating conditions, high velocity compressed air was used to keep the substrate from melting. Each thermal cycle consisted of intense heating period, oxidation period and hot corrosion period. All TBC samples were tested for 3, 6 and 9 cycles. For Ni-191-4 TBC system, samples that have a top ceramic layer thickness of 300 μm (16 passes) and 600 μm (32 passes) were tested.

3.5 Sample preparation for metallographic observation

Oxidized samples were prepared in an orderly manner so that they can be examined using a range of observation techniques. All samples were cut from a ATM Brillant 220 cutting machine with a BUEHLER AcuThin Abrasive Cut-off wheel. Extra care was taken into account for ceramic coated samples prior cutting, where non-conductive resin was used for mounting the sample in place so that ceramic layer can be better protected. In order to minimize stress imposed by cutting, cutting speed was held at 0.005 m/s. Samples without ceramic layer were hot mounted in conductive resin, whereas ceramic coated samples were mounted in non-conductive resin.

To ensure consistence from polishing of all samples and keep the sample surface as flat as possible, samples were ground and polished using a Struers Labopol-5 semi-automatic polishing machine. All samples were first ground using 240p, 400p, 800p and 1200p grid abrasive papers, some light scratches remained after this stage. These scratches were removed by polishing on a 6 μm and 1 μm diamond polishing paste wheel. TBC samples were carbon coated to improve conductivity. Samples prepared to this level were used for SEM observation.

3.5.1 Scanning Electron Microscopy (SEM)

Microstructure characterization is carried out using Philips XL30 SEM-FEG coupled with Phoenix EDS detector system. SEM uses electron beam that shoots directly towards the polished sample surface for characterization. When a sample is hit by a electron beam, a wide range of information can be acquired from the interaction between electrons and the sample surface atoms. In general, two types of image can be used, they are, secondary electron images and back scattered electron images. Secondary electrons are low energy electrons, only the information escaped from the surface can be collected by the detector, and its signal is greatly influenced by the shape of sample surface. On the other hand, backscatted electrons are high energy electrons, it allows for information to be collected from a greater depth of the sample.

Each imaging modes serve different purpose in terms of microstructure characterization. Secondary electron imaging gives a better resolution than backscattered imaging, so that sample surface topographical contrast can be achieved. Backscatterd electron imaging is highly depended on the average atomic number of elements in the sample, this is particularly beneficial to the qualitative analysis of the surface.

3.5.2 Energy Dispersive X-ray (EDS)

Qualitative compositional analysis is often conducted by EDS. This technique works by detecting x-ray emitted from the sample by shooting electron beam onto the surface. As stated earlier, when high energy electrons from the primary incident beam bombarded on the sample surface, electrons are ejected from the atoms on that surface which left with vacancies to be filled by an x-ray. Thus by characterize the counter balance energy differential between electrons states, a quantification of elements within the sample surface can be ultimately achieved. However, EDS analysis also has its limitations such as minimum particle size restriction and phase distribution detection.

3.5.3 X-ray diffraction (XRD)

Bruker D8 advance x-ray diffractometer (XRD) using Cu K-alpha radiation as x-ray source was used to carry out qualitative phase analysis for as-deposited diffusion coating and oxidized samples at room temperature, with scanning range of 2θ from 10° to 110° and step size of 0.01°. The applied voltage and current 40 kV and 25 mA respectively.

3.6 Thermally grown oxide (TGO) thickness measurements

The Matlab image analysis tool was utilized for measuring the thickness of TGO on all samples. The following steps were performed in order to obtain a precise measurement:

1. Prior to the calculation of thickness in Matlab, the GUN image manipulation program (GIMP) was used to process grayscale SEM images into binary images, as shown in Figure 3.10. From this process, the entire oxide layer was selected and traced around its perimeter manually. Depending on the image scale, 10 to 20 images were processed for each sample.
2. The colour of the selected layer was then filled with a single colour (white) and anything outside the selected perimeter was filled with another single colour (black). Each single colour has the extreme pixel value of 0 and 255.
3. The binary image was loaded in Matlab with predefined pixel unit obtained from ImageJ.
4. Matlab thickness measurement algorithm started by calculating the total image area per pixel.
5. Total number of pixel that has the value of 255 (i.e. white) within the oxide perimeter was counted and stored in an array. Size of the array is equivalent to the size of the image.
6. Sum of array elements was stored.

7. Each pixel on the perimeter of the oxide layer was captured (Figure 3.11) using BWPERIM function and stored in an array. Sum of the perimeter array was stored.
8. Prior calculating the length of oxide layer, pixels on left and right perimeter edge were counted, stored and removed in step 9.
9. The length of oxide layer was calculated based on the simple trigonometry, as illustrated in Figure 3.12.
10. The thickness was obtained using the pixel area from step 4 divided by the length obtained in step 9. Standard deviation error was also included.

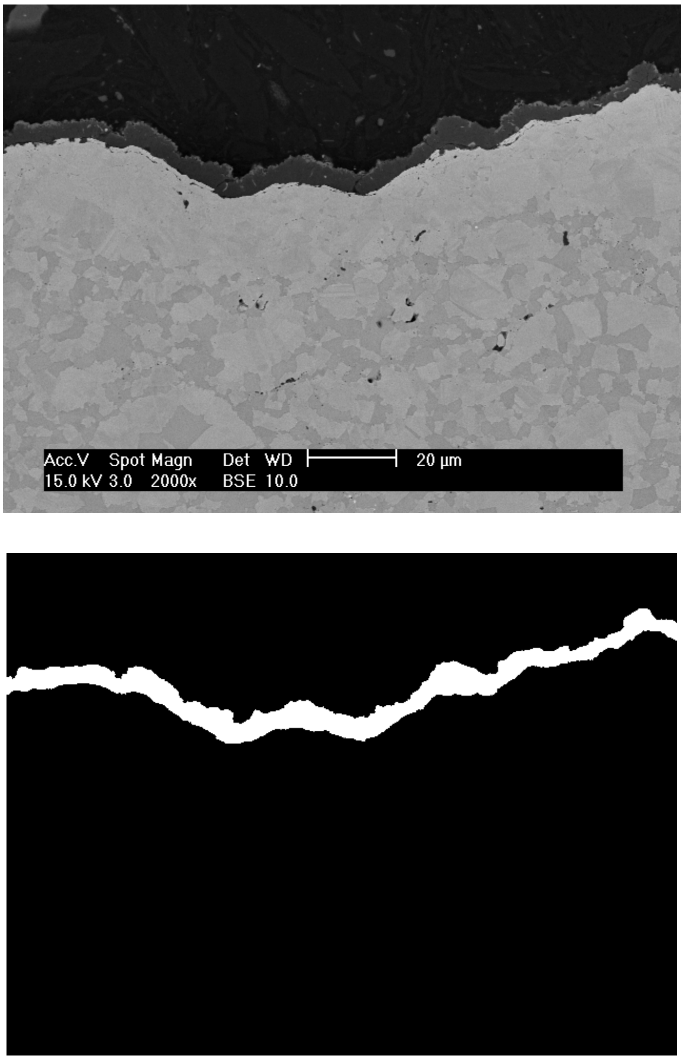

Figure 3.10 – GIMP image process (a) before and (b) after.

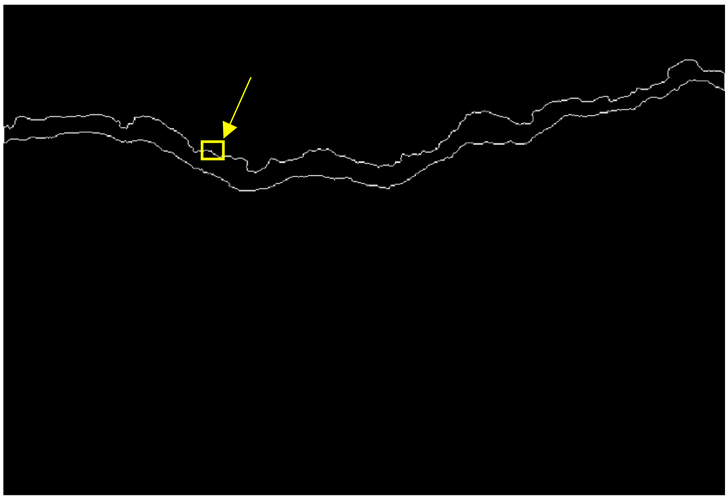

Figure 3.11 – Captured pixels on the perimeter of the oxide layer.

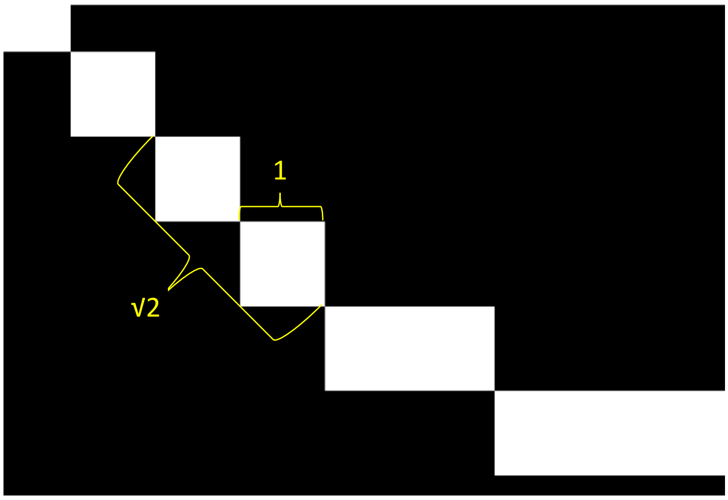

Figure 3.12 – Demonstration of applied simple trigonometry for calculating the length of oxide scale. This image is the enlarged version from Figure 3.11 as indicated by the arrow.

3.7 Conclusion

This chapter has outlined and discussed the coating techniques used to manufacture diffusion and overlay coatings. For diffusion coating system, both pack and above the pack process were carried in order to cross examine the overall coating thickness. An additional step of nickel plating was taken to ensure a better pack aluminized coating quality. High velocity oxygen fuel (HVOF) and air plasma spraying (APS) techniques were used for overlay bond coat and top coat deposition. The thermal behavior of the diffusion coating and overlay coating were studied in which a universal maximum temperature of 1100 °C under isothermal condition was applied to both coating systems. Flame thermal cycling test was carried out with a special designed burner rig. Only the overlay top coating system was tested under a maximum temperature of 1400 °C. The development of the burner rig is presented in Chapter 4. All of the microstructural characterization was carried out using scanning electron microscopy (SEM). Qualitative compositional analysis was conducted out by using energy dispersive x-ray analysis (EDS). Qualitative phase analysis for as-deposited diffusion coating and oxidized samples was carried out by means of x-ray diffraction analysis (XRD). The results of microstructure characterization and thermal tests are discussed in Chapter 5 and 6.

Reference

1 Goward G. W., and D. H. Boone, Mechanisms of formation of diffusion aluminide coatings on nickel-base superalloys, *Oxid. Met.*, 1971, pp. 3, 475–495.

2 Shankar. S and Seigle. L. L, Interdiffusion and intrinsic diffusion in the NiAl Phase of Al-Ni system, Metall. Trans. A, 9, pp 1467-1476.

3 Massalski. T. B, Okamoto. H, Subramanian. P. R and Kacprzak. L, Binary alloy phase diagrams, 2nd edition.

4 Maider. V. P, New methods for the analytical control of a nickel electroplating bath. Application of chemometric techniques. PhD Thesis, 2010.

5 Salmanzadeh. M, Jalali Azizpour. M and Mohammandi Majd. H, Evaluation of the effect of spray distance on fracture toughness of thermally sprayed coatings. Journal of Applied Sciences, 2015, 15, pp 709-714.

6 Saman Saeidi, Microstructure, oxidation and mechanical properties of as-sprayed and anneled HVOF and VPS CoNiCrAlY coatings. PhD Thesis. 2010

7 Praxair,http://www.astroalloys.com/assets/praxair/plasma-brochure.pdf.

Chapter 4

Burner Rig Design Development and Calibration

Novel coating systems and deposition methods are being development at the University of Nottingham and at many other laboratories around the world. There is a need for a low cost and versatile burner rig to suit the needs of relatively small scale facilities. The literature review in Chapter 2 has identified that there are a number of thermal barrier coating burner rig testing facilities in the field of research, most of which are well developed in industry scale. It is evident to see that burner rig developed from each research institutions or companies has their own unique design to serve different types of testing objetives, i.e. thermal shock, cyclic oxidation tests, hot corrosion test, foreign partical impact test, etc.. This reflects the broad range of conditions of interest of thermal barrier coating failure analysis.

No one system can cover this range of conditions, but this study will demonstrate a low cost and highly reconfigurable approach to burner rig design that could be adapted to a broad range of requirements. Design parameters and requirements for this rig have been set out in accordance with the existing burner rigs, but wherever possible simplified and striving for higher flame temperature that pursuits one testing to satisfy both static and dynamic.

4.1 Design Requirment

- Produce high surface temperature greater than 1200 °C.
- Provide external cooling facility in order to simulate actual turbine operating environment.
- Produce high temperature gradient ±5% of surface temperature [1].
- Record temperature at front, middle and back of the sample in real time during testing.
- Minimize heat transfer between test sample substrate with burner rig structure.
- The test sample must be changeable.
- The distance between flame torch nozzle and sample surface must be adjustable. Components should be low cost so that multiple rigs could be achieved for one lab.

4.1.1 Flame choice

Fuel types of natural gas, oxygen propane, diesel oil and even JET A-1 have been used as preferred flame source. However, for this particular rig design, the selection of gas burner fuel is depended on three key factors availability, high flame temperature and budgetary, with natural gas, oxygen propane and diesel oil being a relative low flame temperature heat source and JET A-1 being a high cost fuel source, the use of oxyacetylene flame would make the appropriate choice of fuel due to its high heating rate and temparture and high velocity gas flow. In terms of testing, oxyacetylene torch testing is a comparatively less expensive technique and it is most readily available. It is commonly known that the oxyacetylene flame temperature varies between 1000 °C to 3500 °C along the outer to inner region. For the actual burner rig testing, the desirable maximum sample suface temperature was set to be around 1600 °C, thus the design of the sample holder structure must be capable of making adjustment along the flame axis in order to calibrate the temperature in relation to the sample suface and torch nozzle distance.

4.1.2 Back Cooling

In order to achieve a realistic testing condition [2], simultaneous cooling at the back of the sample is achieved from a compressed air nozzle, this cooling facility must be an essential part of the testing rig. Effect of air nozzle pipe diameter to air flow velocity must be included in the structure design and CFD analysis is to be carried out in order to examine the cooling efficiency of the design.

4.1.3 Temperature Measurement and Data Logging

To create a large through thickness temperature gradient of the TBC sample, appropriate temperature measurement and recording instruments must be considered. For TBC sample surface temperature measurement, a non contact infrared pyrometer from Raytek® was used. For TBC sample middle and back temperature measured uses a N-type and K-type thermocouple respectively. It is worth mentioning that previous research [3,4] has shown that for wavelength less than 9 μm the YSZ APS-TBCs are semi-transparent for coating thickness about 300 μm. However, due to budgetary constraints the pyrometer used for this project only has a single spectral response. This affects the accuracy of the front surface temperature measurement and hence some careful calibration on emssivity needs to be carried out in order to combat such issue. Furthermore, a robust, stand-alone computer control and monitoring system from National Instruments CompactRio must be included in the data logging design in order to ensure that a high accuracy and repeatability recording capability can be achieved throughout the testing phase.

4.1.4 Mounting of Test Sample

To increase TBC test sample easy handling and mounting ability the sample holder must provide a simple access with assembly and replacement of samples. This affects the repeatability of test procedures.

4.2 Detailed Design of a Flame Burner Rig

The schematic for this burner rig is illustrated in Figure 4.1. The actual burner rig setup, as shown in Figure 4.2, consists of an oxy-acetylene flame torch, adjustable robust frame structure that allows changes for sample holder distance relative to the flame, an integrated infra-red thermometer holder and a computer controlled NI compactRIO system and mass flow controllers with appropriate power supply unit. The adopted components in this setup are justified by calibration, modelling and calculation in order to fulfil the requirements that have been outlined in Section 4.1.

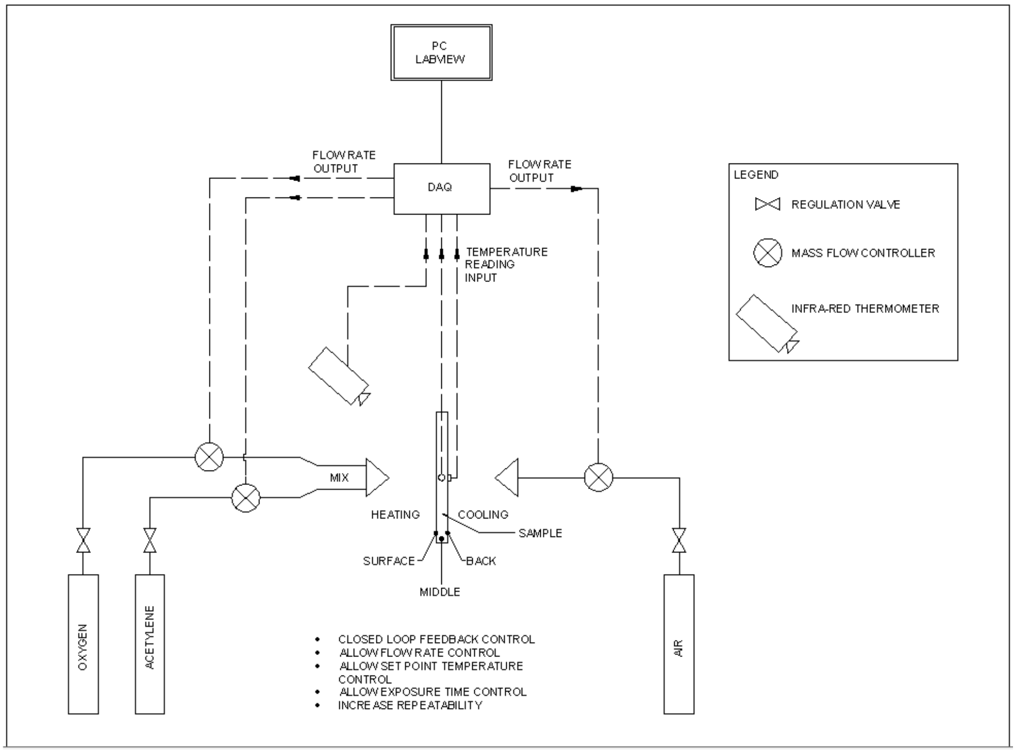

Figure 4.1 – Schematic of burner rig system.

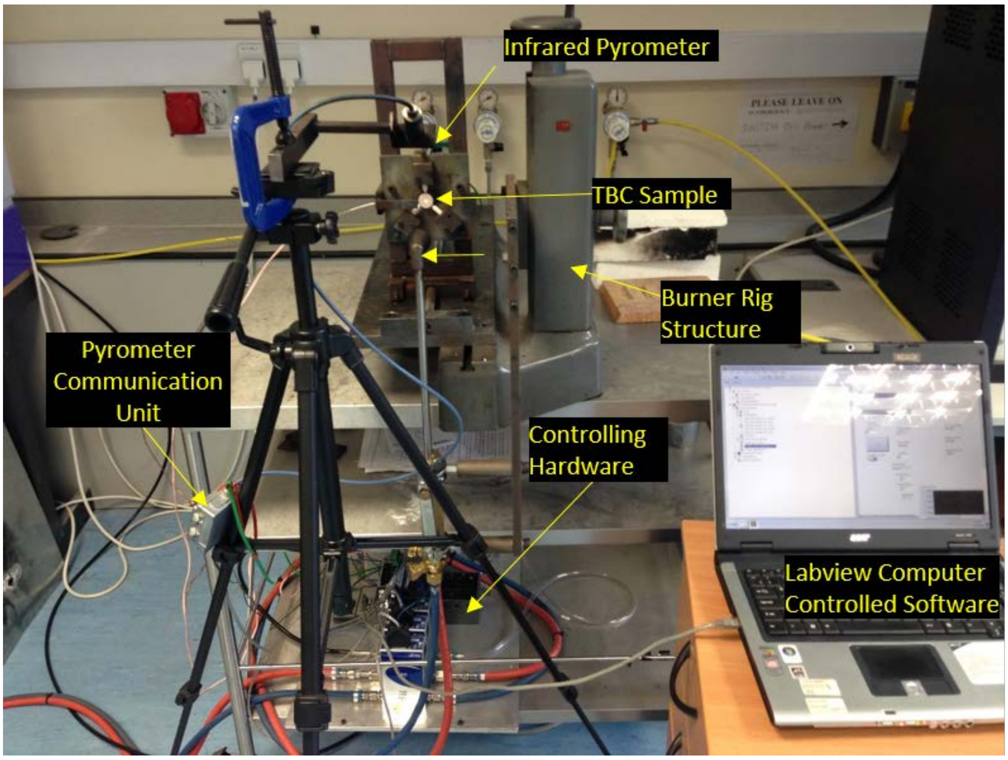

Figure 4.2 – Flame burner rig assembly with computerized control system.

4.2.1 Hot Section Component Design

The sample holder component section consists of a 120mm x 120mm x 5mm backing plate with a 20mm in diameter hole at the centre and a three point screw tight fixing configuration, as shown in Figure 4.3. Ferritic stainless steel Crofer® 22 APU was determined to be the most suitable material due its good oxidation resisitance property at high temperature and was used for backing plate. To minimize heat transfer between sample substrate and backing plate, TBC test sample was supported by three 6mm diameter x 30mm length spinel point bottom crucibles from Almath®. Each crucible was inserted into a 30mm x 17mm x 12mm metallic block and tightened by a M5 screw with 15mm in length. As such the sample has only 3 parts of contacts, <1 mm in diameter, through which heat can be lost to conduction. The intergrated sample holder structure was placed on a single axis movable block. A turning wheel at the end of rig bed was used so that the distance varying from 300 mm to 100 mm between the nozzle to sample surface can be adjusted.

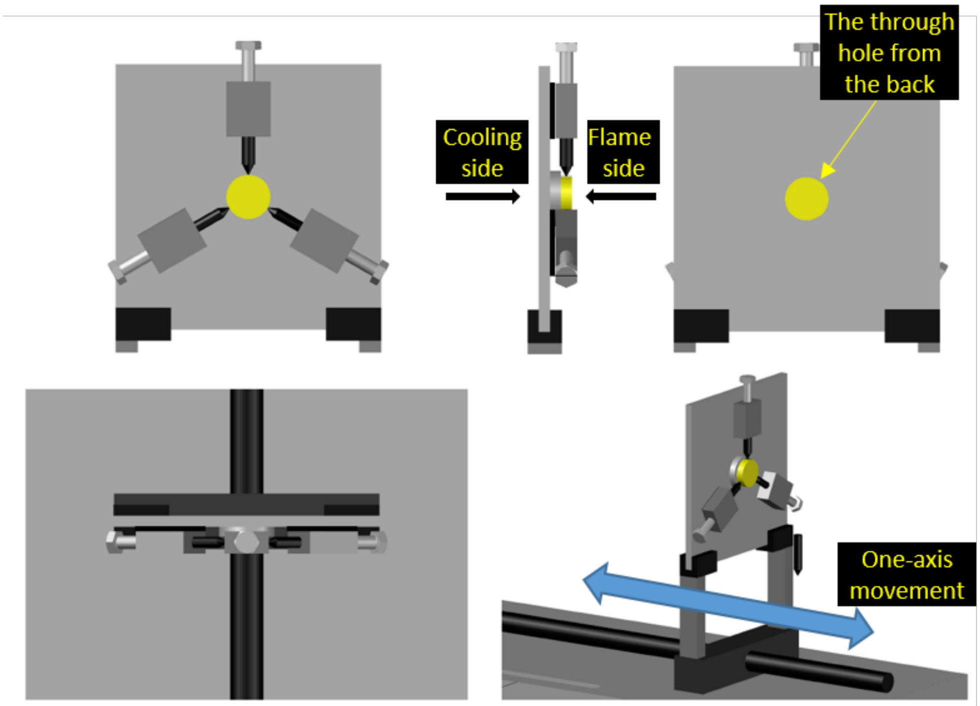

Figure 4.3 – Illustration of hot section sample holder design.

4.2.2 Air Cooling Analysis

This section outlines the numerical model used to determine whether the air cooling section is sufficient for the TBC burner rig design, it also provides an overall estimation on the outcome of the actual test in terms of thermal gradient. The geometry and mesh were constructed and generated respectively in GAMBIT to imitate the volume encompassing the thermal barrier coating test sample, cooling air path, cooling air tube outlet and surrounding space. The meshed model as shown in Figure 4.4, was imported into FLUENT for analysis. Each cell zone with assosiated boundary type and dimensions of the model are shown in Table 4.1.

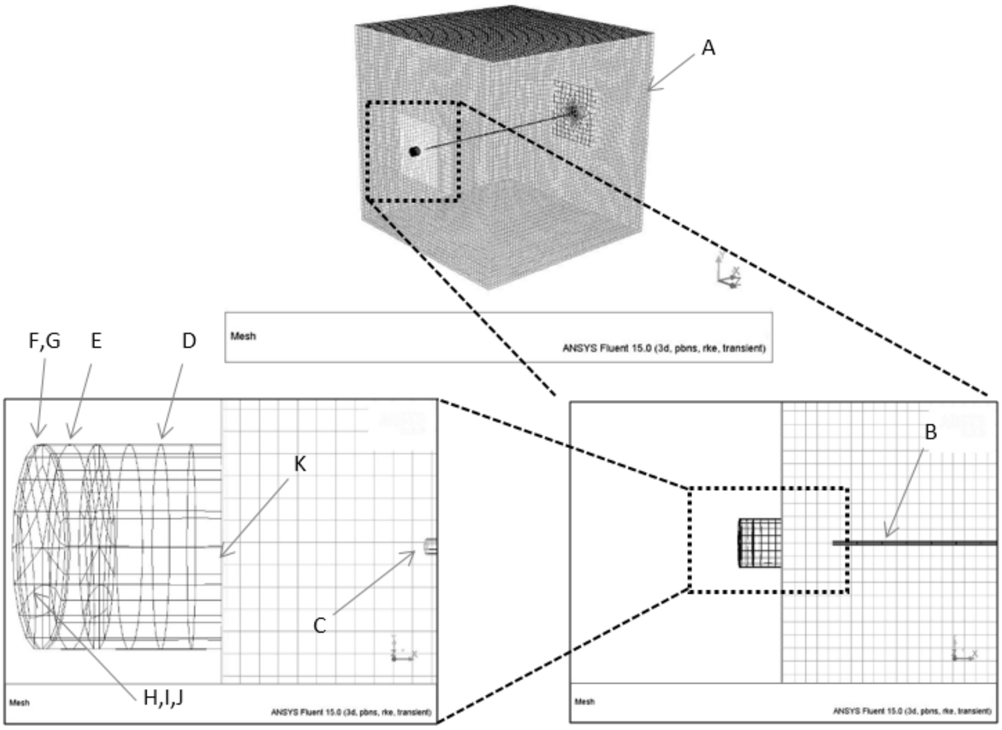

Figure 4.4 – 3D meshed test section imported from GAMBIT to FLUENT.

Table 4.1 – Hot section CFD Model with associated cell zone type, boundary type and dimensions.

Cell Zone/Type	**Boundary Type**	**Boundary Location**	**Dimension, mm**
Surrounding Air Space	Outflow	A	500 x 500 x 500
Cooling Air Tube	Stationary Wall	B	480
Cooling Air Out	Velocity Inlet	C	1.6
Recess Air Path	Stationary Wall	D	15
Substrate	Stationary Wall	E	5
Bond Coating	Stationary Wall	F	0.2
Ceramic Coating	Stationary Wall	G	0.4
Ceramic Coat Surface	Stationary Wall	H	20 Diameter
Ceramic/Bond Coat Boundary	Interface	I	20 Diameter
Bond Coat/Substrate Boundary	Interface	J	20 Diameter
Air Path End/Air Space Boundary	Interface	K	20 Diameter

Assumptions

The following assumptions were made with the numerical model prior to the analysis,

- The cooling air flow condition was steady and turbulent using k-ε equations.
- Air velocity inlet at C was $100ms^{-1}$ and uniform. This matched the actual velocity during rig operation which will be detailed in Section 4.2.3 via calculation. Furthermore, several velocity values were used numerically in order to domenstrate the effect of air velocity on the thermal gradient, the result will also be shown in Section 4.2.4.2.
- The air property was constant, i.e. temperature and density are unchanged. Inlet air temperature was 30°C. This matched the test condition.
- Single phase flow, i.e. the effects of particles and vaporization had been neglected.
- Ceramic top coat surface was kept at a steady state temperature of 1500 K (≈1200 °C). Flame combustion test condition had not been considered.
- Ceramic coating, bond coat and substrate layer were considered as solid. Sintering effect under high temperature operation was not considered.
- Growth of thermally grown oxide had not been considered in the numerical model.
- Test sample back face edge was in perfect contact with hollow sample holder structure, i.e. no gap between E and D.
- Nozzle to target distance kept at 20 mm.
- Material properties were kept constant, as shown in Table 4.2.

Table 4.2 – Material properties

Materials	**Density, kg/m3**	**Specific Heat , C*p*, J/kg-k**	**Thermal Conductivity, w/m-k**	**Viscosity**
Fluid				
Air	1.225	1006.43	0.0242	1.80E-05
Solid				
Nickel Substrate	8740	418	90	-
Metallic Bond Coat	7000	763	10.515	-
Ceramic Coat	5170	706	1.305	-

4.2.3 Cooling Nozzle Diameter Estimation

A good starting point for estimation of air velocity through a hollow tube is to consider that the the air velocity is function differential pressure, air density. Here, the air density had been considered as constant with known pressure drop. In order to estimate the relationship between the cooling nozzle diameter and air velocity, as shown in Figure 4.5, the volume flow rate of air had been considered as constant due to the specification restriction from the mass flow controller. It is not surprised to see that high air flow velocity can be achieved with a smaller nozzle diameter, therefore, a nozzle diameter of 1.6 mm had been chosen for the burner rig cooling design.

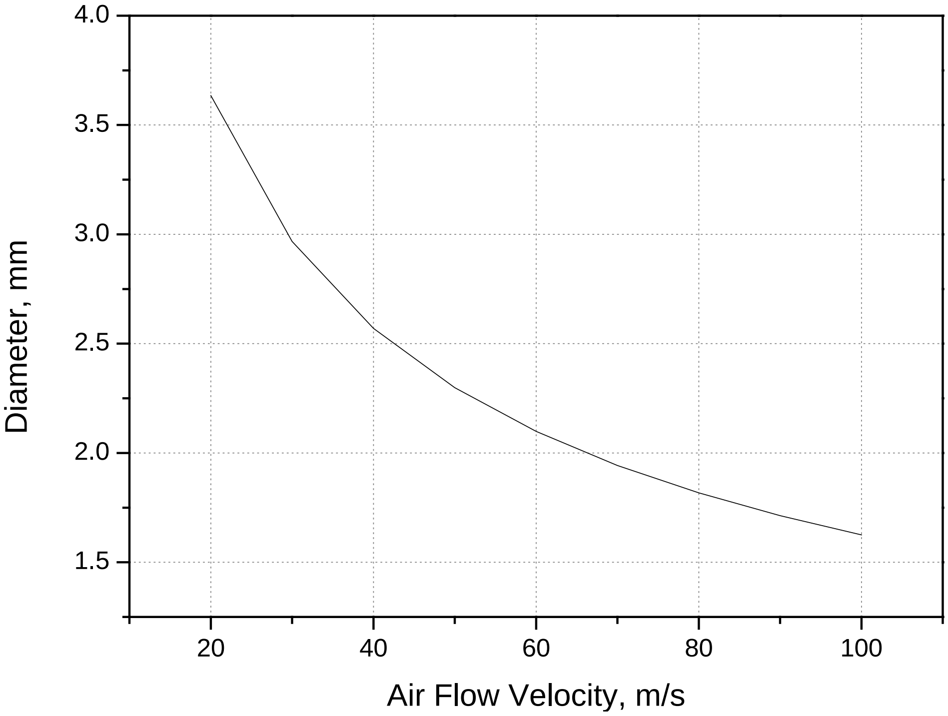

Figure 4.5 – Relationship between nozzle diameter and air flow velocity.

4.2.4 Air Cooling Numerical Validation

4.2.4.1 Governing Equations

Due to the cooling nature of the burner rig, mechanically induced air flow through the air tube that cools the substrate which creates a through thickness temperature gradient has been considered in the calculation domain. Jet impingement method was used due to its high cooling effectiveness. The air flow can be considered as incompressible when the velocity is at the lower region of Mach number spectrum, i.e. less than Mach 0.3 or 100 m/s. Furthermore, the cooling air being a Newtonian fluid has a linear relationship between shear and strain rate. Conservation of mass, momentum and energy are used to describe the flow based on the assumption that the top surface (ceramic) only subject to a steady heat flux and no heat loss from the edge of the sample. Equation (1) to Equation (5) shown below are the 3-dimentional Navier Stokes equations which describe the flow and temperature,

Continuity

$$\frac{\partial}{\partial x}(\rho u)+\frac{\partial}{\partial y}(\rho v)+\frac{\partial}{\partial z}(\rho w)=0 \tag{1}$$

Momentum in x direction

$$\frac{\partial}{\partial t}(\rho u)+\frac{\partial}{\partial x}(\rho u^2)+\frac{\partial}{\partial y}(\rho uv)+\frac{\partial}{\partial z}(\rho uw)=-\frac{\partial p}{\partial x}+\mu\left(\frac{\partial^2 u}{\partial x^2}+\frac{\partial^2 u}{\partial y^2}+\frac{\partial^2 u}{\partial z^2}\right) \tag{2}$$

Momentum in y direction

$$\frac{\partial}{\partial t}(\rho u)+\frac{\partial}{\partial x}(\rho v)+\frac{\partial}{\partial y}(\rho v^2)+\frac{\partial}{\partial z}(\rho vw)=-\frac{\partial p}{\partial y}+\mu\left(\frac{\partial^2 v}{\partial x^2}+\frac{\partial^2 v}{\partial y^2}+\frac{\partial^2 v}{\partial z^2}\right) \tag{3}$$

Momentum in z direction

$$\frac{\partial}{\partial t}(\rho u)+\frac{\partial}{\partial x}(\rho w)+\frac{\partial}{\partial y}(\rho vw)+\frac{\partial}{\partial z}(\rho w^2)=-\frac{\partial p}{\partial z}+\mu\left(\frac{\partial^2 w}{\partial x^2}+\frac{\partial^2 w}{\partial y^2}+\frac{\partial^2 w}{\partial z^2}\right) \tag{4}$$

Energy

$$\frac{\partial}{\partial t}(\rho c_p T)+\frac{\partial}{\partial x}(\rho u c_p T)+\frac{\partial}{\partial y}(\rho v c_p T)+\frac{\partial}{\partial z}(\rho w c_p T)=K\left(\frac{\partial^2 T}{\partial x^2}+\frac{\partial^2 T}{\partial y^2}+\frac{\partial^2 T}{\partial z^2}\right)+q \tag{5}$$

where u, v and w are the velocity components in x, y and z directions respectively. ρ is the mass density, μ is the viscosity. t is time, T is the temperature, and P is the pressure. c_p is the specific heat (J/kgK), K is the conductivity (W/m K) of the air, and $\dot{q}$ is the rate of internal heat generation. For turbulent flow the velocity and temperature vary with time, the model which predicts the turbulent flow of impinging air flow will be described in the next section.

Turbulence model – RNG k-epsilon turbulence model

As it is not possible to utilize a single turbulence model to all applications, considerations such as computational stability and level of accuracy must be taken into account when choosing the appropriate model. For application of burner rig where an impinging air flow onto a flat surface is used to cool down the substrate, RNG k-epsilon turbulence model [7] is the most obvious choice. Renormalization group theory technique is used for this model, derived from the instantaneous Navier Stokes equations. The end product of this derivation produces some contants and adds new terms to the transport equations for the turbulent kinetic energy. The swirl effect is included in the model which increases the level of accuracy of swirling flow.

The transport equations are

$$\frac{\partial}{\partial t}(\rho k)+\frac{\partial}{\partial x_i}(\rho k u_i)=\frac{\partial}{\partial x_j}\left[\alpha_k \mu_{eff}\frac{\partial k}{\partial x_j}\right]+G_k-\rho\varepsilon-Y_M+S_k \qquad (6)$$

$$\frac{\partial}{\partial t}(\rho \varepsilon)+\frac{\partial}{\partial x_i}(\rho \varepsilon u_i)=\frac{\partial}{\partial x_j}\left[\alpha_\varepsilon \mu_{eff}\frac{\partial \varepsilon}{\partial x_j}\right]+C_{1\varepsilon}G_k\frac{\varepsilon}{k}-C_{2\varepsilon}\rho\frac{\varepsilon^2}{k}-R_\varepsilon+S_\varepsilon \qquad (7)$$

where G_k is the generation of turbulent kinetic energy due to velocity gradient, and Y_m is the fluctuating dilation in compressible turbulence contributes to the dissipation rate. α_k and α_ε are inverse effective Prandtl numbers. Source term S_k and S_ε are user defined. $C_{1\varepsilon}$ and $C_{2\varepsilon}$ are constants and defined as 1.42 and 1.68 respectively.

Effective viscosity equation given below has been defined by RNG theory using a scale elimination procedure,

$$d\left(\frac{\rho^2 k}{\sqrt{\varepsilon\mu}}\right) = 1.72\frac{\hat{v}}{\sqrt{\hat{v}^3 - 1 + C_v}}d\hat{v} \qquad (8)$$

where $\hat{v}$ is defined as μ_{eff}/μ and C_v is a constant. This equation gives a more accurate definition on how the effective turbulent transport varies with effective Reynolds numbers, thus results for low-Reynolds number can be obtained more accurately.

4.2.4.2 Effect of air flow velocity

Once the geometry and assumption were completed and defined, the meshed model was input into FLUENT® and computation was performed. In order to examine the validity of air flow path structure and find the relationship between air velocity with through thickness sample temperature profiles, varies air flow velocity ranging from 20 m/s to 100 m/s were applied for temperature calculation at velocity inlet boundary C, as shown in Figure 4.6 and Figure 4.7.

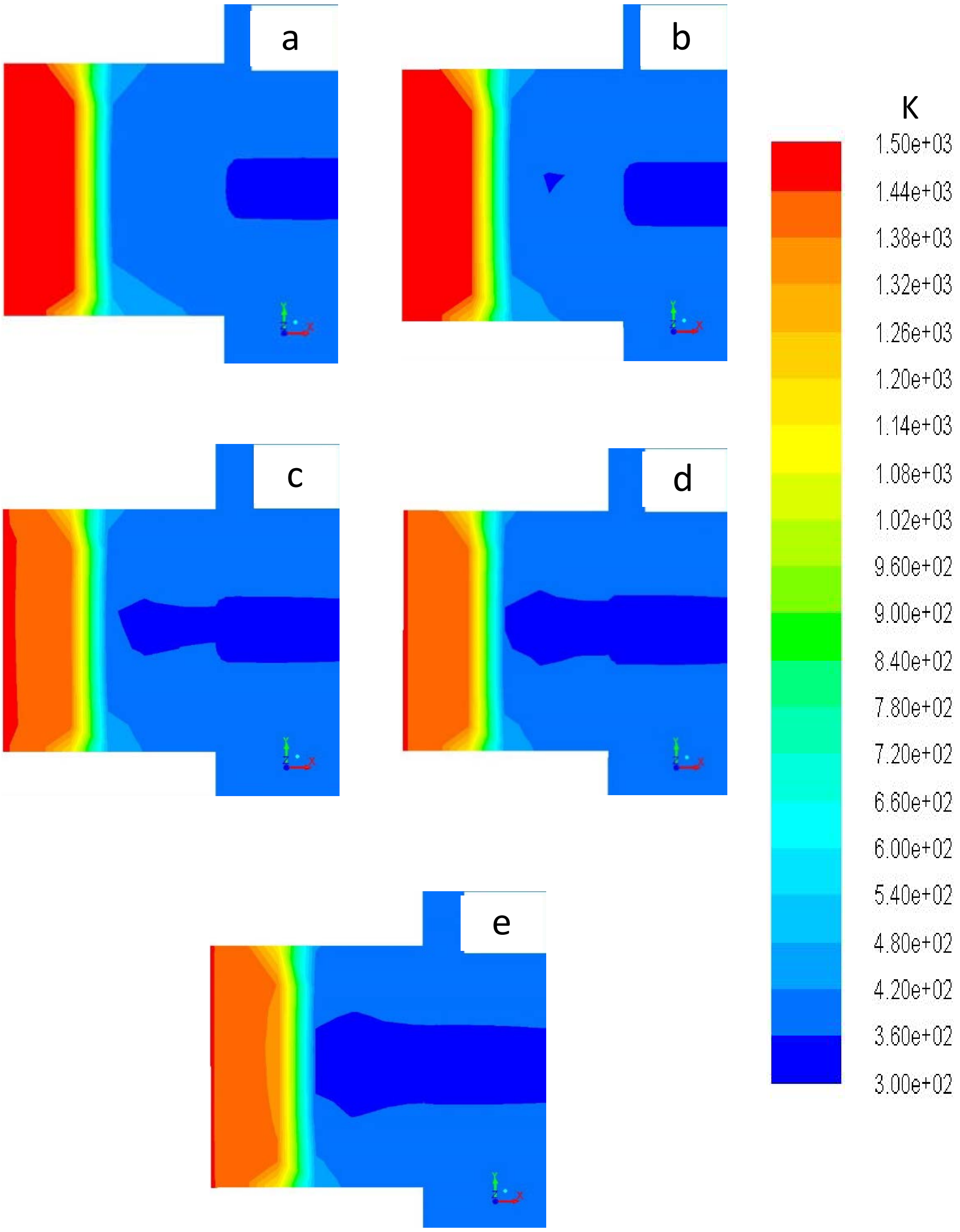

Figure 4.6 - Temperature contour of TBC sample and air flow path structure for air inlet velocity of 20 (a), 40 (b), 60 (c), 80 (d) and 100 (e) m/s.

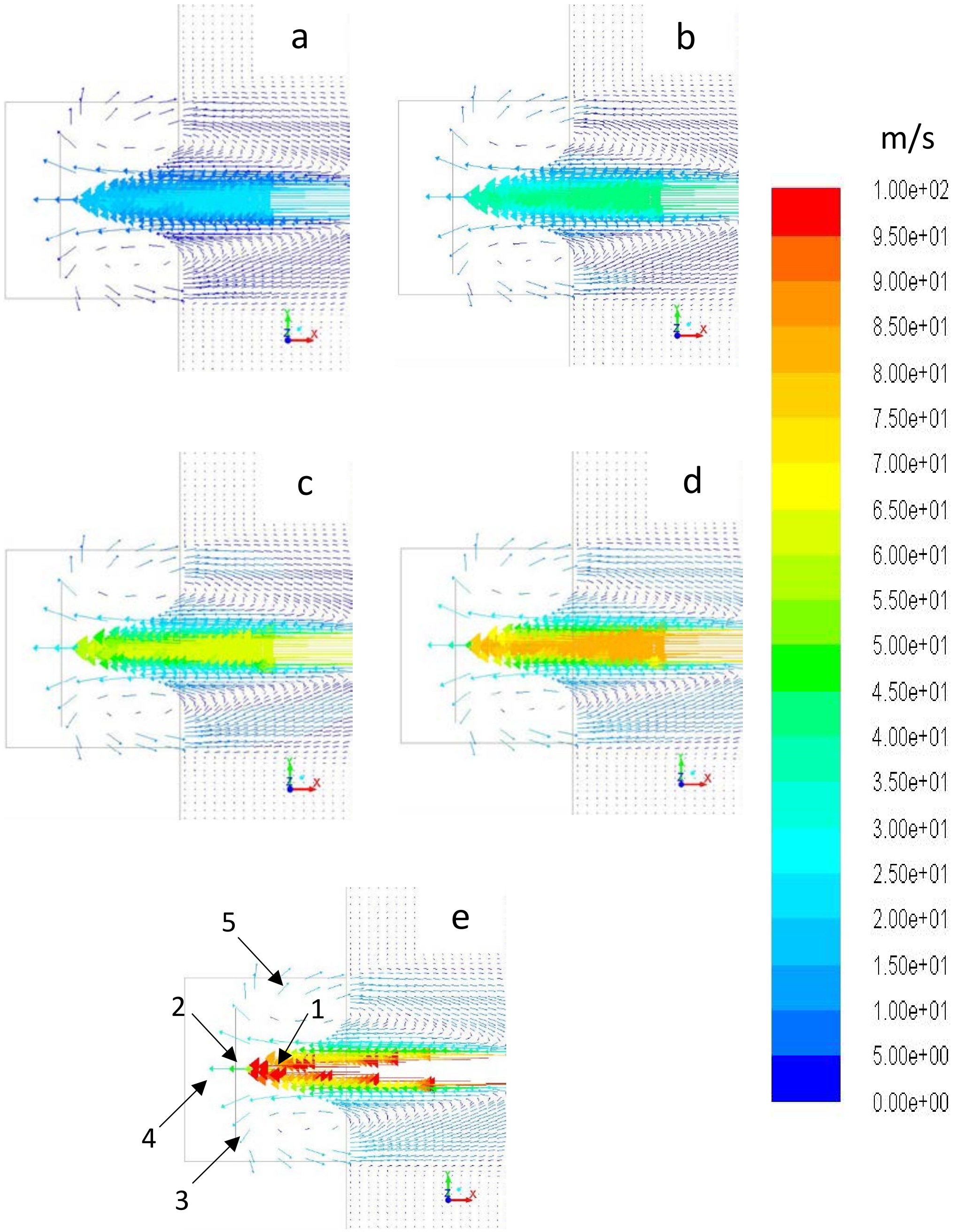

Figure 4.7 – Velocity magnitude for 20 (a), 40 (b), 60 (c), 80 (d) and 100 (e) m/s with a fixed air inlet nozzle to sample back surface distance.

Figure 4.6 shows the through thickness temperature profile of the sample and the interaction with the recess structure at different cooling air velocity. The magnitude of heat flow produced by the front surface and air inlet can also be seen in the same contour plot. Due to the fact that an assumption of static thermal condition was applied at the front surface, the pattern of heat distribution within the solid from each air velocity condition is roughly as expected. However, a large region of edge effect can be observed from each condition, this is due to the assumption of boundaries as solid stationary walls for each layer of materials, thus no heat radiation loss at these boundaies. Also, in reality oxyacetylene flame that has a larger diameter than the sample is used as heat source. Unlike what has reflected in the model, when the entire sample is immersed in the flame, a more uniform distribution of heat pattern around the edge would have occourred.

Figure 4.7 shows impingment jet flow pattern in which sample substrate acts as the flat target has resulted four typical flow regions [9] for all different velocity inlet condition. They are, (1) Initial free jet and core region; (2) Decaying jet region; (3) Wall jet region; (4) Stagnation region and (5) Fountain flow region. The investigation of parameters that effect the such flow regions is not carried out. However with tube nozzle being 1.6 mm and nozzle to target distance being 20 mm, the most effective cooling is at 100 m/s, as shown in Figure 4.8. Furthermore, the model suggests that the effect of air velocity at 40, 60 and 80 m/s to substrate back temperature is less obvious. The exact cause is beyond the scope of this project, but one possible reason could be that the geometry of the hollow air flow path section may have some influence on such result.

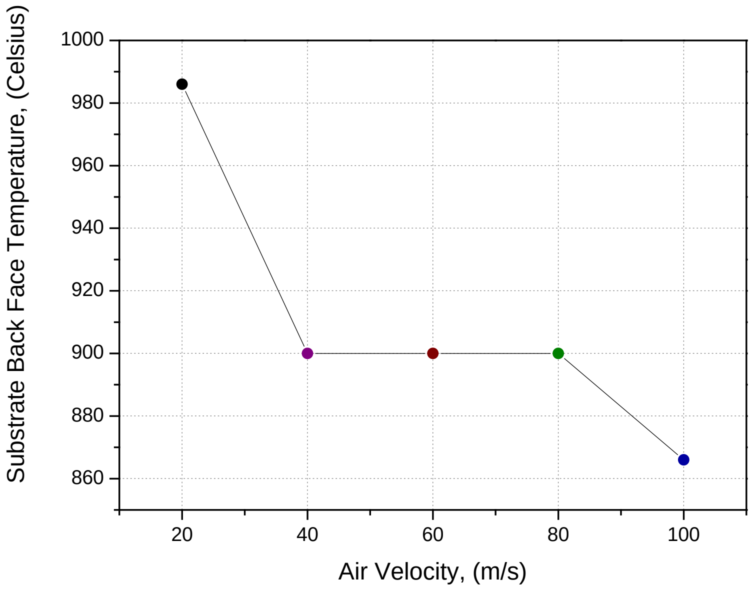

Figure 4.8 – TBC sample back face substrate temperature for air inlet velocity of 20, 40, 60, 80 and 100 m/s.

4.3 Temperature Measurement Hardware

4.3.1 Thermocouple

Commercially available thermocouples are widely used for measuring temperature due to their advantages which include,

- Wide practical temperature range can be served.
- Immune to vibration and suitable under hazardous condition.
- Small size and has low thermal capacity, thus fast response to temperature change.
- Excitation power is not required, thus not prone to self heating and intrinsically safe to handle.

Response Time

The response of a thermocouple is often defined as the time required by the sensor head to reach 63.2% of an instantaneous temperature change under specific operating conditions. Also, the reponse time is depended on the size of the sheath diameter. It is known that sheaths with small diameters have faster reponse time, but sheaths with larger diameters have longer serving life [8].

Thermocouple Selection

Many factors need to be considered prior to the selection of thermocouples, for instance,

- Type of applications and operating environment. For this burner rig, thermocouple temperature measurements were required on two different positions of the TBC sample, i.e sample back and sample middle. In order to achieve a proper physical contact with the substrate at the back, a different thermocouple specification in terms of wire flexibility was required.
- Knowing the operating temperature range would be required.
- Temperature measurement accuracy and response time.
- Compensating cable was required for joining thermocouple to the measuring instruments. It is worth noting that compensating cable uses

different composition alloy wires to thermocouple wires, therefore, compensation cable is less accurate in terms of thermal electromotive force. However, this inaccuracy had been neglected. Table 4.3 shows the specifications of the selected thermocouples

Table 4.3 – Selected thermocouple specification

Thermocouple Type	K	N
Wire Diameter	0.5 mm	1 mm
Wire Material	Chromel-Alumel	Nicrosil-Nisil
Thermocouple Length	300 mm	150 mm
Maximum Temperature	1100 °C	1250 °C
Sheath Material	-	Nicrobell D
Insulation	High Temperature Glass	Magnesium Oxide Powder
Flexibility	Highly Flexible	Rigid
Temperature Measuremnt	Sample Back	Sample Middle

Thermocouple Wire Preparation

For small thermocouple diameter wires such as the one that had been used for this project, a proper preparation of wires was needed in order to carry out arc welding with the sample substrate. For the welding practice a Labfacility® thermocouple and fine wire welder L60+ model was used. The following preparation steps were taken place prior to the welding procedure,

- Approximately 12 mm of insulation material was stripped off.
- Cut wire off square using side cutters leaving sufficient uninsulated wires to give approximately 1 mm protruding when gripped in the welding pliers.
- The tip of the wires were positioned at the centre of the substrate sample with the pliers pressing down.
- Set the energy output level to maximum due to small diameter wire.
- Press ‘weld’ switch and release the switch for examination.
- Repeat last step until the wires are firmly welded on the substrate, as shown in Figure 4.9.

Figure 4.9 – K-type thermocouple wires welded on sample substrate.

4.3.2 Infrared Pyrometer

For TBC sample front surface temperature measurement, a non contact infrared pyrometer was selected. In keeping with the requirements it had to have a temperature range from 500 °C to 1800 °C; temperature range is an MI3 Raytek® sensor with USB interface digital communication box attached to the sensor head. The pyrometer only has a single spectral observation for short wave infrared radiation at 1 μm. Multiple wavelength pyrometers are typically 5-10 times more expensive and would dominate the cost of the test rig. In this wavelength the TBC is considered to be semi-transparent. The emissivity can be set with a precision of 0.001 and the sensor has a 10 ms response time. An integrated laser pointer is used to position the pyrometer accurately and ensures that the temperature measurement is taken from the centre of the TBC sample on a circular laser spot size around 2 mm [12], as shown in Figure 4.10.

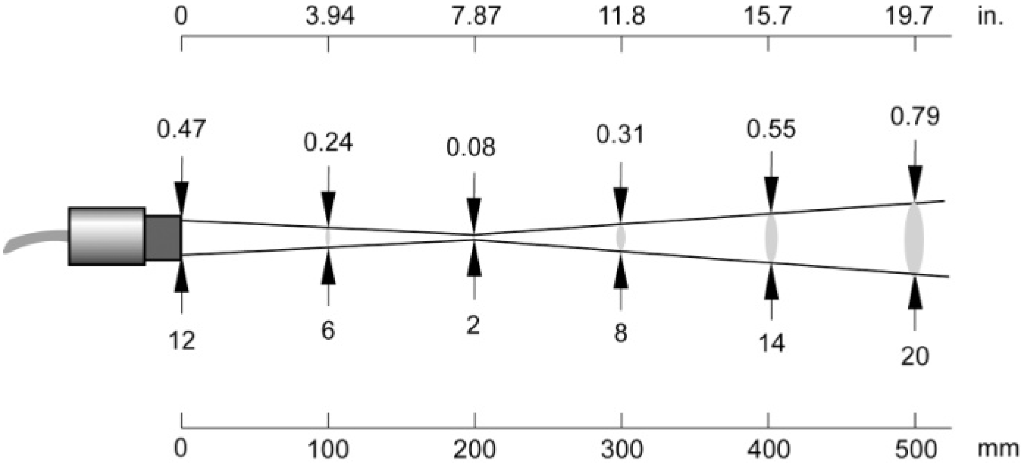

Figure 4.10 – Infrared pyrometer laser spot size. [12]

4.4 Data Acquisition & Controlling Hardware

4.4.1 CompactRIO System

For the purpose of temperature and gas flow control, a 8-slot NI cRIO-9047 configurable chassis and controller has been used along with two NI I/O modules, the NI 9211 and NI 9381, as shown in Figure 4.11. This embedded system features a real-time embedded processor, a reconfigurable chassis containing a user-programmable FPGA, and swappable I/O modules. This relatively low-cost embedded architecture can be programmed with NI LabVIEW graphical programming language. Figure 4.12 shows the general CompactRIO digital architecture. This task will require development in both the Realtime & FPGA environments.

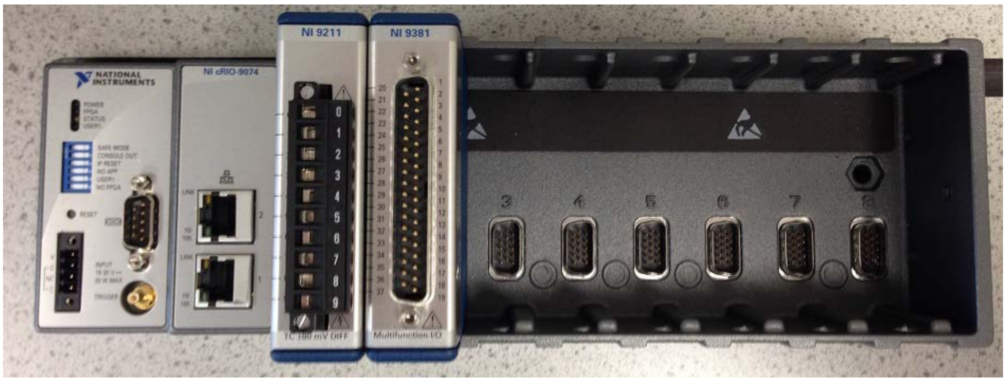

Figure 4.11 – CompactRIO control system.

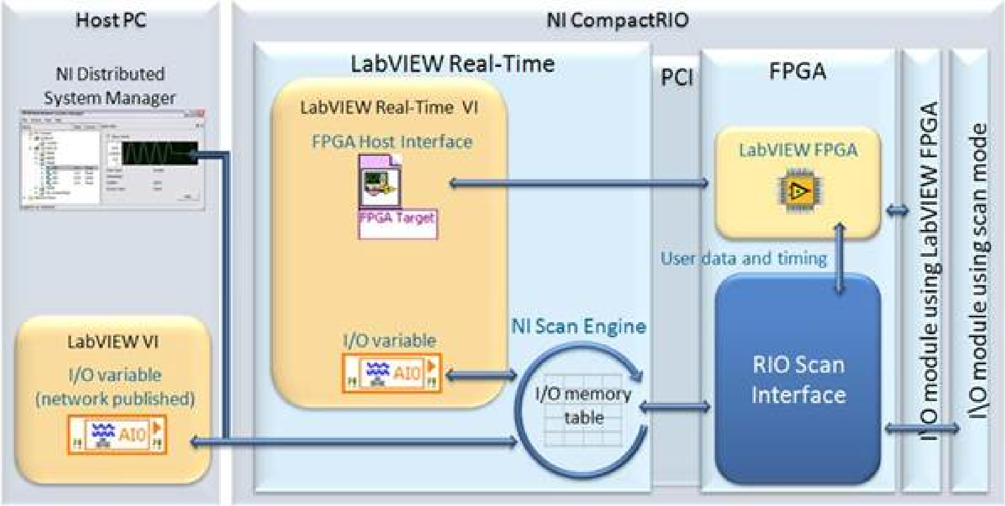

Figure 4.12 – Schematic of the CompactRIO architecture.

4.4.2 C Series I/O Module

4.4.2.1 NI 9211 Thermaocouple Input Module

The NI 9211, as shown in Figure 4.13 (a), has a 10-terminal, detachable screw-terminal connector that provides connections up to four thermocouple input channels. Each channel has a terminal which has the positive lead of the thermocouple, TC+, and a terminal which has the negative lead of the thermocouple, TC–. The NI 9211 also has a common terminal, COM, that is internally connected to the isolated ground reference of the module. One N-type and one K-type thermocouples are connected to this module for middle and back face temperature measurement of the test sample respectively. The thermocouple values are digitalised by an 12 bit digital to analogue converter, giving a measurement of 0.3 °C.

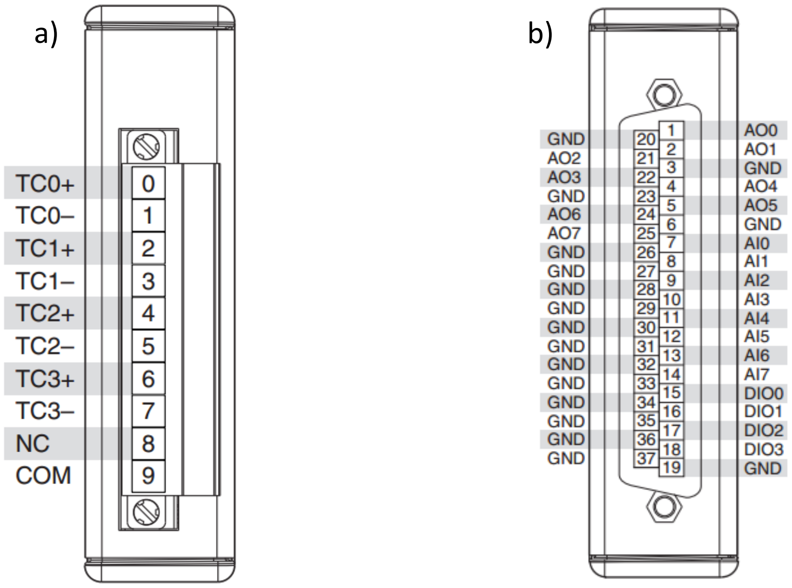

Figure 4.13 – a) Thermocouple module end terminal; b) Multfunction I/O module for MFCs.

4.4.2.2 NI 9381 multifunction Input/Output Module

The NI 9381 , as shown in Figure 4.13 (b), has a D-sub (D-subminiature) connector that provides connections for 8 analogue input channels, 8 analog output channels and 4 digital input/output channels. Each analog input/output channel has a AI/AO pin to provide connections to analogue input or output devices. Each port can be configured in the software for specific input or output. Three mass flow controllers that monitor the gas flow from oxygen, acetylene and compressed air and one infra-red thermometer that monitor the front face temperature of the tested sample are connected to this module. All analog input/output for each device that have been considered for temperature control of the burner rig system are summarized in Table 4.4.

Table 4.4 – Summary of analogue input and output for all control devices.

Analog Input (read)					
Device	Usage	NI Module	Voltage Range	Channel/Pin	Connection Type
Infra-red thermometer	Sample Front	9381	0-5 V	AI 0 (4)	Differential
N-type thermocouple 1	Sample Middle	9211	±80 mV	Channel 1	-
K-type thermocouple 2	Sample Back	9211	±80 mV	Channel 2	-
Mass flow controller 1	Oxygen	9381	0-5 V	AI 1	Differential
Mass flow controller 2	Acetylene	9381	0-5 V	AI 2	Differential
Mass flow controller 3	Compressed Air	9381	0-5 V	AI 3	Differential
Analog Output (to specify)					
Mass flow controller 1	Oxygen	9381	0-5 V	AO 2	Differential
Mass flow controller 2	Acetylene	9381	0-5 V	AO 3	Differential
Mass flow controller 3	Compressed Air	9381	0-5 V	AO 4	Differential

4.5 Data Acquisition Controlling Software

LabVIEW

The software program that monitors the sample temperature and controls the flame temperature is NI Labview, created by National Instrument Corp. The software is a graphically programming platform which is written in G. LabVIEW programs are called Virtual Instruments, or VI. VIs contain a front panel and block diagram. Front panel has various control and display objects while the block diagram are composed from a variety of functions connected together using virtual wires. This task will require development in both the Realtime & FPGA environments.

LabVIEW Real-time

The National Instruments LabVIEW Real-Time Module is an add-on component for the LabVIEW Development System. When installed, this software compiles NI LabVIEW graphical code and optimizes it for the selected real-time target. Using the LabVIEW Real-Time Module, hardware targets like CompactRIO applications can be developed and deployed to all NI real-time.

LabVIEW FPGA

National Instruments LabVIEW and the LabVIEW FPGA Module deliver graphical development for field-programmable gate array (FPGA) chips on NI Reconfigurable I/O (RIO) hardware targets. With an NI LabVIEW FPGA Module, we can develop FPGA VIs on a host computer running Windows, and LabVIEW compiles and implements the code in hardware. We can create embedded FPGA VIs that combine direct access to I/O with user-defined LabVIEW logic to define custom hardware for different applications.

4.5.1 Developing the controller in software

4.5.1.1 LabVIEW FPGA Interface Programming Mode

LabVIEW FPGA interface mode enables the C series modules (I/O modules) from LabVIEW FPGA VIs. Modules that have been used in LabVIEW FPGA interface mode appear directly under the FPGA target item in the project explorer window and the I/O channels appear as FPGA I/O items under the FPGA target. In order to access the I/O channels, FPGA I/O nodes in the FPGA VIs have been configured. In order to create and build the temperature and gas flow control application, the FPGA VIs need to downloaded to the FPGA target, i.e. cRIO chassis. Hence FPGA VIs can then be read from and write to the I/O channels of the correponding modules. The following FPGA VIs structure of the control system which describes the infra-red and mass flow controllers interface were created, as shown in Figure 4.14 and Figure 4.15.

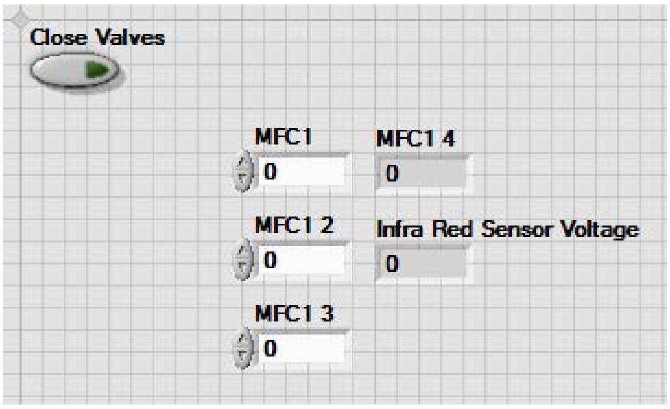

Figure 4.14 – MFCs and IR interface front panel.

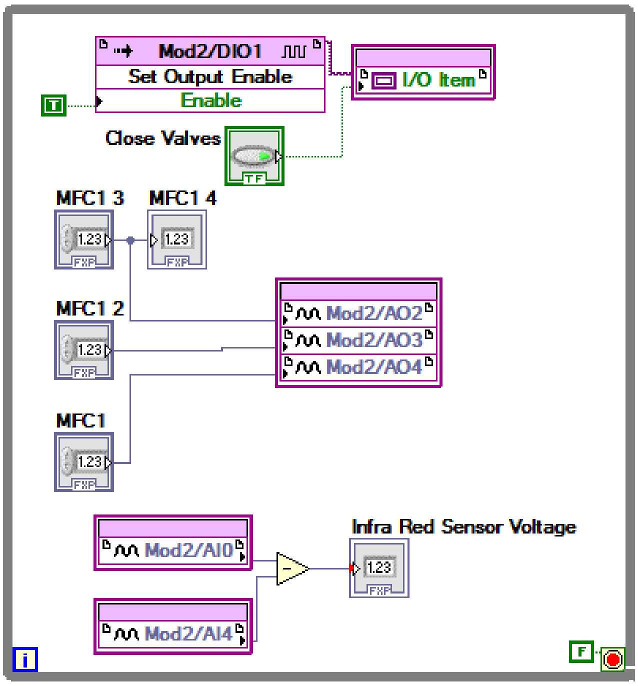

Figure 4.15 - MFCs and IR interface block diagram.

4.5.1.2 Host VI to communicate with FGPA VI

In order for the host VI communicates with the FPGA VI, the host VI as shown in Figure 4.16 and Figure 4.17, needs to run on a Real-Time (RT) target, such as a CompactRIO controller, or on a Windows PC. The host VI uses controls and indicators on the FPGA VI front panel to transfer data between the FPGA on the RIO device and the host-processing engine. These front panel objects are represented as data registers within the FPGA.

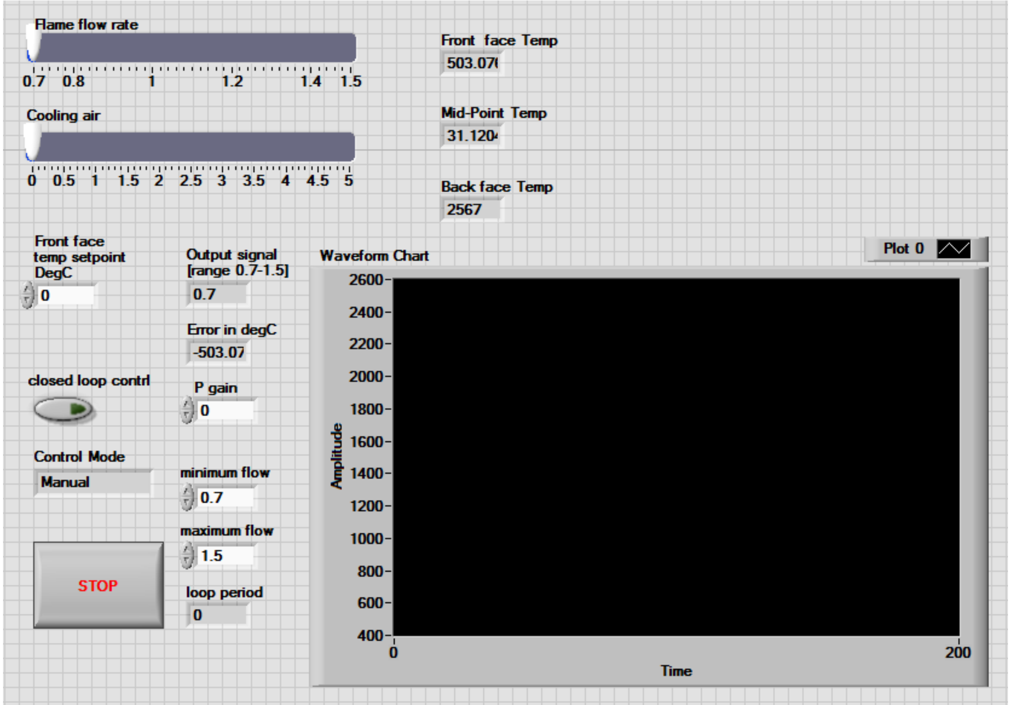

Front face Temp 503.07

Mid-Point Temp 31.120

Back face Temp 2567

Front face temp setpoint DegC 0

Output signal [range 0.7-1.5] 0.7

Error in degC -503.07

P gain 0

Control Mode Manual

minimum flow 0.7

maximum flow 1.5

loop period 0

Figure 4.16 – Realtime main application front panel.

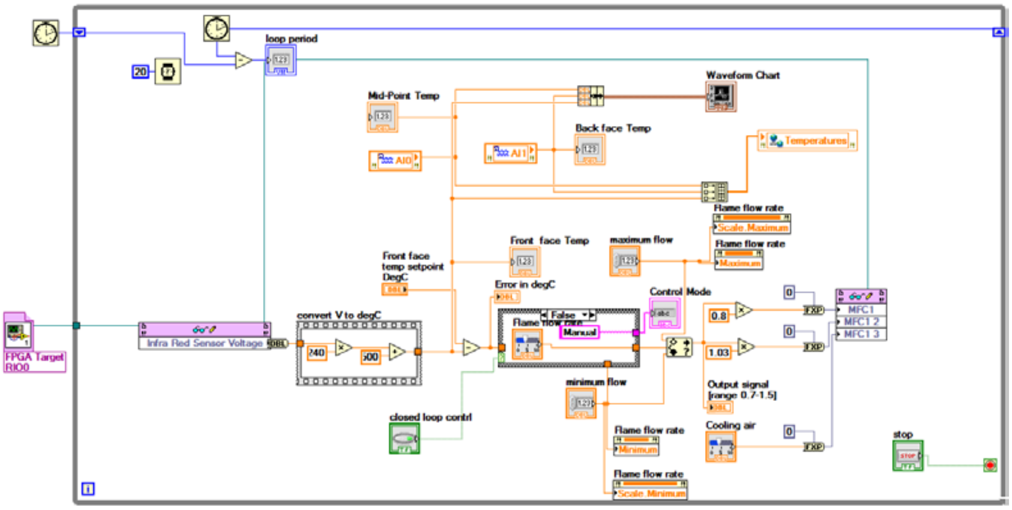

Figure 4.17 – Realtime main application block diagram.

Under Host VI, the front panel in LabVIEW contains controls, indicators and waveform chart in realtime. They are the front surface temperature setpoint (desire temperature), sample middle and back temperature (in degree C) readings from both thermocouples which is handled by the scan engine and temperature (convert voltage to degree C) reading from the infrared pyrometer. A reference FPGA target was created to be able to put into the Read/Write control function for each of input/output element.

The convertion can be set in the USB interface by specifying the relationship between the voltage reading and correspond temperature in degree C. The error is calculated by subtracting the Infra-red themometer reading from the setpoint temperature. A loop control mode is created to increase the control flexibility, manual and closed loop control can be triggered in realtime. The oxy-acetylene mix ratio is kept at a constant value by prescribe a multiplier of 0.8 and 1.03. So to increase the flow rate with constant mix ratio, the output range of 0.7 to 1.5 for the gas mass flow controller is defined.

4.6 Calibration

Once the selection and integration of the control hardware and software was completed, it was necessary to perform a series of studies to establish some of the unknown qualities fo the flame testing equipment. Three key calibration stages were designed prior to the actual test,

- First stage was to estabilish an emissivity estimation method for the single wavelength infrared pyrometer. Due to the fact that the ceramic top coat is semi-transparent at the wavelength that the pyrometer is capable of, two types of samples were used for the calibration procedure, 1) Ni-based substrate with bond coat sample; 2) Thermal barrier coated sample. The test condition for each set of samples was the same and emissivity value from each sample was taken for comparison.
- Second stage was to identify if the presence of the oxy-acetylene flame in the path of the pyrometer can make a strong influence towards the infrared pyrometer temperature measurement. In order to simulate the actual test condition, three sets of flame nozzle to sample surface distance and focal distance were considered during the calibration procedure. Full range of flame flow rate was also included in the test. The results were summarizd with three contour plots.
- Third stage was to use the estimated emissivity value with cooling air switched on, thus the integration of test result, i.e. simultaneous flame heating and cooling on the TBC sample, can be analysed in terms of through-thickness temperature gradient and sample surface to nozzle distance.

4.6.1 Influence of radiation from the flame on pyrometer measurement of sample surface temperature

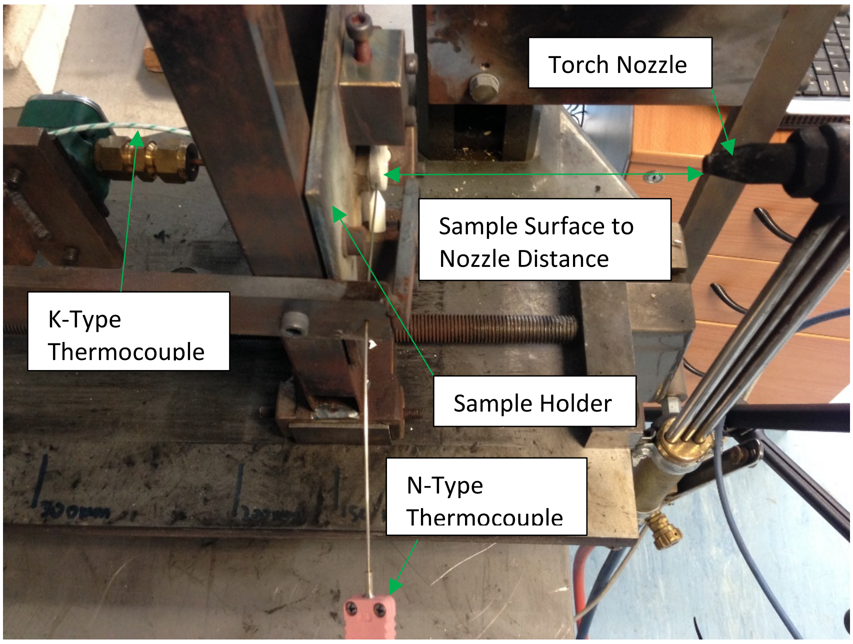

Figure 4.18 – Emissivity estimation test setup.

Calibration of the emissivity for 1 μm wavelength radiation was performed using the conditions described in section 4.2.1. The set up is shown in Figure 4.18. For this test a moderate sample surface to nozzle distance of 200 mm was used. Surface and mid body substrate temperature were monitored using the infrared pyrometer and a N-type thermocouple respectively. The procedure for the test was apply heat from the oxyacetylene flame without any active cooling of the rear surface by the impinging air flow. As such the only heat loss mechanisms were radiation, natural convection and the minimal conduction through the spinel mounting points. By slowing the rate of heat loss sufficiently it was possible to achieve a steady state of sample temperature and where there was minimal thermal gradient from the front to the back of the sample. In this state the mid body temperature was assumed to be equal to front body temperature, within acceptable margin can be used to calibrate the pyrometer.For bond coat sample, the adjustment of emissivity value of the infrared pyrometer started at 1 and finished at 0.65, whereas for sample that had ceramic top coat the adjustment of emissivity value of the infrared pyrometer started at 1 and finished at 0.2, as shown in Figure 4.19 and Figure 4.20. During this process the corresponding emissivity value where pyrometer temperature measurement matched with the thermocouple measurement was considered to be the emissivity of the top coat.

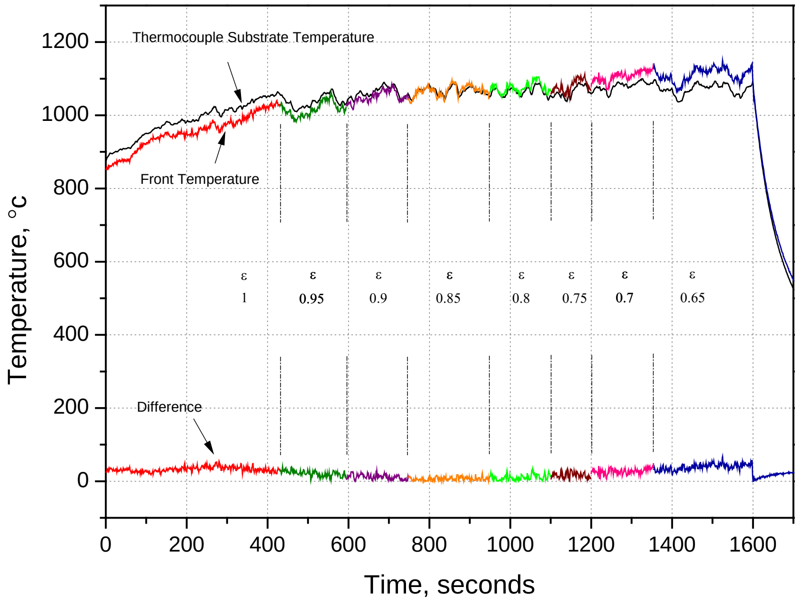

Figrure 4.19 – Temperature measurement for bond coat sample taken from pyrometer and thermocouple during emissivity calibration. The difference between the measured temperature from pyrometer and thermocouple with each corresponding emissivity value is plotted.

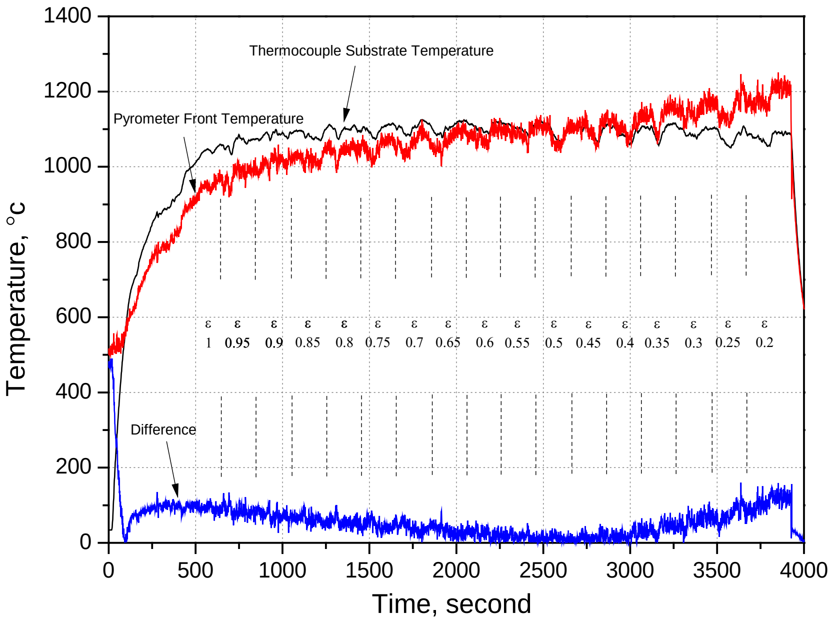

Figrure 4.20 – Temperature measurement for ceramic top coat sample taken from pyrometer and thermocouple during emissivity calibration. The difference between the measured temperature from pyrometer and thermocouple with each corresponding emissivity value is plotted.

It can be seen from the plotted data above that sample thermal equilibrium was reached after about 300 and 600 seconds for type 1 and 2 sample respectively, so in order to estimate emissivity value of the sample the absolute difference temperature reading between the pyrometer and thermocouple must be as small as possible. For modern non-contact temperature measurement equipment, the output signal of the pyrometer is related to the thermal radiation (J*) from the heat source via Stefen-Boltzmann law in which the relationship between emissivity (ε), Stefan constant (σ) and temperature (T) is defined as, $j^* = \varepsilon\sigma T^4$.

The difference between the thermocouple and pyrometer measurement defines the direction of emissivity adjustment. If the difference is positive, the emissivity value should be decreased. If the difference is negative, the emissivity value should be increased. The correct emissivity is defined when the difference is approximately zero. For the sample with a bond coat front surface, Figure 4.19 between 700 to 1100 seconds the bond coat emissivity is considered to be 0.85 with an approximately zero temperature error. For the sample with a top coat front surface, Figure 4.20, the minimum temperature difference error have occurred at a emissivity value 0.4. This observed difference is attributed to the difference in surface property and emission spectra of the two front surfaces of these samples. So, to choose the most suitable emissivity the attention has to be focused on the property of thermal barrier coating itself. The assumption can be made that the low thermal conductivity of ceramic coating would lead to a higher surface temperature than the substrate under isothermal condition. Therefore, 0.4 is estimated to be the ceramic coat emissivity.

4.6.2 Influence of gas flow rate & nozzle to sample distance on sample surface temperature

Flame Type

Depending on the ratio of fuel gas to oxidizing gas, there are three basic types of oxyacetylene flames, shown in Figure 2.21. Out of these three types, oxidizing flame is the most suited for this particular burner rig testing due to the fact that excess amount of oxygen contained in the stable flame, and has the highest heat flux [5], hence oxidizing flame is used throughout the test. Apart from the reducing flame where a acetylene feather is created due to the excess amount of acetylene, each flame type is characterized by a short inner cone and a longer outer envelope. As illustrated in Figure 4.22 two-thirds of the total heat generated from the inner core where the primary combustion takes place via the chemical reaction between oxygen (O_2) and acetylene (C_2H_2). The second combustion which creates the outer envelope takes place from the products, carbon monoxide (CO) and hydrogen gas (H_2), of the primary combustion, reaction then takes place with oxygen (O_2) off the surrounding air and form carbon dioxide (CO_2) and H_2O.

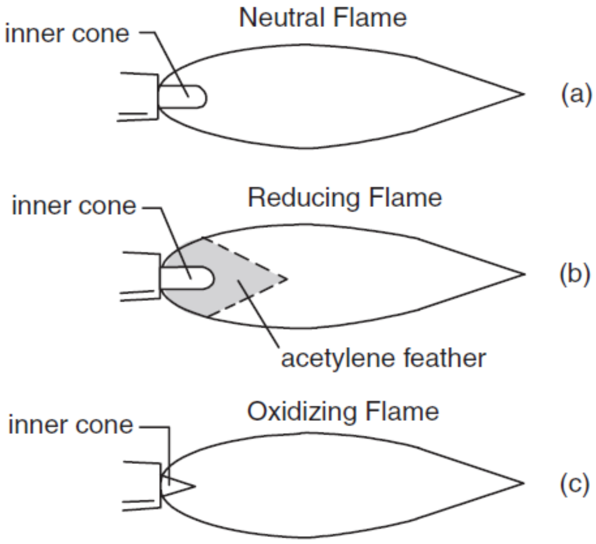

Figure 4.21 – Three types of oxyacetylene flames. a) Neutral flame – equal quantities of oxygen and acetylene mixture; b) Reducing flame – excess amount of acetylene and has relatively low flame temperature; c) oxidizing flame – excess amount of oxygen and has relatively high flame temperature [5].

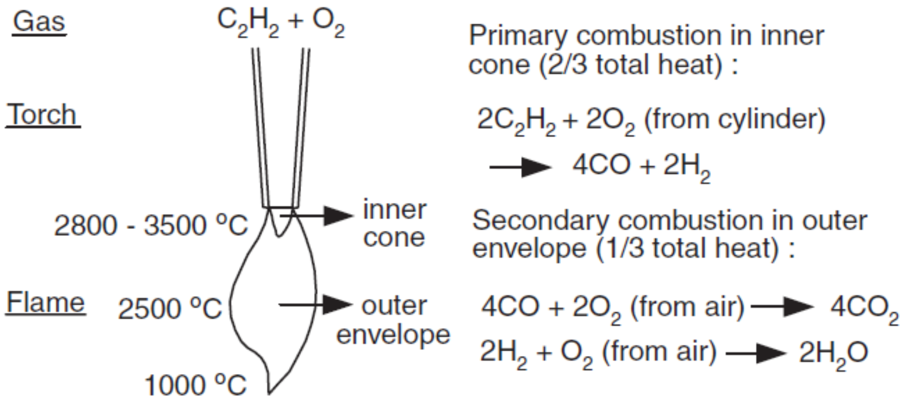

Figure 4.22 – Chemical reaction and temperature distribution in a typical neutal oxyacetylene flame [6].

Flame Temperature Influence

During the development of the burner rig, questions have been arised on how much of a flame temperature contribution towards the overall temperature measurement on the TBC sample surface. So upon the completion of the first stage calibration, flame temperature measurement with various focal distance and torch nozzle to surface distance test was performance to determine the existence of such influence. Here, focal distance is defined as the infrared beam travelling distance from sensor head to the surface of the TBC sample. During each test set, the spectral emissivity setting of the pyrometer was varied from 0.2 to 1 with corresponding flame flow rate ratio between 0.7 to 1.5.

Table 4.5 – Flame temperature influence test scheme

Test Set	Focal Distance, mm	Nozzle to Surface Distance, mm
A	180	100
B	230	150
C	290	200

Since the infrared pyrometer measures the thermal radiation from combustion gas, i.e. oxyacetylene flame, within the its field of view. Therefore the setup of the infrared pyrometer can allow the energy data to be collected without any interference from other objects. Infrared emitted from the flame can be absorbed by other chemical gas products. It has been demonstrated in the literatures [10, 11] that in the infrared spectrum region CO_2 emits at 2.8, 4.2 and 15 μm. CO emits at 2.3 and 4.5 μm. The strongest vibration bands is H_2O which is at 1.8, 2.7 and 6.3 μm. Based on these evidence, it would be desirable to have a infrared pyrometer that has a relatively large bandwidth range. However, as mentioned in previous section, only a single spectral response pyrometer was used. This hardware shortcoming may lead to some degree of uncertainty towards the measured result, but the approach of collecting and interpreting data would be very unique on selecting the appropriate emissivity value.

Results from Figure 4.24, 4.25 and 4.26 indicate that the maximum flame temperature measured using single wavelength pyrometer is around 700 °C which is a lot lower than the surface temperature. Hence infrared emitted from the flame has no influence towards the temperature measured by the pyrometer. The flame test results also indicate that the measured temperature decreases as flame flow rate increases up to a critical value 0.9.

To confirm this finding, a separate flame flow rate ratio adjustment test with ceramic coated sample was carried out, as shown in Figure 4.27. The setup was the same as descriped in Section 4.6.1. The emissivity used in this test was 0.4, the maximum steady state surface temperature of 1100 °C was reached after 600 seconds when the flame flow rate of 0.7 was used with corresponding oxygen and acetylene mass flow rate of 5.6 and 4.33 litre/min respectively, see Table 4.5. Noticed that mass flow rate ratio betwee oxygen and acetylene were kept constant with changing of flow rate ratio. This indicates that the increase of mass flow rate of each gas leads to a decrease in both flame temperature and sample surface temperature, as shown in Figure 4.28. For the purpose of this project, a flame flow rate value between 0.7 and 0.8 was used.

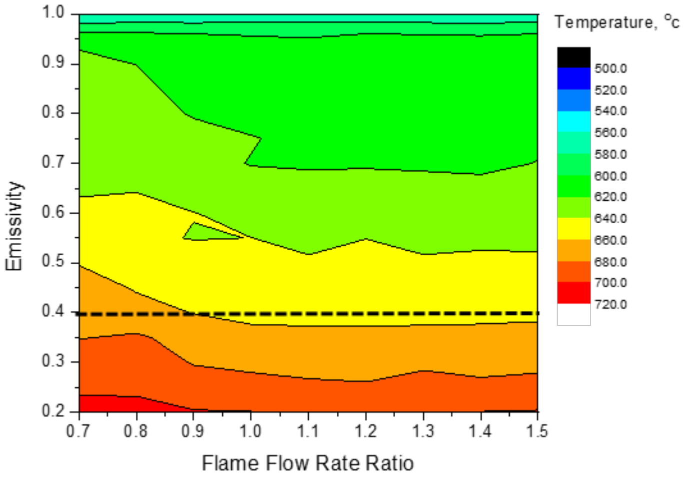

Figure 4.24 – Contour plot of test set A. Focal length 180 mm; Nozzle to surface distance 100 mm.

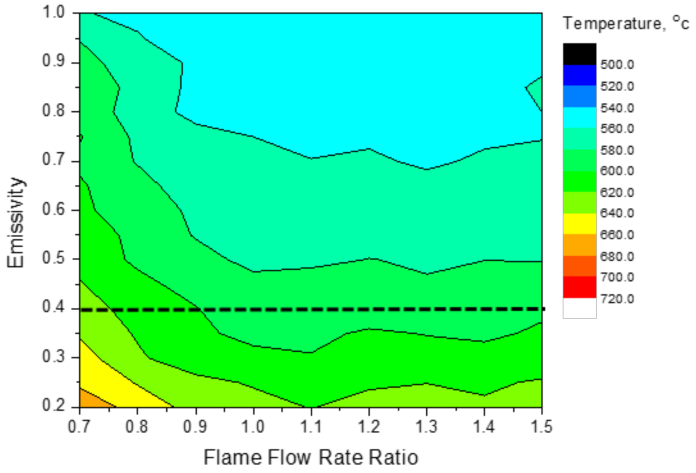

Figure 4.25 – Contour plot of test set B. Focal length 230 mm; Nozzle to surface distance 150 mm.

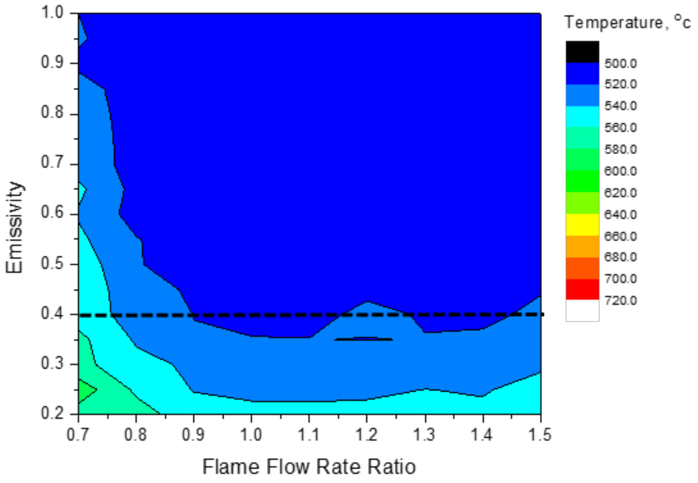

Figure 4.26 – Contour plot of test set C. Focal length 290 mm; Nozzle to surface distance 200 mm.

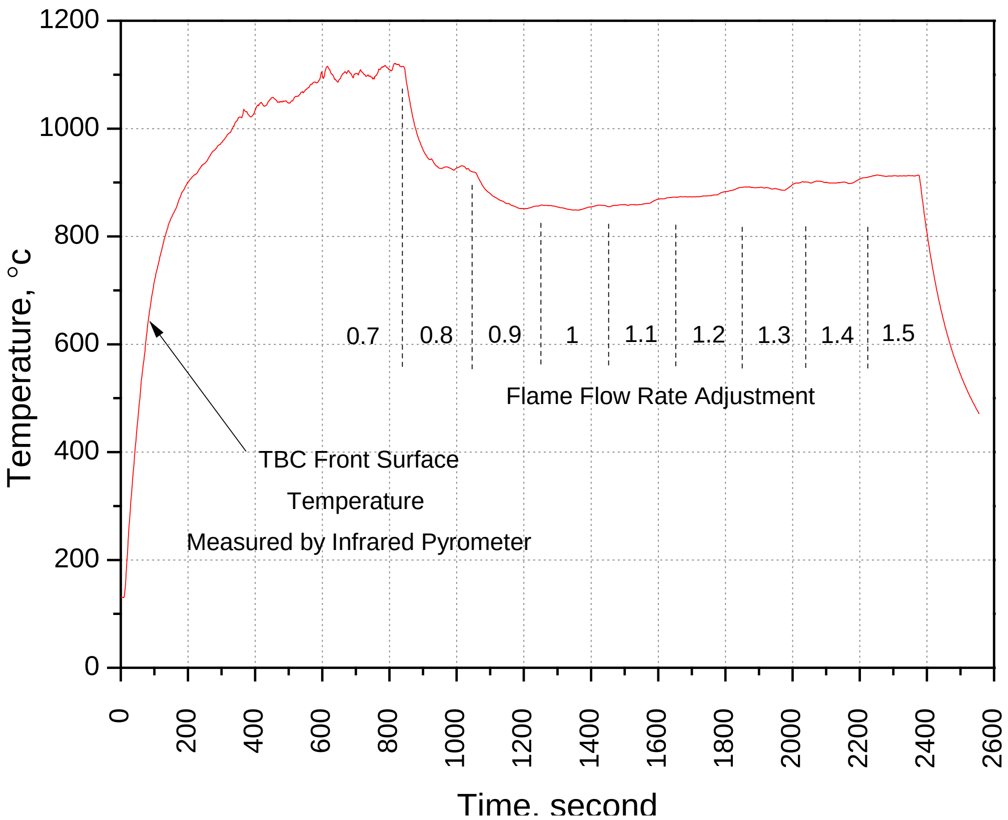

Figure 4.27 – Flame flow rate adjustement test with ceramic coated sample. Focal length 290 mm; Nozzle to surface distance 200 mm.

Table 4.5 – Flame flow rate with corresponding oxygen and acetylene gas MFC output and mass flow rate.

Flame Flow Ratio	Oxygen MFC Output, V	Acetylene MFC Output, V	Oxygen Mass Flow Rate, l/min	Acetylene Mass Flow Rate, l/min
0.7	0.560	0.721	5.60	4.33
0.8	0.641	0.825	6.41	4.95
0.9	0.721	0.929	7.21	5.57
1	0.802	1.032	8.02	6.19
1.1	0.880	1.133	8.80	6.80
1.2	0.961	1.237	9.61	7.42
1.3	1.041	1.341	10.41	8.05
1.4	1.119	1.441	11.19	8.65
1.5	1.2	1.545	12.00	9.27

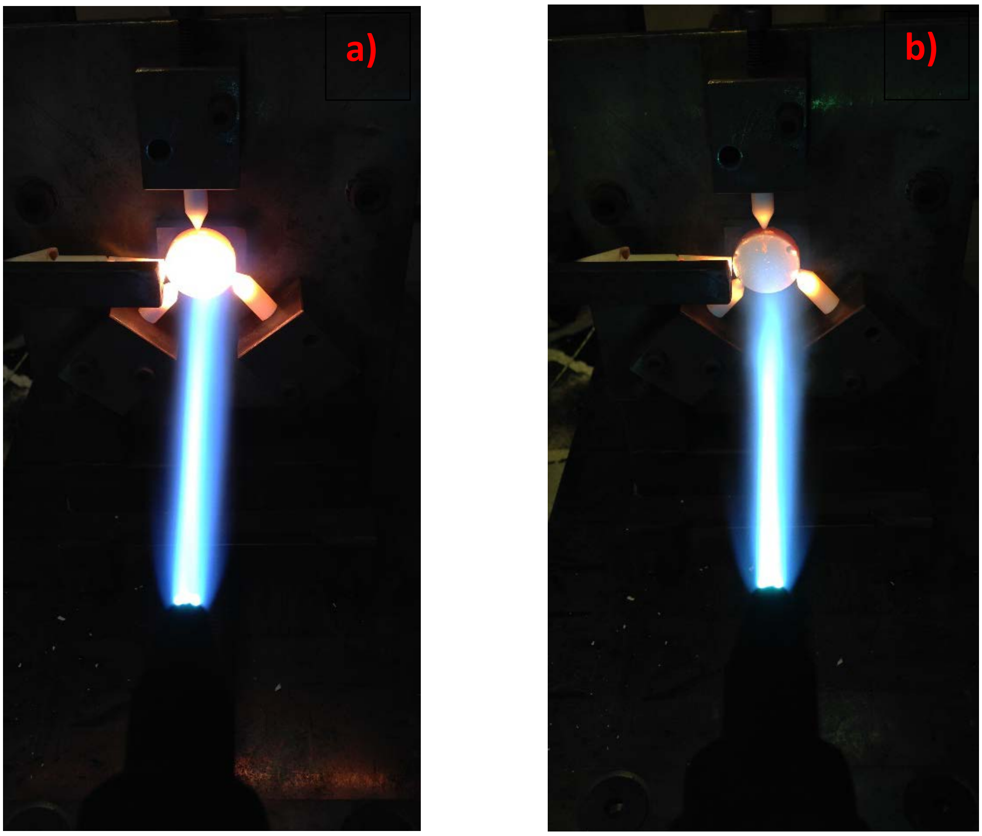

Figure 4.28 – a) flame flow rate of 0.7; b) flame flow rate of 0.8.

4.6.3 Influence of air cooling to the temperature measurement

The setup for third stage calibration was the same as for the first stage. Emissivity of 0.4 was used through out the test. The ceramic coated sample had undergone a total of 20 heating and cooling cycle, each cycle consists of a steady state temperature segment and an air cooling segment. In Figure 4.29, the cooling air velocity was controlled by output voltage from 0 to 5 volt, a maximum temperature difference of 350 °C is achieved when the proportional valve of mass flow controller is at fully opened position. However, a significant drop in surface temperature during cooling indicates that the current sample surface to nozzle distance of 200 mm needs to be reduced in order to achieve a higher surface temperature during the actual flame oxidation test.

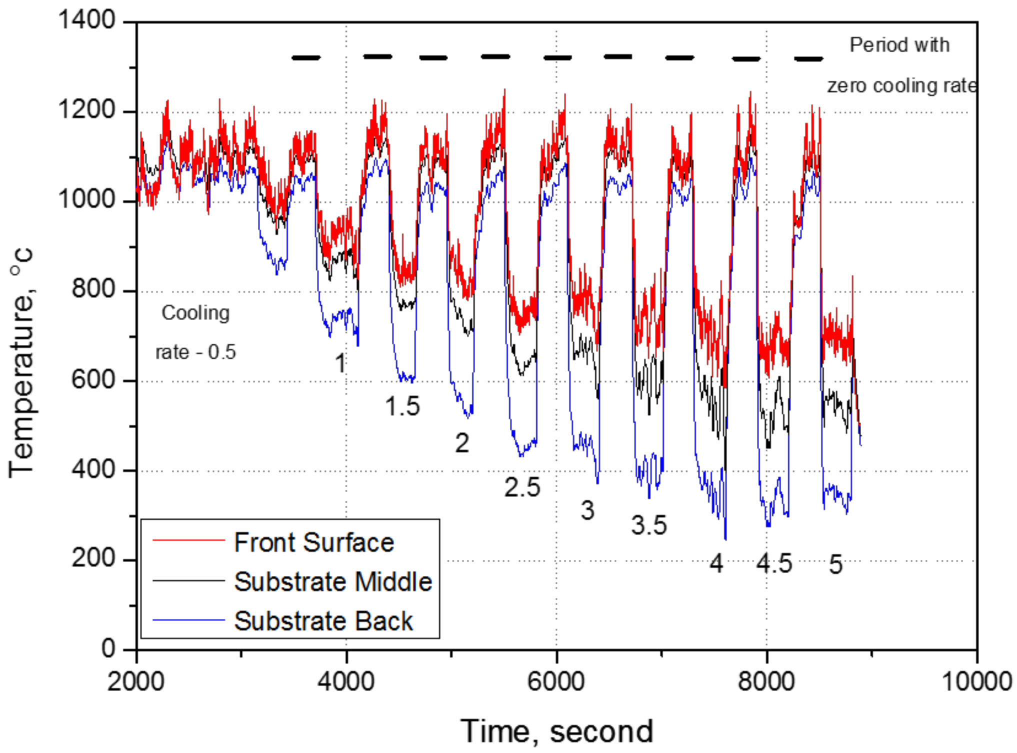

Figure 4.29 – Recorded data for simultaneous flame heating at nozzle to surface distance 200 mm with cooling ouput control from 0.5 to 5v on the TBC sample with cooling ouput control from 0.5 to 5v.

4.7 Conclusion

In order to simulate real operating envirmment for the TBC system and achieve a more accurate thermal gradient through the thickness of the coating system, a high flame temperature burner test rig have been successfully designed, manufactured and assembled. The calibration methods for emissivity estimation of the APS ceramic top coat from a single wavelength infrared pyrometer has been developed to combat the semi-transparent property of the ceramic coating. The results from numerical and experiment studies shown that the air cooling nozzle and sample holder structure have found to be adequate. The sample surface to torch nozzle distance has been found so that a desired front surface temperature can be achieved. Key parameters are listed below,

- Optimum sample surface to torch nozzle distance – 125 mm
- Air cooling diameter – 1.6 mm
- Flame flow ratio – 0.764
- Emissivity – 0.4

By fulfilling the design requirement this type of low cost computer controlled burner rig is clearly suitable for both the static and dynamic test condition, in which the static testing is capable to achieve a thermal gradient greater than 400 °C from front to rear surface of sample, with a front surface exceeding 1100 °C; On the other hand, dynamic testing is capable to achieve a front surface termperature cycle, from 800 °C to 1100 °C and back within 30 seconds.

Reference

1 Institution, B. S., 2011, "Metallic and other inorganic coatings — Test method of cyclic heating for thermal barrier coatings under temperature gradient (ISO 13123:2011)."

2 J. P. Feist, Operation of a burner rig for thermal gradient cycling of thermal barrier coatings. Germany. June 16-20. 2014

3 L. Gonzalez-Fernandez, L. del Campo, R.B. Perez-Saez and M.J. Tello, "Normal spectral emittance of Inconel 718 aeronautical alloy coated with yttria stabilized zirconia films," *J Alloys Comp*, vol 513, pp 101-106, 2012.

4 F. E. Pfefferkorn, F.P. Incropera, Y. C. Shin, "Surface temperature measurement of semi-transparent ceramics by long-wavelength pyrometry." *in Proceedings of IMECE2002*, 2002

5 A. Paul, J. G. Binner, B. Vaidhyanathan, A. C. J. Heaton and P. M. Brown, "Heat flux mapping of oxyacetylene flames and their use to characterize Cf-HfB$_2$ composites," *Adv Applied Ceramics*, pp 158-165, 2016.

6 S. Kou, "Welding Metallurgy," 2nd edition, 1998.

7 V. Yakhot, S. A. Orszag, "Renomalization group analysis of turbulence. Basic theory," *J Sci Computing*, vol 1, pp 3-51, 1986.

8 R. M. Carroll, R. L. Shepard, "Measurement of the transient response of thermocouples and resistance thermometers using an in situ method," *Oak Ridge National Laboratory Report*, 1977.

9 J. N. B. Livingood and P. Hrycak, "Impingement heat transfer from turbulent air jets to flat plates – a literature survey," *NASA Technical Memorandum*, 1973.

10 E. K. Plyler and C. J. Humphreys, "Flame spectrum of acetylene from 1 to 5 microns," *J Research National Bureau Standard*, vol 42, 1979.

11 G. Zizak, "Flame emission spectroscopy: fundamentals and applications," 2000.

12 Reytek Infrared Pyrometer Operating Instruction and Data Sheet.

Chapter 5

Microstructure characterization

In this chapter, the results of the diffusion and overlay coating system before oxidation will be highlighted. The selection process of aluminized NiAl coating in which the effect of aluminium powder content and treatment temperature to the growth (in terms of thickness) of β-phase will also be addressed. Microstructure features and surface roughness from each HVOF sprayed coating system will be cross compared. In order to investigate the effect of surface morphology to the oxidation behavior of the overlay coating, the coating surfaces are polished and compared with the unpolished samples. All images used in the section below were taken with SEM under either SE and BSE mode.

5.1 Initial microstructure of diffusion coating system

5.1.1 Without nickel plating process

The coating thickness after vaccum heat treatment as the function of each sample in Table 3.5 (Chpater 3) is given in Figure 5.1. The aluminium content in sample P-1 to P10 and AP-1 to AP-8 is varied from 2 wt% to 15 wt% and 6 wt% to 15 wt% in the cement pack respectively. For demonstration purposes, SEM images of the microstructure of P-4 and AP-1 sample from each process group are shown in Figure 5.2. The only diffuerence between the two samples is the coating process technique, P-4 was aluminized using Pack arrangement and AP-1 was aluminized using Above-the-Pack arrangement. It can be seen that under the as-deposited condition the inward grown coating P-4 consists of a single β-phase NiAl with small precipitate outer-zone (OZ). On the other hand, the combination of inward and outward grown coating AP-1 has a relative ‘clean’ (no obvious precipitate) OZ, but a mixed of β and γ’ phases have occurred. Between the outer zone and the substrate, a layer of larger and elonged precipitate zone is observed. This zone is often known as the interdiffusion zone

(IDZ). The small island of precipitates in the outer zone of P-4 were identified as α-Cr phase, which is found to be consistent with the literature [1]. Furthermore, γ phase was not indentified for P-4 in the analysis, this may be due to the fact that only a small surface area was tested. The cause of the small precipates is due to the slow diffusion of alloy element trapped in the solid solution matrix as OZ continues to grow. To avoid these precipates forming the possible solution is to add an extra pure nickel layer prior to the alumimizing process.

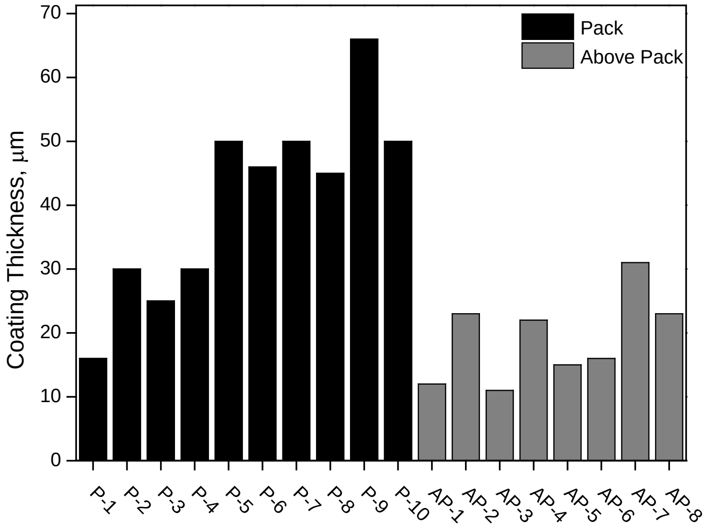

Figure 5.1 – Aluminized coating thickness (without nickel plating) after vacuum heat treatment for pack and above the pack processed samples.

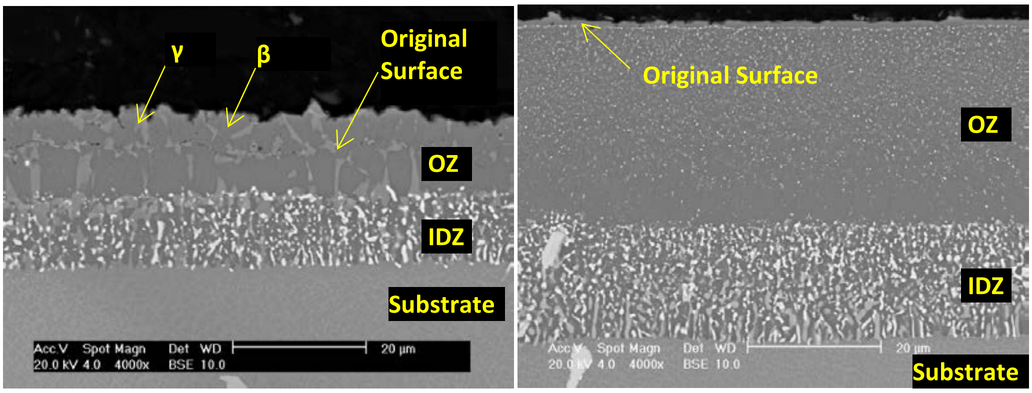

Figure 5.2 – Microstructure of sample AP-1 using above-the-pack technique (left) and P-4 using pack technique (right).

5.1.2 With nickel plating process

Similar to the previous section, the coating thickness after vaccum heat treatment is plotted as the function of each sample in Table 3.6 (Chpater 3) is given in Figure 5.3. Different thickness of pure nickel was electroplated by varying deposition time. A significant amount of increase in aluminium content is applied in cement pack for this set of sample due to the addition of a pure nickel layer on the surface of the Mar-M-246 alloy. SEM images of the microstructure of pack process NP-P-3 and NP-P-4 sample are shown in Figure 5.4. It can be seen that both pack processed coatings under the as-deposited condition consist of a ‘clean’ single phase NiAl without small precipitates outer-zone (OZ). Between outer zone and interdiffusion zone, a secondary outer zone is unexpectedly observed. The microstructure of this region is very similar to the outer zone observed from the previous section. Slightly more pores are observed with NP-P-4 than that of NP-P-3, this maybe due to a higher aluminium powder content used in the cement pack. Localized large precipitate region appeared only in NP-P-4 sample. The nickel aluminide compound in both coatings on the Mar-M-246 alloy for the present case of aluminizing was identified by XRD as β-phase, as shown in Figure 5.5. No other phases such as Ni_2Al_3 were found. This in a way implies that the diffusivity of aluminium and nickle is high enough to produce the equilibrium stable phase of NiAl [2].

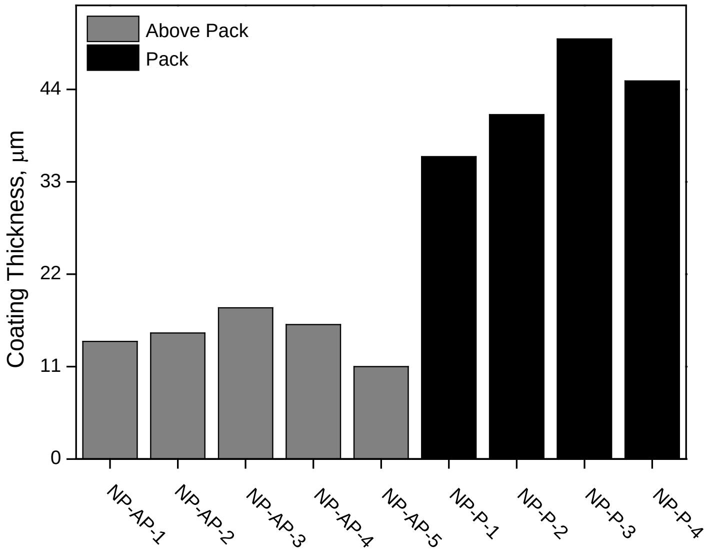

Figure 5.3 - Aluminized coating thickness (with nickel plating) after vacuum heat treatment for pack and above the pack processed samples.

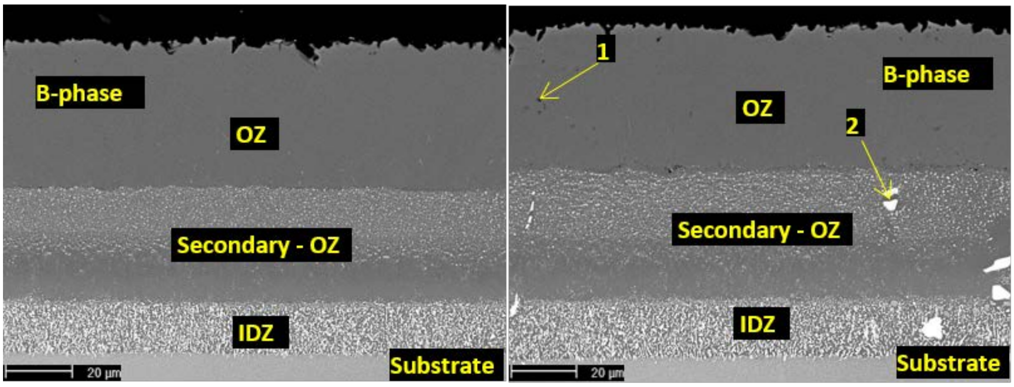

Figure 5.4 – Microstructure of sample NP-P-3 (left) and NP-P-4 (right). Both pack technique was applied for aluminide samples.

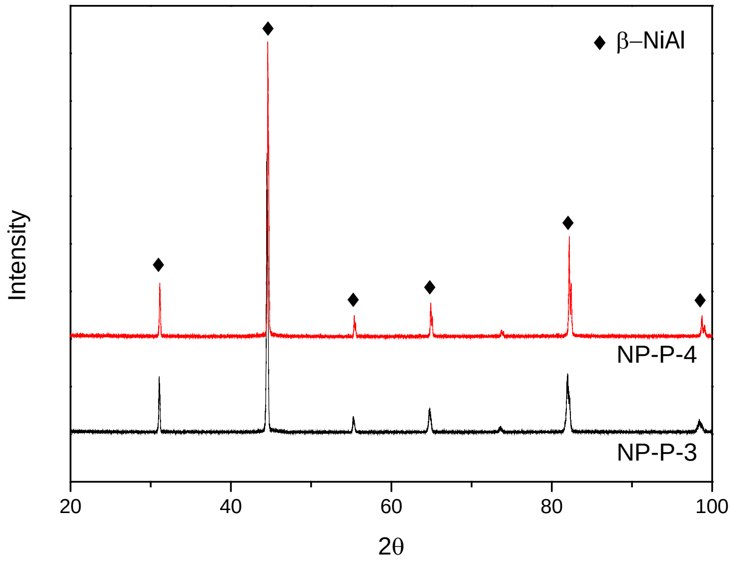

Figure 5.5 - XRD patterns of NP-P-3 and NP-P-4 samples under as-coated condition.

5.1.3 Surface morphology

In the as-coated condition, the surface morphology of the NP-P-3 and NP-P-4 coating, as shown in Figure 5.6 (a) & (b), were irregular with pores about 2μm. Less pores was observed for NP-P-4. The grain size of NP-P-4 was about 2 μm whereas for NP-P-3 the grain size was smaller. It is important to note that the surface morphology is effected by the coating process techniques. In the present work, coatings manufactured from the above pack technique have not been used for any forms of oxidation studies.

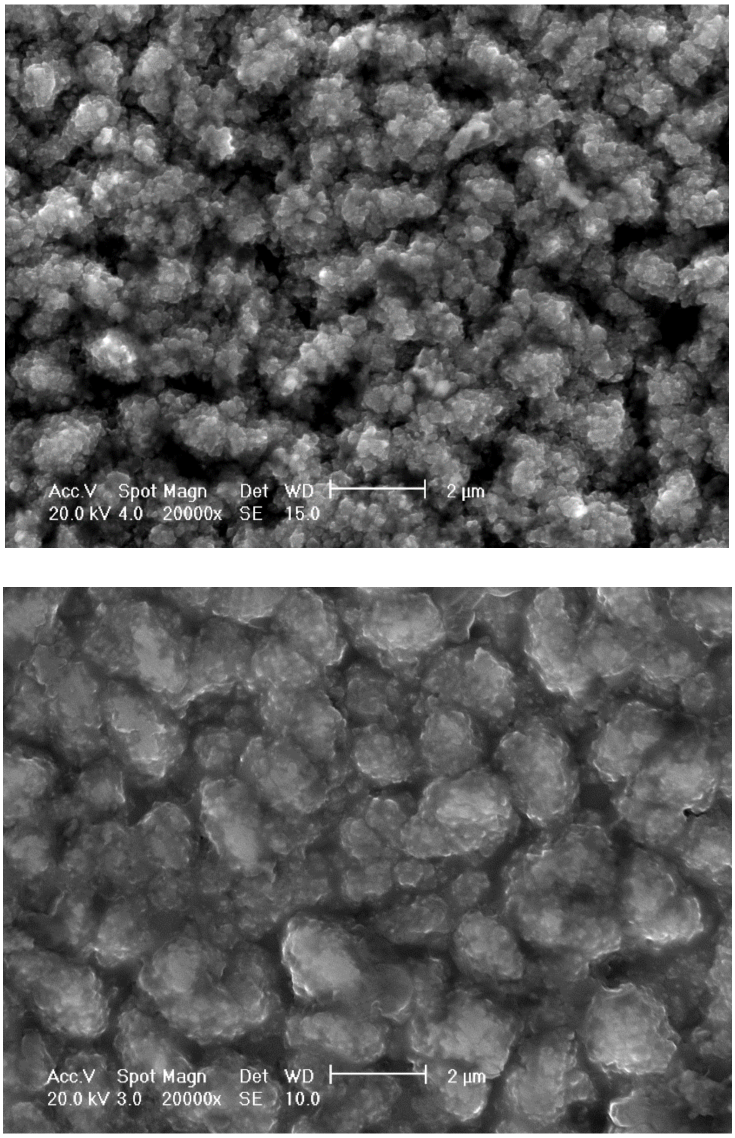

Figure 5.6 –The surface morphology of NP-P-3 and NP-P-4 under as-coated condition.

5.2 Initial microstructure of overlay coating system

Figure 5.6 (a) exhibits the SEM microstructure of the as-coated Ni-191-4 sample. Combining Figure 5.7 with the inset image in Figure 5.6 (a) shows that the as-coated sample primarily consists of β-phase NiAl (dark grey BCC phase) and γ-phase Ni (light grey FCC phase). Quantitative EDX analysis shows that aluminium atomic concentration in β-phase (location 1) is much higher than in γ-phase (location 2) as expected. As for the Ni-528 sample the microstructure (Figure 5.6 (b)) in BSE mode also reveals dark and light grey region within the coating matrix. However, the XRD pattern (Figure 5.7 (b)) combined with EDX measurement suggests that only a single solid solution γ'-phase existed under as-coated condition. Similar observation (Figure 5.6 (c)) was made on Dimalloy 4008 NS sample, a single γ-phase was formed and it was confirmed by XRD analysis (Figure 5.7 (c)). Low aluminium content in both coating powders could be the cause for such observation. All three HVOF sprayed coatings contained pores and oxides. Relatively large scale alumina was also observed at the coating/substrate interface, the origin of these oxides trapped at interface could be the sand particles from the sandblasting surface treatment prior to the thermal spray. Same HVOF spray parameters were used for all thress coatings, including number of passes, however, the coating thickness (Table 5.1) for Ni-528 sample was clearly less than the others.

Table 5.1 – HVOF sprayed coating thickness

	Thickness, µm
Ni-191-4	225 ± 12
Ni-528	146 ± 16
4008 NS	204 ± 15

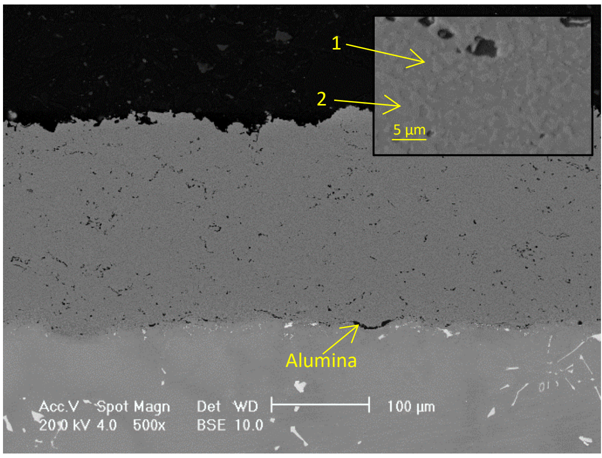

Location 1	
Element	at%
Al	33.45
Si	0.42
Cr	8.28
Co	11.68
Ni	46.17

Location 2	
Element	at%
Al	9.45
Si	0.88
Cr	27.76
Co	26.34
Ni	35.58

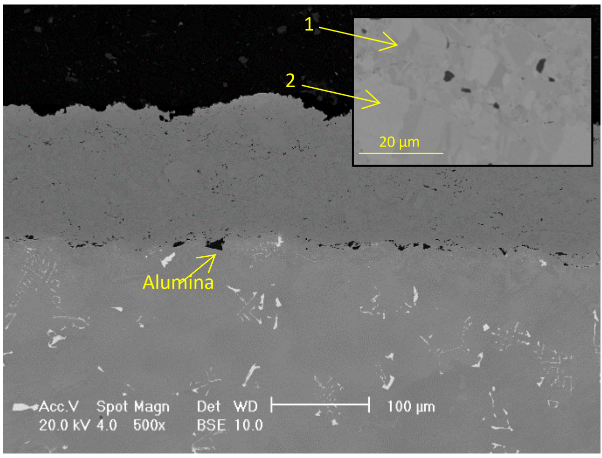

Location 1	
Element	at%
Al	9.62
Cr	15.45
Ni	74.94

Location 2	
Element	at%
Al	9.65
Cr	15.57
Ni	74.78

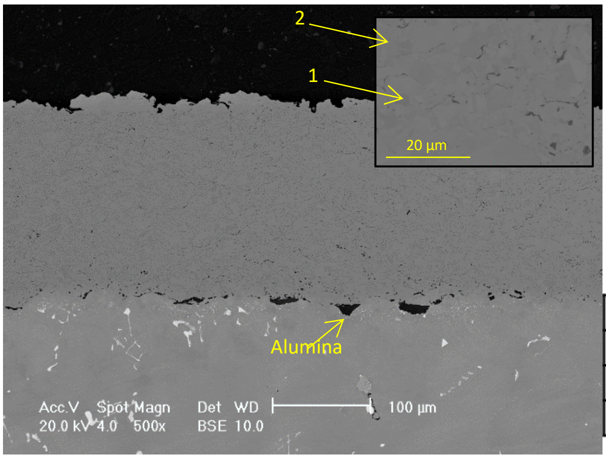

Location 1	
Element	at%
Al	7.69
Ni	92.31

Location 2	
Element	at%
Al	7.71
Ni	92.29

Figure 5.6 – HVOF as-sprayed overlay coating system after vaccum heat treatment, (a) Ni-191-4, (b) Ni-528 and (c) Dimalloy 4008 NS.

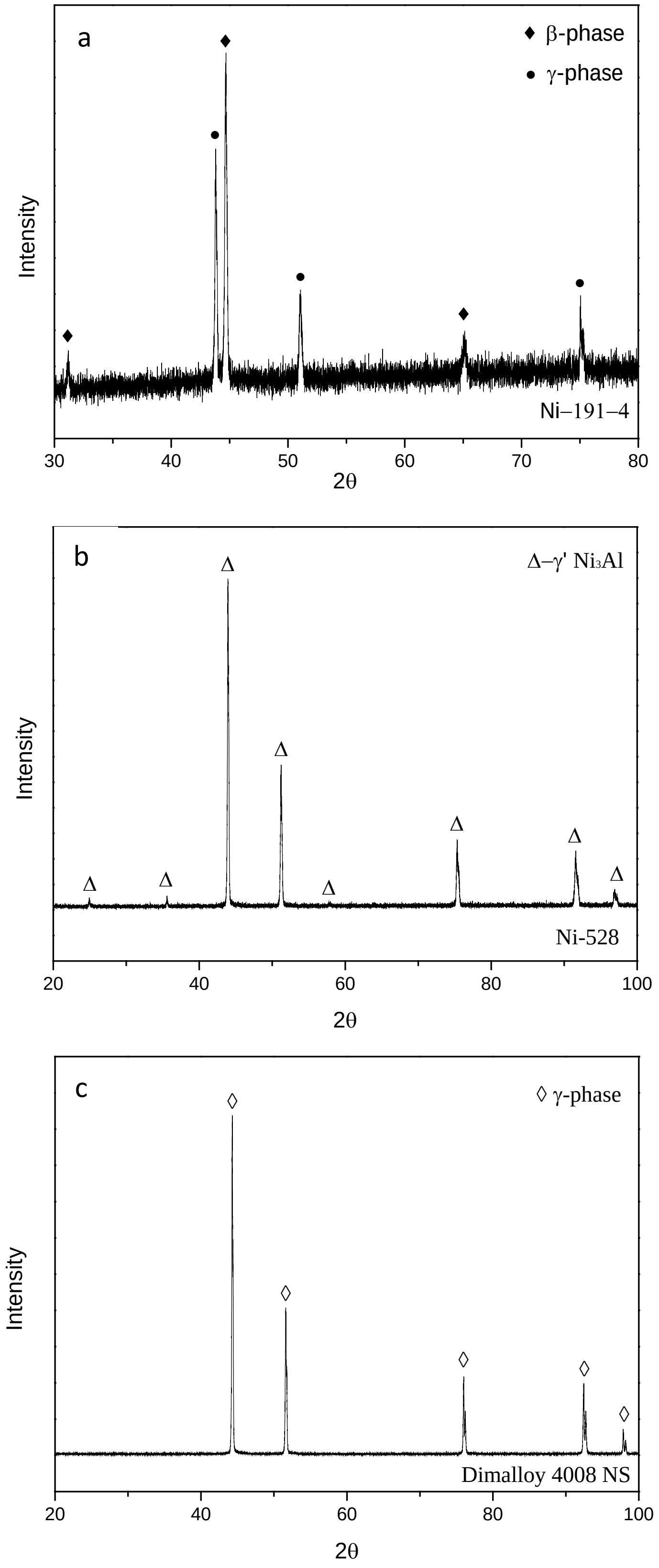

Figure 5.7 - XRD patterns of (a) Ni-191-4, (b) Ni-528 and (c) Dimalloy 4008 NS samples under as-coated condition.

5.3 Conclusion

This chapter has outlined the initial microstructure of diffusion and overlay coating system formed on Mar-M-246 and Mar-M-247 respectively. The thickness of nickel aluminide coating formed on Mar-M-246 depend on the aluminizing methods.

In this case, when same cementation activity is applied, the increase in coating thickness using pack cementation is observed when compare with ones that manufactured using above the pack cementation.

The aluminide coating from pack cementation consists of β phase layer mixed with small precipates as outer zone matrix and precipitate interdiffusion zone, whereas for above the pack cementation, the aluminide coating consists of β + γ phase outer zone matrix and precipitate interdiffusion zone.

The microstructure of aluminide coating on a nickel plated substrate includes a β phase layer without small precipates outer zone, a β phase mixed with small precipates secondary outer zone and a interdiffusion zone.

Overlay coating produced using high velocity oxygen fuel (HVOF) spraying method contains pores and oxides within the matrix. Relatively large scale alumina was also observed at the coating/substrate interface, the origin of these oxides trapped at interface could be the sand particles from the sandblasting surface treatment prior to the thermal spray.

Reference

1. Angenete. J, Stiller. K, Comparison of inward and outward grown Pt modified aluminide diffusion coatings on a Ni based single crystal superalloy. Surface and coating technology, 150, 2-3, pp 107-118, 2002.

2. Das. K. D, Joshi. V. S and Singh. V, Evolution of aluminide coating microstructure on nickel-base cast superalloy CM-247 in a single-step high-activity aluminizing process, 29, 8, pp 2173-2188, 1998.

Chapter 6

Oxidation Test Results

6.1 Mass change due to oxidation

Mass changes of all the coating samples are given in Figure 6.1 (left), where Figure 6.1 (right) is a magnified version of Figure 6.1 (left). It can be seen that NP-P-3 had more oxide growth after 500 hours whereas NP-P-2 and 4 had a slow down in oxide growth after 100 hours. Oxide scale spallation could be the cause of mass loss after prolonged oxidation. The trend of mass change during early stage oxidation was the same across all sampels.

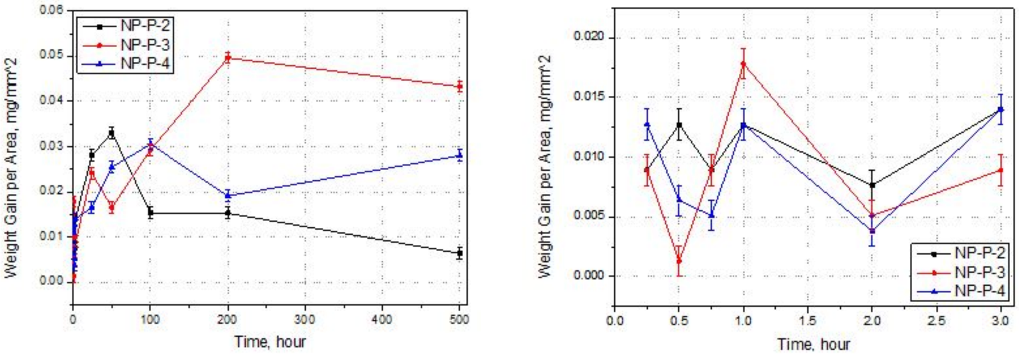

Figure 6.1 – Mass change of diffusion coating after isothermal oxidation test.

6.2 Microstructure development of aluminized β-NiAl coating at 1100 °C

Figure 6.2, 6.4 and 6.6 illustrate the microstructure development for NP-P-2, NP-P-3 and NP-P-4 at selected exposure times after isothermal oxidation. Oxide scale had formed on all oxidized coating surface. Three distinct zones in all coatings were observed, an outer coating matrix zone (OZ), a secondary coating with precipitates zone (SOZ) and an interdiffusion zone (IZ). Thickness of each zone varied between each coating after oxidation. For NP-P-2, after 200 hours oxidation, precipitates SOZ disappeared which suggests that type of the precipitate in the SOZ is mainly the alpha-phase chromium. Furthermore, precipitates in IZ were enhanced, elongated and remained. The disappearing of precipitates in SOZ did not occur for NP-P-3 and 4. Also, β-phase (dark grey) was visible after 50 hours in the interdiffusion zone where precipitates were heavily presented. The most interesting feature observed from these results were the nucleation of γ' phase Ni_3Al. It was expected that depletion of aluminium within the β-phase coating matrix due to oxide forming would occur at some point during oxidation. For NP-P-2, coating matrix transformation from β→γ' phase happened after 50 hours whereas for NP-P-3 and NP-P-4 phase transformation was delayed to 100 hours and 200 hours respectively. The veins-like depletion zone (light grey) grew and became larger as oxidation time increased.

The growth of interdiffusion zone thickness with column-like precipitates penetrating into the substrate had occurred for all coatings after 50 hours, but the thickness remained constant for NP-P-2. XRD patterns in Figure 6.3, 6.5, 6.7 identified the phase of the oxide scale which mainly consisted of α-Al_2O_3, spinel oxide and γ' solid solution. Except for NP-P-4, no γ' phase was detected.

Another interesting observation was made on the formation of voids in the coating matrix. Significant amount of void were found within the outer zone during the first hour oxidation for all coatings. These voids were gradually disappeared after 50 hours and 100 hours for NP-P-2 and 3, whereas the existence of voids were persistent throughout the oxidation process for NP-P-4.

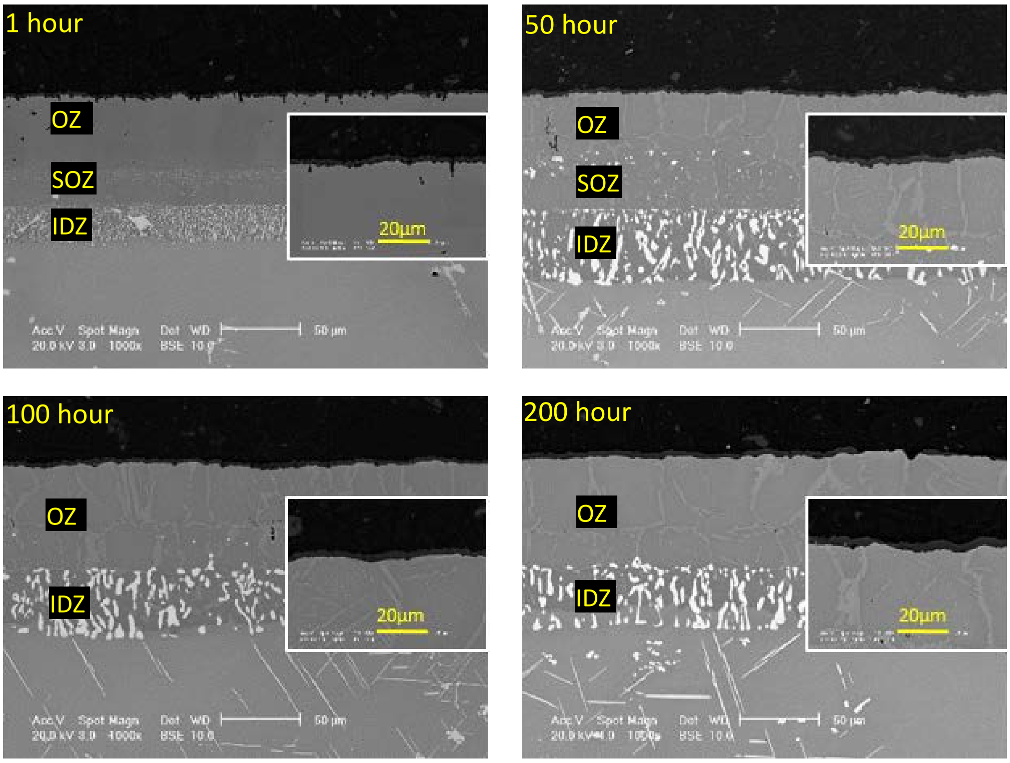

Figure 6.2 – Cross section microstructure development of NP-P-2 after 1, 50, 100 and 200 hours of isothermal oxidation at 1100 °C.

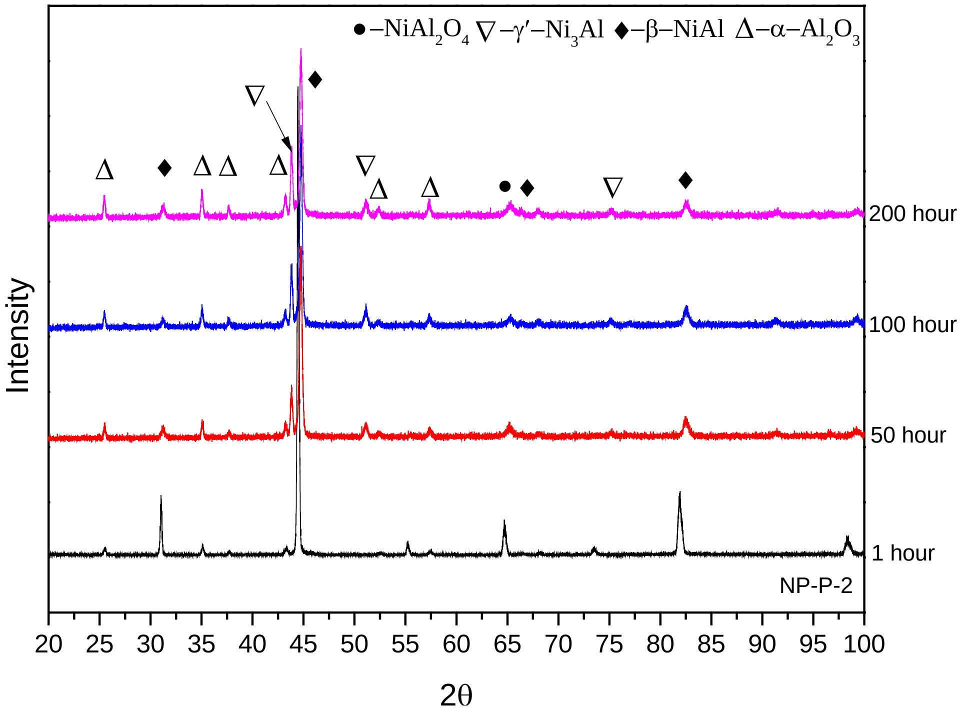

Figure 6.3 – XRD patterns of NP-P-2 after after 1, 50, 100 and 200 hours of isothermal oxidation at 1100 °C.

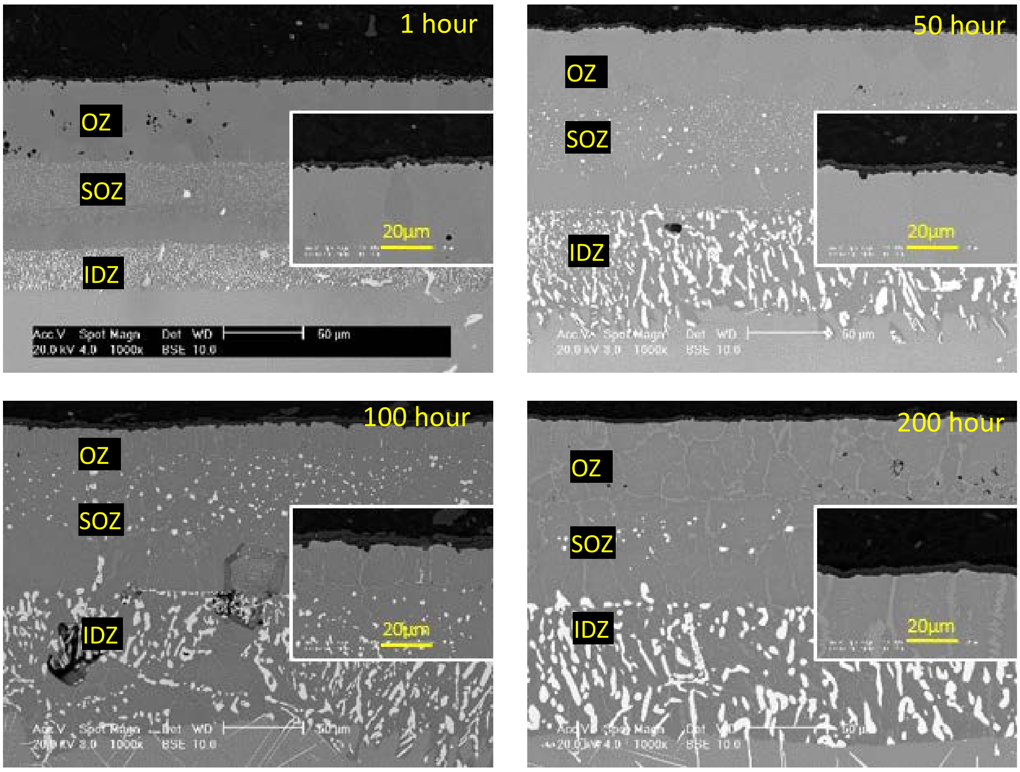

Figure 6.4 – Cross section microstructure development of NP-P-3 after 1, 50, 100 and 200 hours of isothermal oxidation at 1100 °C.

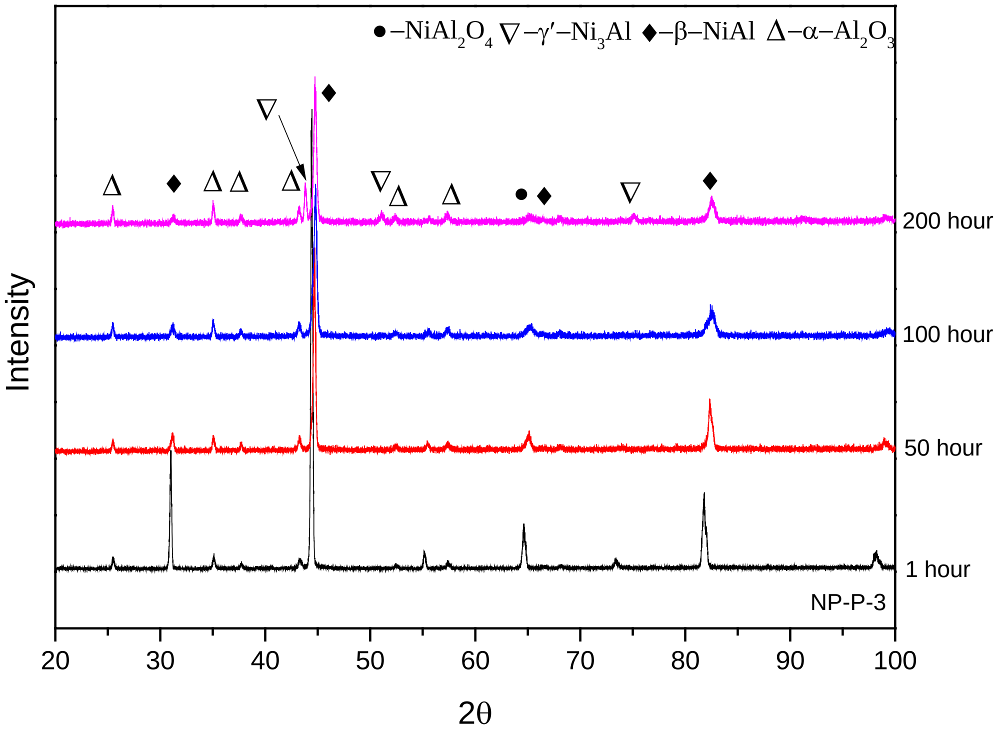

Figure 6.5 – XRD patterns of NP-P-3 after after 1, 50, 100 and 200 hours of isothermal oxidation at 1100 °C.

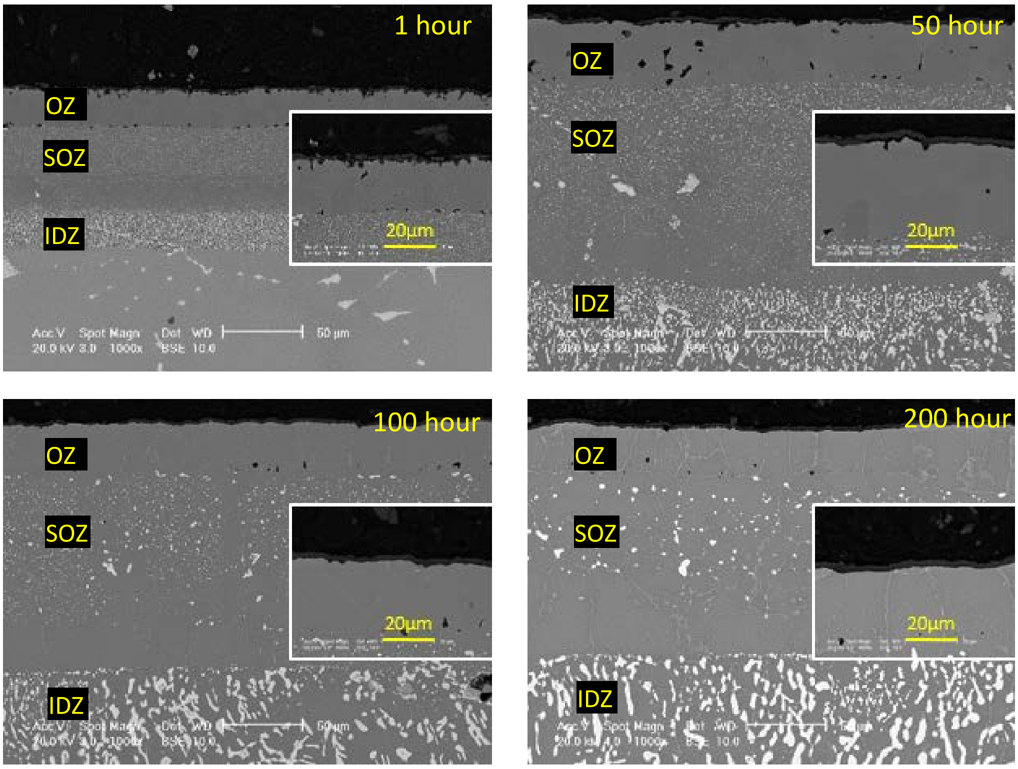

Figure 6.6 - Cross section microstructure development of NP-P-4 after 1, 50, 100 and 200 hours of isothermal oxidation at 1100 °C.

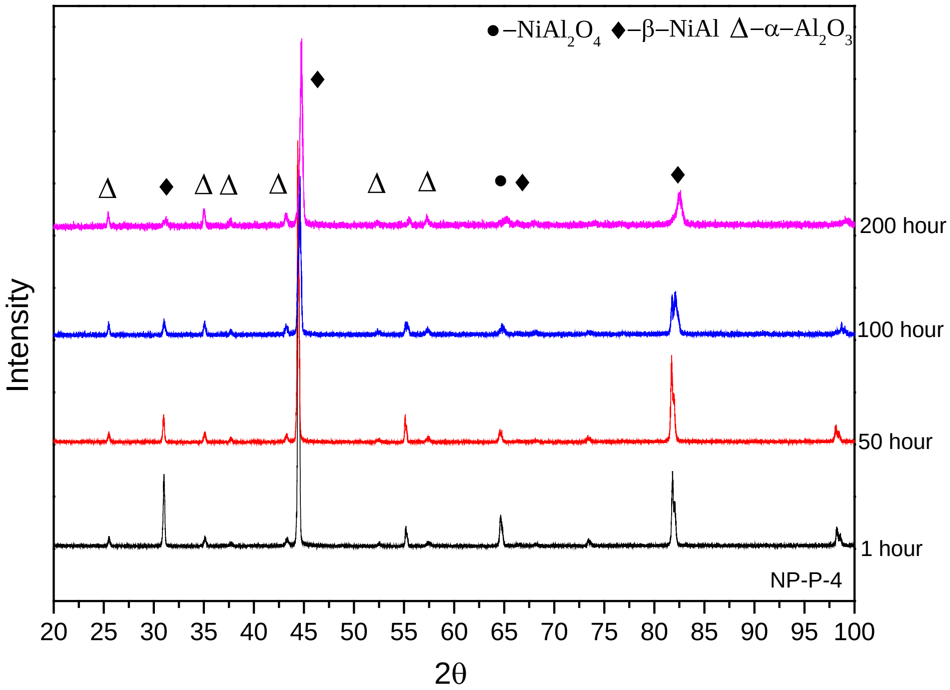

Figure 6.7 – XRD patterns of NP-P-4 after after 1, 50, 100 and 200 hours of isothermal oxidation at 1100 °C.

6.3 Microstructure development of overlay coating system at 1100 °C

Figure 6.8 illustrates the oxide layer of HVOF sprayed coating systems of Ni-191-4, Ni-528 and 4008-NS after 50, 100 and 200 hours exposures. A continues dual phase oxide scale (bright upper and dark lower layer) was formed on Ni-528 whereas discontinues island-like foreign phase started to form on Ni-191-4 after 50 hours. These discontinues foreign phase joined together as exposure time proceeded. On the other hand, 4008-NS coating had a completely different oxide in terms of microstructure morphology. EDX analysis, Table 6.1, shows that this foreign phase bright layer was enriched in Ni, Cr, Co, Al and oxygen. The dark layer had a relatively higher amount of Al and O which indicates the stable α phase oxide. Due to the difference in coating matrix microstructrure between each coating system, aluminium depletion zone was only observed on Ni-191-4. With increase in exposure time, the thickness of this depletion zone was also increased along with reduction in beta phase grain fraction within the matrix. Figure 6.9 gives the relationship of beta phase fraction as a function of exposure time.

Table 6.1 – Composition for upper and lower oxide scale on overlay coatings after 200 hour oxidation.

	Ni-191-4, at%		**Ni-528, at%**		**4008-NS, at%**	
Composition	**Upper**	**Lower**	**Upper**	**Lower**	**Upper**	**Lower**
Ni	4.88	-	12.52	1.01	43.99	12.98
Al	15.07	35.85	25.96	38.1	-	26.63
Co	3.57	-	-	-	-	-
Cr	11.72	-	2.56	0.37	-	0.18
O	64.77	64.15	58.96	60.52	56.01	60.22

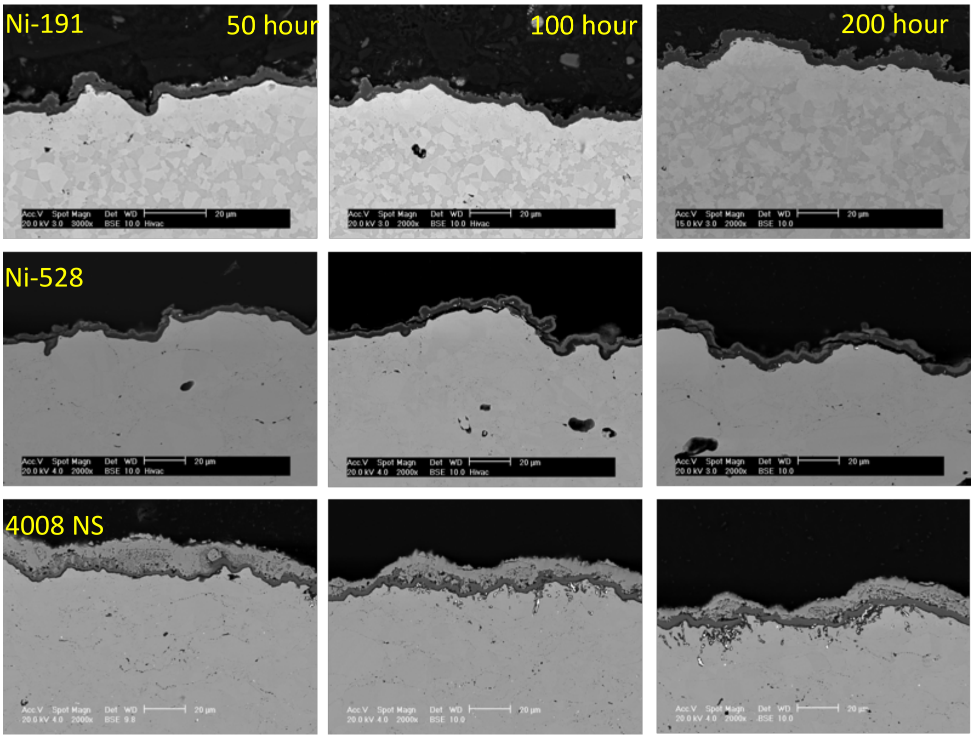

Figure 6.8 – Cross section microstructure development of overlay coatings after 50, 100 and 200 hours of isothermal oxidation at 1100 °C.

In order to demonstrate the effect of post surface treatment on the formation of oxide scale, microstructures of each coating system with surface treatment after 50, 100 and 200 hour thermal exposure is shown in Figure 6.9. It appeared that surface treatment had a huge influence on formation of oxide scale for Ni-528. Dual phase oxide was no longer visible after 200 hours. Instead, there was significant amount of Hf[1] oxides formed and surrounded by the α-Al_2O_3 near the oxide/coating interface. Similar observation was made for 4008-NS where Hf oxides appeared underneath the oxide scale near the interface.

---

[1] Hf element diffuses from substrate

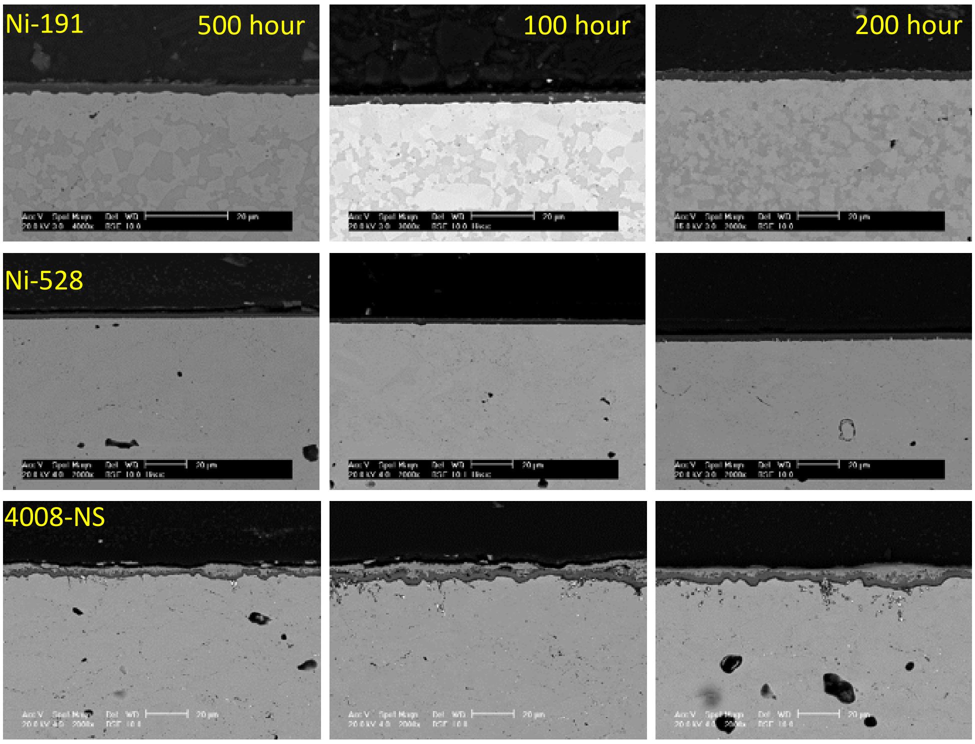

Figure 6.9 - Cross section microstructure development of post surface treated overlay coatings after 50, 100 and 200 hours of isothermal oxidation at 1100 °C.

XRD analysis in Figure 6.10 - 6.12 gives a strong indication that the dual phase oxide structure contained a mixture of α-phase alumina, spinel oxides and γ/γ’ solid solution. Furthermore, the peaks for these spinel oxides were significantly reduced with post surface treated oxidized coating samples. As for 4008-NS, the top light grey layer was rich in Ni, only a very weak peak was identified as α-Al_2O_3, which suggests NiO formed first on the surface and spinel oxides then appeared after the reaction with α-Al_2O_3.

Figure 6.13 illustrates the effect of the oxide microstructure development without substrate attached to the Ni-191-4 coating after 50, 100 and 200 hours oxidation. The oxide morphology on samples with and without post surface treatment was similar to that in Figure 6.9. Large scale mixed spinel oxide was not observed or identified by EDS analysis. Furthermore, as illustrated in Figure 6.14, percentage of reduction in beta phase fraction seemed to have affected by absence of substrate during oxidation.

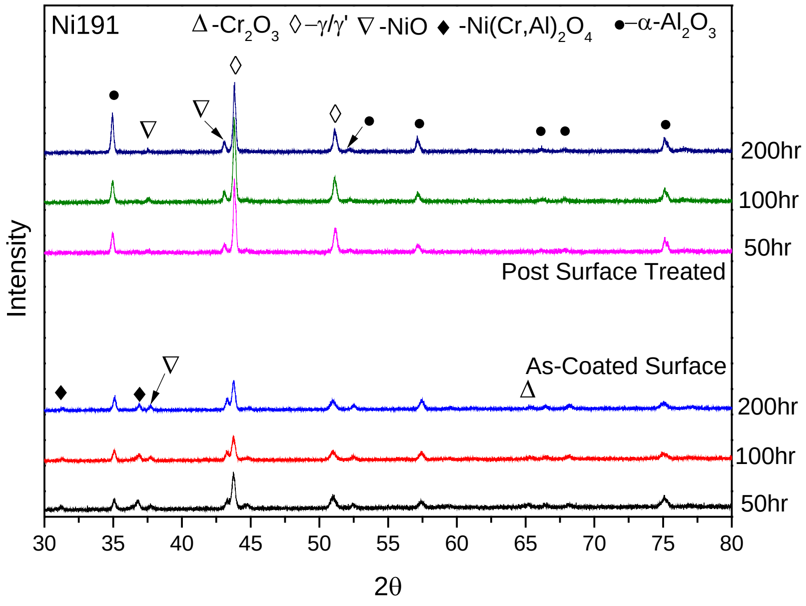

Figure 6.10 – XRD patterns comparison for post surface treated and as-coat Ni-191-4 after 50, 100 and 200 hour oxidation.

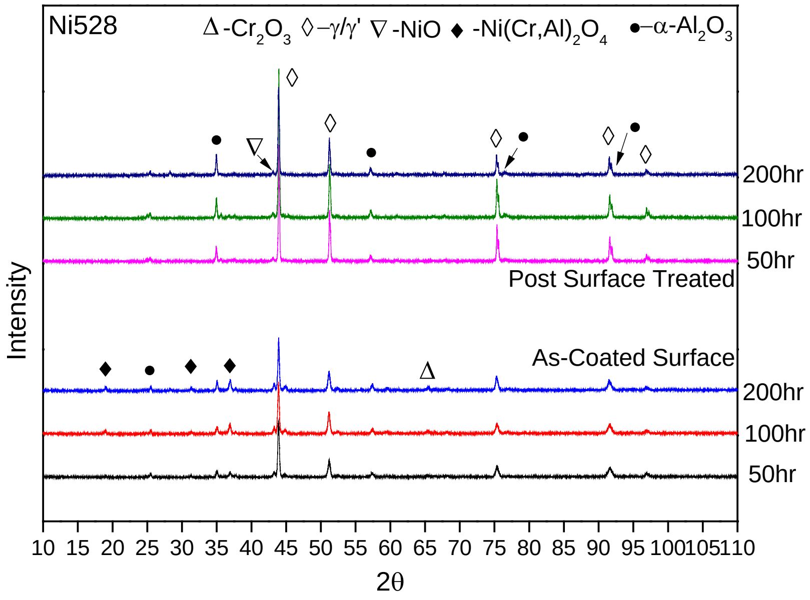

Figure 6.11 – XRD patterns comparison for post surface treated and as-coat Ni528 after 50, 100 and 200 hour oxidation.

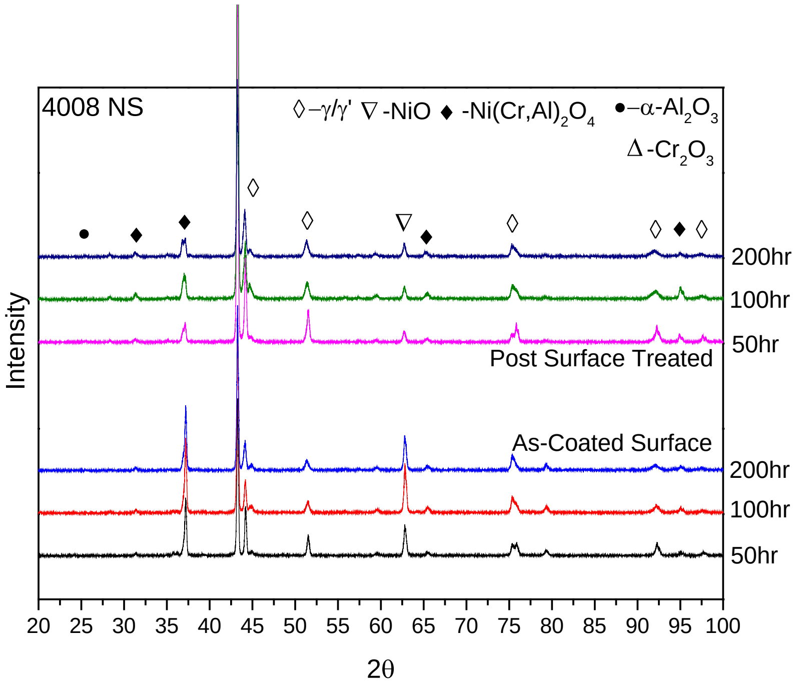

Figure 6.12 – XRD patterns comparison for post surface treated and as-coat 4008-NS after 50, 100 and 200 hour oxidation.

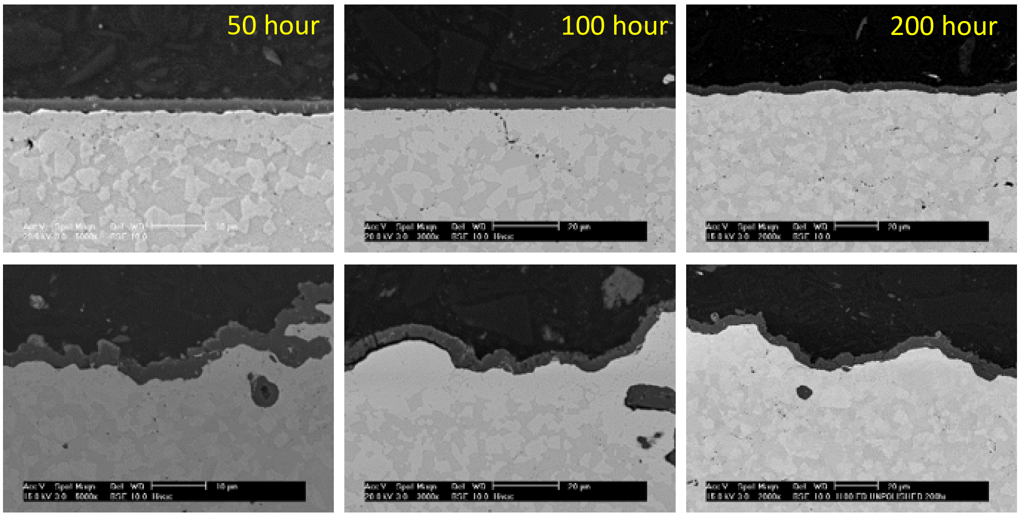

Figure 6.13 - Cross section microstructure development of post surface treated and as-coated surface free standing Ni-191-4 after 50, 100 and 200 hours of isothermal oxidation at 1100 °C.

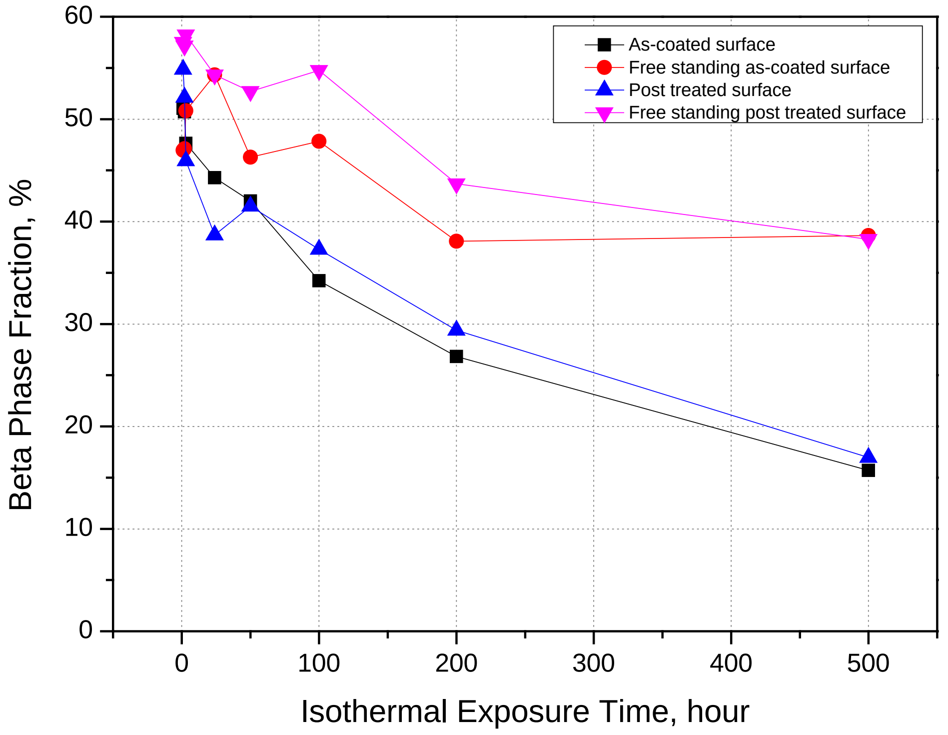

Figure 6.14 – Illustration of Beta phase fraction as a function of exposure time for Ni-191-4. Image analysis was used to calculate beta phase fraction.

6.4 Oxide surface roughness development

The oxide surface roughness of the overlay and diffusion coating system measured after 1, 50, 100, 200 hours of oxidation is presented in Figure 6.15 using the value of R_t. Due to significant amount of NiO formation on the surface roughness measurement on Dimalloy 4008 NS was not included in the Figure 6.15. The results demonstrated that oxide surface roughness had a minimum impact on all the post surface treated overlay coatings over the course of oxidation, whereas for overlay coatings without surface treatment an increase in roughness was recorded. Specially for Ni-191 coating sample, a huge jump in roughness from 1 hour to 50 hours oxidation was clearly reflected in the measurement. On the other hand, oxide surface roughness behaved differently across all three diffusion coatings. Although no post surface treatment was applied to these coating surfaces, when compared with overlay coatings, the trend of change in roughness were not singular. NP-P-2 had an increase in roughness whereas NP-P-3 had no obvious variation although a slight dip in roughness was observed. The most interesting one was the NP-P-4 in which the oxide roughness had clearly decreased indicating an occurance of stress relaxation with increased oxidation time.

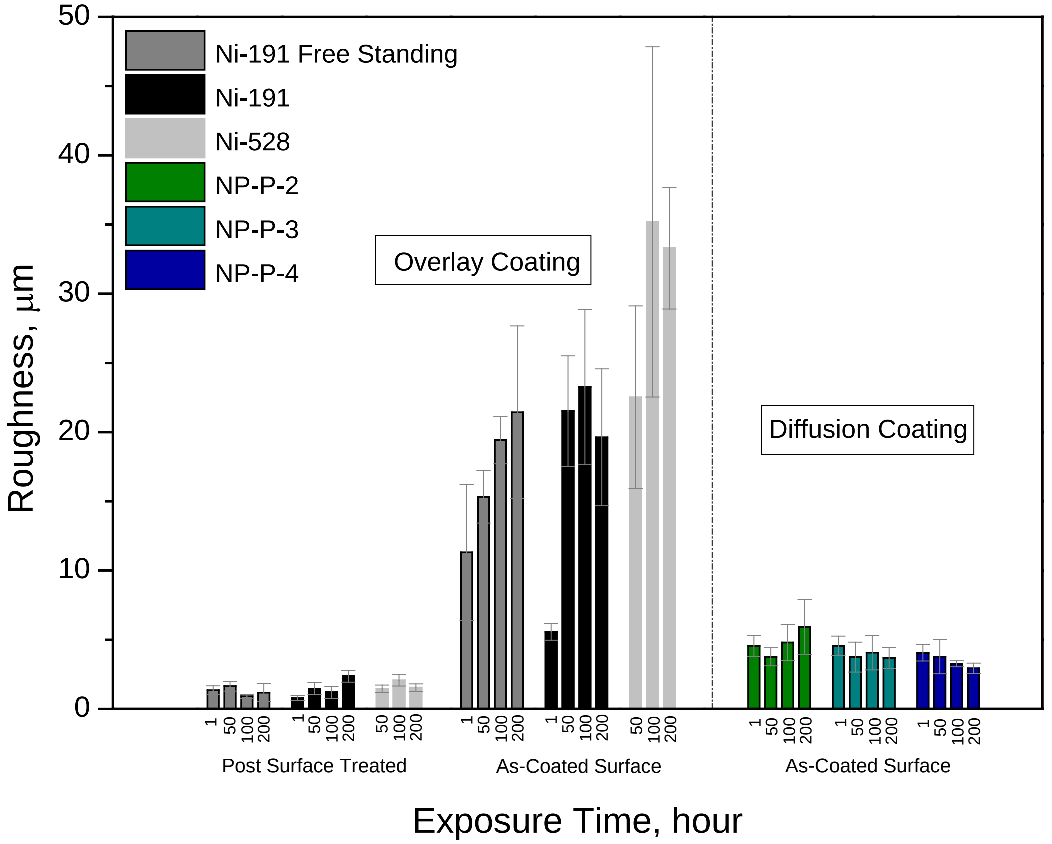

Figure 6.15 – Oxide surface roughness development. In average, three samples were used for each time intervals and five roughness measurements were taken on each sample.

6.5 Oxide thickness development

Figure 6.16 shows the oxide thickness measured for overlay and diffusion coating system after 1, 50, 100 and 200 hours oxidation. As expected, the growth of oxide over the course of oxidation was observed. The results show that growth in oxide thickness has affected by the change in surface profile for overlay coatings. After 200 hours, coatings with as-coated surface obtained a higher oxide thickness than that of coatings with post surface treatment. Again, Ni-528 seemed to have the least oxidation resistance at high temperature. This observation was in correlation with the evidence found from cross section microstructure in which spinel oxides were the contributing factor in overall thickness measurement. In comparison, diffusion coatings had shown a much better oxidation resistance after 200 hours. In particular, a decrease in growth of oxide was observed for both the NP-P-3 and 4 after 100 and 50 hours respectively.

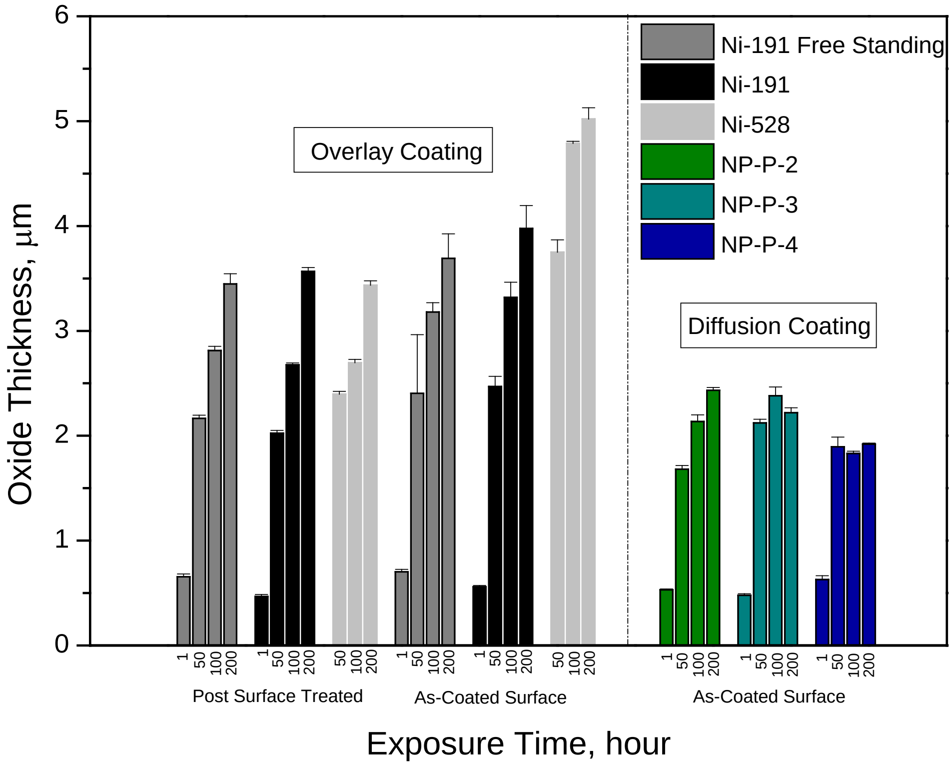

Figure 6.15 – Measured oxide thickness for overlay and diffusion coating system after 1, 50, 100 and 200 hours oxidation.

6.6 Oxyacetylene flame rig testing

In previous sections, results of isothermal oxidation tests for overlay and diffusion coatings have shown the microstructure behavior of each coatings after certain exposure times. This however has not present a overall picture on the performance of a complete thermal barrier coating system. Therefore, in order to demonstrate the utilization of successfully developed flame rig in leading to the investigation of the failure of the APS TBC systems, more rigorous oxidation tests were carried out. In this section, samples of APS TBC systems using an overlay coating as bond coat was used except for Ni-528 and Dimalloy 4008 NS. Microstructure of Ni-191-4 TBC sample under isothermal and flame thermal cycling condition will be compared. Overall oxide growth and failures will also be outlined.

As previously stated in Chapter 3, a typical flame thermal cycle, Figure 6.16, consisted of three high temperature up to 1400 °C oxidation period, each period had 10 minutes dwell time. Each oxidation stage was followed by the hot corrosion stage which also had a 10 miniutes dwell time. Hence, three typical flame thermal cycles would take about 1 hour to complete. Table 6.2 shows the test scheme that was applied.

Table 6.2 – High temperature flame thermal cycle test scheme for TBCs.

TBC system	**Test Cycle (hour)**		
	3 cycle (≈1 hr)	6 cycle (≈2 hr)	9 cycle (≈3 hr)
Ni-191-4	✓	✓	✓

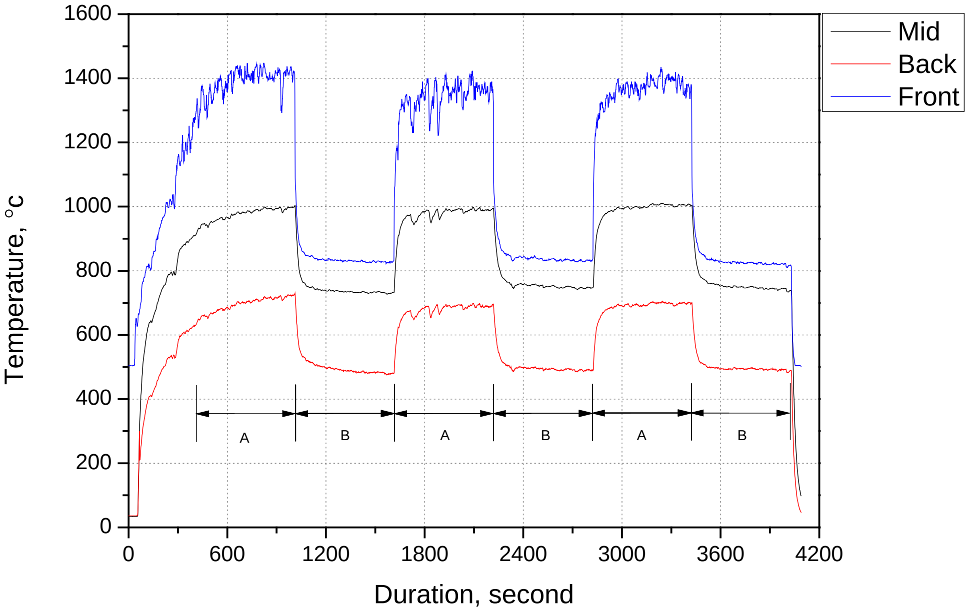

Figure 6.16 – Illustration of a typical one-hour burner rig thermal cycle. Region A represents 10 minutes oxidation segment and region B represents 10 minutes hot corrosion segement.

6.6.1 Microstructure development of TBC coating under high temperature flame condition

Figure 6.17 shows the SEM microstructure images of cross sections from 16-pass, 32-pass and 16-pass TBCs under flame thermal cycling and isothermal test conditions respectively. In general, 16 passes thermal spray produces a ceramic top coat layer thickness around 300 µm. The measured thickness of the compact oxide scale is given in Figure 6.18. With a temperature gradient of 700 °C across the depth of the sample, the thickness of compact oxide scale for both TBC samples was at sub-micron level whereas 1.1 µm thick oxide layer was measured when TBC was oxidized under isothermal condition. This result demonstrated the usefulness of thermal property, i.e. low thermal conductivity, of the ceramic top coating.

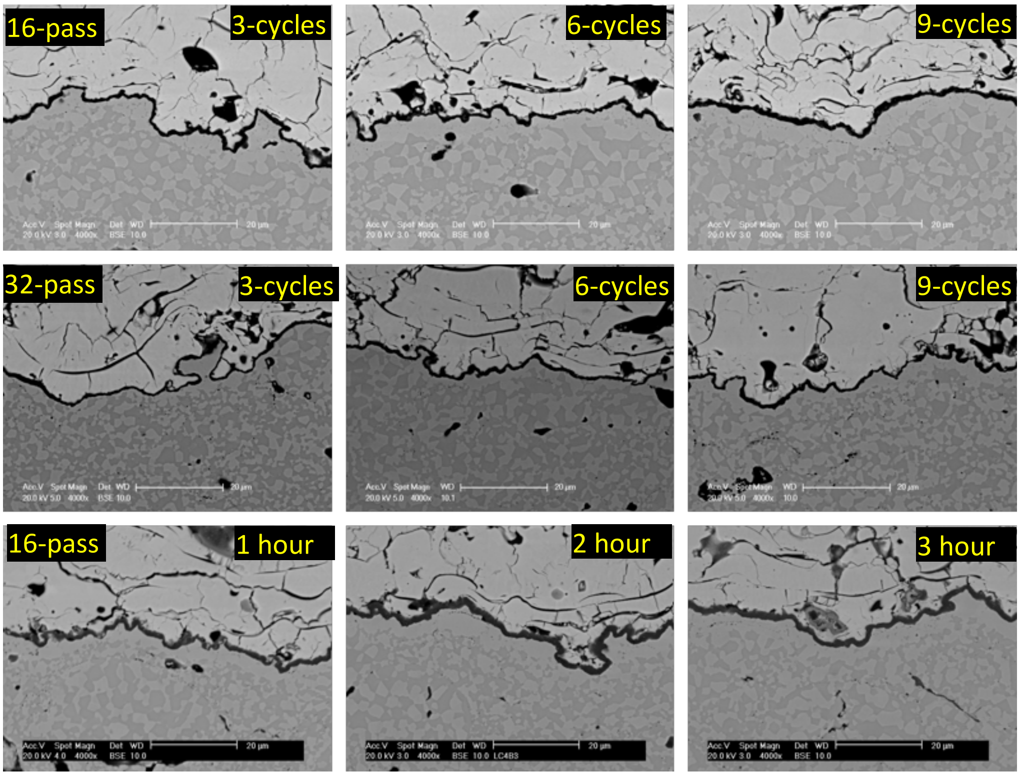

Figure 6.17 - SEM microstructure images of cross sections from 16-pass, 32-pass and 16-pass TBCs under flame thermal cycling and isothermal test conditions respectively.

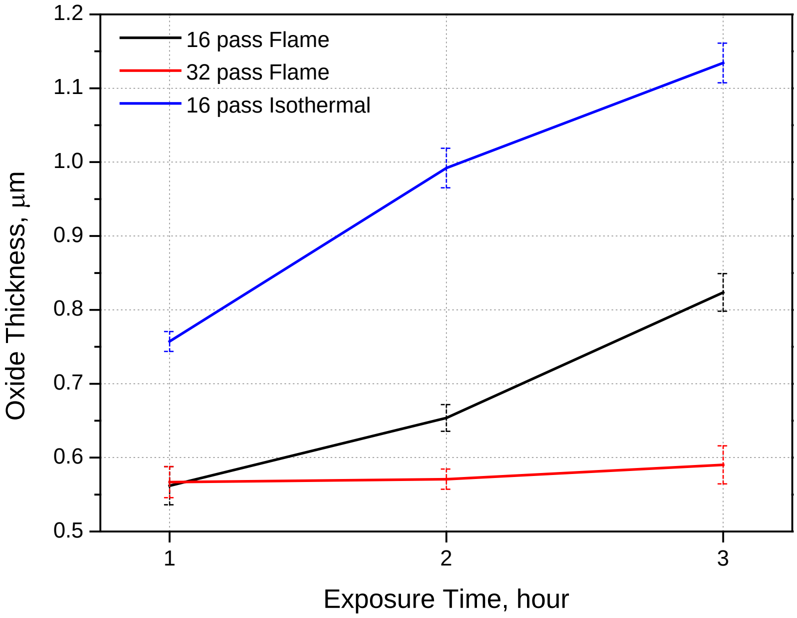

Figure 6.18 – Measured oxide thickness of TBC samples after burner rig thermal cycling and isothermal test.

6.6.2 Damage development and failure mode

Microcracks at the edge of the sample started to appear after 3 cycles and after 9 cycles a large section of ceramic coating was spalled off, as shown in Figure 6.19. Delamination near the oxide/ceramic coating interface was observed on the thicker ceramic coating sample after 9 cycles. The difference between the two failure modes was clearly demonstrated within the inserted images which also illustrate the extent of the damage to the sample surface as a whole. It was a surprise to observe such failures at early stage of thermal cycling, because spallation of ceramic coating often occurs in association with other type of damages within the oxide layer. As shown in Figure 6.20, complete failure of ceramic coating occurred after 500 hours of oxidation under isothermal conditions. It was clear to see a completely depleted β-phase aluminum bond coat microstructure along with cracks formed in the oxide layer, ceramic coat, at the oxide/ceramic and oxide/bond coat interface. However, under the flame thermal cycling test condition, these types of damage which is summarised in Table 6.3, were not observed piror to the failure of the coatings, except for type 2 damage.

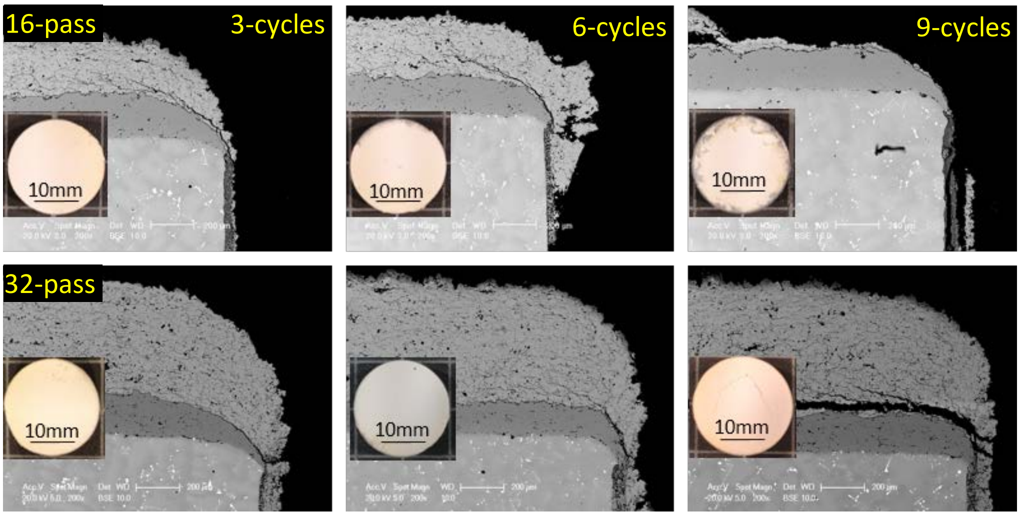

Figure 6.19 – SEM images of 16-pass and 31-pass TBC system after 3, 6 and 9 burner rig thermal cycles.

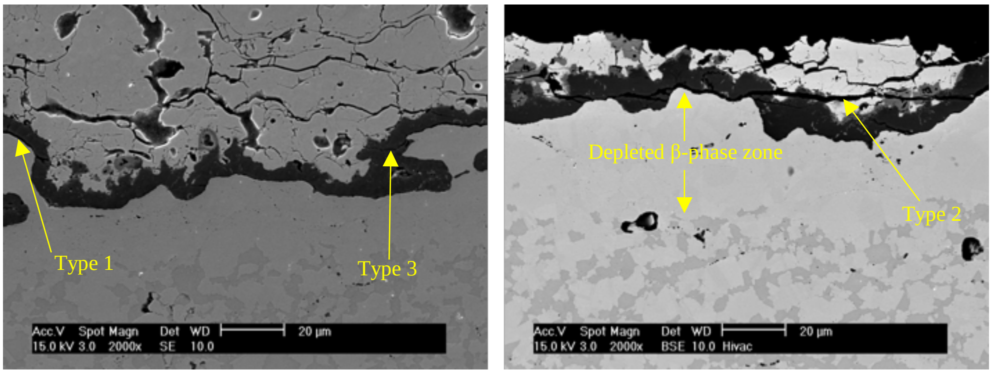

Figure 6.20 – SEM images of 16-pass TBC system after 200 and 500 hour isothermal oxidation.

Table 6.3 – Failure types of TBC system.

Type	Observation
1	Lateral cracks parallel to the oxide/bond coat interface
2	Delamination in ceramic coating
3	Cracks in the oxide
4	Edge Failure

6.7 Oxidation kinetics

6.7.1 Diffusion coating

Figure 6.21 gives the SEM cross section image of aluminide single β-phase NiAl coating before oxidation. Due to different coating manufacturing process, the aluminide coating surface is relatively smooth compared with that of HVOF (High Velocity Oxygen Fuel) MCrAlY coating system. EDX (Energy-dispersive X-ray) was used to examine the elemental content which is given in Table 6.4.

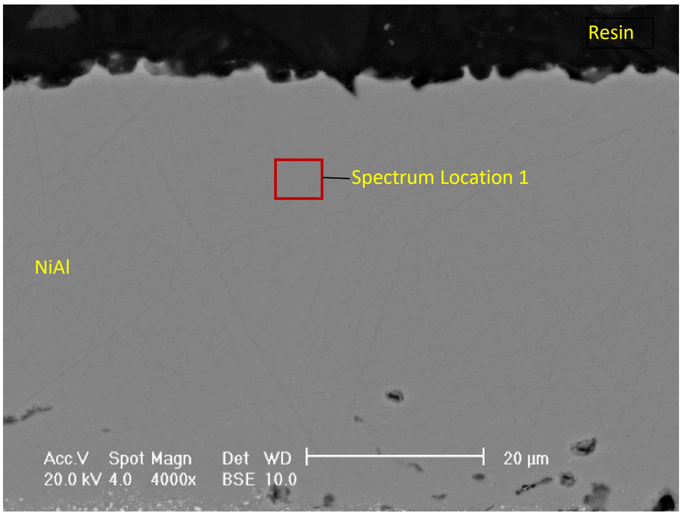

Figure 6.21 – Cross section β-phase NiAl coating before oxidation.

Table 6.4 – Element content β-phase NiAl coating before oxidation.

Spectrum 1	
Element	Atomic %
Ni	48.81
Al	51.19

Figure 6.22 gives the oxide thickness data measured on β-phase NiAl samples after 0.25, 0.5, 0.75, 1, 2, 3, 24, 50, 100, 200 and 500 hours of oxidation in air at 1100 °C. It can be seen that two different regions of oxide growth has

occurred. The first region is in the early stage oxidation comprises times less than 3 hours. During this period, there is a clear rapid initial rate of oxide growth which slows down with increase of exposure time. a thickness around 1 µm is reached. This rapid growth of oxide may have associated with the appearance of transitional oxide, such as $\theta - Al_2O_3$ and $\gamma - Al_2O_3$ [1, 2, 3]. It is likely that the differences in the time scale for which the oxide transition occurs is due to the higher temperature used in this study compared with other studies in the literatures. Once the oxide transition is finished, a continues stable $\alpha - Al_2O_3$ begins to grow this is where the second region is shown in Figure 6.23, the growth rate becomes slower in this region.

For high temperature oxidation, the oxide growth is normally observed to follow a parabolic relationship in which the rate of growth decreases as oxidation time increases [4, 5, 6]. However, the results from this study can only be described as a power law dependence. The overall thickness, first region and second region results can be appreciated in a log-log plot, as shown in Figure 6.23. The best fit line given here is based on the expression of $\Delta y_e = k_\beta t_e^{n_e}$, where Δy_e is the oxide thickness, k_β is the oxidation rate constant and n_e is the power law exponent. Table 6.5 summarised the results.

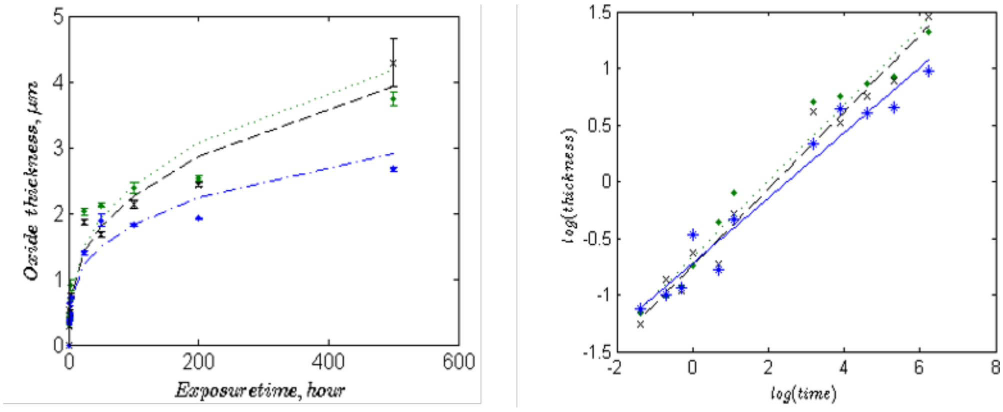

Figure 6.22 – Measured oxide thickness as a function of time for β-phase NiAl over a period of 500 hours at 1100 °C. (a) mean oxide thickness and (b) log-log plot of oxide thickness.

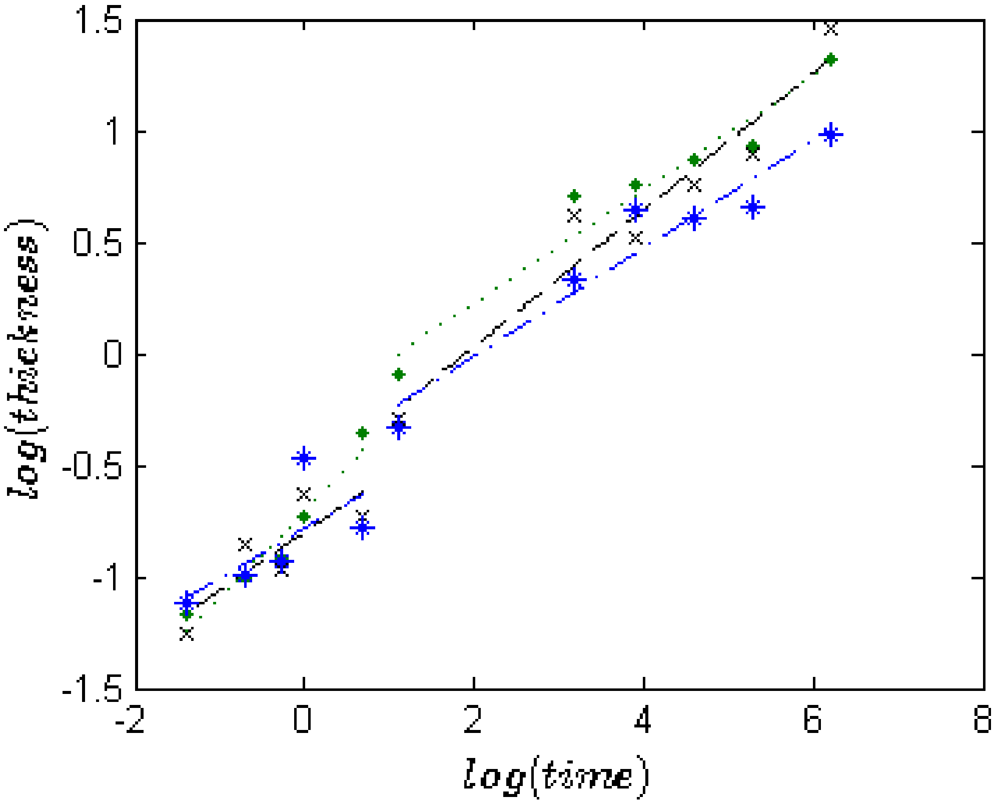

Figure 6.23 – log-log plot measured early stage and longer stage oxide thickness as a function of thermal exposure time for β-phase NiAl over a period of 500 hours at 1100 °C.

Table 6.5 – Summary of power law exponent and rate constant for diffusion coatings.

Sample	**Power law dependence, n_e**			**Overall rate constant, k_e, x 10^{-8} m/s^{ne}**
	early stage	later stage	overall	
NP-P-2	0.26	0.307	0.339	3.250
NP-P-3	0.388	0.253	0.337	2.914
NP-P-4	0.224	0.242	0.288	4.20

6.7.2 Overlay coating

Figure 6.24 gives the SEM cross section images of MCrAlY bond coat with unpolished and polished surface before oxidation. Unlike the single phase aluminide coating, the microstructure of MCrAlY coating typically exhibits a two-phase beta+gamma (β+γ). Darker grey indicates β-phase (blue arrow) and light grey indicates gamma-phase (orange arrow). Table 6.6 detailed the compostion of each location using EDX. Note that free standing MCrAlY coating samples were also used in order to minimise interdiffusion effect from the substrate.

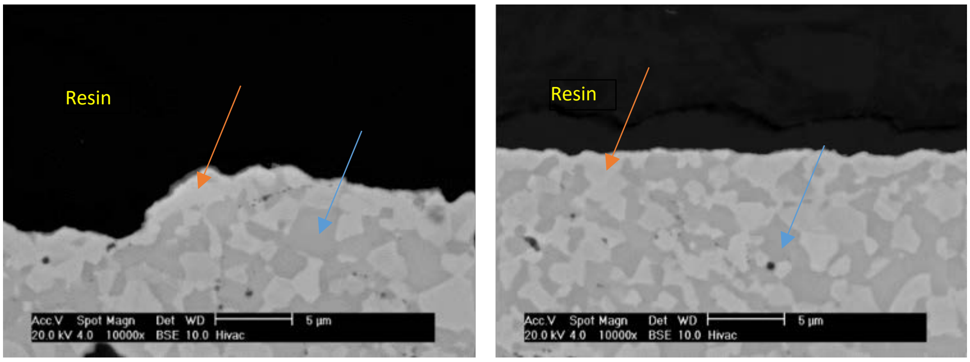

Figure 6.24 – SEM cross section image of MCrAlY mictrostructure before oxidation. (a) Unpolished and (b) Polished.

Table 6.6 – Compostion of MCrAlY bond coat

Phase	Composition (atomic%)			
	Ni	Al	Co	Cr
Beta (β)	47.75	35.55	10.50	6.20
Gamma (γ)	36.95	10.75	25.00	27.31

Due to large number of oxide thickness measurement under various sample conditions, each set of results will be plotted with different symbol attached for clarity in Figure 6.25. Sample set-1 to set-4 represent free standing as-coated surface coating, as-coated surface coating with substrate, free standing post surface treated and post surface treated coating with substrate respectively. To keep consistency with the section above, in each figure below, the best fit line is included in the plot and the expression of the best fit line will be summaried in Table 6.7 for comparison purposes.

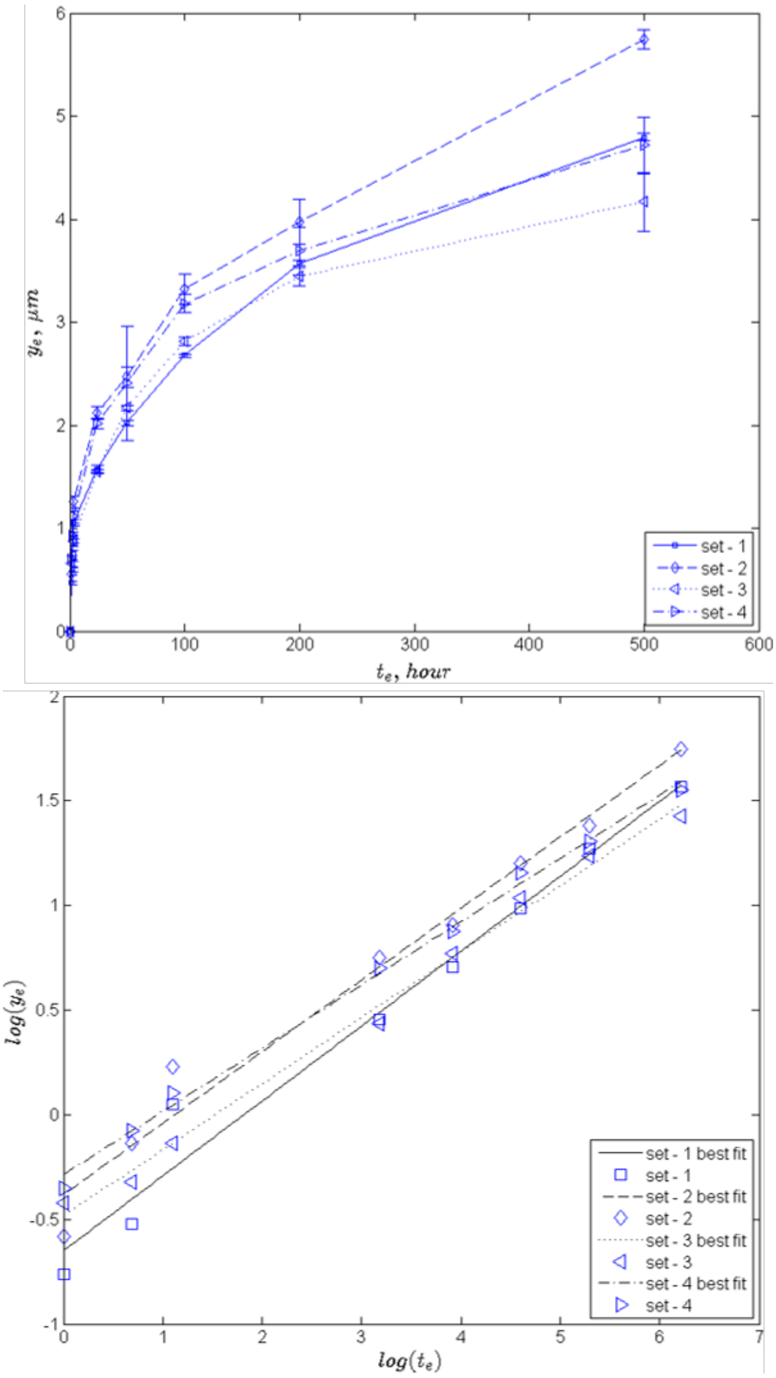

Figure 6.25 – Measured oxide thickness as a function of time for MCrAlY over a period of 500 hours at 1100 °C. (a) mean oxide thickness and (b) log-log plot of oxide thickness.

Table 6.7 – Parameters of oxidation kinetics for MCrAlY samples. Coating sample set 1 – Free standing; set 2 – with substrate; set 3 – post surface treated free standing; set 4 – post surface treated with substrate.

Sample Set	**Power law dependence, n_e**			**Rate constant, k_e, x 10^{-8} m/s^{ne}**
	early stage	later stage	overall	
1	0.697	0.374	0.358	2.689
2	0.728	0.332	0.342	4.343
3	0.250	0.326	0.316	4.266
4	0.416	0.285	0.302	6.504

Similar to the single β-phase NiAl, the results of two phase MCrAlY coating system can only be described as a power law dependence with growth exponent n_e ranging from 0.35 to 0.3. Furthermore, oxide thickness is clearly effect by the sample surface condition in which oxide grown thicker on rouge surface than that of smooth surface.

6.7.3 Oxide thickness on the thermal barrier coating system (TBC)

Thus far, the analysis is based on the exposed bond coat surface in which oxygen only diffuses through oxide layer. For a complete thermal barrier coating system where a ceramic top layer is added to the bond coat layer, the immediate question will be raised on the effect of oxygen transportation on oxide growth. Previously studies [7] have concluded that under operation condition, oxygen transport through the ceramic layer is sufficiently fast in order to ensure the oxide growth rate is controlled by diffusion within the oxide layer. The literature also suggested that the diffusion of oxygen via oxide layer is faster than that of the through ceramic layer. Therefore, the assumption made on the oxygen diffusion in later chapter seems to be reasonable. It is, however, still important to look at the oxide growth with top coat in order to fully appreciate the result obtained from experimental and numerical studies. Figure 6.26 gives the oxide thickness data measured on TBC samples over a periof of 500 hours of oxidation in air at 1100 °C. The bond coat system of NiCoCrAlY was used for TBC sampes.

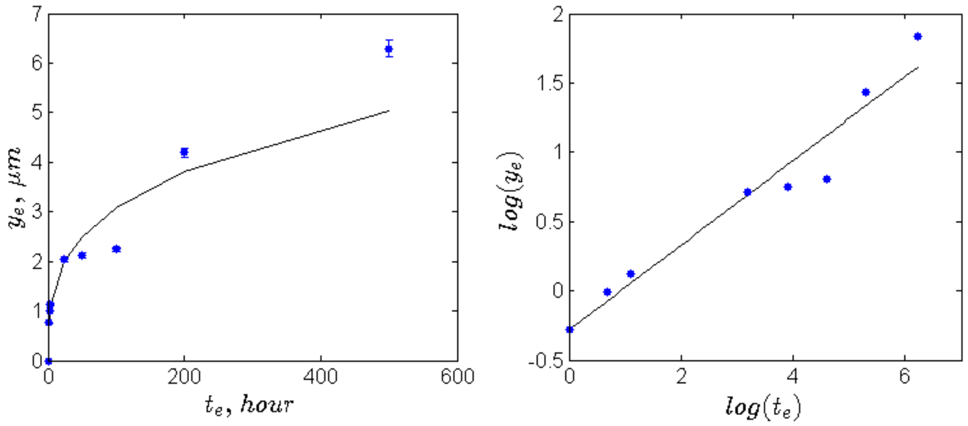

Figure 6.26 – Measured oxide thickness as a function of time for TBC samples over a period of 500 hours at 1100 °C. (a) mean oxide thickness and (b) log-log plot of oxide thickness.

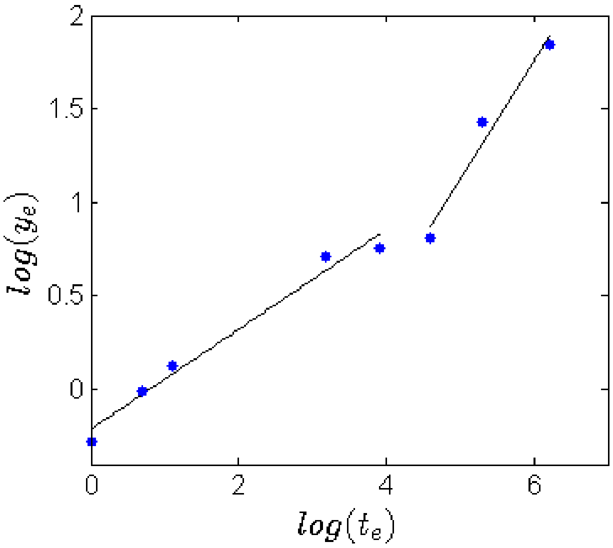

Figure 6.27 – log-log plot measured early stage and longer stage oxide thickness as a function of expoture time for TBC samples over a period of 500 hours at 1100 °C. Black solid line is the best fit line for each stage of growth.

Once again, parabolic growth relationship has not occurred for TBC samples, as shown in Figure 6.27. Similar to previous cases, the oxidation kinetic parameters for the simple power law dependence is summaried in Table 6.5.

Table 6.5 - Parameters of oxidation kinetics for TBC samples.

	Power law dependence, n_e	**Rate constant, k_e, x 10^{-8} m/s^{ne}**
Early stage	0.267	9.771
Later stage	0.632	16.985
Overall	0.305	6.344

6.8 Conclusion

In this chapter, microstructure development of aluminized and overlay coating system after isothermal oxidation at 1100 °C was investigated and their oxidation kinetics anaylsis from oxide thickness were performed. It was found that both coating systems obeyed the power law dependence oxide growth, instead of the parabolic rate law. The aluminide coating that was manufactured with high aluminum powder content has the better oxidation resistance due to the slow coating matrix transformation.

Oxide formed on rough as sprayed and free standing overlay coating system surface exhibit a different morphology compared to the oxide formed on a relatively flat surface, especially for coatings that has a low aluminum content within the matrix, in which the spinel formation in oxide scale on flat surface was significantly reduced after oxidation. However, surface condition had a limited impact on the overall rate of oxide growth.

Oxyacetylene flame rig testing was successfully conducted on the thermal barrier coating system samples. It was found that the main failure mode was from the edge spallation after 9-thermal cycles at 1400 °C. The damage resistance improves by increasing the thickness of ceramic top coat.

Reference

1 Doychak J, R¨ uhle M. TEMstudies of oxidized NiAl and Ni3Al cross sections. Oxid. Met. 31:431–52, 1989.

2 Yang JC, Nadarzinski K, Schumann E, R¨ uhle M. Electron microscopy studies of NiAl/γ-Al2O3. 1995.

3 Andoh A, Taniguchi S, Shibata T. TEM observation of phase transformations of alumina scales formed on Al-deposited Fe-Cr-Al foils. Mater. Sci. Forum 369–372:303–10, 2001.

4 W. Pragnell, H. Evans, D. Naumenko, and W. Quadakkers, Aluminium depletion in FeCrAlY steel during transitional alumina formation," Materials at High Temperatures, vol. 22, no. 3-4, pp. 561 2005

5 Wagner C. Diffusion and high temperature oxdiation of metals. Atom movements, pp 153-173, 1951.

6 Pieraggi B. Calculations of parabolic reaction rate constants. Oxidation of metals, pp 177-185, 1987.

7 Fox A C, Oxygen transport by gas permeation through the zirconia layer in plasma sprayed thermal barrier coatings. Surface and Coatings Technology, pp 311-321, 2004.

Chapter 7

Mathematical modelling of the oxidation of binary β-phase nickel aluminium alloys

7.1 - Description of the developed model

The phenomenon of inter-diffusion triggered by the selective oxidation of the bond coat will result in stress generation and void growth in the TBC system. The existence of thermally grown oxide has been in discussion in the field of material science for a long time. In order to fully appreciate this phenomenon, it is crucial to understand the physical nature of inter-diffusion at the microscopic level. Figure 7.1 shows a simplified schematic of this diffusion process in a complete TBC system.

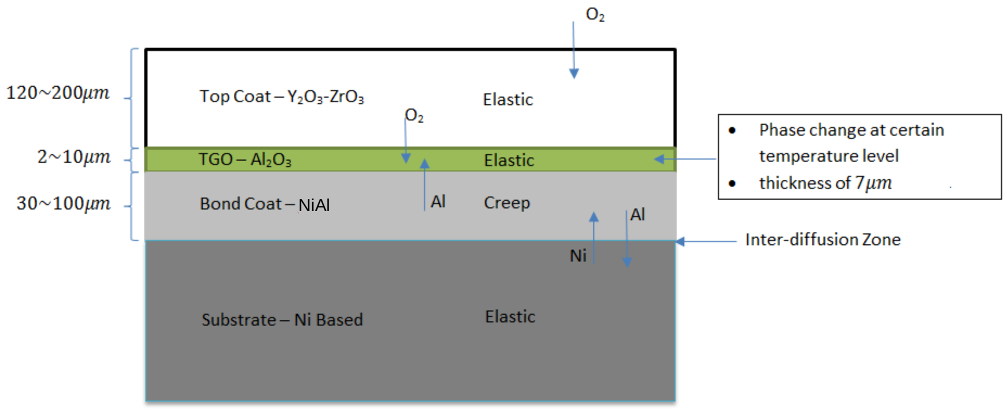

Figure 7.1 – Schematic of diffusion process of a complete TBC system.

The bond coat is primarily made of nickel based chromium aluminium alloy. As aluminium diffuses upwards to the surface of the bond coat and also downwards to the substrate, the content of aluminium within this layer acts as a reservoir to facilitate the growth of thermally grown oxide. This oxidation process creates a fine layer of α-Al_2O_3 which protects the substrate from being further oxidized. The concentration of aluminium in the bond coat decreases due to the formation of oxides at the top coat and the bond coat interface.

From an alloy physics perspective, if the elements in the alloy do not have the same rate of diffusion, this is called non-reciprocal diffusion and leads to atomic planes shifting in order to compensate for a net flux of vacancies. This phenomenon, also known as the Kirkendall effect, was first demonstrated experimentally by Smigelskas and Kirkendall [1]. It has been reported [2] that the diffusivities of nickel and aluminium are different with the diffusivity of Nickel, denoted by D_{Ni}, approximately three times higher than the diffusivity of aluminium, denoted by D_{Al}. However, after aluminium has been depleted sufficiently, the diffusion of nickel through the thermally grown oxide would allow the formation of nickel oxide. This nickel oxide permits additional stresses to be generated in the thermally grown oxide layer and leads to failure at the interface. Ultimately, both the coating structure and properties will evolve causing failure to the coating system.

One of the most important issues of failure of TBC system is the growth of thermally grown oxide as the result of oxidation of aluminium. So to fully understand the diffusion mechanism process, we have developed a mathematical model. To start with, we have considered a binary diffusion model since the bond coat is mainly consisting of aluminium and nickel.

7.1.1 - Formulation of the problem in 3-D

The three dimensional physical based mathematical model has been developed based on the theory of reciprocal diffusion and literature [3]. For simplicity a binary alloy system which consists of atoms A (aluminium) and B (nickel) is considered. We assume that the alloy has a constant volume per atom, denoted by Ω. The concentration of each atom is denoted by C^A and C^B and assumed to have a uniform distribution in the alloy. We also assume that oxidation occurs upon diffusion of atom A. Top ceramic layer has been omitted and only the substrate/bond coat layer has been considered for simplicity. Before formulating the problem for the system, linear creep law was assigned to the alloy system (region R_1), and this was used to set-up the governing equations for the stress, the diffusion flux and the concentration gradient. Linear elasticity was assumed for the oxide layer (region R_2) on the basis that the deformation of this layer is small. In Figure 7.2, a Cartesian coordinate system is used so that the alloy-oxide interface is positioned at the x-y plane and oxide layer grows along the y-axis. In the three dimensional formulation, this coordinate system is considered as the frame of reference. The growth of the thermally grown oxide layer was included and modeled as a moving boundary problem, the moving boundary being the TGO/Alloy interface. In the following section, the development of the mathematical model in three dimension will be presented.

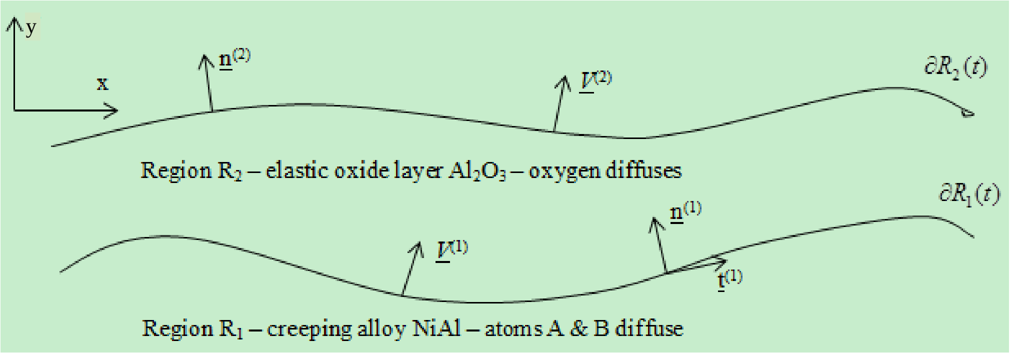

Figure 7.2 – Schematic representation of the substrate and oxide layer.

Governing Equations in 3-D

Region R1

Based on the law of conservation of mass for atom A, namely, aluminium, the rate at which the concentration of aluminium changes is governed by the divergence of the net flux

$$\frac{\partial C^A}{\partial t} = -\nabla . \underline{N}^A , \qquad (7.1)$$

where C^A is the concentration of aluminium, $\underline{N}^A$ is the net flux of aluminium.

From Darken's methodology [4], for a given binary alloy (consisting of elements A and B) system the interdiffusion flux of element A and B at the interface is expressed as the sum of the intrinsic diffusion flux and convection. However, in his approach the stress caused by the chemical potential on diffusion is ignored. Prager [5] suggested that the true driving force for concentration gradient during diffusion is the chemical potential of each element in the system. Therefore, following the fundamental concepts [6], the diffusion flux for both atoms A and B is given by

$$\underline{J}^A = -\frac{D^A \nabla c}{\Omega} - \frac{cD^A}{\phi KT} \nabla p , \qquad (7.2)$$

$$\underline{J}^B = \frac{D^B \nabla c}{\Omega} - \frac{cD^B}{\phi KT} \nabla p , \qquad (7.3)$$

where Ω represents the total volume per atom in the alloy system, c is the specified atom composition in relation to the number of atoms A (C^A) and atom B (C^B), D^A and D^B are the diffusivities of aluminium and nickel respectively, p is the pressure (mean stress), K is the gas constant, T is the absolute temperature and ϕ is the thermodynamic factor.

The total diffusion fluxes of element A and B is expressed as

$$\underline{J} = J^A + J^B = -\frac{(D^A - D^B)}{\Omega}\nabla c - \frac{\left[cD^A + (1-c)D^B\right]}{\phi KT}\nabla p\,. \quad (7.4)$$

It is obvious that from (7.4) that the specific composition gradient is proportional to the differential diffusivity $(D^A - D^B)$ of element A and B. Take for example when D^A is greater than D^B, the specific composition gradient will drive the diffusion flux to lower diffusivity region. The contribution of pressure gradient is governed by the weighted concentration diffusivity $(cD^A + (1-c)D^B)$ of both elements. This implies that the stress gradient will drive the diffusion flux to the region which has a larger mean stress.

Furthermore, the transport (net flux) of atoms A is contributed by the diffusion flux which is driven by the concentration and stress gradient, and the advection driven by the motion of the atoms ($C^A\underline{v}^{(1)}$) where $\underline{v}^{(1)}$ is the marker velocity within the alloy region. The similar relation applies to atoms B

$$\underline{N}^A = \underline{J}^A + C^A\underline{v}^{(1)}, \quad (7.5)$$

$$\underline{N}^B = \underline{J}^B + C^B\underline{v}^{(1)}. \quad (7.6)$$

The total number of atoms is conserved when the divergence of the sum of net flux $\underline{N}$ is equal to zero

$$\nabla.(\underline{N}^A + \underline{N}^B) = 0\,. \quad (7.7)$$

If we substitute (7.2) and (7.3) into (7.5), (7.6) and (7.7), we obtain

$$\nabla.(\underline{J} + \frac{\underline{v}^{(1)}}{\Omega}) = 0\,. \quad (7.8)$$

After combining (7.4) to (7.8), this leads to the continuity equation which has the relationship between the rate of volume change and the differential diffusion and the mean stress gradient

$$\nabla.\underline{v}^{(1)} = (D^A - D^B)\nabla^2 c + \frac{\Omega}{\phi KT}\nabla.\left[\left(cD^A + (1-c)D^B\right)\nabla p\right]. \quad (7.9)$$

The diffusion equation for atoms A is governed by the divergence of net flux which gives

$$\frac{\partial c}{\partial t} + \nabla.(\Omega \underline{\mathrm{J}}^{A} + c\underline{v}^{(1)}) = 0, \tag{7.10}$$

If we substitute (7.9) to (7.10), (7.10) becomes

$$\frac{\partial c}{\partial t} + \nabla.(\underline{v}^{(1)}c) = \mathrm{D}^{A}\,\nabla^{2}c + \frac{D^{A}\Omega}{\phi KT}\nabla.(c\nabla p). \tag{7.11}$$

Equation (7.11) tells us the rate at which the composition of atoms A changes by allowing the individual intrinsic diffusivity D^A as the function of concentration *c(t).*

The force balance is given by

$$\eta\left[\nabla^{2}\underline{v}^{(1)} + \frac{1}{3}\nabla(\nabla.\underline{v}^{(1)})\right] - \nabla p = 0, \tag{7.12}$$

where η is the viscosity. The stress tensor is given by

$$\sigma_{ij}^{(1)} = \eta\left(\frac{\partial v_i^{(1)}}{\partial x_j} + \frac{\partial v_j^{(1)}}{\partial x_i}\right) - \frac{2}{3}\eta\nabla.\underline{v}^{(1)}\delta_{ij} - p\delta_{ij}. \tag{7.13}$$

For atoms A, initially the concentration, as the function of displacement and time is equal to an constant (uniform concentration) which is given by

$$c(\underline{x},0) = C_i, \tag{7.14}$$

subject to

$$c \to C_i,\ as\ y \to -\infty\ . \tag{7.15}$$

The initial velocity is stationary and with no pressure

$$\underline{v}(\underline{x},0) = 0,\ p(\underline{x},0) = 0,\ \text{as}\ y \to -\infty. \tag{7.16}$$

Boundary of Region R1

Atoms B do not penetrate through the boundary of R$_1$, i.e. there is no flux of atoms B through the boundary ∂R_1. This can be expressed as

$$\underline{n}^{(1)}.\left(\underline{J}^{B}+\frac{(1-c)}{\Omega}(\underline{v}^{(1)}-\underline{V}^{(1)})\right)=0, \qquad \text{for } \underline{\mathrm{x}} \in \partial R_1, \tag{7.17}$$

Whereas flux of atom A is given by the reaction with the oxygen at the interface as,

$$\underline{n}^{(1)}.\left(\underline{J}^{B}+\frac{(1-c)}{\Omega}(\underline{v}^{(1)}-\underline{V}^{(1)})\right)=\frac{4}{3}D_o\underline{n}^{(1)}.\nabla c_o, \qquad \text{for } \underline{\mathrm{x}} \in \partial R_1, \tag{7.18}$$

where $\underline{V}^{(1)}$ is the velocity vector of the interface when atoms A react with the oxygen. $\underline{v}^{(1)}$ is a marker velocity and its relationship to the boundary velocity $\underline{V}^{(1)}$ through constitutive law is defined as

$$\underline{n}^{(1)}.\underline{v}^{(1)}=\alpha\underline{n}^{(1)}.\underline{V}^{(1)}, \qquad \text{for } \underline{\mathrm{x}} \in \partial R_1, \tag{7.19}$$

The sign of constant parameter α determines the flux at the interface and subsequently the sign of stress gradient at the interface is also depending on this parameter.

If we combine (7.3) into equation (7.17), we obtain

$$\underline{n}^{(1)}.\left(\frac{D^B\nabla c}{\Omega}-\frac{(1-c)\mathrm{D}^B}{\phi KT}\nabla p+\frac{(1-c)}{\Omega}(\underline{v}^{(1)}-\underline{V}^{(1)})\right)=0, \text{ for } \underline{\mathrm{x}} \in \partial R_1, \tag{7.20}$$

After rearranging (7.20), it becomes

$$\underline{n}^{(1)}.\underline{V}^{(1)}=\underline{n}^{(1)}.\left(\frac{D^B\nabla c}{1-c}-\frac{D^B\Omega}{\phi KT}\nabla p+\underline{v}^{(1)}\right) \text{for } \underline{\mathrm{x}} \in \partial R_1. \tag{7.21}$$

Equation (7.21) gives the normal velocity of the boundary.

Region R2

For linear elasticity

$$(\lambda+\mu)\nabla(\nabla.\underline{v}^{(2)})+\mu\nabla^2\underline{v}^{(2)}=0 \qquad (7.22)$$

where λ and μ are the elastic moduli, namely, Lame’s first parameter and shear modulus respectively.

The strain tensor is

$$\frac{\partial\varepsilon_{ij}^{(2)}}{\partial t}=\frac{1}{2}\left(\frac{\partial v_i^{(2)}}{\partial x_j}+\frac{\partial v_j^{(2)}}{\partial x_i}\right). \qquad (7.23)$$

The stress tensor is expressed in terms of strain

$$\sigma_{ij}^{(2)}=\lambda\delta_{ij}\varepsilon_{kk}^{(2)}+2\mu\varepsilon_{ij}^{(2)}. \qquad (7.24)$$

Oxide is formed due to the reaction of aluminium with the oxygen at the boundary ∂R_1; the diffusion equation for the oxygen is

$$\frac{\partial c_o}{\partial t}+\nabla.(\underline{v}^{(2)}c_o)=\mathrm{D}_o\nabla^2c_o, \qquad (7.25)$$

where c_o is the concentration of oxygen and D_o is the diffusivity of the oxygen. Due to fast reaction of aluminium and oxygen at the boundary between R1 and R2, the concentration of oxygen is zero

$$c_o=0 \ at \ \partial R_1(t). \qquad (7.26)$$

At the boundary ∂R_2, the concentration of oxygen is equal to the atmospheric concentration

$$c_o=c_{oa} \ at \ \partial R_2(t). \qquad (7.27)$$

Based on the reaction equilibrium equation of $4Al+3O_2\rightarrow 2Al_2O_3$, we can assume that three times the flux of aluminium is equal to four times the flux of oxygen at the boundary $\partial R_1(t)$

$$3D^A\underline{n}^{(1)}.\nabla c=-4D^B\underline{n}^{(1)}.\nabla c_o. \qquad (7.28)$$

At $\partial R_2(t)$, $\underline{n}^{(2)}.\underline{\underline{\sigma}}^{(2)} = 0$ (there is no stress at the free outer boundary). The normal velocity in the elastic oxide layer is equal to the normal velocity field at the boundary $\partial R_2(t)$, $\underline{n}^{(2)}.\underline{v}^{(2)} = \underline{n}^{(2)}.V^{(2)}$. For continuity of stress at boundary $\partial R_1(t)$, the stress in region R_1 is equal to the stress in region R_2, $\underline{n}^{(1)}.\underline{\underline{\sigma}}^{(1)} = \underline{n}^{(1)}.\underline{\underline{\sigma}}^{(2)}$. The continuity of tangential component of velocity at boundary $\partial R_1(t)$ is expressed as $\underline{t}^{(1)}.\underline{v}^{(1)} = \underline{t}^{(1)}.\underline{v}^{(2)}$.

As aluminium flows through the boundary ∂R_1, the density changes in the oxide layer which in turn produces a volume change. Therefore the mass balance at boundary ∂R_1 is expressed as

$$-\rho^{(1)} D^A \underline{n}^{(1)}.\nabla c = \rho^{(2)} \underline{n}^{(1)}.(v^{(2)} - \underline{V}^{(1)}), \qquad (7.29)$$

where $\rho^{(1)}$ is the density of aluminium and $\rho^{(2)}$ is the density of oxide. Equation (7.29) describes the mass flux of aluminium through the interface has to be balanced, in the frame of reference of the moving boundary $\underline{n}^{(1)}.\underline{V}^{(1)}$, by the density change in the oxide layer.

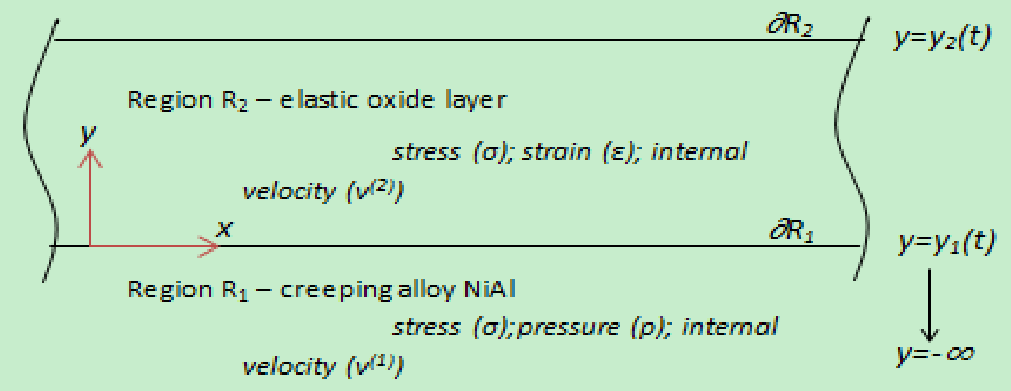

Figure 7.3 - Schematic representation of substrate and oxide layer in one dimension.

7.2 - Mathematical Model in one-dimensional

In Figure 7.3, a Cartesian coordinate system has been used so that the alloy-oxide interface is positioned at x-y plane and oxide layer grows along the y-axis. The problem from the previous section is simplified into the one-dimensional reaction-diffusion moving boundary problem in order to solve for aluminium concentration and boundary positions. Equation (7.11), (7.14)-(7.15) and (7.18)-(7.21) are given below,

Diffusion equation of aluminium

$$\frac{\partial c}{\partial t}=\frac{\partial}{\partial y}\left[\left(D^A(1-c)-D^Bc\right)\frac{\partial c}{\partial y}\right]+\frac{\left(D^A-D^B\right)\Omega}{\phi kT}\frac{\partial}{\partial y}\left[c(1-c)\frac{\partial p}{\partial y}\right], \tag{7.30}$$

with initial and boundary conditions

$$c(y,0)=c_i, \tag{7.31}$$

$$c(-\infty,\mathrm{t})=c_i, \tag{7.32}$$

$at\ y = y_1(t)$

$$-\frac{\left[D^A(1-c)+D^B c\right]}{\Omega(1-c)}\frac{\partial c}{\partial y}+\frac{(D^A-D^B)}{\phi kT}c\frac{\partial p}{\partial y}=-\frac{4}{3}\left(-D^o\frac{\partial c_o}{\partial y}+c^o(\mathrm{v}^{(2)}-V^{(1)})\right). \tag{7.33}$$

Diffusion equation of oxygen is

$$\frac{\partial c_o}{\partial t}+\frac{\partial}{\partial y}(v^{(2)}c_o)=D^o\frac{\partial c_o}{\partial y}, \tag{7.34}$$

with boundary conditions of

$$c_o(y_1(t),t)=0, \tag{7.35}$$

$$c_o(y_2(t),t)=c_{oa}. \tag{7.36}$$

The boundary condition (7.33) was derived based on the fact that once aluminium and oxygen diffuse, they react to form the TGO. The growth of this layer comes from the reaction equilibrium equation of $4Al+3O_2 \rightarrow 2Al_2O_3$. Therefore, equation (7.33) describes the flux and convection of aluminium is balanced by the flux and convection of oxygen at the TGO/Alloy interface.

Assuming no flux of atom B through the boundary $y_1(t)$, the boundary velocity condition is expressed as

$at\ y = y_1(t)$

$$\frac{dy_1}{dt}=V^{(1)}=\frac{D^A(1-c)+D^B c}{1-c}\frac{\partial c}{\partial y}+\frac{(D^A-D^B)\Omega}{\phi kT}c\frac{\partial p}{\partial y}, \tag{7.37}$$

$$\frac{dy_2}{dt}=v^{(2)}=\left[\frac{D^A(1-c)+D^B c}{1-c}-\frac{\rho^{(1)}}{\rho^{(2)}}D^A\right]\frac{\partial c}{\partial y}+\frac{(D^A-D^B)\Omega}{\phi kT}c\frac{\partial p}{\partial y}, \tag{7.38}$$

where $\rho^{(1)}$ and $\rho^{(2)}$ represent the density of aluminium and oxide respectively.

Nickle alloys are ideal for turbine engine application due to its high melting temperature and creep resistance properties, i.e. viscoelastic. Considering the binary alloy is highly incompressible solid, creeping flow has been used to derive the relationship between the pressure field and velocity field in which the velocity field $v^{(1)}$ is expressed as the function of aluminium concenctration gradient and pressure gradient. An additional boundary condition at interface is considered for the pressure by describing the internal velocity near the interface is proportional to the interface velocity through the constitutive law with α a dimensionless constant. Hence, the pressure in one dimension is given by

$$p = \frac{4}{3}\eta\left[\left(D^A - D^B\right)\frac{\partial^2 c}{\partial y^2} + \frac{\Omega}{\phi kT}\frac{\partial}{\partial y}\left(\left(cD^A + (1-c)D^B\right)\frac{\partial p}{\partial y}\right)\right], \tag{7.39}$$

with initial and boundary conditions of

$$p(y,0) = 0, \tag{7.40}$$

$$p(-\infty,\mathrm{t}) = 0, \tag{7.41}$$

$$at\ y = y_1(t)$$

$$\left[D^A - D^B - \alpha\left(\frac{D^A(1-c) + D^B c}{1-c}\right)\right]\frac{\partial c}{\partial y} + \frac{\Omega}{\phi kT}\left[cD^A + (1-c)D^B - \alpha(D^A - D^B)c\right]\frac{\partial p}{\partial y} = 0. \tag{7.42}$$

To nondimensionalize the system of equations (7.30) – (7.42), the new dimensionless parameters introduced are

$$y = L\bar{y}, \qquad t = \frac{L^2}{D^A}\bar{t}, \qquad V^{(1)} = \frac{D^A}{L}\bar{V}, \quad v^{(2)} = \frac{D^A}{L}\bar{v}, \qquad p = \frac{\phi kT}{\Omega}\bar{p},$$

$$\bar{D}^{oa} = \frac{D^o}{D^A}, \qquad \bar{\Omega}^{oA} = \frac{\Omega^A}{\Omega^o}, \qquad c_o = c_{oa}\bar{c}_o, \tag{7.43}$$

where the characteristic length scale is $L = \left(\bar{T}D^A\right)^{1/2}$, with timescale $\bar{T}$.

The resulting system of equations are

$$\frac{\partial c}{\partial \bar{t}} = \frac{\partial}{\partial \bar{y}}\left[\left(1 - c(1-\bar{D}\right)\frac{\partial c}{\partial \bar{y}}\right] + (1-\bar{D})\frac{\partial}{\partial \bar{y}}\left[c(1-c)\frac{\partial \bar{p}}{\partial \bar{y}}\right], \tag{7.44}$$

$$\frac{3}{4}\bar{p} = (1-\bar{D})\frac{\partial^2 c}{\partial \bar{y}^2} + \frac{\partial}{\partial \bar{y}}\left[c + (1-c)\bar{D}\frac{\partial \bar{p}}{\partial \bar{y}}\right], \tag{7.45}$$

$$\frac{\partial \bar{c}_o}{\partial \bar{t}} + \frac{\partial}{\partial \bar{y}}(\bar{v}^{(2)}c_o) = \bar{D}^o\frac{\partial^2 \bar{c}_o}{\partial \bar{y}^2}. \tag{7.46}$$

The far field conditions are now

$$\bar{c} \to c_i \;\; as \;\; \bar{y} \to -\infty, \tag{7.47}$$

$$\bar{p} \to 0 \;\; as \;\; \bar{y} \to -\infty. \tag{7.48}$$

The conditions at interface and free surface are now

$$-\frac{1-c+c\bar{D}}{1-c}\frac{\partial c}{\partial \bar{y}} + c(\bar{D}-1)\frac{\partial p}{\partial \bar{y}} = -\frac{4}{3}\left(-\frac{\bar{D}^o}{\bar{\Omega}^{oa}}\frac{\partial c_o}{\partial \bar{y}} - \frac{\bar{c}_o}{\bar{\Omega}^{oa}}(\bar{\mathrm{v}}^{(2)} - \bar{V}^{(1)})\right), \tag{7.49}$$

$$\left[1 - \bar{D} - \alpha\left(\frac{1-c+c\bar{D}}{1-c}\right)\right]\frac{\partial c}{\partial \bar{y}} + \left[c + (1-c)\bar{D} - \alpha(1-\bar{D})c\right]\frac{\partial \bar{p}}{\partial \bar{y}} = 0, \tag{7.50}$$

$$\frac{d\bar{y}_1}{d\bar{t}} = \bar{V}^{(1)}, \tag{7.51}$$

$$\frac{d\overline{y}_2}{d\overline{t}} = \overline{v}^{(1)}, \tag{7.52}$$

$$\overline{V}^{(1)} = \frac{1-c(1-\overline{D})}{1-c}\frac{dc}{d\overline{y}} + (1-\overline{D})c\frac{dp}{d\overline{y}}, \tag{7.53}$$

$$\overline{v}^{(2)} = \left[\frac{1-c(1-\overline{D})}{1-c} - \overline{\rho}\right]\frac{dc}{d\overline{y}} + (1-\overline{D})c\frac{dp}{d\overline{y}}, \tag{7.54}$$

$$\overline{c}_o(\overline{y}_1(\overline{t}), \overline{\mathrm{t}}) = 0, \tag{7.55}$$

$$\overline{c}_o(\overline{y}_2(\overline{t}), \overline{\mathrm{t}}) = 1, \tag{7.56}$$

while at $t = 0$, the initial conditions read

$$c\left(\overline{y}\right) = c_i, \tag{7.57}$$

7.3 – Asymptotic analysis

7.3.1 - Small time behaviour

In this section, a limit of t << 1 is taken for which an initial aluminium oxide layer forms. As illustrarted in Figure 7.2, oxidation takes place at lower boundary $y_1(t)$. Oxygen diffuses from the free surface $y = y_2(t)$ to the reaction boundary, where unoxidised aluminium is first encountered. Assuming fast reaction, this prevents oxygen penetrate beyond reaction boundary. At the same time, aluminium diffuses from the alloy (region 1) to encounter and react with oxygen at the lower boundary. Nickel, however, is not considered to react with oxygen. Oxide formation results in a change of density ($\overline{\rho} > 0$) and causes the boundary reaction layer $y = y_1(t)$ to move into the alloy as the aluminium is depleted. However, the position of both $y = y_1(t)$ and $y = y_2(t)$ are unknown moving boundary and needed to be solved for. In the following, a study will be carried out on how the change of parameters, such as diffusivity $\overline{D}$, $\overline{D}^{oa}$ and α , would effect the solution of concentration profile of aluminium, pressure in the bond coat as well as oxide growth.

To determine the singular initial behaviour of the oxide growth upon isothermal exposure, a power law dependence of time with an exponent of 1/2 was used. This is was defined by balancing terms in the diffusion equation. So that the new boundary layer region in which the oxidation of bond coat is taking place can be defined as $\overline{y} = O(t^{1/2})$. Then the new variable can be introduced as $\overline{y} = t^{1/2}\hat{y}$, where $\hat{y} = O(1)$. This transformation of coordinates allows for the analysis to be carried out asymptotically by finding the small time solution when t << 1 within the newly defined region of $\hat{y}_1 \le \hat{y} \le \hat{y}_2$.

It is important to point out that the purpose of small time asymptotic solution is to give a nonsingular initial condition to the numerical simulation.

By introducting new variables scaling with $t^{1/2}$ so that

$$\bar{y} = t^{1/2}\hat{y}, \qquad \bar{y}_1 = t^{1/2}\hat{y}_1, \qquad \bar{y}_1 = t^{1/2}\hat{y}_1, \ \bar{v}^{(2)} = \frac{1}{t^{1/2}}\hat{v}^{(2)}, \qquad \bar{v}^{(2)} = \frac{1}{t^{1/2}}\hat{v}^{(2)}$$

(7.58)

Then equation (7.44) – (7.46) for small *t* at leading order become

$$-\frac{\hat{y}}{2}\frac{d\hat{c}}{d\hat{y}} = \frac{d}{d\hat{y}}\left[(1-\hat{c}+\bar{D}\hat{c})\frac{d\hat{c}}{d\hat{y}}\right] + (1-\bar{D})\frac{d}{d\hat{y}}\left[\hat{c}(1-\hat{c})\frac{d\hat{p}}{d\hat{y}}\right], \tag{7.59}$$

$$\frac{d\hat{p}}{d\hat{y}} = -\frac{1-\bar{D}}{\hat{c}+(1-\hat{c})\bar{\mathrm{D}}}\frac{d\hat{c}}{d\hat{y}}, \tag{7.60}$$

$$-\frac{\hat{y}}{2}\frac{d\hat{c}_o}{d\hat{y}} + \frac{d}{d\hat{y}}(\bar{v}^{(2)}\hat{c}_o) = \bar{D}_o\frac{d^2\hat{c}_o}{d\hat{y}^2}. \tag{7.61}$$

Conditions at far field and at interface can also be obtained by the same scaling variables.

The general solution of equation (7.61) is solved and expressed as

$$\hat{c}_o = 1 - \frac{erf\left((\hat{y}-\hat{y}_2)\sqrt{1/4\bar{D}^o}\right)}{erf\left((\hat{y}_1-\hat{y}_2)\sqrt{1/4\bar{D}^o}\right)}, \tag{7.62}$$

subject to boundary condition of (7.55) and (7.56).

At this point, by substitute equation (7.60) to (7.59) along with boundary conditions, small time solution for the concentration of aluminium and the lower and upper boundary position can be solved numerically as boundary value problem. However, in order to obtain the numerical solution for *O(1)* time using finite difference method, initial values of aluminium concentration (c), pressure (p), oxygen concentration (c_o), lower boundary position (y_1), upper boundary position (y_2), interface velocity ($V^{(1)}$) and internal velocity ($v^{(2)}$) are required. From equation (7.60) and boundary condition (7.50) the only possible solution at this stage for pressure gradient and concentration gradient is zero which isn't correct. Therefore, this suggests that the pressure is developing on two different length scales and the size of growth for pressure is large. Hence, developing an asymptotic expansion in two regions that approximates the solution of pressure is required.

7.3.2 – Small time expansion for pressure

Equation (7.60) is formulated based on the assumption that linear creep law is assigned to the alloy system which the stress is being proportional to the strain rate $d\bar{v}_1 / d\bar{y}$, where $\bar{v}_1$ is the internal marker velocity that has been eliminated. For nonlinear creep, the stress is depended on the power of exponent *n (Appendix A for derivation)*. Hence, the pressure equation reads as

$$\operatorname{sgn}(\bar{p})\left(\frac{3}{4}\bar{p}\right)^n = (1-\bar{D})\frac{\partial^2 c}{\partial \bar{y}^2} + \frac{\partial}{\partial \bar{y}}\left[c + (1-c)\bar{D}\frac{\partial \bar{p}}{\partial \bar{y}}\right]. \tag{7.63}$$

7.3.2.1 - Inner expansion: for $n \geq 1$

The initial behavior of at/near the interface a small time asymptotic expansion of the pressure is carried out by writing

$$\bar{p} = \bar{p}_0 + t^{\varepsilon}\bar{p}_1 + O(t^{2\varepsilon}), \tag{7.64}$$

where ε is a positive constant and due to the diffusion scale obeys the power law, $\varepsilon = 1/(n+1)$. Large size of growth for pressure is considered by scaling

$$\bar{p} = t^{-\frac{1}{n+1}}\hat{p}, \tag{7.65}$$

along with (7.58), the asymptotic expansion of (7.64) becomes

$$\hat{p} = \hat{p}_0 + t^{\frac{1}{n+1}}\hat{p}_1 + O(t^{\frac{2}{n+1}}). \tag{7.66}$$

Substituting the above expansion into equation (7.63) the inner solution of the pressure is obtained by equating the coefficients of the each powers of *t*.

At $O(t^{-1/n})$, the zeroth-order equation is then given by

$$\frac{d\hat{p}_0}{d\hat{y}} = \frac{A_0}{c_0 + (1-c_0)\bar{D}}, \tag{7.67}$$

in order to saftisfy the condition (7.50) the integration constant $A_0 = 0$ as the pressure gradient is one order of magnitude bigger than then concentration gradient, hence $\hat{p}_0 = \text{constant}$.

At *O(1)*, the first-order equation is given by

$$\frac{d\hat{p}_1}{d\hat{y}} = -\frac{1-\bar{D}}{c_0 + (1-c_0)\bar{D}}\frac{d\hat{c}_0}{d\hat{y}} + \frac{k}{c_0 + (1-c_0)\bar{D}}, \tag{7.68}$$

where c_0 has been solved numerically, see section 7.3.3.

From integration of equation (7.68), $\hat{p}_1$ in the inner region yields the approximation of

$$\begin{aligned}\hat{p}_1 = -\log(c_0 + (1-c_0)\bar{D}) + k\int_0^{\hat{y}}\left(\frac{1}{c_0(s) + (1-c_0(\mathrm{s}))\bar{D}} - \frac{1}{c_i + (1-c_i)\bar{D}}\right)ds \\ + \frac{k\hat{y}}{c_i + (1-c_i)\bar{D}} + L.\end{aligned} \tag{7.69}$$

Inner solution of pressure can then be obtained by substituting equation (7.67) (7.69) into the expansion (7.66), yields

$$\begin{aligned}p = t^{-1/2}\hat{p}_0 - \log(c_0 + (1-c_0)\bar{D}) + k\int_0^{\hat{y}}\frac{ds}{c_0(s) + (1-c_0(\mathrm{s}))\bar{D}} \\ + \frac{k\hat{y}}{c_i + (1-c_i)\bar{D}} + L + o(1),\end{aligned} \tag{7.70}$$

where $\hat{p}_0$ and L can be found from matching to the outer solution.

7.3.2.2 - Outer expansion

Recall equation (7.45), as described from the initial condition (7.40) and far field condition (7.41), leads to $d^2c/d\hat{y}^2 \ll 1 \text{ as } t \to 0$. Outer variables after scaling on the outer region are given by

$$\bar{p} = t^{\frac{1}{n+1}}\hat{p}, \qquad \bar{y} = t^{\frac{1}{2}}\hat{y}, \tag{7.71}$$

$$\hat{p} = \tilde{p}, \qquad \hat{y} = t^{-\frac{1}{n+1}}\tilde{y}. \tag{7.72}$$

On the outer length scale aluminium concentration c becomes trivial, i.e. $c=c_i$. Therefore, (7.63) become

$$\left(\frac{3}{4}\tilde{p}\right)^n = (c_i + (1-c_i)\bar{D})\frac{d^2\tilde{p}}{d\tilde{y}^2}. \tag{7.73}$$

Thus, the exact solution for the pressure at outer region is then obtained as

$$\tilde{p} = -\left(\frac{n-1}{2}\right)^{-\frac{2}{n-1}}\left(\frac{2}{M}\left(\frac{3}{4}\right)^n\frac{1}{n+1}\right)^{-\frac{1}{n-1}}\left(-\tilde{y}+\tilde{y}_o\right)^{-\frac{2}{n-1}}, \tag{7.74}$$

where $M = c_i + (1-c_i)\bar{D},$ rearrange (7.74), the outer solution is then given as

$$\tilde{p} = \left(\frac{3}{4}\right)^{-\frac{n}{n-1}}\left(\frac{2}{M}\frac{1}{n+1}\left(\frac{n-1}{2}\right)^2\right)^{-\frac{1}{n-1}}\left(\tilde{y}_o-\tilde{y}\right)^{-\frac{2}{n-1}}, \tag{7.75}$$

where constant $\tilde{y}_0$ a constant of integration is to be fixed from matching with both solutions.

7.3.2.3 - Matching

For clarity purposes, both the inner and outer solutions are restated below,

inner solution:

$$p = t^{-1/2}\hat{p}_0 - \log(c_0 + (1-c_0)\bar{D}) + k\int_0^{\hat{y}} \frac{ds}{c_0(s) + (1-c_0(\mathrm{s}))\bar{D}} + \frac{k\hat{y}}{c_i + (1-c_i)\bar{D}} + L + o(1), \tag{7.76}$$

outer solution:

$$\tilde{p} = \left(\frac{3}{4}\right)^{-\frac{n}{n-1}} \left(\frac{2}{M}\frac{1}{n+1}\left(\frac{n-1}{2}\right)^2\right)^{-\frac{1}{n-1}} \left(\tilde{y}_o - \tilde{y}\right)^{-\frac{2}{n-1}}, \tag{7.77}$$

where the inner and outer variables are related and will be matched, assuming that both express the same function in an overlap region.

From Taylor's series as $\hat{y} = O(1),$ the outer solution in terms of inner variables is expressed as

$$\tilde{p} = \left(\frac{3}{4}\right)^{-\frac{n}{n-1}} \left(\frac{2}{M}\frac{1}{n+1}\left(\frac{n-1}{2}\right)^2\right)^{-\frac{1}{n-1}} \tilde{y}_o^{\,-\frac{2}{n-1}} \left(1 + \frac{2}{n-1} t^{\frac{1}{n+1}} \frac{\hat{y}}{\tilde{y}_o}\right)^{-\frac{2}{n-1}}, \tag{7.78}$$

and the inner solution in terms of outer variables for large spatial variable of $\hat{y}$ is expressed as

$$\begin{aligned} \hat{p} = \hat{p}_0 + t^{\frac{1}{n+1}} &\left(\frac{k\,\tilde{y}\,t^{-\frac{1}{n+1}}}{M} + L - \log(c_0 + (1-c_0)\bar{D})\right) \\ &+ k\int_0^{-\infty}\left(\frac{1}{c_0(s) + (1-c_0(\mathrm{s}))\bar{D}} - \frac{1}{c_i + (1-c_i)\bar{D}}\right)ds \\ &- k\int_{\hat{y}}^{-\infty} t^{-\frac{1}{n+1}}\left(\frac{1}{c_0(s) + (1-c_0(\mathrm{s}))\bar{D}} - \frac{1}{c_i + (1-c_i)\bar{D}}\right)ds. \end{aligned} \tag{7.79}$$

Equation (7.79) implied that as $\hat{y} \to -\infty$, the aluminium concentration $c \to c_i$, and by subtracting the constant part from the integrant, the behaviour of the growth integral term can be presented by taking the limit from 0 to $-\infty$ so that the integral term can be calculated from numerical solution of the aluminium concentration. The large $\hat{y}$ behaviour of $c_o\left(\hat{y}\right)$ suggests that the last term of (7.79) can be neglected.

From direct matching of each term in equation (7.78) with equation (7.79), we obtain

First term:

$$\hat{p}_0 = \left(\frac{3}{4}\right)^{-\frac{n}{n-1}} \left(\frac{2}{M}\frac{1}{n+1}\left(\frac{n-1}{2}\right)^2\right)^{-\frac{1}{n-1}} \tilde{y}_o^{-\frac{2}{n-1}}, \tag{7.80}$$

Second term:

$$\frac{k}{c_i+(1-c_i)\bar{D}} = \left(\frac{3}{4}\right)^{-\frac{n}{n-1}} \left(\frac{2}{M}\frac{1}{n+1}\left(\frac{n-1}{2}\right)^2\right)^{-\frac{1}{n-1}} \left(\frac{2}{n-1}\tilde{y}_o^{-\frac{n+1}{n-1}}\right), \tag{7.81}$$

where $\hat{y}$ is determined from (7.81) and yields

$$\tilde{y}_o = \left(\frac{k}{c_i+(1-c_i)\bar{D}}\left(\frac{3}{4}\right)^{\frac{n}{n-1}} \left(\frac{2}{M}\frac{1}{n+1}\left(\frac{n-1}{2}\right)^2\right)^{\frac{1}{n-1}} \frac{n-1}{2}\right)^{-\frac{n-1}{n+1}}. \tag{7.81}$$

By subtracting the matched part from the sum of inner and outer solution, the composite solution for pressure is obtained

$$\begin{aligned}\tilde{p}_{composite} = {} & \left(\frac{3}{4}\right)^{-\frac{n}{n-1}} \left(\frac{2}{M}\frac{1}{n+1}\left(\frac{n-1}{2}\right)^2\right)^{-\frac{1}{n-1}} \left(\tilde{y}_o - \tilde{y}\right)^{-\frac{2}{n-1}} \\ & + t^{\frac{1}{n+1}}\left(L - \log(c_o+(1-c_o)\bar{D}) + k\int_0^{t^{-\frac{1}{n+1}}\tilde{y}} \left(\frac{1}{c_0(s)+(1-c_0(s))\bar{D}} - \frac{1}{c_i+(1-c_i)\bar{D}}\right) ds\right).\end{aligned} \tag{7.82}$$

where c_o is obtained from small time solution of aluminium diffusion (7.59). The solution of (7.82) is shown in Section 7.3.3.

7.3.3 - Boundary Value Problem for Solving Aluminium Concentration

The concentration of aluminium can be solved numerically as boundary value problem by substituting equation (7.68) into equation (7.59), where the constant of integration *k* as the function of pressure and concentration gradient will appear in the diffusion equation. Note that both equations are at $O(1)$ state. The system of equations are

$$\frac{d}{d\hat{y}}\left[\frac{\bar{D}}{\hat{c}+(1-\hat{c})\bar{D}}\frac{\partial\hat{c}}{\partial\hat{y}}\right]+(1-\bar{D})\frac{d}{d\hat{y}}\left[\frac{k(\hat{c}-\hat{c}^2)}{\hat{c}+(1-c)\bar{D}}\right]=-\frac{\hat{y}}{2}\frac{\partial\hat{c}}{\partial\hat{y}}, \tag{7.83}$$

with boundary conditions of

$$\hat{c}(-\infty)=c_i, \tag{7.84}$$

$at\ \hat{y}=\hat{y}_1(t)$

$$\left(-\frac{\bar{D}}{(1-\hat{c})(\hat{c}+\bar{D}-\hat{c}\bar{D})}\right)\frac{\partial\hat{c}}{\partial\hat{y}}+\frac{k\hat{c}(\bar{D}-1)}{\hat{c}+(1-\hat{c})\bar{D}}=\frac{4}{3}\bar{D}^{oa}\bar{c}^{oa}\frac{\partial\hat{c}_o}{\partial\hat{y}}, \tag{7.85}$$

$$\hat{y}_1=\frac{2\bar{D}}{(1-\hat{c})(\hat{c}+\bar{D}-\hat{c}\bar{D})}\frac{\partial\hat{c}}{\partial\hat{y}}+\frac{2k\hat{c}(1-\bar{D})}{\hat{c}+(1-\hat{c})\bar{D}}, \tag{7.86}$$

$$\left\{1-\bar{D}-\alpha\left(\frac{1-\hat{c}+\hat{c}\bar{D}}{1-\hat{c}}\right)-\frac{(1-\bar{D})\left[\hat{c}+\bar{D}(1-\hat{c})-\alpha(1-\bar{D})\hat{c}\right]}{\hat{c}+(1-\hat{c})\bar{D}}\right\}\frac{\partial\hat{c}}{\partial\hat{y}} \\ +\frac{k\left[\hat{c}+\bar{D}(1-\hat{c})-\alpha(1-\bar{D})\hat{c}\right]}{\hat{c}+(1-\hat{c})\bar{D}}=0. \tag{7.87}$$

$$\hat{y}_1-\hat{y}_2=\frac{8}{3}\bar{\rho}\bar{D}^{oa}\bar{c}^{oa}\frac{\partial\hat{c}_o}{\partial\hat{y}}, \tag{7.88}$$

It is convenient to define a new coordinate where $\hat{y} = \tilde{y} + \hat{y}_1(t)$, whose origin is at the moving interface, i.e.lower boundary. The unknown function of $\hat{y}_1(t)$ will appear in the governing ordinary differential equation for aluminium concentration. The above system of equations were solved by using MATLAB BVP5C solver and depending on the ratio of $\bar{D}^{oa}$ the oxidation rate is limited either by aluminium diffusion or oxygen diffusion via oxide layer. Figure 7.3 illustrates the qualitative structure of the interface region based on the analysis in section 7.3. We can see that the solution structure which has a diffusion length of $O(t^{1/2})$ is obtained by considering five physical parameters at temperature of 1100 °C, namely, initial concentration ($\hat{c}_i$), ratio of diffusivity of aluminium and nickel ($\bar{D}$), ratio of aluminium density and oxide density ($\bar{\rho}$), ratio of diffusivity of oxygen and aluminium ($\bar{D}^{oa}$) and dimensionless constant c_{oa} and α.

The parameters listed below are fixed for both the small time solution and numerical solution :

$$c_i = 0.48, \quad c_{oa} = 0.00001, \quad \bar{\rho} = 0.68, \quad n = 6. \tag{7.89}$$

The values of $\bar{D}^{oa}$, $\bar{D}$ *and* α are specific to each figure and hence are not listed above. Note that $\bar{D}^{oa}$ *and* $\bar{D}$, the dimensionless diffusivity ratio of oxygen/aluminium and nickel/aluminium respectively, are taken to be constant in the simulation here and in the numerical studies.

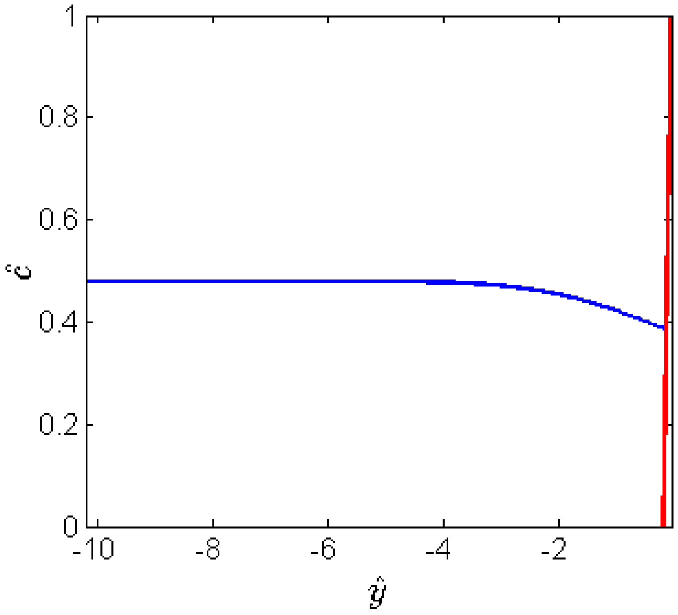

Figure 7.3 – Asymptotic small time solution of problem (7.62) and (7.83) – (7.88) oxygen diffusion limited case. Aluminium concentration profile (blue solid) and oxygen profile (red solid) for parameter values (7.89), $\bar{D}^{oa} = 1000$, $\bar{D} = 3$, $\alpha = 0$.

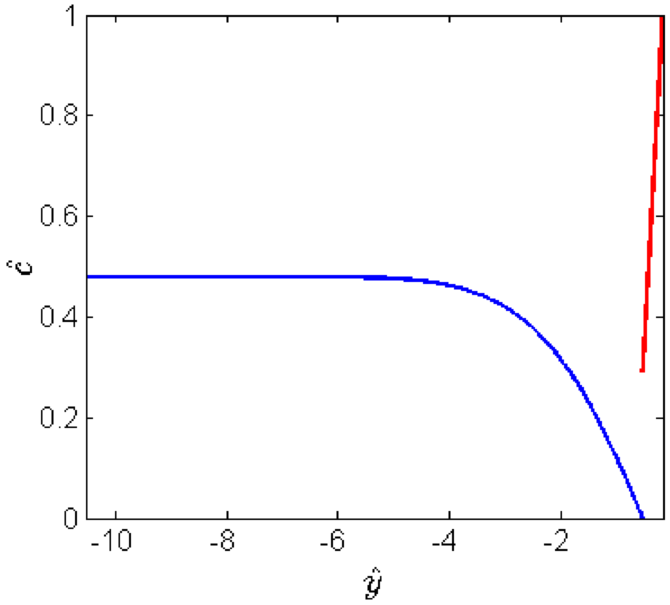

Figure 7.4 – Asymptotic small time solution of problem (7.62) and (7.83) – (7.88) aluminium diffusion limited case. Aluminium concentration profile (blue solid) and oxygen profile (red solid) for parameter values (7.89), $\bar{D}^{oa} = 10000$, $\bar{D} = 3$, $\alpha = 0$.

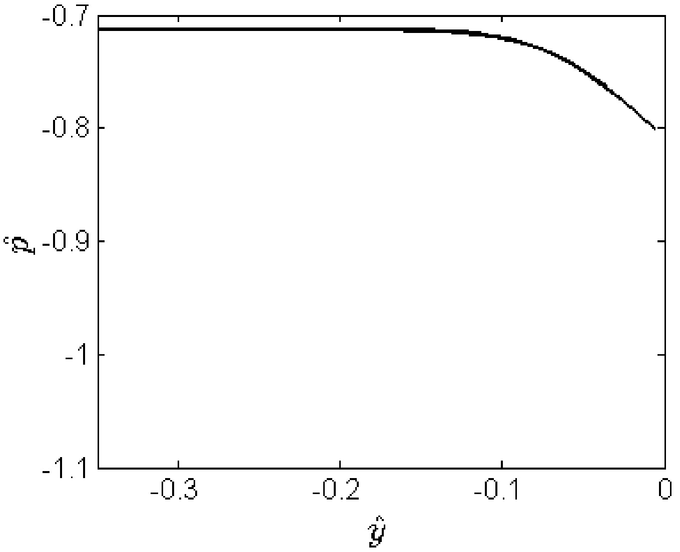

Figure 7.5 – Asymptotic small time solution of problem (7.82) oxygen diffusion limited case. Pressure profile for parameter values (7.89), $\bar{D}^{oa} = 1000$, $\bar{D} = 3$, $\alpha = 0$.

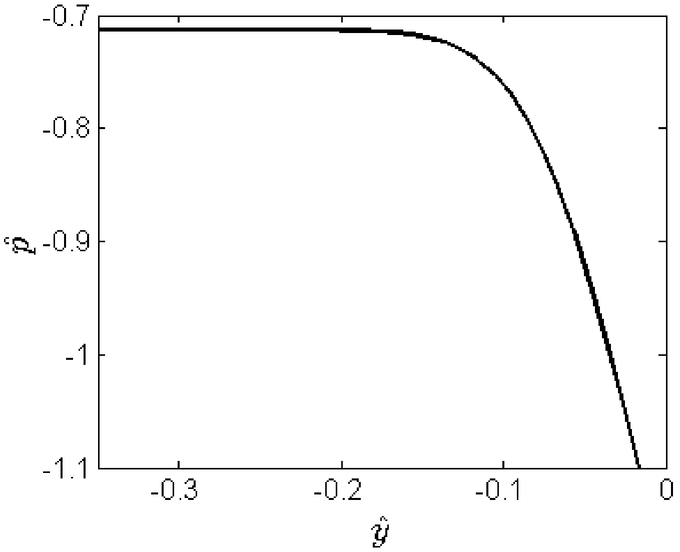

Figure 7.6 – Asymptotic small time solution of problem (7.82) aluminium diffusion limited case. Pressure profile for parameter values (7.89), $\bar{D}^{oa} = 10000$, $\bar{D} = 3$, $\alpha = 0$.

From Figure 7.3-7.6 the initial behaviour of the beta phase oxidation model is revealed by considering the asymptotic analysis for the small time behaviour of problem (7.82) and (7.83) – (7.88). The small time solution is important for numerical solution detailed in Section 7.4 as they serve as the initial conditions. A relative larger value of $\bar{D}^{oa}$ in Figure 7.4 indicates a lower diffusivity value of aluminium that leads to a condition where the oxidation process is controlled by aluminium at the interface, i.e. $\hat{c} = 0,\ at\ \hat{y}_1$. When the value of $\bar{D}^{oa}$ is one order of magnitude smaller, the oxidation process is changed and controlled by oxygen at the interface, i.e. $\hat{c}_o = 0,\ at\ \hat{y}_1$. The small time solution reveals that there is an initial transient period during which aluminium is non-negligible near the boundary $\hat{y} = 0$ and aluminium is able to diffuse over a distance $\hat{y} = O(t^{1/2})$ and also generates a velocity $\hat{v} = O(t^{-1/2})$. Whereas the pressure develops a thin inner layer over a length $\hat{y} = O(t^{1/(n+1)})$ in both cases.

In order to capture full range of possibilities, different values of parameter $\bar{D}\ and\ \alpha$ are chosen, hence the combined effect from nonreciprocal diffusion $\bar{D}$ and oxidation process α to the small time solution under oxygen and aluminium diffusion limited cases is presented in the section below.

7.3.3.1 – Oxygen Diffusion Limited Case

Figure 7.7 gives $\hat{c}$ for different values of $\bar{D}$ *and* α, where Figure 7.7 (b) and (d) are a magnified version of Figure 7.7 (a) and (c) respectively. At the beginning of oxidation, aluminium depletes more near the interface with a faster aluminium diffusion condition ($\bar{D}=1/3$) than for a slower aluminium diffusion condition ($\bar{D}=3$). This seemed reasonable because more aluminium atoms are available for reaction to take place at the interface. However, as the sign of α changes from negative to positive, a slight change in aluminium concentration at the oxidation front occurs for both conditions. Smaller value of $\bar{D}$ meant a faster aluminium diffusion which also indicates nickel does not move relative to aluminium, and this results in increased aluminium consumption when marker (atoms embedded within the alloy region, far away from the interface) moves toward the interface ($\alpha < 0$) than when marker moves in the same direction as the interface ($\alpha > 0$). However, as illustrated in Figure 7.8, there was a critical value range of $\bar{D}$ for which the switch between diffusion controlling process of oxygen and aluminium occurs.

Also, at the interface, the diffusion flux, which was defined from (7.88), indicates a negative α would lead to a positive flux, whereas a positive α would lead to a negative flux that drives the marker away from the interface. The opposite happens with large value of $\bar{D}$, this is because at the interface nickel is assumed not to react with oxygen and the composition gradient in the bond coat ($D_{ni} > D_{al}$) combined with diffusion flux would cause the reaction to search for more aluminium as the interface moves into the bond coat. The diffusion length under both conditions are very similar. Oxygen diffusion via oxide layer occurs linearly and diminishes at the interface as expected.

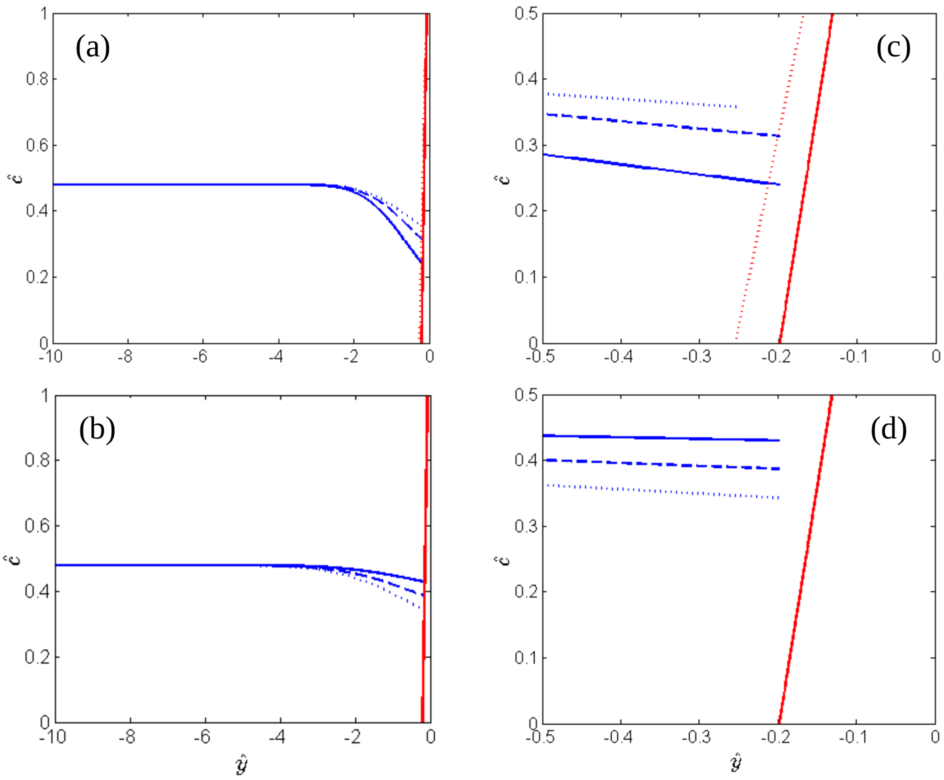

Figure 7.7 – Small time solution for the composition gradient at parameter values of (7.89), (a) $\bar{D} = 1/3,\ \alpha = -1(solid); 0(dashs); 1(dots)$. (b) $\bar{D} = 3,\ \alpha = -1(solid); 0(dashs); 1(dots)$.

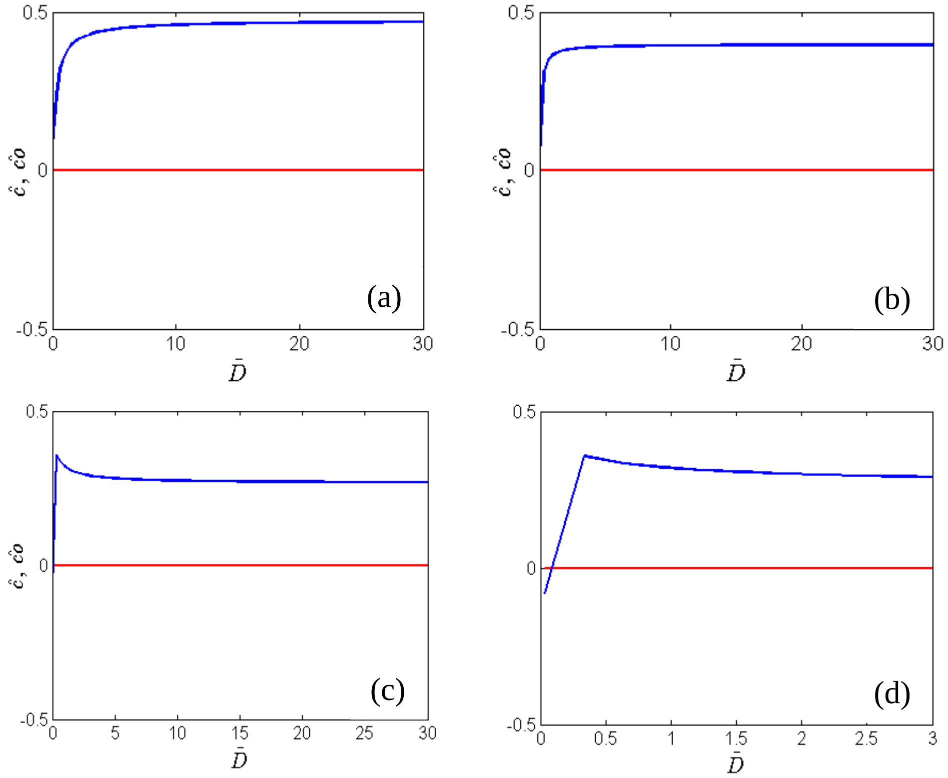

Figure 7.8 – Wide range value of $\bar{D}$ from 1/30 to 30 under oxygen diffusion limited oxidation case. Small time solution of oxygen (red solid) and aluminium (blue solid) at interface. Parameters value of (7.89) and (a) $\alpha = -1$. (b) $\alpha = 0$ (c) $\alpha = 1$. (d) Magnified version $\alpha = 1$.

Figure 7.8 gives small time solution of aluminium and oxygen at interface as a function of $\bar{D}$ which has a value ranging from 1/30 to 30. Figure 7.8 (d) is a magnified version of Figure 7.8 (c). As expected, oxygen remains zero at interface as the oxidation process is limited by the availbility of oxygen at interface. $\bar{D} >> 1$ has no profound affect on the small time solution structure which means no maximum limits for $\bar{D}$. However, with $\bar{D} << 1$ and $\alpha > 0$, a minimum limit is reached in which the solution of aluminium become negative at interface which indicates as aluminium diffusivity decreases, beyond the critical value of aluminium diffusivity the oxidation controlling process would change from oxygen limited to aluminium limited.

7.3.2.2 – Aluminium Diffusion Limited Case

Figure 7.9 gives $\hat{c}$ for different values of $\bar{D}$ *and* α, where Figure 7.9 (b) and (d) are a magnified version of Figure 7.9 (a) and (c) respectively. A relative large value $\bar{D}^{oa}$ causes the reaction front has more oxygen available during the reaction process in which aluminium is consumed completely at the interface. Again, both bond coat conditions are considered here, the most noticeable difference is the oxide thickness, as reflected in Figure 7.11. The small time solution reveals that both upper and lower boundary have advanced further than that of oxygen diffusion limited case at the beginning. Varying the parameter α from negative to positive causes a decrease in initial oxide growth under $D_{Ni}/D_{Al} >> 1$ condition, whereas under $D_{Ni}/D_{Al} << 1$ condition paratemer α causes an increase in initial oxide growth.

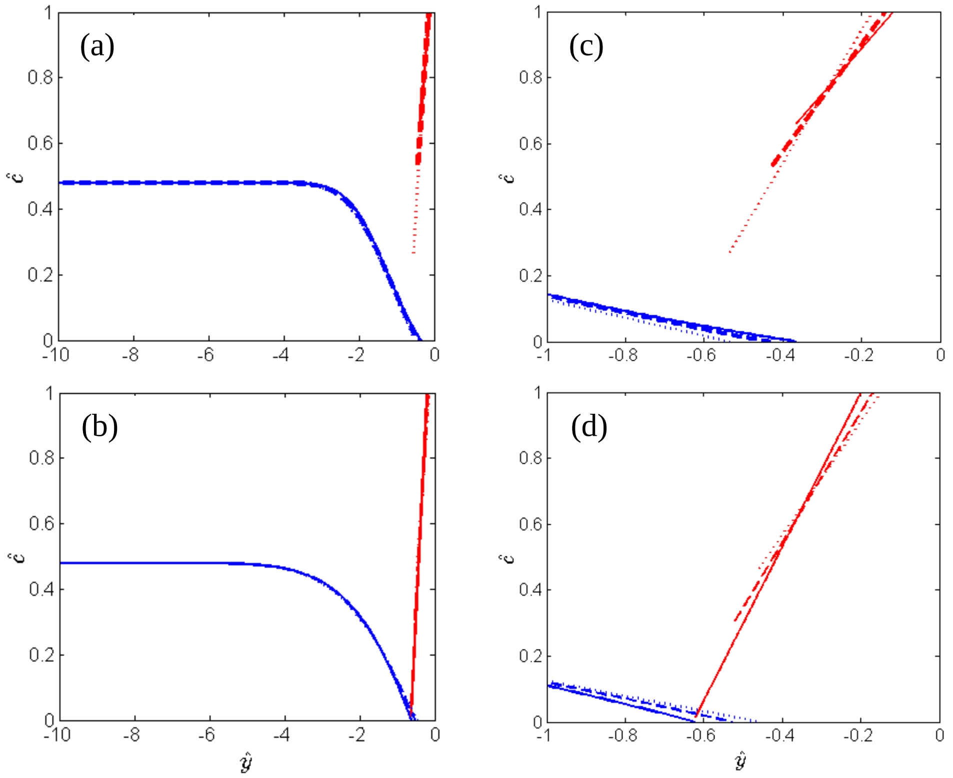

Figure 7.9 – Small time solution for the composition gradient at parameter values of (7.89), (a) $\bar{D} = 1/3$, $\alpha = -1(solid); 0(dashed); 1(dotted)$. (c) $\bar{D} = 3$, $\alpha = -1(solid); 0(dashed); 1(dotted)$.

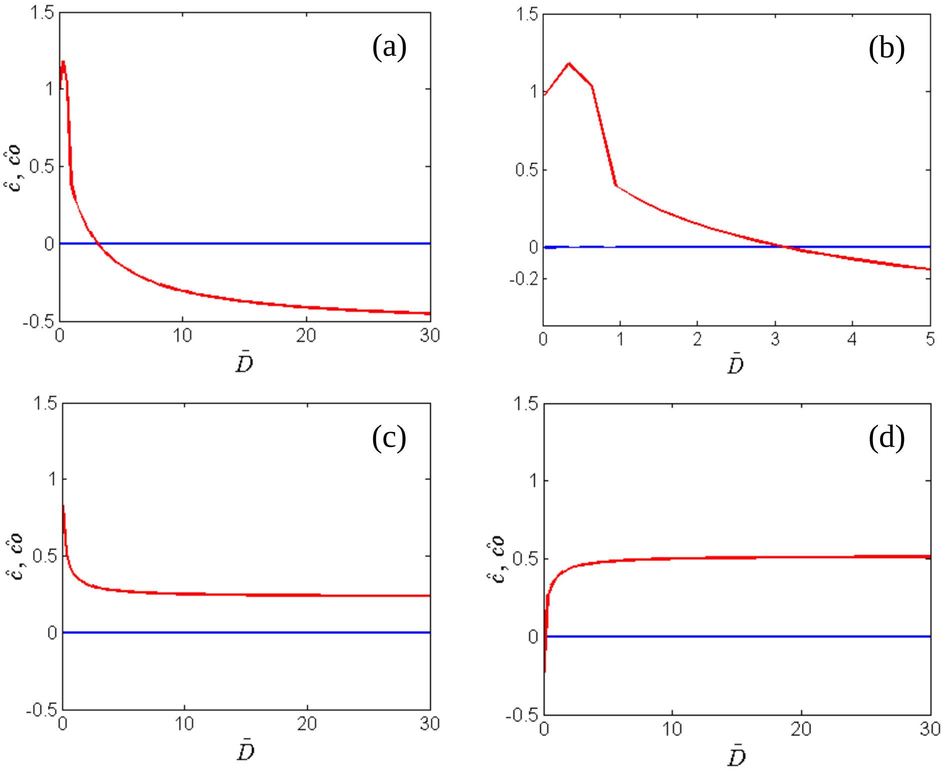

Figure 7.10 – Wide range value of $\bar{D}$ from 1/30 to 30 under aluminium diffusion limited oxidation case. Small time solution of oxygen (red solid) and aluminium (blue solid) at interface. Parameters value of (7.89) and (a) $\alpha = -1$. (b) Magnified version $\alpha = -1$. (c) $\alpha = 0$ (d) $\alpha = 1$.

Figure 7.10 gives small time solution of aluminium and oxygen at interface as a function of $\bar{D}$ which has a value ranging from 1/30 to 30. Figure 7.10 (b) is a magnified version of Figure 7.10 (a). The behaviour of small time solution with varying $\bar{D}$ is different under aluminium limit case to what has been illustrated in Figure 7.8. Aluminium at interface is zero indicating the oxidation process is limited by the availability of aluminium. For $\alpha < 0$, small time solution for oxygen does not satisfy the boundary condition at two values of $\bar{D}$ indicating a maximum and minimum limit for which the switch of oxidation controlling process would occur. Whereas for $\alpha > 0$, only a minimum limit is identified for $\bar{D} << 1$.

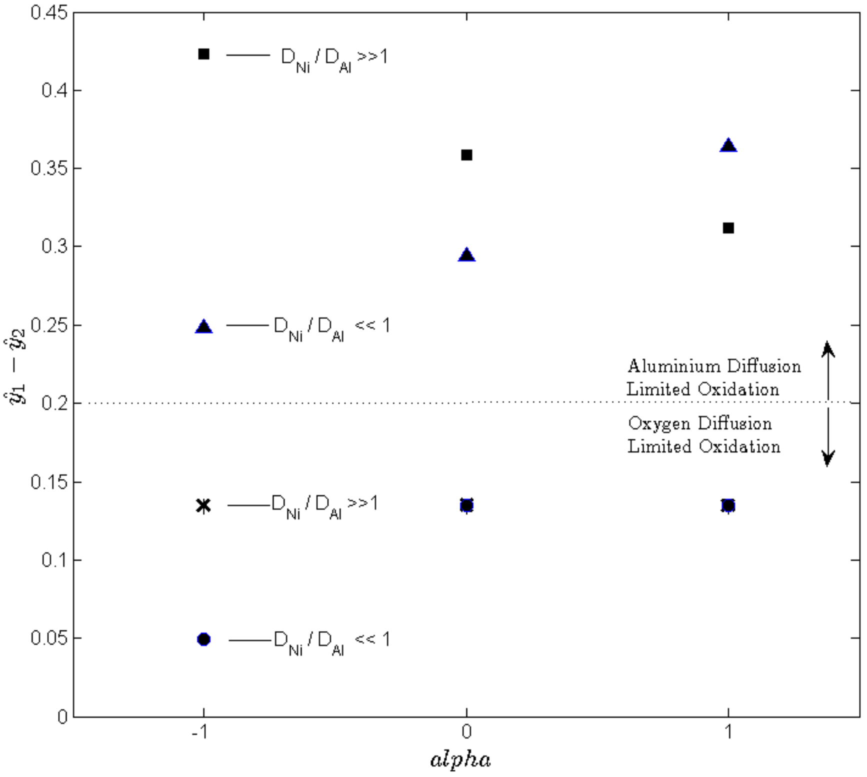

Figure 7.11 – Small time solution of initial oxide thickness for parameter values of $\bar{D} = 3$ & $1/3$, $\alpha = -1, 0, 1$.

7.4 – Numerical Scheme

7.4.1 - Finite Difference Discretization

Upon the completion of small time solution, all the initial values have been effectively established that would be needed for the *O(1)* time solution. In this section, we utilise the finite difference method and Newton's iteration method to solve system of nonlinear partial differential equations. Due to the nature of this diffusion model where two of the boundaries are changing with time, such moving boundary problems is much more difficult to solve. Therefore, one method is often used to solve the one-dimensional problem is to transform the moving boundary into fixed boundary problem where the fixed boundary problem is solved numerically. To do this, two variables have been introduced in oxide and alloy layer, namely Y_+ expression (7.90) and expression Y_- (7.91) with fixed domain with equal intervals from 0 to 1 for oxide region and –L to 0 for alloy region, as shown in Figure 7.12, so that solutions of aluminium concentration, pressure, boundary position and boundary velocity can be obtained.

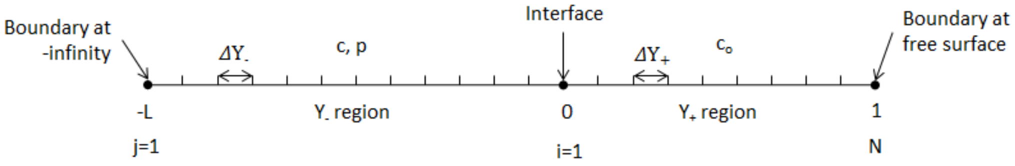

Figure 7.12– Schematic showing the idea behind the finite difference method.

In Figure, physical domain has been discretized into a finite number of points; each segment is denoted as ΔY_- and ΔY_+. The numerical results of dependent variables in alloy region (Y_-), such as aluminium concentration (c) and pressure (p), are to be approximated. In oxide region (Y_+), the dependent variable of oxygen concentration (c_o) is to be approximated.

$$Y_+ = \frac{\overline{y} - \overline{y}_1(t)}{\overline{y}_2(t) - \overline{y}_1(t)},\ \ with\ \ 0 < Y_+ < 1, \tag{7.90}$$

$$Y_- = \overline{y} - \overline{y}_1(t),\ \ with\ \ Y_- < 0. \tag{7.91}$$

where $\overline{y}_1(t)$ is lower boundary, $\overline{y}_2(t)$ is upper boundary and $\overline{y}$ is oxide thickness. Both Y_+ and Y_- are functions of boundary position and time, therefore, equation (7.90) and (7.91) are rewritten in terms of position and time partial derivatives, then become (7.92) and (7.93) for oxide region, (7.94) and (7.95) for alloy region, respectively.

For Y+

$$\left.\frac{\partial}{\partial t}\right|_{\overline{y}} = \left.\frac{\partial}{\partial t}\right|_{Y_+} - \frac{\partial}{\partial Y_+}\left(\frac{\frac{dy_2}{dt} Y_+}{\overline{y}_2(t) - \overline{y}_1(t)} \right), \tag{7.92}$$

$$\left.\frac{\partial}{\partial \overline{y}}\right|_{t} = \frac{1}{\overline{y}_2(t) - \overline{y}_1(t)} \left.\frac{\partial}{\partial Y_+}\right|_{t}. \tag{7.93}$$

For Y-

$$\left.\frac{\partial}{\partial t}\right|_{\overline{y}} = \left.\frac{\partial}{\partial t}\right|_{Y_-} - \frac{d\overline{y}_1}{dt} \left.\frac{\partial}{\partial Y_-}\right|_{t}, \tag{7.94}$$

$$\left.\frac{\partial}{\partial \overline{y}}\right|_{t} = \left.\frac{\partial}{\partial Y_-}\right|_{t}. \tag{7.95}$$

Substitute (7.92) – (7.95) into all relevant dimensionless equations, then (7.44), (7.82) and (7.46) become,

$$\frac{\partial c}{\partial \bar{t}} = \bar{V}^{(1)}\frac{\partial c}{\partial Y_-} + \frac{\partial}{\partial Y_-}\left[1 - c(1-\bar{D})\frac{\partial c}{\partial Y_-}\right] + (1-\bar{D})\frac{\partial}{\partial Y_-}\left[c(1-c)\frac{\partial \bar{p}}{\partial Y_-}\right], \tag{7.96}$$

$$\mathrm{sgn}(\bar{p})\left(\frac{3}{4}\bar{p}\right)^n = (1-\bar{D})\frac{d^2c}{dY_-^{\,2}} + \frac{d}{dY_-}\left[(c+(1-c)\bar{D})\frac{d\bar{p}}{dY_-}\right], \tag{7.97}$$

$$\frac{\partial c_o}{\partial \bar{t}} = \left[\frac{(1-Y_+)(\bar{V}^{(1)} - \bar{v}^{(2)})}{\bar{y}_2(t) - \bar{y}_1(t)}\right]\frac{\partial c_o}{\partial Y_+} + \frac{\bar{D}}{\left(\bar{y}_2(t) - \bar{y}_1(t)\right)^2}\frac{\partial^2 c_o}{\partial Y_+^{\,2}}. \tag{7.98}$$

Corresponding far field and flux boundary conditions for equation (7.96) is given by

$$\bar{c}(-\infty, \bar{t}) = 1, \tag{7.99}$$

$at\ \bar{y} = \bar{y}_1(\bar{\mathrm{t}}),$

$$-\frac{1-c+c\bar{D}}{1-c}\frac{\partial c}{\partial Y_-} + c(\bar{D}-1)\frac{\partial p}{\partial Y_-} = -\frac{4}{3}\left(-\frac{\bar{D}^o}{\bar{\Omega}^{oa}}\frac{\partial c_o}{\partial Y_+}\frac{1}{(\bar{y}_2 - \bar{y}_1)} - \frac{\bar{c}_o}{\bar{\Omega}^{oa}}(\bar{\mathrm{v}}^{(2)} - \bar{V}^{(1)})\right). \tag{7.100}$$

Interface continunity boundary condition for equation (7.97) is given by

$$\left[1 - \bar{D} - \alpha\left(\frac{1-c+c\bar{D}}{1-c}\right)\right]\frac{\partial c}{\partial Y_-} + \left[c + (1-c)\bar{D} - \alpha(1-\bar{D})c\right]\frac{\partial p}{\partial Y_-} = 0. \tag{7.101}$$

Boundary velocity equation (7.51) is given by

$$\frac{d\bar{y}_1}{d\bar{t}} = \bar{V}^{(1)} = \frac{1-c(1-\bar{D})}{1-c}\frac{dc}{dY_-} + (1-\bar{D})c\frac{dp}{dY_-}. \tag{7.102}$$

Oxide internal velocity (7.53) is given by

$$\frac{d\bar{y}_2}{d\bar{t}} = v^{(2)} = \left[\frac{1-c(1-\bar{D})}{1-c} - \bar{\rho}\right]\frac{dc}{dY_-} + (1-\bar{D})c\frac{dp}{dY_-}. \tag{7.103}$$

We can now apply a finite difference scheme to (7.96) – (7.98) and (7.101)-(7.103). Normally when finite difference schemes are applied to moving boundary problems, a fully explicit scheme or a semi implicit scheme is used to treat spatial derivative implicitly and time derivative explicitly. Hence the resulting discretised system of equations is become linear and straightforward to solve. However, one thing needs to bear in mind is that the restriction on the size of time step that can be used in order to maintain the stability. With semi implicit scheme, it does not suffer such constraint. Moreover, semi-implicit scheme lies between implicit and explicit scheme.

For space derivatives, central differencing strategy has been used for first and second order derivatives as shown below

$$\frac{\partial c}{\partial Y_-} \approx \frac{c_{j+1}^{t+\Delta t} - c_{j-1}^{t+\Delta t}}{2\Delta Y_-}, \tag{7.104}$$

$$\frac{d^2 c}{dY_-^{\,2}} \approx \frac{c_{j-1}^{t+\Delta t} - 2c_j^{t+\Delta t} + c_{j+1}^{t+\Delta t}}{\Delta Y_-^2}, \tag{7.105}$$

$$\frac{\partial}{\partial Y}\left(f\frac{\partial c}{\partial Y}\right) \approx \frac{1}{2(\Delta Y_-)^2}\left[(f_{j+1}+f_j)^t(c_{j+1}-c_j)^{t+\Delta t} - (f_j+f_{j-1})^t(c_j-c_{j-1})^{t+\Delta t}\right], \tag{7.106}$$

$$\frac{\partial c_o}{\partial Y_+} \approx \frac{c_{oj+1}^{t+\Delta t} - c_{oj-1}^{t+\Delta t}}{2\Delta Y_-}, \tag{7.107}$$

$$\frac{\partial^2 c_o}{\partial Y_+{}^2} \approx \frac{c_{oj-1}^{t+\Delta t} - 2c_{oj}^{t+\Delta t} + c_{oj+1}^{t+\Delta t}}{\Delta Y_-^2}. \tag{7.108}$$

For time derivatives, forward differencing strategy has been used as shown below,

$$\frac{\partial c}{\partial t} \approx \frac{c_j^{t+\Delta t} - c_j^t}{\Delta t}, \tag{7.109}$$

$$\frac{\partial c_o}{\partial \overline{t}} \approx \frac{c_{oj}^{t+\Delta t} - c_{oj}^t}{\Delta t}. \tag{7.110}$$

A backward difference expression with second order accuracy has been used for the space derivative for boundary conditions in the negative region. They are,

$$\frac{\partial c}{\partial Y_-} \approx \frac{c_{j-2}^{t+\Delta t} - 4c_{j-1}^{t+\Delta t} + 3c_j^{t+\Delta t}}{2\Delta Y_-}, \tag{7.111}$$

$$\frac{\partial p}{\partial Y_-} \approx \frac{p_{j-2}^{t+\Delta t} - 4p_{j-1}^{t+\Delta t} + 3p_j^{t+\Delta t}}{2\Delta Y_-}. \tag{7.112}$$

A forward difference expression with second order accuracy was used for the space derivative for boundary conditions in the posivive region,

$$\frac{\partial c_o}{\partial Y_+} \approx \frac{-3c_{oj}^{t+\Delta t} + 4c_{oj+1}^{t+\Delta t} - c_{oj+2}^{t+\Delta t}}{2\Delta Y_+}. \tag{7.113}$$

Substitution of equation (7.104) – (7.113) into equation (7.96) – (7.103) produce a system of linear equations which, after applying the boundary condition, can be solved efficiently for the variable that we are interested in. For stability purposes, the size of the time increment Δt must be restricted by a stability criterion which is given as,

$$\Delta t >> \Delta x^2 / 2, \tag{7.114}$$

where delta x is the grid spacing. A full discretised system of equations are shown in Appendix B.

7.4.2 - Numerical Experimentation

Numerical simulations, Figure 7.13 and 7.14 confirm the asymptotic analysis in section 7.4, with concentration of aluminium being constant in far field alloy region, while oxygen diffuses linearly across the oxide layer. The model describing the oxidation of beta phase bond coat has three main constant parameters $\bar{D}^{oa}$, $\bar{D}$ and α. The parameters $\bar{D}^{oa}$ is the diffusivity ratio of oxygen and aluminium atoms and is important for determining whether the oxidation process is limited by the supply of aluminium or oxygen at the bond coat and oxide interface. The initial behaviour of varying this parameter has been demonstrated in section below. The parameter $\bar{D}$ is the diffusivity ratio of aluminium and nickel within the bond coat region along with interfacial dimensionless parameter α , both are important for determining the stress state at the interface. The effects of varying these parameters are now carried out. The other physical inputs such as initial aluminium composition, density ratio (Pilling-Bedworth) and the creep exponent are kept constant throughout the experiments and they are assigned values of 0.48 [2], 0.68 and 6 [7] respectively.

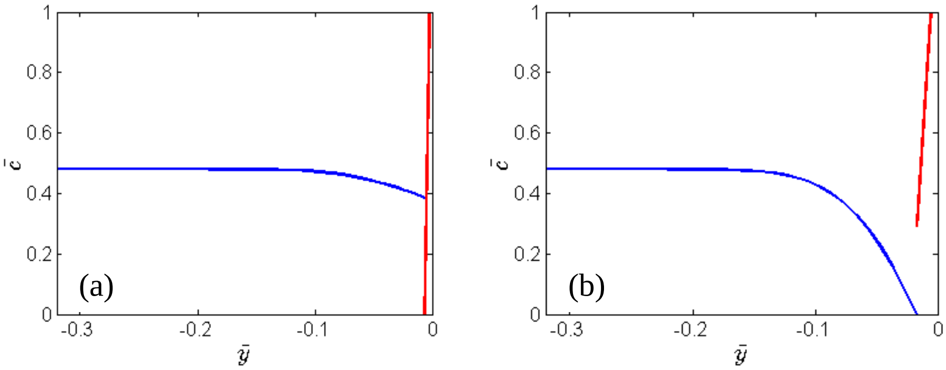

Figure 7.13 – Numerical simulation of the non-dimensionalized model; Aluminium concentration profile (blue solid) and oxygen profile (red solid), (a) $\bar{D}^{oa} = 1000$; (b) $\bar{D}^{oa} = 10000$. for parameter values (7.89), $\bar{D} = 3$, $\alpha = 0$, $t = 0.001$.

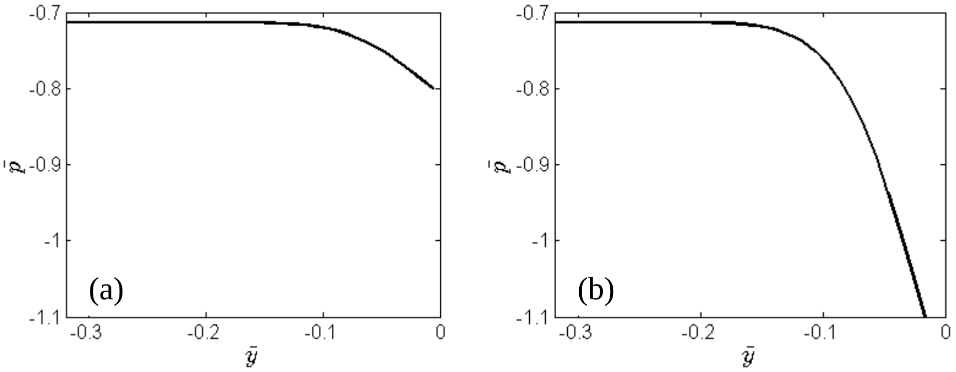

Figure 7.14 – Numerical simulation of the non-dimensionalized model for pressure. (a) $\bar{D}^{oa} = 1000$; (b) $\bar{D}^{oa} = 10000$, for parameter values (7.89), $\bar{D} = 3$, $\alpha = 0$, $t = 0.001$.

7.4.2.1 – The effect of varying $\bar{D}$

It has been previously reported [2] that for nickel rich aluminide beta phase NiAl coating, the intrinsic diffusivites of nickel and aluminium are different in which nickel diffuses faster than aluminium $D_{Ni} \approx 3D_{Al}$. This nonreciprocal diffusion causes atomic planes to shift in order to compensate for net flux vacancies, such phenomenon is often referred as Kirkendall effect [1]. Therefore, two different values, $\bar{D} = 3$ *and* $1/3$ were chosen in order to capture the effect of the nonreciprocal diffusion on stress within the bond coat. The other parameter $\alpha = 0$ is assigned so that the effect from interfacial velocity is ignored. Since $\bar{D}^{oa}$ has no profound effect on qualitative structure of the stress due to oxidation, both aluminium and oxygen diffusion limited oxidation cases are considered.

From varying diffusivity ratio $\bar{D}$, a typical set of concentration profiles is illustrated in Figure 7.15. As expected, in both cases larger value of $\bar{D}$ leads to a faster growth of oxide. The effect of varying $\bar{D}$ is more significant under aluminium limited case, however, the trend of the concentration profile is insensitive to the selected choice of $\bar{D}$. The evolution of the concentration profiles in Figure 7.16 show the dependence of the solution on $\sqrt{t}$. Note that in oxygen limited case, a slight increase of aluminium concentration at the interface for $t<1, \bar{D}>1$ is predicted, whereas for $t<1, \bar{D}<1$ the opposite is predicted. However, for $t>1$ aluminium concentration at interface remains unchanged for both value of $\bar{D}$.

With $\alpha=0$, the boundary condition (7.88) is simplifed and the effect of movement of marker within the alloy is eliminiated, so that the stress generated during oxidation is only caused by the nonrecipocal diffusion between nickle and aluminium. As shown in Figure 7.17, the numerical solution predicted that for large value of $\bar{D}$, a dominant nickel flux causes a mass loss at the bond coat oxide interface which leads to a tensile stress (positive pressure) and the stress changes to compression (negative pressure) over distance into the alloy. Whereas for small value of $\bar{D}$ the dominant aluminium flux causes a mass gain at the interface which results in compressive stress (negative stress) and changes to tensile (positive pressre) over distance into the alloy. These stress states prediction at the interface is similar for both oxidation process cases. Numerical solution in Figure 7.14 shows that for $t<1$, the pressure develops a thin inner layer over a length $\bar{y}=O(t^{(n-1)/2(n+1)})$ near the interface and its width is depended on the creep exponent , n .

However, for $t>1\,\&\,\bar{D}<1$ in Figure 7.18 (a) & (c), pressure decays exponentially with a longer distance into the alloy in which the pressure changes from positive to negative and remains almost constant. Whereas for $\bar{D}>1$ in Figure 7.18 (b) & (d), pressure at the interface changes from positive to negative with increase of time and remains positive in alloy region.

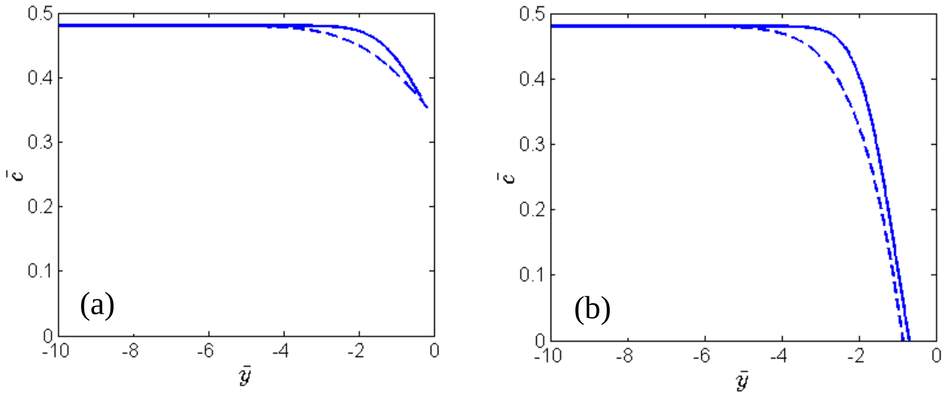

Figure 7.15 – The concentration profile for (a) $\bar{D}^{oa}=1000$, $\bar{D}=1/3(solid)$; $3(dashs)$. (b) $\bar{D}^{oa}=10000$, $\bar{D}=1/3(solid)$; $3(dashs)$. The other parameter values are (7.89), $\alpha=0, t=1$.

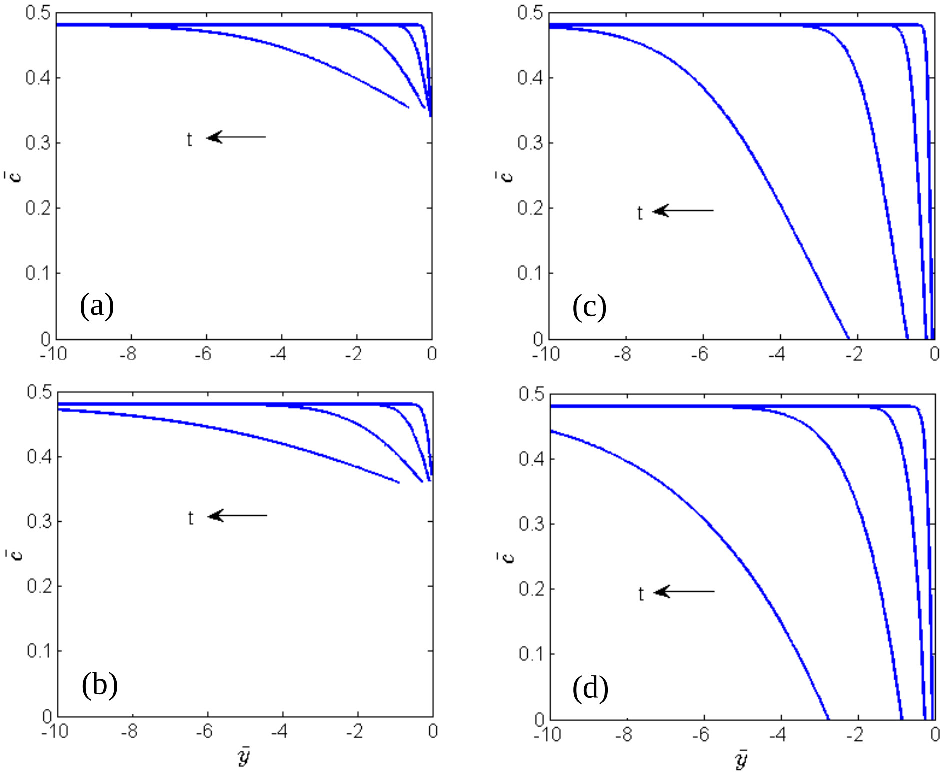

Figure 7.16 – The evolution of the concentration profiles for $t=0.01$, 0.1, 1, 10. with parameter values of (a) $\bar{D}^{oa}=1000$, $\bar{D}=1/3$; (b) $\bar{D}^{oa}=1000$, $\bar{D}=3$. (c) $\bar{D}^{oa}=10000$, $\bar{D}=1/3$; (d) $\bar{D}^{oa}=10000$, $\bar{D}=3$. The other parameter values are (7.89), $\alpha=0$.

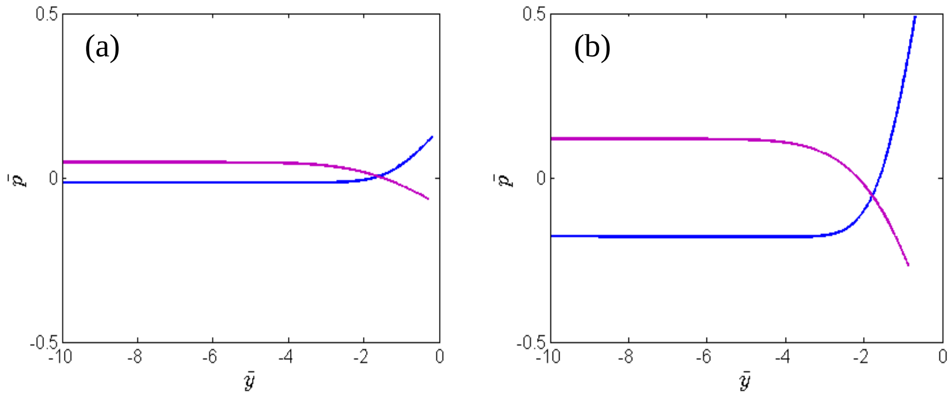

Figure 7.17 – Numerical results for nonreciprocal diffusion induced pressure for (a) $\bar{D}^{oa}=1000$, $\bar{D}=1/3(blue)$; $3(pink)$. (b) $\bar{D}^{oa}=10000$, $\bar{D}=1/3(blue)$; $3(pink)$. The other parameter values are (7.89), $\alpha=0, t=1$.

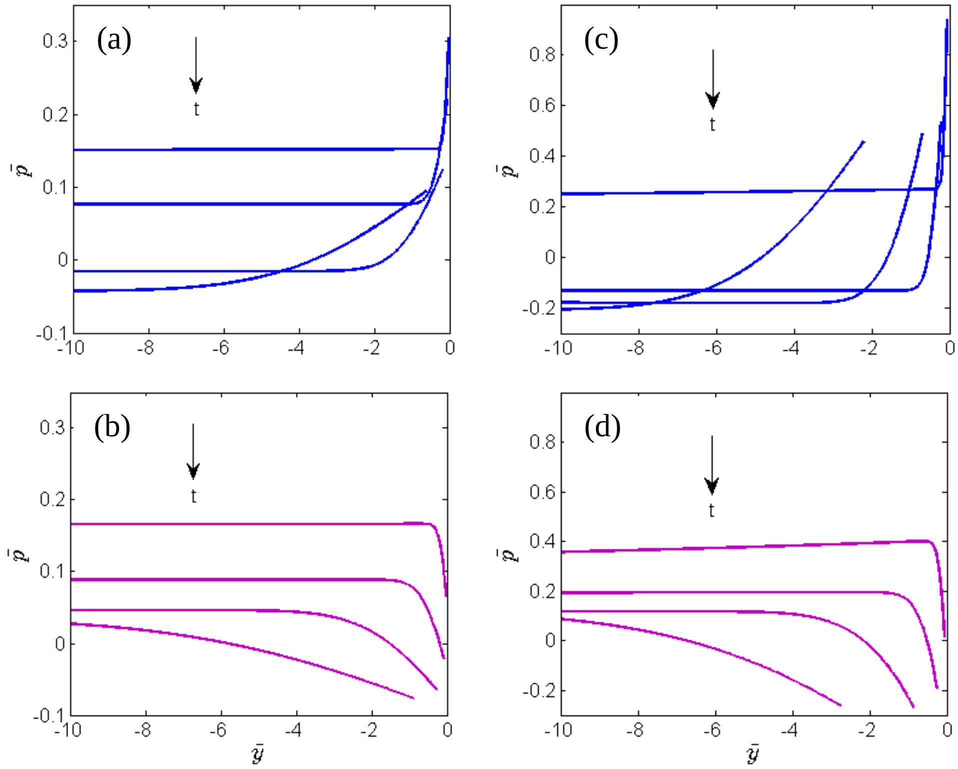

Figure 7.18 – Numerical results for nonreciprocal diffusion induced pressure for $t=0.01, 0.1, 1, 10$. with parameter values of (a) $\bar{D}^{oa}=1000$, $\bar{D}=1/3$; (b) $\bar{D}^{oa}=1000$, $\bar{D}=3$. (c) $\bar{D}^{oa}=10000$, $\bar{D}=1/3$; (d) $\bar{D}^{oa}=10000$, $\bar{D}=3$. The other parameter values are (7.89), $\alpha=0$.

7.4.2.2 – The effect of varying α

The parameter α is a dimensionless constant that relates marker velocity to the boundary velocity through constitutive law. The effect of varying α is examined on the behaviour of concentration and pressure during oxidation of the binary alloy system. In the following comparisons, small and large value $\bar{D}$ with both oxidation limited cases are considered.

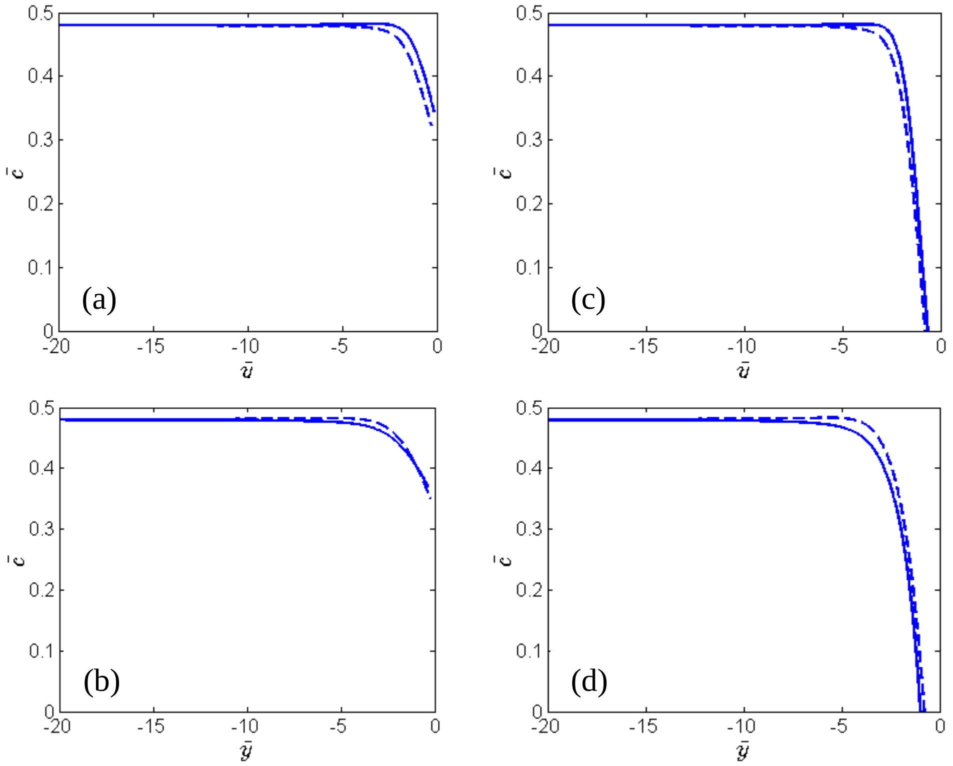

Figure 7.19 – The concentration profile for (a) $\bar{D}^{oa} = 1000$, $\bar{D} = 1/3$, (b) $\bar{D}^{oa} = 1000$, $\bar{D} = 3$, (c) $\bar{D}^{oa} = 10000$, $\bar{D} = 1/3$, (d) $\bar{D}^{oa} = 10000$, $\bar{D} = 3$, The other parameter values are (7.89), $\alpha < 0\,(solid), \alpha > 0\,(dashs)$, $t = 1$.

Figure 7.19 (a) to (d) give the concentration profile comparison between positive and negative α parameter. In each cases, $\bar{D}$ is varied from small to large value representing relative faster and slower diffusion of aluminium within the binary system. Localized increase in aluminium near the interface is predicted for negative α with $\overline{D}=1/3$ and positive α with $\overline{D}=3$. Although the increase in concentration is not dramatic for the paramters chosen in the numerical simulation, it is however clear to see the difference in terms of aluminium concentration profile when $\alpha=0$. Experimentally, localized increase in nickel concentration was observed below the oxide layer in NiTi binary alloy system during high temperature oxidation [8], but to date, experimental determination of parameter α which describes the relative marker displacement to the position of the moving interface with the oxide, especially for NiAl binary alloy system, have not been found. Therefore, in Section 7.6, the results of such experimental study will be discussed.

Figures 7.20 (a)-(d) give the evolution of the concentration profile from the selected parameters and the numerical result has the dependence of the solution on $\sqrt{t}$. In order to demonstrate the effect on localized increase in aluminium by changing parameter α, Figure 7.20 (e)-(h) are the magnified version of of (a)-(d). As aluminium and oxygen diffuse at comparable rate, under aluminium diffusion limited case, where aluminium diffuses faster than oxygen, higher peak of concentration is predicted than it would be otherwise in oxygen diffusion limited case for both negative and positive α. This higher peak in concentration close to the alloy oxide interface can be explained as faster rate of aluminium diffusion causes an accumulation of atoms near the interface during which oxidation is taking place, regardless which direction marker moves relative to the interface.

Figure 7.21 compares the numerical solution for pressure with negative and positive α. From both graphs, the solution structure for positive α is very similar for each are under both oxygen and aluminium diffusion limited cases. Indicating that positive α has a very limited impact to the solution. Quantatively the solution structure with negative α is similar, but the inner layer behaves differently near the interface. Especially in Figure 7.21 (b), a drop in pressure has occurred for $\alpha < 0, \bar{D} > 1$; suggesting aluminium diffusivity combined with α have a certain but limited impact to the pressure near the interface as oxidation proceeds. Unlike when $\alpha = 0$, the change of pressure state along the depth of the alloy has not occurred, as shown in Figure 7.22. For $\alpha < 0$, the pressure is positive which indicates a compressive stress has occurred near the interface and remained compressive as $t > 1$. For $\alpha > 0$, rise of negative pressure indicates a tensile stress near the interface for $t < 1$, the stress decreases and remained tensile as $t > 1$. Both stress decays to zero far away from the interface which satisfied the far field condition, i.e. $d\bar{p}/d\bar{y} \to 0, as\ \bar{y} \to -\infty$. Here, regardless of the value $\bar{D}$, negative α gives a compressive stress that would suppress the void and positive α gives a tensile stress that could be acting as the source of voids formation near/at the interface. Furthermore, it can be seen from the solution that initial stage of oxidation could give rise to void formation, and parameter α seems to be the controlling factor on pressure development during oxidation. Therefore, in order to validate such a finding, an experimental study designed to determine α was carried out and will be detailed in Section 7.7.

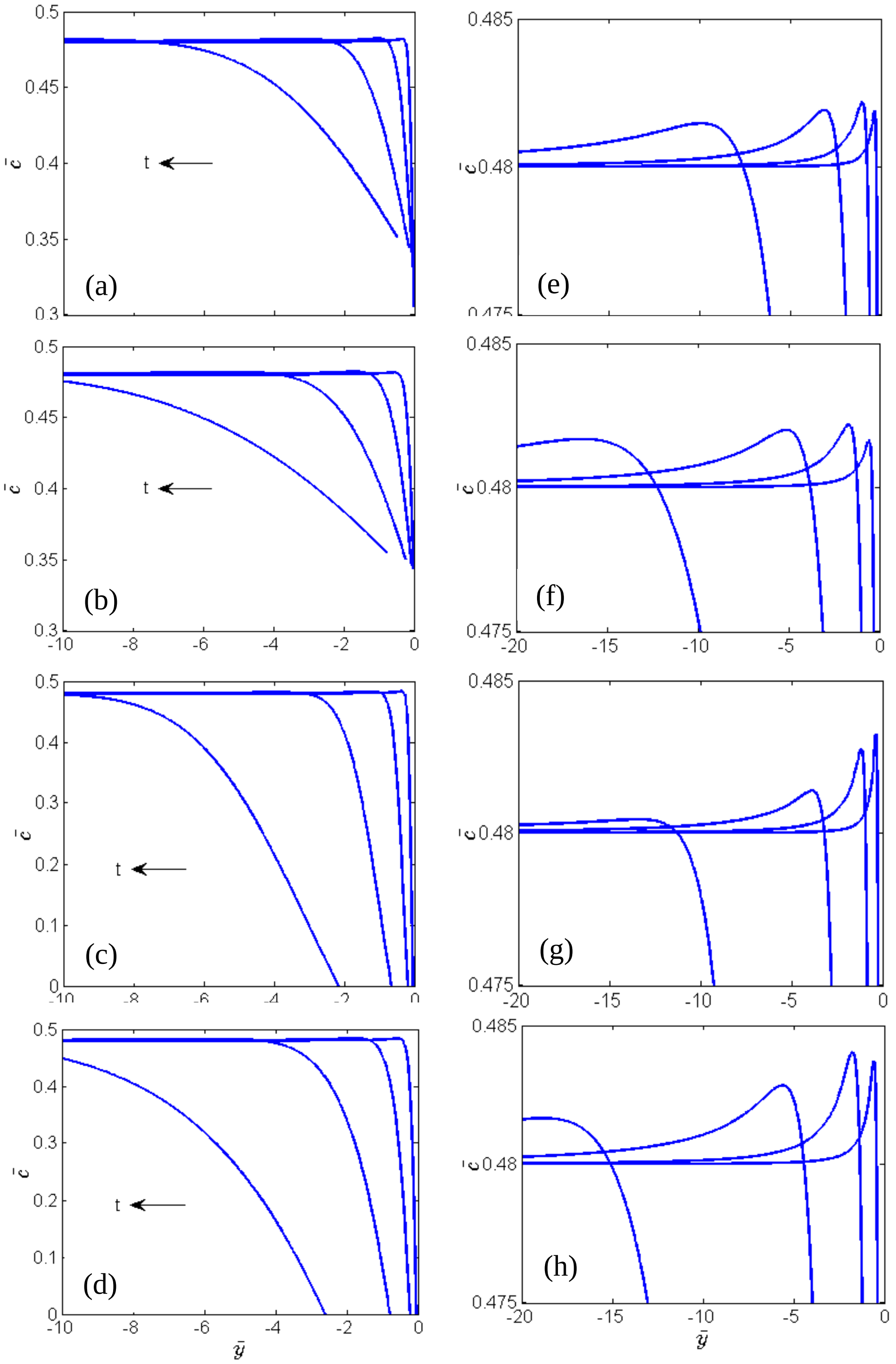

Figure 7.20 – The evolution of the concentration profiles for $t = 0.01, 0.1, 1, 10$. with parameter values of (a) $\bar{D} = 1/3$, $\alpha < 0$. (b) $\bar{D} = 3$, $\alpha < 0$. (c) $\bar{D} = 1/3$, $\alpha > 0$. (d) $\bar{D} = 3$, $\alpha > 0$. The other parameter values are (7.89), (a)-(b) $\bar{D}^{oa} = 1000$, (c)-(d) $\bar{D}^{oa} = 10000$.

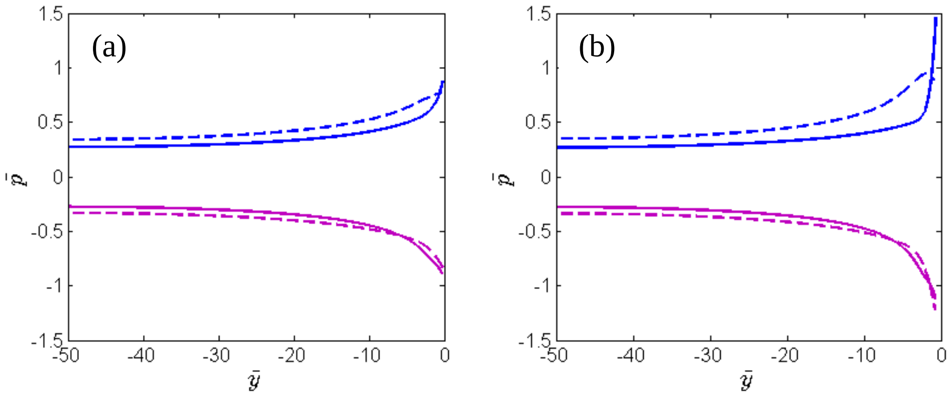

Figure 7.21 – Numerical results for pressure from varying alpha parameter for (a) $\bar{D}^{oa}=1000$, $\bar{D}=1/3(solid)$;$3(dashs)$. (b) $\bar{D}^{oa}=10000$, $\bar{D}=1/3(solid)$;$3(dashs)$. The other parameter values are (7.89), $\alpha=-1(blue),1(pink)$ $t=1$.

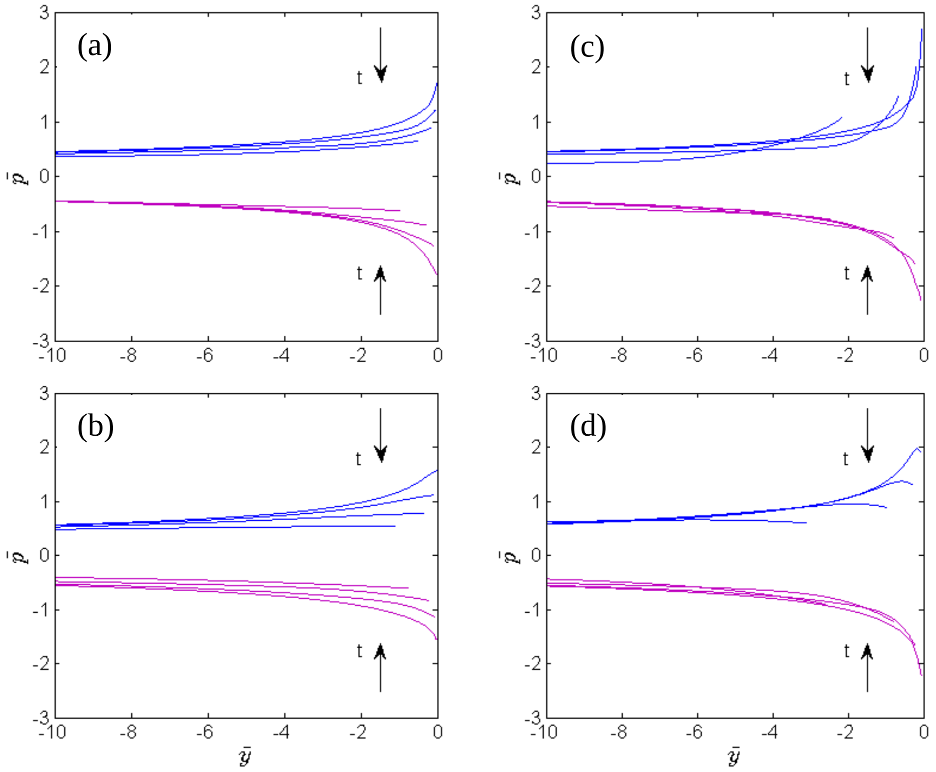

Figure 7.22 – Numerical results for pressure from varying alpha parameter for $t=0.01,\ 0.1,\ 1,\ 10$. (a) $\bar{D}^{oa}=1000$, $\bar{D}=1/3$. (b) $\bar{D}^{oa}=1000$, $\bar{D}=3$. (c) $\bar{D}^{oa}=10000$, $\bar{D}=1/3$. (d) $\bar{D}^{oa}=10000$, $\bar{D}=3$. ; The other parameter values are (7.89), $\alpha<0(blue),\alpha>0(pink)$.

7.5 Experimental Determination of Parameter α

Numerical study in previous section has shown that the stress state near/at the interface strongly depended on the sign of parameter α. Therefore, in order to determine α, an experimental study was carried out in which aluminium oxide particles act as markers were embedded close to the surface in the beta-phase aluminide coating, as shown in Figure 7.23. The manufacturing process has been described in Chapter 3. For comparison purposes, 20 mm in diameter circular samples with 2 mm in thickness were manufactured. The particle embedded sample was sectioned into half using ATM Brillant 220 cutting machine with a BUEHLER AcuThin Abrasive Cut-off wheel, cutting speed was held at 0.005 m/s so that the damage of the sample during cutting can be minimised. After cutting, samples were cleaned in an ultrasonic bath and with acetone. One half was kept as reference and another half was oxidised under isothermal condition at 1100 °C for 50 hours. After oxidation, the sample was mounted using conductive epoxy resin for polishing and characterisation. SEM images were taken at the centre of the sample for consistency. In the follow text, parameter α is determined by looking at the marker displacement relative to the fixed reference site, i.e. sample surface.

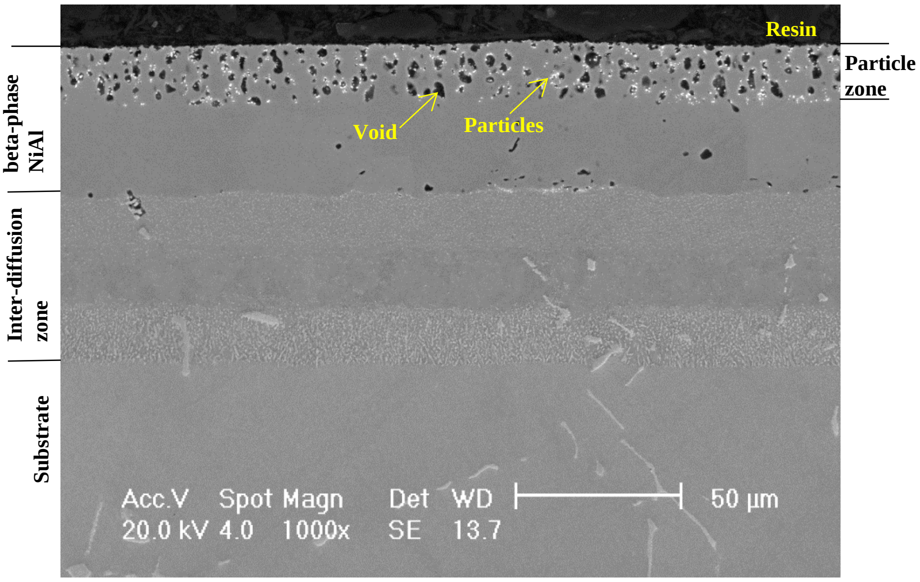

Figure 7.23 – Beta-phase nickel aluminide overlay coating with aluminium oxide particles embedded near the surface before oxidation.

It can be seen from Figure 7.23 that an evenly distributed alumina particle layer with voids near the surface was created after vacuum heat treatment. The formation of voids could be due to:

1. During aluminizing process, fast inward aluminium diffusion leaves vacancies. At the same time, higher nickel content in the coating also diffuses into the lower nickel content substrate. These vacanices hence congregate as more diffuses inward and react with nickel to form beta-phase NiAl.

2. Impurity to crystal structure is introduced when particles deposited on the metallic surface, during aluminizing process, dislocation between crystal structure caused by impurity could also contributed towards void formation.

3. Congregate alumina particles near the surface could fall off to create voids during sample preparation which include cutting, ultrasound cleaning, polishing etc..

Nevertheless, these voids created by the introduction of alumina particles are helpful in the sense that by looking at the behaviour (growth/shrinkage) of voids after oxidation, a better understanding of the stress state near the surface can be achieved from the comparison with the numerical results.

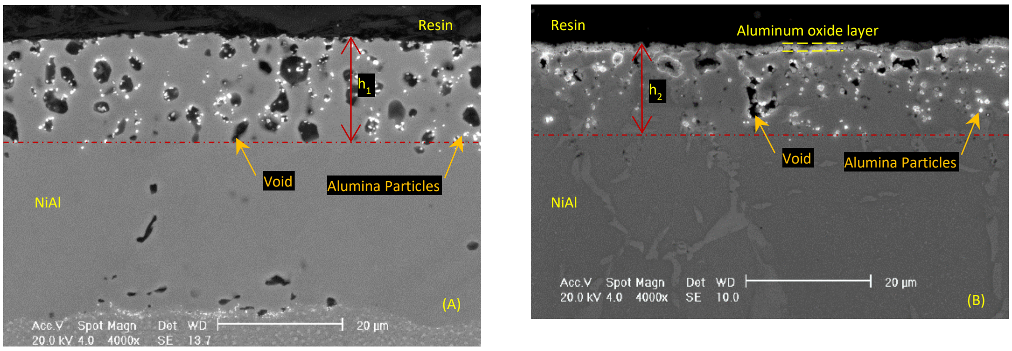

Figure 7.24 – Cross section SEM images of (A) beta-phase nickel aluminide coating with particles; (B) oxidised beta-phase nickel aluminide coating at 1100 °C for 50 hours.

Figure 7.24 gives the comparison between the oxidised and unoxidised beta-phase nickel aluminide coating for determination of parameter α. Both images are re-scaled with the same aspect ratio in order to fit within the text space for direct comparison purposes. Because the sample was sectioned in half, it would be impossible to locate a number of particles at a fixed reference location relative to each other. However, due to the fact the particles are evenly distributed below the surface (Figure 7.23), a bold assumption with confidence can be made on the thickness of particle layer (h_1) in Figure 7.24 (a) is almost the same to the thickness of particle layer (h_2) in Figure 7.24 (b) before oxidation. Therefore, comparison between h_1 and h_2 that yields parameter α can be justitifed. Table 7.1 shows the average thickness of h_1 and h_2 using ImageJ in which the surface of the coating was used for the fixed reference point. It can be seen that the thickness of particle layer is reduced after oxidation indicating a displacement of marker has occurred. Furthermore, as beta-phase nickel aluminide coating is oxidized, aluminium oxide is formed from reaction with oxygen. At the same time the growth of oxide is contributed by the continuous consumption of aluminium in the alloy [9]. Hence, the movement of interface is towards the alloy. Note that from this experiment, markers close to the surface were consumed by the moving oxide interface, as shown in Figure 7.24 (b). A reduction of particle layer thickness after oxidation and inwards movement of oxide strongly indicating that parameter α is negative. This finding is also confirmed from the numerical solution as shown in Figure 7.25.

Table 7.1 – Thickness of particle layer.

	h_1, µm	h_2, µm
Thickness	15.88±1.18	12.68±0.46

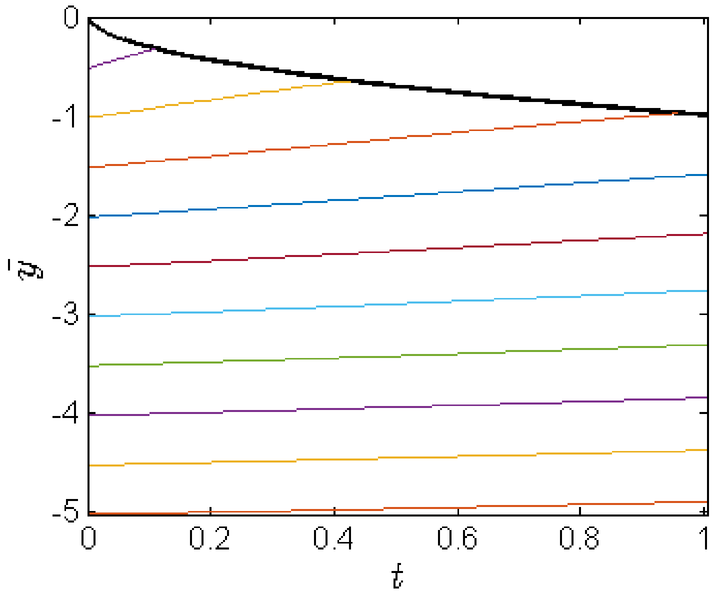

Figure 7.25 – Marker displacement in relation to the oxide lower boundary $\bar{y}_1$ for $\bar{D}^{oa} = 10000$, $\bar{D} = 3$, $\alpha < 0$. The other parameter values are (7.89), $t = 1$.

In Figure 7.25, the coloured solid lines represent the marker distribution near the coating surface, and the black solid line represents the position of oxide lower boundary $\bar{y}_1$ over time. The numerical solution which in conjunction with the finding from the experiment reveals that the thickness of particle layer decreases over time and markers close to the surface vanish due to the moving oxide interface.

Lastly, the experimental study of determination of parameter α is completed by looking at the pressure development near the interface. In Figure 7.24 (b) vanish of voids near the interface after oxidation seems to support the numerical solution in Figure 7.25 where for $\alpha < 0$ compressive stress (positive pressure) suppress voids. However, there are still a number of voids in existence just below the oxide layer. This could be caused by the continuous supply of aluminium (diffusion) towards the interface to form oxide, the motion of aluminium atoms leaves vacancies. Also, the growth of interdiffusion layer strongly indicates that these vacancies are not filled with inwards diffusion of nickel for the duration of oxidation.

7.6 Predicted Growth of Oxide

Thus far, the investigation of the concentration and pressure behaviour is carried out under two distinct oxidation limited processes, namely, oxygen diffusion limited and aluminium diffusion limited. With oxygen diffusion limited case, the oxide scale grows predominantly by aluminium outward diffusion, such oxide growing mechanism is studied experimentally [10] and often occurs during transitional alumina formation (from thermodynamically less stable cubic θ phase, γ phase to the most stable hexagonal α-Al_2O_3 phase) at elevated temperature. Since the transition of alumina has not been taken into account in the mathematical model, only the most stable oxide growth is considered. Experimental study [12, 13] shows that α-Al_2O_3 grows predominantly by oxygen inward diffusion. Therefore, the numerical results generated from aluminium diffusion limited case is better suited for comparison with experiments in terms of oxide thickness. In this section, determination of oxidation kinetics from numerical solution will be discussed and compared with the experimental measurements on two bond coat systems, namely binary β-phase nickel aluminide coating (NiAl) and conventional MCrAlY (NiCoCrAlY).

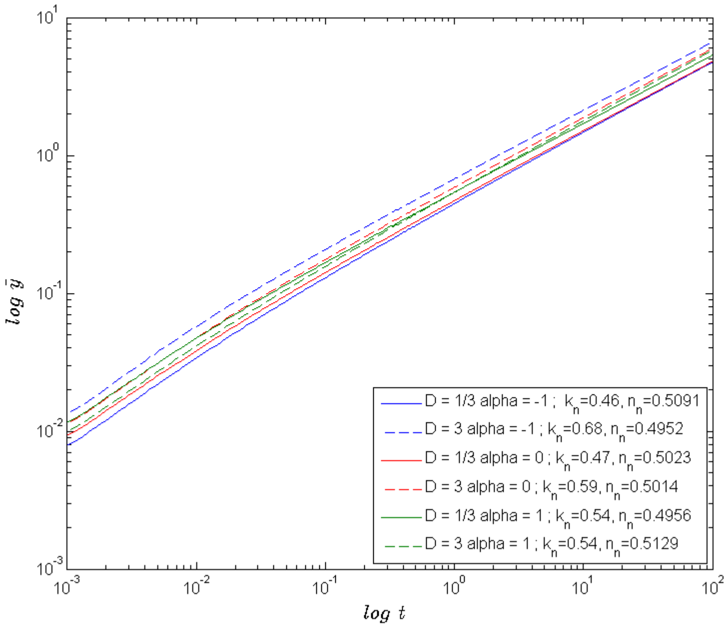

Figure 7.26 – log-log plot of numerical solution demonstrating the growth of oxide scale as a function of time for parameter values of (7.89) and $t = 100$.

The growth of oxide scale as a function of time obtained from numerical solution is shown in Figure 7.26. In order to embrace the full possibilities and demonstrate the effect of varying parameters, values of $\bar{D} = 1/3, 3$ and $\alpha < 0, = 0, > 0$ are considered. k_n and n_n are the numerical parabolic rate constant and exponent respectively. As expected from large t solution that k_n appears to be sensitive to the change of $\bar{D}$. Increase in $\bar{D}$ leads to an increase value of k_n except for when $\alpha > 0$ in which k_n remained constant. In addition, a parabolic law behaviour of oxide growth is predicted with $n_n \approx 0.5$ from linear regression in $t >> 1$ region for all values of $\bar{D}$ and α. This indicates that the effect of parameter variation of $\bar{D}$ and α is insignificant on the large t oxide growth behaviour. However, from the fact that for $t << 1$ initial oxide grows over the range $\hat{y} = O(t^{1/2})$, a slight change in gradient from $t << 1$ to $t = O(1)$ suggests a disturbance to the numerical solution has occurred, as the result this disturbance would have influenced on the overall oxide thickness for $t >> 1$.

7.7 Conclusion

In this chapter, a one-dimensional diffusion reaction model for the oxidation of NiAl alloys has been proposed. The model predicts the growth of oxide at the alloy surface and stress due to nonreciprocal diffusion of aluminum and nickel atom in the interior of the alloy. By solving the boundary value problem for aluminum concentration at small time, the diffusion process between oxygen and aluminum was found to be controlled by the physical parameter $\bar{D}$. A subsequent critical value range of 1/3 to 3 was also found in each diffusion limited cases. Numerical results predicted that the oxide growth obeys a parabolic law behaviour and stress generated in the alloy can be compressive or tensile depending on the parameters of oxidation process & $\bar{D}$. However, in this analysis at small times in particular, the length scale is small which could lead to inaccurate results in the numerical solution for the full system of reaction diffusion equations. Nevertheless, the study that presented in this chapter has set a benchmark for the long-time behaviour of the model in the future.

Reference

1 Smigelskas, A. and E. Kirkendall, Zinc diffusion in alpha brass. Trans. Aime, 1947. 171: p. 130-142.

2 Shankar, S. and L. Seigle, Interdiffusion and intrinsic diffusion in the Ni AI (δ) phase of the Al-Ni system. Metallurgical transactions A, 1978. 9(10): p. 1467-1477.

3 Suo, Z., et al., Stresses induced in alloys by selective oxidation. Acta materialia, 2003. 51(4): p. 959-974.

4 Darken, L.S., Diffusion, mobility and their interrelation through free energy in binary metallic systems. Trans. AIME, 1948. 175(184): p. 41.

5 Prager, S., Diffusion in binary systems. The Journal of Chemical Physics, 1953. 21: p. 1344.

6 Stephenson, G.B., Deformation during interdiffusion. Acta Metallurgica, 1988. 36(10): p. 2663-2683.

7 Pan D, Glynn M, Chen M, Wright PK, Hemker KJ. Evolution of a diffusion aluminide bond coat for thermal barrier coating thermal cycling, 2003, Acta materilalia, Vol 51(8), pp 2205-2217.

8 Chan, C. M., Trigwell, S. & Duerig, T. (1990) Oxidation of an NiTi alloy. Surf. Interface Anal., 15, 349–354.

9 Brumm M W, Grabke H J, oxidation behaviour of NiAl-II cavity formation beneath the oxide scale on NiAl of Different Stoichiometeries. 1993, Corrosion Science, 34, 547-561

10 Jedlinski J, Borchardt G, Mrowec S. 1992. Transport properties of alumina scales on the β-NiAl intermetallic. Solid State Ionics, 50(1-2), pp 67-74.

11 Pint BA, Martin JR, Hobbs LW. 1995. The oxidation mechanism of θ-Al2O3 scales. Solid State Ionics 78:99–107

12 Prescott R, Mitchell DF, Graham MJ. 1994. A study of the growth of α-Al2O3 scales using highresolution imaging secondary ion mass spectrometry. Corrosion 50:62–71

Chapter 8
Discussion

8.1 Numerical results comparison with experiment

Figure 8.1 and Table 8.1 show the comparison between the numerical and experimental results over a period of 500 hours of oxidation in air at 1100 °C. Based on the polycrystals nature of oxide scale, when diffusion is driven by concentration and pressure gradient through grain boundaries, so that the length scale is defined by the grain size [1], $L = d/\sqrt{42}$ where d is the grain size of oxide. Previous studies [2, 3] have shown that transport of reactive species via alumina grain boundary is the main pathway due to the small grain size which is around 2 μm. Therefore, the dimensions for length scale and time scale can be determined as in μm and hours respectively.

As has been reflected in Chapter 7, the predicted oxide growth has a parabolic-law relationship, whereas results from experiments only shown a simple power-law relationship in two regions. The discrepancy in oxidation kinetics and oxide thickness results from the model compared with experiments could be caused by number of conditions.

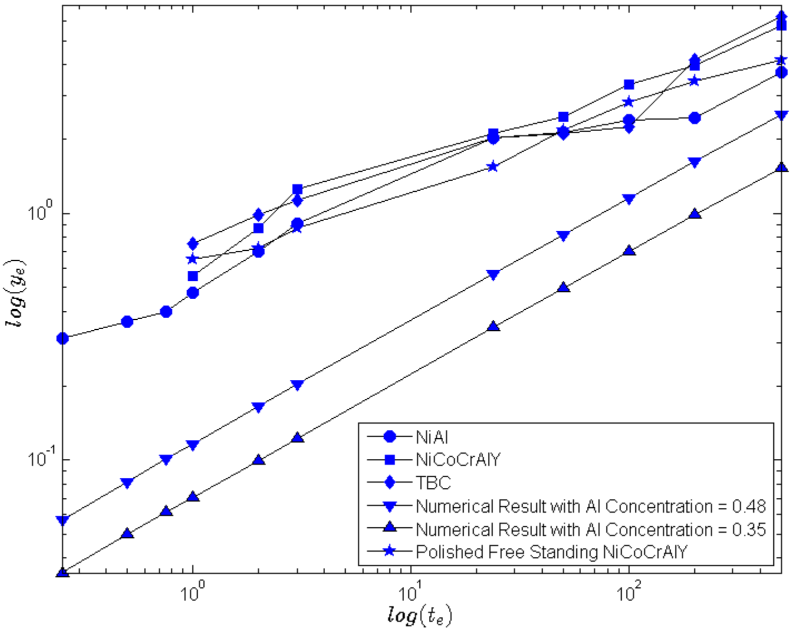

Figure 8.1 – Oxide thickness comparison between numerical and experimental results. Here, NiAl and NiCoCrAlY represent NP-P-3 and Ni-191-4.

Table 8.1 – Summary of oxide thickness measurement on different coating system and results from numerical solution with two values of concentration of aluminium. Here, FS presents Free Standing.

Time , hr	**Oxide Thickness, µm**					
	NP-P-3	Ni-191-4	Surface treated FS Ni-191-4	TBC	Numerical $c_{al} = 0.48$	Numerical $c_{al} = 0.35$
0	0	0	0	0	0	0
0.25	0.31	-	-	-	0.06	0.03
0.5	0.37	-	-	-	0.08	0.05
0.75	0.40	-	-	-	0.10	0.06
1	0.48	0.56	0.65	0.76	0.12	0.07
2	0.70	0.87	0.73	0.99	0.16	0.10
3	0.91	1.26	0.87	1.13	0.20	0.12
24	2.02	2.12	1.55	2.03	0.57	0.34
50	2.12	2.47	2.17	2.12	0.82	0.50
100	2.38	3.32	2.81	2.24	1.15	0.70
200	2.53	3.98	3.45	4.19	1.62	0.99
500	3.74	5.75	4.17	6.30	2.53	1.53

8.1.2 Early stage oxidation behaviour and other oxide formation

As mentioned earlier, the formation of series transit alumina oxide prior to the formation of continues stable α-Al_2O_3 oxide layer could alter the overall oxide growth behaviour. Experimental study has shown that early stage oxide growth exponent for diffusion coating system is 0.22 to 0.38, whereas the oxide growth for small time solution was scaled with $\sqrt{t}$. Other oxide, such NiO, can not be ignored either. From the study done by Brumm and Grabke [4], specially on nickel aluminide coatings, NiO formation during early stage oxidation may have the tendency to react with Al_2O_3 to form a so called spinel oxide, $NiAl_2O_4$. Other study [5] suggested spinel oxide could form initially which allow outward diffusion of cation and formation of unstable θ phase oxide at upper oxide interface. θ phase oxide then transforms to stable α-Al_2O_3 leaving spinel oxide sitting at the alloy/oxide interface. Figure 8.2 shows the observation made on coating surfaces after short oxidation, with large amount of whisker shaped oxide grains, which could indicate the formation of metastable θ-phase oxide on the surface.

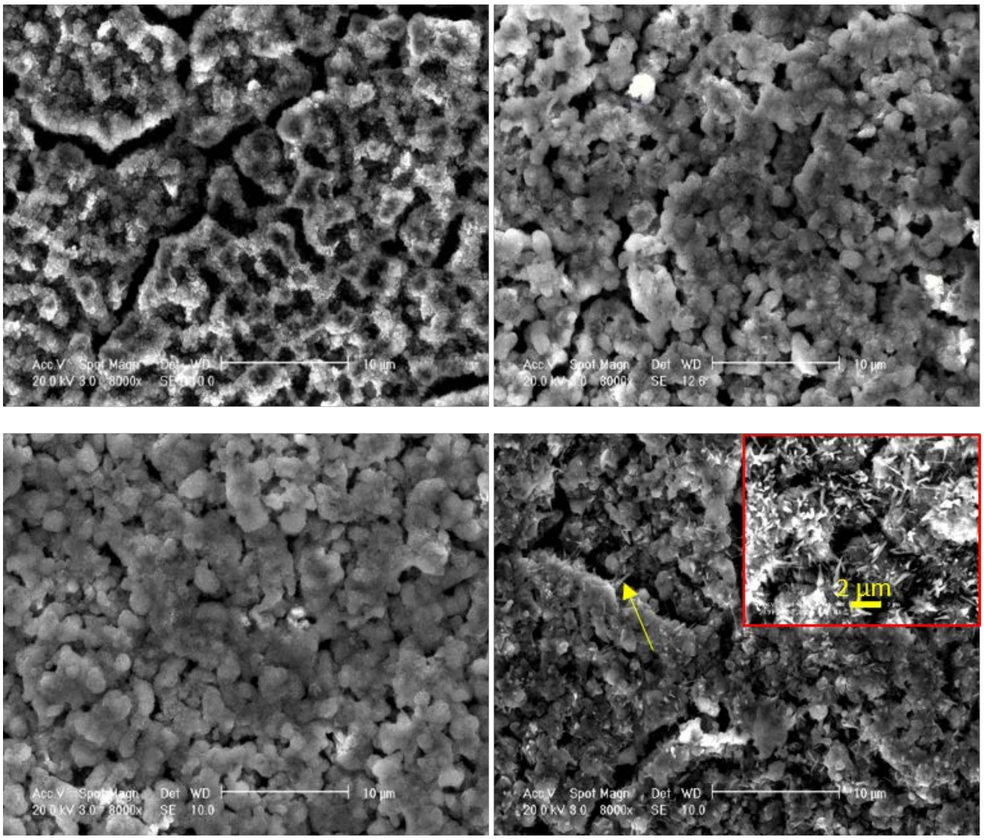

Figure 8.2 - Surface morphology of the oxidized NP-P-3 sample after (a) 15 mins, (b) 30 mins, (c) 45 mins and (d) 1 hour. Whisker shaped oxide grain is indicated by the arrow.

In our mathematical model, reaction equation to describe such oxide transformation has not been considered. Our experimental study on diffusion coating system shows that spinel oxide existed after 15 mins oxidation. Whereas for overlay coating system, a spinel oxide layer on top of α-Al_2O_3 was observed after 100 hours. This unusual top layer spinel oxide layer must be linked to the rapid outward diffusion of Ni, Co and Cr through the oxide layer as well as the aluminium content in at% (atomic%) in the coating matrix [6]. Formation of other oxides can be a consequence of reduction of aluminium to form continuous layer of oxide, thus a reduction of growth rate can be observed.

8.1.3 Oxide porosity

Apart from the formation of spinel oxide that could cause a reduction in the oxide growth, high level pores content within the oxide layer could also lead to formation of cracks. The oxide scale on diffusion coating samples contained appreciable amount of pores which are located on top the continuous α-Al_2O_3 layer after 50 hours oxidation. The formation of these pores could be explained by the rapid oxide formation and phase transformation in the early stage. Studies [7, 8] have shown that the formation of other oxides along with pores could lead to an increase in stress that promotes crack generation and propagation within the oxide layer. For our NP-P series coatings, cracks in the oxide layer were observed after 100 hours and propagated thereafter, spallation of oxide was then observed after 500 hours. A similar crack propagation and spallation was observed for overlay coating system mainly due to spinel oxide formation. From the experimental point of view (Table 8.1) that the oxide layer become unstable when the oxide thickness reaches to 2.5 μm, this value is way below the critical thickness of 5~7 μm as suggested by some studies [9, 10]. This is due to the fact that top ceramic layer was absent during the oxidation. For TBC samples, spallation had occurred after 500 hours with oxide thickness at around 6 μm. From modelling point of view, the results have shown that an increase in aluminium content in the coating system resulting in an increase of oxide growth rate. However, the study [11] on the oxide growth rate as function of composition shown that growth rate decreases with increase aluminium content. This discrepancy maybe due to the fact that constant diffusivity was applied to the numerical simulation. Furthermore, the behaviour of oxide growth could be better understand if there was a large time solution implemented in the simulation. The stability of oxide layer could be further analyzed by formulating a 2-D model.

8.1.4 Oxide moving boundary

It has been described from the model that the aluminium oxide grows solely by the inward depletion of aluminium due to the reaction with oxygen at the interface. This assumption however may be oversimplified [12]. In some cases [13] where the NiAl coating system was exposed at 1200 °C in air, the results shown that oxide scales grown on both the upper and lower boundary. In other words, the growth of oxide is governed by both the inward oxygen grain boundary diffusion and outward aluminium lattice diffusion. This observation can be checked by looking at the oxide microstructure, as shown in Figure 8.3. From the present experimental study of the overlay coating system, the microstructure of the oxide has a combination of a thin outer layer equiaxed grain on top of a thicker inner layer columnar grain adjacent to the coating interface. This type of microstructure orientation confirms that the initial assumption made in the direction of moving oxide boundary seems applicable. Furthermore, since diffusion path within the oxide scale is defined by the oxide grain boundaries, it would be expected that smaller grain size leads to a faster oxide growth. Comparison in oxide grain size was not made in this study, but the results obtained from Chaper 6 section 6.5 oxide thickness development between post surface treated and as-coated surface samples showed that the finer the surface finish of the coating, the lower the growth rate hence, the larger the oxide grain size can be expected, this finding is in close agreement with other studies [14].

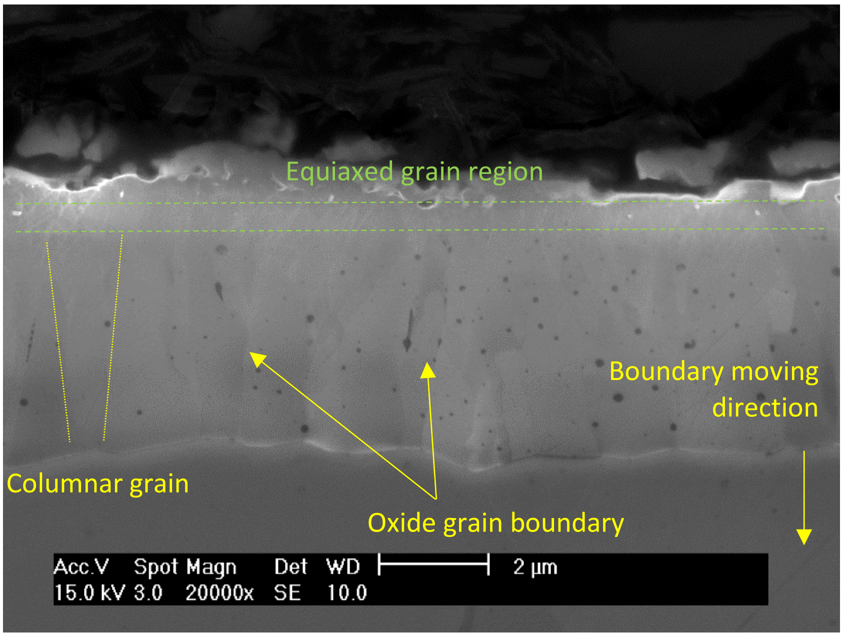

Figure 8.3 – Secondary electron image of oxide mircrosture.

8.1.5 Void formation at the interface

Numerical solution has revealed that the direction of marker displacement dictates the pressure state at the alloy/oxide interface. That is, $\alpha < 0$ leads to $p > 0$ (compression) and $\alpha > 0$ leads to $p < 0$ (tension). Tensile stress favors voids to form at the interface. Results from section 6.6 have suggested voids at the interface are unlikely to form after prolonged oxidiaton based on the determination of α . However, the conclusion reached here so far may be premature. Experiments on oxidation of single β-phase NiAl coating system without particles suggested a change in stress state at the interface due early oxide formation and transformation. Previous study [15] shown that initial transformation of θ to α-Al_2O_3 oxide generates a tensile stress due to volume contraction (mass loss due to dominant nickel flux). Although the magnitude of stress is unknown in the present study, but formation of voids near/at the interface from the first 45 minutes of oxidation may have confirmed that tensile stress was induced by the oxide transformation. Other studies [16,17] show that as transformation continues, the level of stress in newly form stable oxide relaxed to zero. Upon the completion of the transformation, compressive stress is built up in the oxide layer which leads to suppress voids. As demonstrated in Figure 8.4, voids at the interface are vanished after a prolonged oxidiaton. Numerical solution also revealed that a localised concentration of aluminium has occurred with positive or negative α . This however, has not been observed from the present experimental results. In fact, selective oxidation of NiAl leads to a depletion of aluminium along the coating grain boundary, as the result the coating itself become unstable and eventually internal crack formation would lead to failure after long oxidation. Furthermore, it is expected that bulk aluminium content in β-NiAl phase would decrease drastically as the solubility of other alloy elements (i.e. Tungsen, Chromium) from substrate increases during oxidation.

The analysis so far seems to suggest that the influence of parameter α on voids formation may not be as strong as previously thought. In other words, the stress generated at the interface could be solely induced by the non-reciprocal diffusion of individual atoms and relaxed by creep. Furthermore, aluminide nickel rich β-phase NiAl coating system (Table 8.1) used in the present experiments and combined with measured diffusivity data [18] indicate that the diffuvisity of nickel is far greater than that of aluminium ($D_{Ni} / D_{Al} > 1$). Therefore, the predicted stress state at the interface from mathematical model is consistent with the experiemental work, providing $\alpha = 0$, in which the dominant nickel flux causes a tensile stress leads to the initial formation of voids at the interface.

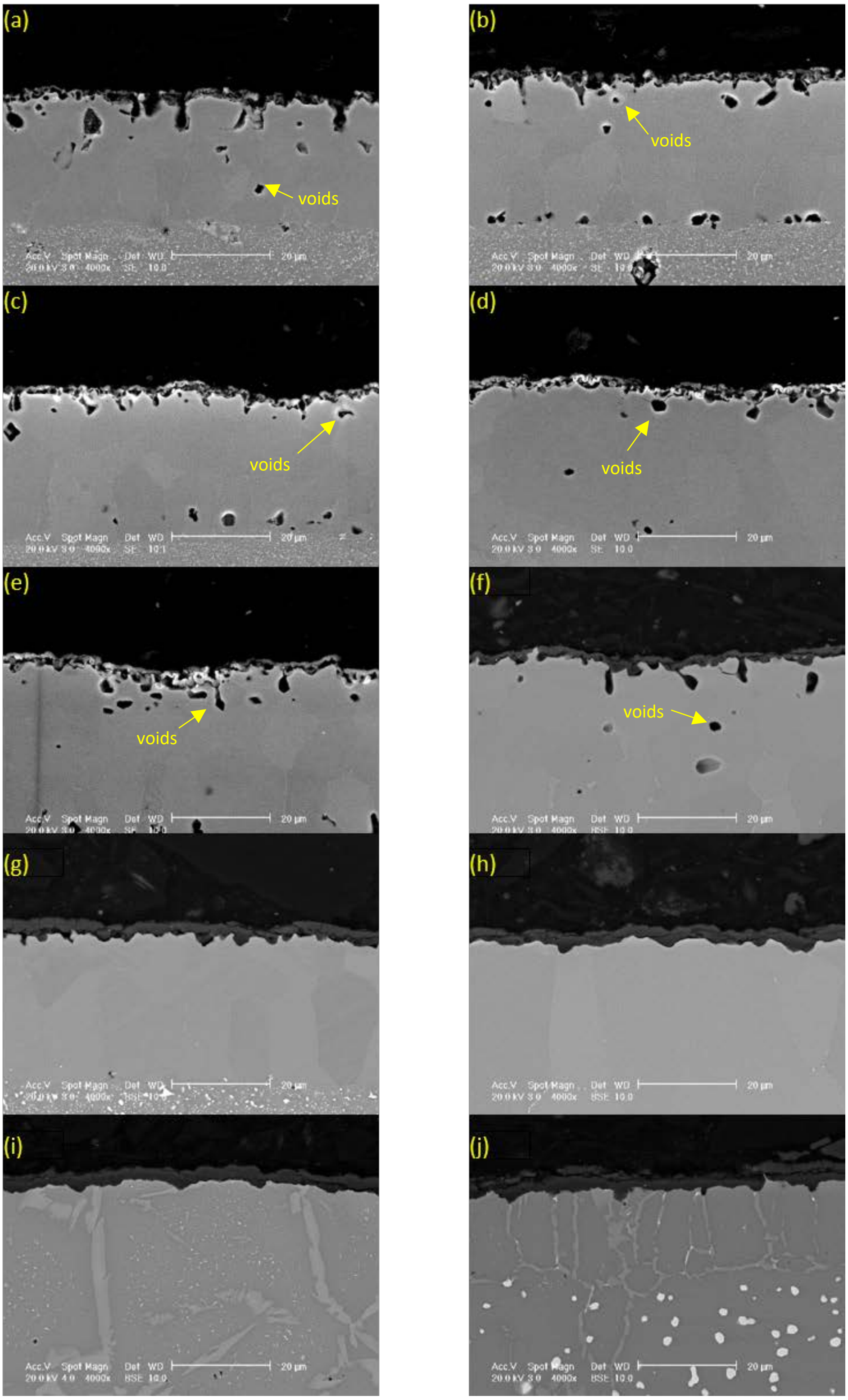

Figure 8.4 – SEM cross section image of single phase β-phase NiAl mictrostructure after (a) 0.25 h, (b) 0.5 h, (c) 0.75 h, (d) 1 h, (e) 2 h, (f) 3 h, (g) 24 h, (h) 50 h, (i) 100 h and (j) 200 h oxidation.

Reference

1 Frost, H. J., and Ashby, M. F., 1982, Deformation-Mechanism Maps, Pergamon.

2 F. H. Stott, High Temperature Corrosion and Protection of Materials 4, Pts 1 and 2, 251-2 19-32 (1997).

3 P. Y. Hou, Journal of the American Ceramic Society, 86, 660-68 (2003).

4 Brumm M W, Grabke H J, Oxidation behaviour of NiAl-II cavity formation beneath the oxide scale on NiAl of Different Stoichiometeries. 1993, Corrosion Science, 34, 547-561

5 Doychak J and Ruhle M, TEM studies of oxidized NiAl and Ni_3Al cross section. Oxid. Metal, 31, 431-452, 1989.

6 Demirkiran. A. S, Elik. E. C, Yargan. Avci. M. E, Oxidation behavior of functionally gradient coatings including different composition o f cermets, Surf. Coat. Technol., 142-144 (2001) 551-556

7 Chen WR, Wu X, Marple BR, Lima RS, Patnaik PC (2008) Preoxidation and TGO growth behavior of an air-plasma-sprayed thermal barrier coating. Surf Coat Technol 02:3787–3796

8 Nijdam TJ, Jeurgens LPH, Sloof WG (2005) Promoting exclusive a-Al2O3 growth upon high-temperature oxidation of NiCrAl alloys: experiment versus model predictions. Acta Mater 53:1643–1653

9 Spitsberg I, More K (2006), Effect of thermally grown oxide(TGO) microstructure on the durability of TBCs with PtNiAl diffusion bond coats. Mater Sci Eng A 417:322–333

10 Chen X, He MY, Spitsberg I, Fleck N, Hutchinson JW, Evans AG (2004) Mechanisms governing the high temperature erosion of thermal barrier coatings. Wear 256:735–746

11 Pettit, F.S, Oxidation mechanism for NiAl alloys at temperatures between 900-1300. AIME Met Soc Trans, 1967, 239, pp 1296-1305.

12 Prescott R, Graham M J, The formation of aluminum oxide scales on high-temperature alloys. Oxidation of Metal 1992, 38, pp 233-254.

13 Pint B, Martin J R, Hobbs, L W, 18 O/SIMS characterization of the growth mechanism of doped and undoped α-Al_2O_3. Oxidation of Metal, 1993, 39, pp 167-195.

14 Tolpygo. V.K, The morphology of thermally grown α-Al_2O_3 scales on Fe-Cr-Al alloys. Oxid. Met., 1999, 51(5), pp 449-477.

15 Hou PY, Paulikas AP, Veal BW. 2007. Stress development and relaxation in Al_2O_3 during early stage oxidation of β-NiAl. Mater. High Temp. 22:373–81

16 Tortorelli PF, More KL, Specht ED, Pint BA, Zschack P. 2003. Growth stress-microstructure relationships for alumina scales. Mater. High Temp. 20:303–10

17 Hou PY, Paulikas AP, Veal BW. 2004. Growth strains and stress relaxation in alumina scales during high temperature oxidation. Mater. Sci. Forum 461–464:671–80

18 Shankar, S. and L. Seigle, Interdiffusion and intrinsic diffusion in the Ni AI (δ) phase of the Al-Ni system. Metallurgical transactions A, 1978. 9(10): p. 1467-1477.

Chapter 9

Conclusion & Future Work

In order to analysis the oxidation behaviour of thermal barrier coating under high temperature isothermal condition, two different types of bond coat systems, namely diffusion coating and overlay coating, manufactured by pack cementation and HVOF techniques were investigated.

Coating matrix produced by traditional pack cementation often results in a beta-phase outer layer with precipitates. During the process development and manufacturing of diffusion coating, a clean coating matrix with a single beta-phase outer layer was successfully obtained by adding a pure nickel layer prior to the aluminizing process. Three sets of diffusion coating samples, NP-P-2, 3, and 4, were produced from a pack cement where aluminium content was varied from 12.5 wt% to 50 wt%. It was found after 200 hour isothermal oxidation that sample produced with lower aluminium content had a higher oxide growth rate.

Isothermal oxidation of three conventional overlay coating systems, Ni-191-4 (NiCoCrAlY), Ni-528 (NiCr6Al) and Dimalloy 400-NS (Ni6Al), revealed the important role of alloy element Cr with low aluminium content in the coating matrix and demonstrated formation of foreign phase, such as spinel oxide, in preference to the most stable α-Al_2O_3. Oxidation kinetics was quantitatively analysed based on the oxide scale growth as a function of exposure time.

The life assessment of a complete thermal barrier coating system in which the ceramic top coating deposited by APS technique was made possible from the development of a low cost and versatile burner rig. Several damage/failure types were identified in comparison with samples tested under isothermal loading. From these test results, the selection of flame fuel and carefully designed calibration procedure of a single wavelength pyrometer was proven to be adequate.

A novel approach of mathematical modelling focusing on the growth of oxide has been carried out in this study. This moving boundary problem describes the growth of oxide coupled with creep and diffusion with no external loading acting in the system. Here the asymptotic behaviour of oxygen/aluminium concentration and pressure in the limit $t \to 0^+$ was analysed. In the small time solution, two distinct diffusion limited oxidation cases were found to be strongly depended on the diffusivity ratio ($\bar{D}^{oa}$) of oxygen and aluminium. In both cases, the diffusivity of aluminium was assumed small compared to that of oxygen, and the asymptotic structure contained a thin aluminium depleted layer near the interface and a uniform aluminium concentration outer region. On the other hand, the asymptotic structure for pressure contained an inner layer whose width is strongly depended on the creep exponent, n, and a slow exponential decaying outer layer. It was also found that large pressure appeared to be assosciated with aluminium diffusion limited oxidation case.

The mathematical model was solved numerically by Newton's iteration method with finite diffierence approximation. In the numerical results, a localized increase in aluminium concentration was predicted for certain parameters in the alloy reigon close to the alloy/oxide interface. However, such finding was inconsistent with the results obtained experimentally since oxide scale growth is caused by the continuous consumption of aluminium at the interface. Furthermore, the oxide growth kinetic predicted from the model follows a parabolic law, whereas experimental results from different types of coating system suggested a simple power law relationship is likely to occur due to number of factors. On the other hand, depending the nonreciprocal diffusion between nickel and aluminium in the alloy, the model predicted that stress state at the interface can be tensile or compressive and relaxed by creep over time. Numerical results obtained from this model had shown a good qualitative agreement from comparison with the experimental studies.

Strictly speaking, our model incorporates the fundamental physical and chemical processes that act in the system, but the overall numerical investigation with comparison to the experimental results demonstrated that the predicted results can still be used in a qualitative way, and as a stepping stone towards a more robust analysis, so that the effect of subtle interplay between physical processes on crack formation and propagation as a function of material properties and environmental variables can be acheived.

Future Work

Furnace thermal cycling oxidation test could be conducted in order to study the oxidation kinetics and microstructure development of the coating systems further. Such test could be carried out by adapting a more rapid heating and cooling to the coated samples, so that the failure of the thermal barrier coating systems could be assessed further.

Oxide microstructure characterization could be analysis further using FIBSEM and TEM technique, so that the effect of oxide grain size and composition on the growth kinetics can be investigated.

A closed loop control condition could be implemented to the oxy-acetylene flame burner rig computer controlled system, so that variation of temperature management in relation to the flame fuel ratio could be achieved with ease. A refinement to the rig structure design, such as protection to thermocouples, would be needed in order to increase the testing repeatability.

From the mathematical modelling prospective, the behaviour of oxide growth could be predicted more accurately by introducing a large time solution in the simulation. The stability of oxide layer based upon the small amplitude of the surface roughness relative to the thickness of the coating system could be further analyzed by formulating a two dimensional model.

Appendix A

Derivation of nonlinear creep expression in the alloy (Region 1). The following expressions are developed in conjunction with reference [34].

In one-dimensional, the velocity marker field is

$$v_{ij} = \frac{dv}{dy}, \quad i = j = 2,\ 0\ otherwise. \tag{A.1}$$

Creep strain rate is

$$d_{ij}^{c} = \frac{2}{3}\frac{dv}{dy}, \quad i = j = 2,\ 0\ otherwise. \tag{A.2}$$

The deviatoric stress is related to the creep stratin rate which expressed as

$$s_{ij} = 2\eta d_{ij}^{c} = \frac{4}{3}\eta\frac{dv}{dy}, \quad i = j = 2,\ 0\ otherwise, \tag{A.3}$$

where η is the viscosity. For nonlinear creep, the viscosity is assumed as a function of the effective creep strain rate which is expressed as

$$d_{e}^{c} = \left(\frac{2}{3}d_{ij}^{c}d_{ij}^{c}\right)^{1/2} = \left(\frac{8}{27}\right)^{1/2}\left|\frac{dv}{dy}\right|. \tag{A.4}$$

The nonlinear viscosity is defined as function of effective creep strain rate which reads

$$\eta = \frac{1}{3B^{1/n}}\left(\frac{1}{\left(\frac{8}{27}\right)^{1/2}\left|\frac{dv}{dy}\right|}\right)^{1-\frac{1}{n}}, \tag{A.5}$$

where B and n are constatnt.

Therefore, from force balance equation (6.12), one dimensional expression is

$$\frac{\partial}{\partial y}\left(\frac{4}{3}\eta\frac{\partial v}{\partial y}\right)-\frac{\partial p}{\partial y}=0. \qquad \text{(A.6)}$$

Integrate once we get,

$$p=\frac{4}{3}\eta\frac{\partial v}{\partial y}, \qquad \text{(A.7)}$$

no stress at free surface, therefore, constant of integration is zero.

By using the definition of viscosity, the pressure equation is expressed as

$$p=\frac{4}{3}\eta\frac{\partial v}{\partial y}\frac{1}{3B^{1/n}}\left(\left(\frac{8}{27}\right)^{1/2}\left|\frac{dv}{dy}\right|\right)^{\frac{1}{n}-1}, \qquad \text{(A.8)}$$

$$\text{let } B_o = p=\frac{1}{3B^{1/n}}\left(\left(\frac{8}{27}\right)^{1/2}\left|\frac{dv}{dy}\right|\right)^{\frac{1}{n}-1}, \qquad \text{(A.9)}$$

hence,

$$p=\frac{4}{3}B_o\frac{dv}{dy}\left(\left|\frac{dv}{dy}\right|\right)^{\frac{1}{n}-1}. \qquad \text{(A.10)}$$

This indicates that the stress is depended on the power of n and the exponential is defined from the material property.

Recall equation (6.9) , the 1D dimensionless expression for the marker velocity field is

$$\frac{d\bar{v}_1}{dy}=(1-\bar{D})\frac{d^2c}{d\bar{y}^2}+\frac{d}{d\bar{y}}\left[\left(c+(1-c)\bar{D}\right)\frac{d\bar{p}}{d\bar{y}}\right], \qquad \text{(A.11)}$$

and

$$p^n=\frac{4}{3}B_o\left|\frac{dv}{dy}\right|^{1/n}\operatorname{sgn}\left(\frac{dv}{dy}\right). \qquad \text{(A.12)}$$

Substitute the derivative of marker velocity $\overline{v}_1$ to the pressure equation yields the nonlinear expression which reads

$$\operatorname{sgn}(\overline{p})\left(\frac{3}{4}\overline{p}\right)^n = (1-\overline{D})\frac{\partial^2 c}{\partial \overline{y}^2} + \frac{\partial}{\partial \overline{y}}\left[c + (1-c)\overline{D}\frac{\partial \overline{p}}{\partial \overline{y}}\right]. \tag{A.13}$$

Appendix B

Discretization of aluminium diffusion equation

$$c_j^t = \left[\frac{\Delta t V^{(1)^t}}{2\Delta Y_{-}} - \frac{\Delta t}{2(\Delta Y_{-})^2}\left(2 - c_j(1-\bar{D}) - c_{j-1}(1-\bar{D})\right) \right] c_{j-1}^{t+\Delta t}$$

$$+\left[1 + \frac{\Delta t}{2(\Delta Y_{-})^2}\left(2 - c_j(1-\bar{D}) - c_{j-1}(1-\bar{D})\right) \right] c_j^{t+\Delta t}$$

$$-\left[\frac{\Delta t V^{(1)^t}}{2\Delta Y_{-}} + \frac{\Delta t}{2(\Delta Y_{-})^2}\left(2 - c_{j+1}(1-\bar{D}) - c_j(1-\bar{D})\right) \right] c_{j+1}^{t+\Delta t}$$

$$-\frac{(1-\bar{D})\Delta t}{2(\Delta Y_{-})^2}\left[c_j(1-c_j) + c_{j-1}(1-c_{j-1}) \right] p_{j-1}^{t+\Delta t}$$

$$+\frac{(1-\bar{D})\Delta t}{2(\Delta Y_{-})^2}\left[c_{j+1}(1-c_{j+1}) + 2c_j(1-c_j) + c_{j-1}(1-\mathrm{c}_{j-1}) \right] p_j^{t+\Delta t}$$

$$-\frac{(1-\bar{D})\Delta t}{2(\Delta Y_{-})^2}\left[c_{j+1}(1-c_{j+1}) + c_j(1-c_j) \right] p_{j-1}^{t+\Delta t}$$

Discretization for pressure

$$\frac{1-\bar{D}}{\Delta Y_{-}^2} c_{j-1}^{t+\Delta t} - \frac{2(1-\bar{D})}{\Delta Y_{-}^2} c_j^{t+\Delta t} + \frac{(1-\bar{D})}{\Delta Y_{-}^2} c_{j+1}^{t+\Delta t}$$

$$+\frac{1}{2(\Delta Y_{-})^2}\left[(c_j + (1-c_j)\bar{D} + c_{j-1} + (1-c_{j-1})\bar{D} \right] p_{j-1}^{t+\Delta t}$$

$$-\frac{1}{2(\Delta Y_{-})^2}\left[(c_{j+1} + (1-c_{j+1})\bar{D} + 2(c_j + (1-c_j)\bar{D}) + c_{j-1} + (1-c_{j-1})\bar{D} \right] p_j^{t+\Delta t} - \frac{3}{4} p_j^{t+\Delta t}$$

$$+\frac{1}{2(\Delta Y_{-})^2}\left[(c_{j+1} + (1-c_{j+1})\bar{D} + c_j + (1-c_j)\bar{D} \right] p_{j+1}^{t+\Delta t} = 0$$

Appendix

Discretization for oxygen diffusion equation

$$c_{oj}^{t} = -\left[\frac{\Delta t}{\Delta Y_{+}^{\,2} (\bar{y}_2 - \bar{y}_1)^{2^t}} + \frac{\Delta t}{2\Delta Y_{+}} \left(\frac{(1 - Y_{+})(\bar{V}^{(1)} - \bar{v}^{(2)})}{\bar{y}_2 - \bar{y}_1} \right) \right] c_{oj+1}^{t+\Delta t}$$

$$+ \left[\frac{2\Delta t \bar{D}^{o}}{\Delta Y_{+}^{\,2} (\bar{y}_2 - \bar{y}_1)^{2^t}} + 1 \right] c_{oj}^{t+\Delta t}$$

$$- \left[\frac{\Delta t \bar{D}^{o}}{\Delta Y_{+}^{\,2} (\bar{y}_2 - \bar{y}_1)^{2^t}} - \frac{\Delta t (1 - Y_{+})(\bar{V}^{(1)} - \bar{v}^{(2)})}{2\Delta Y_{+} (\bar{y}_2 - \bar{y}_1)} \right] c_{oj-1}^{t+\Delta t}$$

Discretization for interfacial continunity boundary condition

$$\frac{1}{2\Delta Y_{-}} \left[1 - \bar{D} - \alpha \left(\frac{1 - c_N + c_N \bar{D}}{1 - c_N} \right) \right] c_{j-2}^{t+\Delta t}$$

$$- \frac{4}{2\Delta Y_{-}} \left[1 - \bar{D} - \alpha \left(\frac{1 - c_N + c_N \bar{D}}{1 - c_N} \right) \right] c_{j-1}^{t+\Delta t}$$

$$\frac{3}{2\Delta Y_{-}} \left[1 - \bar{D} - \alpha \left(\frac{1 - c_N + c_N \bar{D}}{1 - c_N} \right) \right] c_{j}^{t+\Delta t}$$

$$\frac{1}{2\Delta Y_{-}} \left[c_N + (1 - c_N) \bar{D} - \alpha (1 - \bar{D}) c_N \right] p_{j-2}^{t+\Delta t}$$

$$- \frac{4}{2\Delta Y_{-}} \left[c_N + (1 - c_N) \bar{D} - \alpha (1 - \bar{D}) c_N \right] p_{j-1}^{t+\Delta t}$$

$$\frac{3}{2\Delta Y_{-}} \left[c_N + (1 - c_N) \bar{D} - \alpha (1 - \bar{D}) c_N \right] p_{j}^{t+\Delta t} = 0$$

Appendix

Discretization for flux boundary condition

$$-\frac{1}{2\Delta Y_{-}}\left[\frac{1-c_N+c_N\bar{D}}{1-c_N}\right]c_{j-2}^{t+\Delta t}+\frac{4}{2\Delta Y_{-}}\left[\frac{1-c_N+c_N\bar{D}}{1-c_N}\right]c_{j-1}^{t+\Delta t}-\frac{3}{2\Delta Y_{-}}\left[\frac{1-c_N+c_N\bar{D}}{1-c_N}\right]c_{j-1}^{t+\Delta t}$$

$$+\frac{1}{2\Delta Y_{-}}\left[c_N(\bar{D}-1)\right]p_{j-2}^{t+\Delta t}-\frac{4}{2\Delta Y_{-}}\left[c_N(\bar{D}-1)\right]p_{j-1}^{t+\Delta t}+\frac{3}{2\Delta Y_{-}}\left[c_N(\bar{D}-1)\right]p_{j}^{t+\Delta t}$$

$$-\frac{4}{3}\frac{3}{2\Delta Y_{+}}\left[\frac{\bar{D}^o}{\bar{\Omega}^{oa}}\frac{1}{(\bar{y}_2-\bar{y}_1)}+\frac{(\bar{\mathrm{v}}^{(2)}-\bar{V}^{(1)})}{\bar{\Omega}^{oa}}\right]c_{oj}^{t+\Delta t}$$

$$+\frac{4}{3}\frac{4}{2\Delta Y_{+}}\left[\frac{\bar{D}^o}{\bar{\Omega}^{oa}}\frac{1}{(\bar{y}_2-\bar{y}_1)}\right]c_{oj+1}^{t+\Delta t}$$

$$-\frac{4}{3}\frac{1}{2\Delta Y_{+}}\left[\frac{\bar{D}^o}{\bar{\Omega}^{oa}}\frac{1}{(\bar{y}_2-\bar{y}_1)}\right]c_{oj}^{t+\Delta t}=0$$

Discretization for boundary velocity V1

$$\frac{1}{2\Delta Y_{-}}\left[\frac{1-c_N(1-\bar{D})}{1-c_N}\right]c_{j-2}^{t+\Delta t}-\frac{4}{2\Delta Y_{-}}\left[\frac{1-c_N(1-\bar{D})}{1-c_N}\right]c_{j-1}^{t+\Delta t}+\frac{3}{2\Delta Y_{-}}\left[\frac{1-c_N(1-\bar{D})}{1-c_N}\right]c_{j}^{t+\Delta t}$$

$$+\frac{1}{2\Delta Y_{-}}\left[(1-\bar{D})c_N\right]p_{j-2}^{t+\Delta t}-\frac{4}{2\Delta Y_{-}}\left[(1-\bar{D})c_N\right]p_{j-1}^{t+\Delta t}+\frac{3}{2\Delta Y_{-}}\left[(1-\bar{D})c_N\right]p_{j}^{t+\Delta t}-V^{(1)t+\Delta t}_{\;\;j}=0$$

Discretization for oxide internal velocity v2

$$\frac{1}{2\Delta Y_{-}}\left[\frac{1-c_N(1-\bar{D})}{1-c_N}-\bar{\rho}\right]c_{j-2}^{t+\Delta t}-\frac{4}{2\Delta Y_{-}}\left[\frac{1-c_N(1-\bar{D})}{1-c_N}-\bar{\rho}\right]c_{j-1}^{t+\Delta t}+\frac{3}{2\Delta Y_{-}}\left[\frac{1-c_N(1-\bar{D})}{1-c_N}-\bar{\rho}\right]c_{j}^{t+\Delta t}$$

$$+\frac{1}{2\Delta Y_{-}}\left[(1-\bar{D})c_N\right]p_{j-2}^{t+\Delta t}-\frac{4}{2\Delta Y_{-}}\left[(1-\bar{D})c_N\right]p_{j-1}^{t+\Delta t}+\frac{3}{2\Delta Y_{-}}\left[(1-\bar{D})c_N\right]p_{j}^{t+\Delta t}-v^{(2)t+\Delta t}_{\;\;j}=0$$

Discretization for lower and upper boundary, y1 and y2

$$\frac{dy_1}{dt} = V^{(1)}$$

$$\frac{y_1^{t+\Delta t} - y_1^t}{\Delta t} = V^{(1)t+\Delta t}$$

$$y_1^{t+\Delta t} - V^{(1)t+\Delta t}\Delta t = y_1^t$$

$$\frac{dy_2}{dt} = v^{(2)}$$

$$\frac{y_2^{t+\Delta t} - y_2^t}{\Delta t} = v^{(2)t+\Delta t}$$

$$y_2^{t+\Delta t} - v^{(2)t+\Delta t}\Delta t = y_2^t$$

Appendix C

Small time solution

```
function           [c1,ci,co1,sol,xleft,y1_st,y2_st]          =
stsol(do,ci,r,d,coa,alpha,t0,n,Lcons)
%function          [c1,ci,co1,sol,xleft,y1_st,y2_st]          =
stsol(do,ci,r,d,coa,alpha)
set(0,'DefaultFigureWindowStyle','docked')
%==============================================================
====================================================%
sol = [];
xleft=-10;
xright=0;
x = linspace(xleft,xright,1000);
xp = linspace(0,1,500);
%===look for initial value in the limit of ci << 1===%
co1 = -ci^2*3*r/2/do/coa/pi+1;
y1=-8*sqrt(do*coa)*sqrt(1-co1)/3/sqrt(8*r/3);
c0=-4*sqrt(pi*do*coa)*(1-co1)/3/sqrt(8*r/3)+ci;
y2=y1-sqrt(8*r*do*coa*(1-co1)/3);
k=alpha*(c0-ci)/sqrt(pi);

c = c0 +(c0 - ci)*erf(x/2);

%==============================================================
====================================================%
options = bvpset('RelTol',1e-6);
%==============================================================
====================================================%
i=1;
%===solve aluminium diffusion equation===%
if co1<=0 && isempty(sol)
    for ci = ci:0.01:0.35
        if isempty(sol)
            solinit = bvpinit(x,@cinit,[y1 k y2]);
        else
            solinit = sol;
        end
        sol                =                bvp5c(@(y,x,params)
conode(y,x,params,d),@(xa,xb,params)
conbc2(xa,xb,params,alpha,ci,do,r,d,coa),solinit,options);

        c = deval(sol,x);
        Almat(i,:) = c(1,:);
        %mat(i,:)=c;
        c1_con(i)=c(1,end);
        y1_st_con(i) = sol.parameters(3);
        k_con(i)= sol.parameters(2);
        y2_st_con(i) = sol.parameters(1);
        co1_con(i) = 0;

        co_con          =          1-(1-co1_con(end))*erf(((xp-
1)*(y2_st_con(end)-
y1_st_con(end)))/2/sqrt(do))/erf((y1_st_con(end)-
y2_st_con(end))/2/sqrt(do));
        Comat(i,:)=co_con;
        %===Save solution===%
```

```
        %save stsol_con c1_con y1_st_con k_con y2_st_con co1_con
co_con ci
        i=i+1;
    end
else
    for ci = ci:0.01:0.35
        if isempty(sol)
            solinit = bvpinit(x,@cinit,[y1 k y2 co1]);
        else
            solinit = sol;
        end
        sol                =                bvp5c(@(y,x,params)
conode(y,x,params,d),@(xa,xb,params)
conbc(xa,xb,params,alpha,ci,do,r,d,coa),solinit,options);
        c = deval(sol,x);
        Almat(i,:) = c(1,:);
        %mat(i,:)=c;
        c1_con(i)=c(1,end);
        y1_st_con(i) = sol.parameters(3);
        k_con(i)= sol.parameters(2);
        y2_st_con(i) = sol.parameters(1);
        co1_con(i) = sol.parameters(4);

        co_con          =          1-(1-co1_con(end))*erf(((xp-
1)*(y2_st_con(end)-
y1_st_con(end)))/2/sqrt(do))/erf((y1_st_con(end)-
y2_st_con(end))/2/sqrt(do));
        Comat(i,:)=co_con;
        %===Save solution===%
        %save stsol_con c1_con y1_st_con k_con y2_st_con co1_con
co_con ci
        i=i+1;
    end
end
c1 = c1_con(end); co1 = co1_con(end); ci = ci(end); co = co_con;
k = k_con(end);  y1_st = y1_st_con(end); y2_st = y2_st_con(end);

N=1000;
L=10;
clog = log(c(1,:)+d*(1-c(1,:)));
%k = sol.parameters(2);
m = ci+(1-ci)*d;
Y_inner_min = sol.x*t0^(1/(n+1));
Nmin = floor(N*(Y_inner_min+L)/L);
%y0       =       t0^(1/(n+1))*(abs(k)/m*(3/4)^(n/(n-1))*(2*(n-
1)^2/m/(n+1)/4)^(1/(n-1))*(n-1)/2)^(-(n-1)/(n+1));
y0   =   (abs(k)/m*(3/4)^(n/(n-1))*(2*(n-1)^2/m/(n+1)/4)^(1/(n-
1))*(n-1)/2)^(-(n-1)/(n+1));
A0 = zeros(size(x));
A0(1:(Nmin-1)) = Lcons-clog(1:(Nmin-1));
for Num = Nmin:N
    A0(Num)  =  A0(Num-1)-  clog(Num)+clog(Num-1)+k*integral(@(s)
cint(s,sol,d,ci),x(Num-1),x(Num));
end
A1 = ((3/4)^(-n/(n-1))*(2*(n-1)^2/m/(n+1)/4)^(-1/(n-1)));

p = t0^(1/(n+1))*A0 + A1*(y0 - t0^(1/(n+1))*x).^(-2/(n-1));
% %figure(2),plot(x+y1_st,p)
```

```
save stsol x xp c y1_st k y2_st co1 co ci p
%===Plot solution===%
figure(1),plot(x+y1_st,c(1,:),xp*(y2_st-
y1_st)+y1_st,co_con,x+y1_st,p),...
    xlabel('$$-\infty   <---(towards)---\hat{y}---(towards)--->
Interface$$','Interpreter','Latex'),...
    ylabel('$$Concentration               of               Al,
\hat{c}$$','Interpreter','Latex')
 figure(2),plot((x+y1_st)*sqrt(t0),c(1,:),(xp*(y2_st-
y1_st)+y1_st)*sqrt(t0),co_con,(x+y1_st)*sqrt(t0),p),...
%     xlabel('$$\hat{y}$$','Interpreter','Latex'),...
%     ylabel('$$\hat{c}$$','Interpreter','Latex')
grid on
axis tight
drawnow


%================================================================
=====================================================%
function cint = cint(s,sol,d,ci)
cint = zeros(size(s));
N = length(s);
for k = 1:N
    if s(k)>sol.x(1)
        c = deval(sol,s(k),1);
        cint(k) = 1./(c+(1-c)*d)-1/(ci+(1-ci)*d);
    end
end


function v = cinit(x)
ci=0.01;
y1 = -2*ci/sqrt(pi);
c0 = ci*erf(y1/2)/(1+erf(y1/2));
v = [c0+(c0-ci)*erf(x/2)
    (c0-ci)/sqrt(pi)/exp(y1^2/4)];

%================================================================
=====================================================%
function dydx = conode(y,x,params,d)
y1 = params(1);k = params(2);
dydx = [x(2)...
    (-x(2)^2*(d^2-d)/(x(1)+(1-x(1))*d)^2+k*(1-d)^2*x(2)*(x(1)-
x(1)^2)/(x(1)+(1-x(1))*d)^2-k*(1-d)*x(2)*(1-2*x(1))/(x(1)+(1-
x(1))*d)-(y-y1)*x(2)/2)/(d/(x(1)+(1-x(1))*d))]';

%===boundary conditions for c ZERO===%
function res = conbc(xa,xb,params,alpha,ci,do,r,d,coa)
y2 = params(1); k = params(2); y1 = params(3); co1 = params(4);
%where a = -inf and b = 0
erf1 = erf((y2-y1)/2/sqrt(do));
ex1 = exp(-(y1-y2)^2/4/do);
res = [xa(1)-ci...
    xb(1)...
    (-d/(1-xb(1))/(xb(1)+d-xb(1)*d))*xb(2)+k*xb(1)*(d-
1)/(xb(1)+(1-xb(1))*d)+4*sqrt(do)*ex1*coa*(co1-
1)/3/erf1/sqrt(pi)...
    y1-(2*d*xb(2))/(1-xb(1))/(xb(1)+d-xb(1)*d)-2*k*xb(1)*(1-
d)/(xb(1)+(1-xb(1))*d)...
```

```
    erf1*(y2-y1)+(8/3)*r*sqrt(do/pi)*ex1*coa*(co1-1)...
    (1-d-alpha*(1-xb(1)+xb(1)*d)/(1-xb(1))-(1-d)*(xb(1)+d*(1-
xb(1))-alpha*xb(1)*(1-d))/(xb(1)+(1-
xb(1))*d))*xb(2)+k*(xb(1)+d*(1-xb(1))-alpha*xb(1)*(1-
d))/(xb(1)+d*(1-xb(1)))]';

function res = conbc2(xa,xb,params,alpha,ci,do,r,d,coa)
y2 = params(1); k = params(2); y1 = params(3); %co1 = params(4);
%where a = -inf and b = 0
erf1 = erf((y2-y1)/2/sqrt(do));
ex1 = exp(-(y1-y2)^2/4/do);
co1=0;
res = [xa(1)-ci...
    (-d/(1-xb(1))/(xb(1)+d-xb(1)*d))*xb(2)+k*xb(1)*(d-
1)/(xb(1)+(1-xb(1))*d)+4*sqrt(do)*ex1*coa*(co1-
1)/3/erf1/sqrt(pi)...
    y1-(2*d*xb(2))/(1-xb(1))/(xb(1)+d-xb(1)*d)-2*k*xb(1)*(1-
d)/(xb(1)+(1-xb(1))*d)...
    erf1*(y2-y1)+(8/3)*r*sqrt(do/pi)*ex1*coa*(co1-1)...
    (1-d-alpha*(1-xb(1)+xb(1)*d)/(1-xb(1))-(1-d)*(xb(1)+d*(1-
xb(1))-alpha*xb(1)*(1-d))/(xb(1)+(1-
xb(1))*d))*xb(2)+k*(xb(1)+d*(1-xb(1))-alpha*xb(1)*(1-
d))/(xb(1)+d*(1-xb(1)))]';
```

Numerical Solution

```
function                    [c,p,co,y1,y2,v1,v2,y,t]                    =
bvpfd_NoSub(do,ci,r,coa,alpha,d,N,M,tmax,t0,dt0,dt1,dtout,t_fac
tor,n,Lcons,L)
set(0,'DefaultFigureWindowStyle','docked')

format
%==============================================================
====================================================%
Marker_Dist = linspace(-5,-1/2,10);
Marker_Position_1 = Marker_Dist(1);
Marker_Position_2 = Marker_Dist(2);
Marker_Position_3 = Marker_Dist(3);
Marker_Position_4 = Marker_Dist(4);
Marker_Position_5 = Marker_Dist(5);
Marker_Position_6 = Marker_Dist(6);
Marker_Position_7 = Marker_Dist(7);
Marker_Position_8 = Marker_Dist(8);
Marker_Position_9 = Marker_Dist(9);
Marker_Position_10 = Marker_Dist(10);
%==============================================================
====================================================%
%Set up model domain
Y_positive = linspace(0,1,M);           %Oxygen region
Y_negative = linspace(-L,0,N);          %Aluminium concentration
and pressure region
Ndy = Y_negative(2)-Y_negative(1);      %Grid spacing in negative
region
Mdy = Y_positive(2)-Y_positive(1);      %Grid spacing in positive
region
%==============================================================
====================================================%
```

```
%[c1,ci,co1,sol,xleft,y1_st,y2_st]                              =
stsol(do,ci,r,d,coa,alpha); %Call small time solution
[c1,ci,co1,sol,xleft,y1_st,y2_st]                               =
stsol(do,ci,r,d,coa,alpha,t0,n,Lcons); %Call small time solution
%===============================================================
====================================================%
rt = sqrt(t0);
%===============================================================
====================================================%
%Set up initial conditions from small time solution
c = ci*ones(1,N);
%c(Y_negative<(-L+L2)) = c_sub;                   %Concentration
of aluminium in substrate region
c_x_order1 = (Y_negative>xleft*rt);                   %Determine
O(1) region for c y_bar=sqrt(t)*y_hat
c(c_x_order1) = deval(sol,Y_negative(c_x_order1)/rt,1);   % O(1)
solution of aluminium concentration
%===============================================================
====================================================%
%obtain initial value for p
p_x_order1           =           (Y_negative>xleft*(t0^(-(1-
n)/2/(n+1))));    %determine  O(1)  region  for  p  y_bar=t^(-(n-
1)/(2/(n+1))))*y_tilde
% Y_inner_min = sol.x(1)*rt;                             % x-axis
y_bar=sqrt(t)*y_hat
m = ci+(1-ci)*d;
clog = log(c+d*(1-c));
ci_log = log(ci+d*(1-ci));
k = sol.parameters(2);
if n==1
    Y_inner_min = sol.x(1)*rt;
    Nmin = floor(N*(Y_inner_min+L)/L);
    P0 = k/m/sqrt(3/4/m);
    A0 = k*integral(@(s) cint(s,sol,d,ci),0,min(Y_negative));
    Outer_P    =    (rt*P0    +    Lcons    -    ci_log    +
A0).*exp(sqrt(3/4/m)*Y_negative);
    A2 = zeros(size(Y_negative));
    A2(1:(Nmin-1)) = -clog(1:(Nmin-1));
    for Num = Nmin:N
        A2(Num)        =        A2(Num-1)-clog(Num)+clog(Num-
1)+k*integral(@(s)          cint(s,sol,d,ci),Y_negative(Num-
1)/rt,Y_negative(Num)/rt);
    end
    p = Outer_P + A2 + ci_log + A0;
else
    Y_inner_min = sol.x(1)*t0^((n-1)/2/(n+1));
    Nmin = floor(N*(Y_inner_min+L)/L);
    y0 = (abs(k)/m*(3/4)^(n/(n-1))*(2*(n-1)^2/m/(n+1)/4)^(1/(n-
1))*(n-1)/2)^(-(n-1)/(n+1));
    A0 = zeros(size(Y_negative));
    A0(1:(Nmin-1)) = Lcons-clog(1:(Nmin-1));
    for Num = Nmin:N
        A0(Num)      =      A0(Num-1)-      clog(Num)+clog(Num-
1)+k*integral(@(s)                    cint(s,sol,d,ci),t0^(-
(n+1)/2/(n+1))*Y_negative(Num-1),t0^(-
(n+1)/2/(n+1))*Y_negative(Num));
    end
    A1         =         t0^(-1/(n+1))*((3/4)^(-n/(n-1))*(2*(n-
1)^2/m/(n+1)/4)^(-1/(n-1)));
```

```
    p = A0 + A1*(y0 - t0^((n-1)/2/(n+1))*Y_negative).^(-2/(n-1));
end

%===============================================================
=====================================================%
%Marker Velocity
c_prime = (c(3:N)-c(1:N-2))/2/Ndy;
p_prime = (p(3:N)-p(1:N-2))/2/Ndy;
v = (1-d)*c_prime+(d+(1-d)*c(2:N-1)).*p_prime;

%===============================================================
=====================================================%
%y1_st=sol.parameters(1);
y1 = y1_st*rt;
y2 = y2_st*rt;
v1 = y1_st/2/rt;             %obtain initial value for v1
v2 = y2_st/2/rt;             %obtain initial value for v2
%===============================================================
=====================================================%
aldiffltd = (c1(1,end)<=0);     %Define if the case is aluminium
diffusion limited or oxygen diffusion limited
%obtain initial value for co
if aldiffltd
    %co        =        1-(1-co1(end))*erf(((Y_positive-1)*(y2-
y1))/2/sqrt(do)/rt)/erf((y1-y2)/2/sqrt(do)/rt);
    co          =          1-(1-co1).*erf(((Y_positive-1)*(y2-
y1))/2/sqrt(do))/erf((y1-y2)/2/sqrt(do));

else
    %co              =              1-erf(((Y_positive-1)*(y2-
y1))/2/sqrt(do)/rt)/erf((y1-y2)/2/sqrt(do)/rt);
    co   =   1-erf(((Y_positive-1)*(y2-y1))/2/sqrt(do))/erf((y1-
y2)/2/sqrt(do));

end
%===============================================================
=====================================================%
y1out = [0 y1]; y2out = [0 y2];
tplot = [0 t0];
c1out = c(end); co1out=co(1);
pout=p(end);
vout=v(end);
v1out=[v1 v1];
v2out=[v2 v2];
%===============================================================
=====================================================%
%dependent variables
y = [c p co y1 y2 v1 v2];

t = t0; tout = 0; dt=dt0;
rt=[0 sqrt(t)];
ini_cless=c(c<(ci-1e-4));
[row]=size(ini_cless);
ini_Dlength=abs(Y_negative(N-row(2))+y1);
ot=abs(y1-y2);
% %subplot(2,2,1);

figure(3),plot(Y_negative+y1,y(1:N),Y_negative+y1,y((N+1):(2*N)
),...
```

```
     Y_positive*(y2-y1)+y1,y((2*N+1):(2*N+M))),     xlabel('$$-
\infty                  <---(towards)---\bar{y}---(towards)--->
Interface$$','Interpreter','Latex'),ylabel('$$Concentration  of
Al, \hat{c}$$','Interpreter','Latex')
title({'Initial    Condition'    ;    ['Diffusion    Length    =
' ,num2str(ini_Dlength), ',  c at boundary=' num2str(c(end))];...
    ['Oxide  Thickness  =  '  ,num2str(ot)]  ;  ['c  at  boundary='
num2str(c(1,end))];['co at boundary=' num2str(y(2*N+1))];...
    ['p at boundary=' num2str(p(1,end)) , ', n = ',num2str(n) ,
', initial guess of p =' , num2str(Lcons)]})
legend('Al Con','Pressure','Oxygen',-1)
grid on
axis tight
%===============================================================
=====================================================%
%Allocate memory for the matrix and RHS
A = spalloc(2*N+M+4,2*N+M+4,12*N+3*M);
J = spalloc(2*N+M+4,2*N+M+4,N-2);
f = zeros(2*N+M+4,1);
NonLin = zeros(2*N+M+4,1);
tol = 1e-6;
%===============================================================
=====================================================%
%Matrix
while t < tmax

    c_old = y(1:N);
    co_old = y((2*N+1):(2*N+M));
    y1_old = y(2*N+M+1);
    y2_old = y(2*N+M+2);
    v1_old = y(2*N+M+3);
    v2_old = y(2*N+M+4);

    %===========================================================
=========================================================%
    %Boundary value at -L for c
    A(1,1) = 1; f(1) = ci;           %first line of matrix and
RHS
    %===========================================================
=========================================================%
    %for equation 1 involve c and p
    for j = 2:N-1
        A(j,j-1)  =  (-dt*v1_old/2/Ndy+dt*(2-(1-d)*c_old(j)-(1-
d)*c_old(j-1))/2/Ndy^2);
        A(j,j)    =    -(1+dt*(2-c_old(j+1)*(1-d)-c_old(j)*(1-
d))/2/Ndy^2+dt*(2-c_old(j)*(1-d)-c_old(j-1)*(1-d))/2/Ndy^2);
        A(j,j+1)  =  (dt*v1_old/2/Ndy+dt*(2-(1-d)*c_old(j+1)-(1-
d)*c_old(j))/2/Ndy^2);
        A(j,j+N-1)   =   ((c_old(j)*(1-c_old(j))+c_old(j-1)*(1-
c_old(j-1))))*(dt*(1-d)/2/Ndy^2);
        A(j,j+N)  =  -((c_old(j+1)*(1-c_old(j+1))+2*c_old(j)*(1-
c_old(j))+c_old(j-1)*(1-c_old(j-1))))*(dt*(1-d)/2/Ndy^2);
        A(j,j+N+1)   =   (c_old(j+1)*(1-c_old(j+1))+c_old(j)*(1-
c_old(j)))*(dt*(1-d)/2/Ndy^2);
        f(j) = -c_old(j);
    end
```

```
    %=============================================================
==========================================================%
    % Flux continuity

    A(N,N-2)          =          -((1-c_old(N)+c_old(N)*d)/(1-
c_old(N)))*(1/2/Ndy);
    A(N,N-1) = ((1-c_old(N)+c_old(N)*d)/(1-c_old(N)))*(4/2/Ndy);
    A(N,N) = -((1-c_old(N)+c_old(N)*d)/(1-c_old(N)))*(3/2/Ndy);
    A(N,2*N-2)= c_old(N)*(d-1)*(1/2/Ndy);
    A(N,2*N-1)= -c_old(N)*(d-1)*(4/2/Ndy);
    A(N,2*N) = c_old(N)*(d-1)*(3/2/Ndy);
    A(N,2*N+1)         =         -((4*do/3/(y2_old-y1_old))*(-
3/2/Mdy)+(4/3)*(v2_old-v1_old))*coa;
    A(N,2*N+2) = -(4*do/3/(y2_old-y1_old))*(4/2/Mdy)*coa;
    A(N,2*N+3) = -(4*do/3/(y2_old-y1_old))*(-1/2/Mdy)*coa;

    %=============================================================
==========================================================%
    %p=0 at y=-L
    A(N+1,N+1) = 1;
    A(N+1,N+2) = -1;
    %=============================================================
==========================================================%
    %Pressure equation
    for j = 2:N-1
        A(j+N,j-1) = (1-d)/Ndy^2;
        A(j+N,j) = -2*(1-d)/Ndy^2;
        A(j+N,j+1) = (1-d)/Ndy^2;
        A(j+N,j+N-1)  =  (c_old(j)+c_old(j-1)+  (1-c_old(j))*d  +
(1-c_old(j-1))*d)*(1/2/Ndy^2);
        A(j+N,j+N)             =             -((c_old(j+1)+(1-
c_old(j+1))*d+2*(c_old(j)+(1-c_old(j))*d)+c_old(j-1)+(1-
c_old(j-1))*d)*(1/2/Ndy^2)+(3/4));
        A(j+N,j+N+1)    =    (c_old(j+1)+c_old(j)    +    (1-
c_old(j+1))*d+(1-c_old(j))*d)*(1/2/Ndy^2);
        f(j+N) = 0;
    end
    %=============================================================
==========================================================%
    %Interfacial continuity v1=alpha*V1 at y=0
    A(2*N,N-2)      =      (1-d-alpha*((1-(c_old(N)*(1-d)))/(1-
c_old(N))))*(1/2/Ndy);
    A(2*N,N-1)      =      (1-d-alpha*((1-(c_old(N)*(1-d)))/(1-
c_old(N))))*(-4/2/Ndy);
    A(2*N,N)       =       (1-d-alpha*((1-(c_old(N)*(1-d)))/(1-
c_old(N))))*(3/2/Ndy);
    A(2*N,2*N-2)  =  (c_old(N)+d*(1-c_old(N))-alpha*c_old(N)*(1-
d))*(1/2/Ndy);
    A(2*N,2*N-1)  =  (c_old(N)+d*(1-c_old(N))-alpha*c_old(N)*(1-
d))*(-4/2/Ndy);
    A(2*N,2*N)   =   (c_old(N)+d*(1-c_old(N))-alpha*c_old(N)*(1-
d))*(3/2/Ndy);
    %=============================================================
==========================================================%
    if aldiffltd
        %c = 0 at y=0
        A(2*N+1,N) = 1;
        A(2*N+1,2*N+1) = 0;
    else
```

```
        %co = 0 at y=0
        A(2*N+1,N) = 0;
        A(2*N+1,2*N+1) = 1;
    end
    %==========================================================
========================================================%
    %Oxygen diffusion equation
    for j = 2:M-1
        A(2*N+j,2*N+j-1)   =   -(dt*do/Mdy^2/(y2_old-y1_old)^2-
dt*(1-Y_positive(j))*(v1_old-v2_old)/(y2_old-y1_old)/2/Mdy);
        A(2*N+j,2*N+j) = (1+2*dt*do/Mdy^2/(y2_old-y1_old)^2);
        A(2*N+j,2*N+j+1)        =        -(dt*do/Mdy^2/(y2_old-
y1_old)^2+dt*(1-Y_positive(j))*(v1_old-v2_old)/(y2_old-
y1_old)/2/Mdy);
        f(2*N+j) = co_old(j);
    end
    %==========================================================
========================================================%
    %co = 1 at y=1
    A(2*N+M,2*N+M) = 1;
    f(2*N+M) = 1;
    %==========================================================
========================================================%
    %dy1dt = v1
    A(2*N+M+1,2*N+M+1) = 1;
    A(2*N+M+1,2*N+M+3) = -dt;
    f(2*N+M+1) = y1_old;
    %==========================================================
========================================================%
    %dy2dt  = v2
    A(2*N+M+2,2*N+M+2) = 1;
    A(2*N+M+2,2*N+M+4) = -dt;
    f(2*N+M+2) = y2_old;
    %==========================================================
========================================================%
    %for v1
    A(2*N+M+3,N-2) = ((1-c_old(N)*(1-d))/(1-c_old(N)))/2/Ndy;
    A(2*N+M+3,N-1) = -2*((1-c_old(N)*(1-d))/(1-c_old(N)))/Ndy;
    A(2*N+M+3,N) = 3*((1-c_old(N)*(1-d))/(1-c_old(N)))/2/Ndy;
    A(2*N+M+3,2*N-2) = (1-d)*c_old(N)/2/Ndy;
    A(2*N+M+3,2*N-1) = -2*(1-d)*c_old(N)/Ndy;
    A(2*N+M+3,2*N) = 3*(1-d)*c_old(N)/2/Ndy;
    A(2*N+M+3,2*N+M+3) = -1;
    f(2*N+M+3) = 0;
    %for v2
    A(2*N+M+4,N-2) = ((1-c_old(N)*(1-d))/(1-c_old(N))-r)/2/Ndy;
    A(2*N+M+4,N-1) = -2*((1-c_old(N)*(1-d))/(1-c_old(N))-r)/Ndy;
    A(2*N+M+4,N) = 3*((1-c_old(N)*(1-d))/(1-c_old(N))-r)/2/Ndy;
    A(2*N+M+4,2*N-2) = (1-d)*c_old(N)/2/Ndy;
    A(2*N+M+4,2*N-1) = -2*(1-d)*c_old(N)/Ndy;
    A(2*N+M+4,2*N) = 3*(1-d)*c_old(N)/2/Ndy;
    A(2*N+M+4,2*N+M+4) = -1;
    f(2*N+M+4) = 0;

    %==========================================================
========================================================%
    %solve the equation
    error = 1e12;
    iter = 0; itermax = 10;
```

```
    yold = y;
    while (error>tol)&&(iter<itermax)
        for j = (N+3):2*N
            J(j-1,j-1) = -n*(abs(y(j-1))).^(n-1)*(3/4)^n+3/4;
        end
        NonLin((N+2):(2*N-1))       =       -sign(y((N+2):(2*N-
1))).*(abs(y((N+2):(2*N-1)))).^n*(3/4)^n+3/4*y((N+2):(2*N-1));

        dy=(A+J)\(f-NonLin-A*y');
        y = y+dy';
        error = norm(dy);
        iter = iter+1;
        disp(error)
    end
    %check if c at y=y1

    if y(N)<0
        y = yold;
        aldiffltd = 1;
    else

        drawnow
        %=====================================================
==============================================================%
        %Initial Marker Velocity v
        c_prime = (y(3:N)-y(1:N-2))/2/Ndy;
        p_prime = (y((N+3):(2*N))-y((N+1):(2*N-2)))/2/Ndy;
        v = (1-d)*c_prime+(d+(1-d)*y(2:N-1)).*p_prime;
        v_marker = interp1(Y_negative(2:N-1),v,Marker_Dist);

        %save NumData tplot y1out y2out c1out co1out pout v1out
v2out vout t
        %=====================================================
=====================================================%
        t = t+dt; tout = tout+dt;   %rt=sqrt(t);
        rt=[rt sqrt(t)]; %rt_plot = [ rt];
        y1out = [y1out y(end-3)];     y2out = [y2out y(end-2)];
tplot = [tplot t];
        c1out = [c1out y(N)];         co1out=[co1out y(2*N+1)];
pout=[pout y(2*N)];    v1out= [v1out y(end-1)];
        v2out = [v2out y(end)];      vout = [vout v(end)];
        %=====================================================
=====================================================%
        %save NumData2 tplot y1out y2out c1out co1out pout v1out
v2out vout t
        Marker_Dist = Marker_Dist+dt*(v_marker-y(end-1));
        Marker_Position_1 = [Marker_Position_1 Marker_Dist(1)];
        Marker_Position_2 = [Marker_Position_2 Marker_Dist(2)];
        Marker_Position_3 = [Marker_Position_3 Marker_Dist(3)];
        Marker_Position_4 = [Marker_Position_4 Marker_Dist(4)];
        Marker_Position_5 = [Marker_Position_5 Marker_Dist(5)];
        Marker_Position_6 = [Marker_Position_6 Marker_Dist(6)];
        Marker_Position_7 = [Marker_Position_7 Marker_Dist(7)];
        Marker_Position_8 = [Marker_Position_8 Marker_Dist(8)];
        Marker_Position_9 = [Marker_Position_9 Marker_Dist(9)];
        Marker_Position_10        =        [Marker_Position_10
Marker_Dist(10)];
        %=====================================================
==============================================================%
```

```
        %Plot
        if (tout>=dtout)
            save data y y1out y2out tplot t pout Y_negative

            Ex_cless=c_old(c_old<(ci-1e-4));
            [row]=size(Ex_cless);
            Ex_Dlength=abs(Y_negative(N-row(1))+y1);

            %subplot(2,2,2);
            figure(4)
            %subplot(2,1,1)

plot(Y_negative+y1,y(1:N),Y_negative+y1,y((N+1):(2*N)),Y_positi
ve*(y2-y1)+y1,y((2*N+1):(2*N+M)))
            xlabel('$$-\infty        <---(towards)---\bar{y}---
(towards)---> Interface$$','Interpreter','Latex'),...
                ylabel('$$Concentration         of          Al,
\hat{c}$$','Interpreter','Latex')
            %legend('Al Con','Pressure','Oxygen',-1)
%               title({['Time = ' num2str(t) ',c at boundary='
num2str(y(N))] ; ['co at boundary=' num2str(y(2*N+1))];...
%                ['Diffusion Length = ' ,num2str(Ex_Dlength),]})
            grid on

            tout = tout-dtout;

            subplot(2,1,2)

plot(tplot(2:end),c1out,tplot(2:end),pout,tplot(2:end),co1out)
            title({'Al    Concentration    and    Pressure    at
Boundary' ;...
                [' c(first)='  ,num2str(c1out(1)),  ', c(end)='
num2str(y(N))] ;...
                ['  co(first)='    ,num2str(co1out(1)),    ',
co(end)='  num2str(y(2*N+1))];...
                [' P(first) =' ,num2str(pout(1)), ', P(end) =
' ,num2str(y(2*N))]})
            %legend('Al Con','Pressure','Oxygen',-1)
            grid on
            %axis tight
            figure(4)
%             subplot(2,1,1)
            plot(tplot,y1_st*rt,'--
',tplot,y1out,tplot,y2_st*rt,'--',tplot,y2out)
            %legend('y1 STS','y1 Asym','y2 STS','y2 Asym',-1)
            xlabel('$$Dimensionless                        Time
$$','Interpreter','Latex'),ylabel('$$Upper  and  Lower  Boundary
Position, \hat{y_1} , \hat{y_2} $$','Interpreter','Latex')
            title({['y1
small='    ,num2str(y1_st*sqrt(tplot(end))),    '             y2
small' ,num2str(y2_st*sqrt(tplot(end))),];['y1=' ,num2str(y(end
-3)),'   y2=' ,num2str(y(end-2)),];['Time = ' num2str(t) '   T
initial =' num2str(t0)]})
            grid on
            axis tight

            figure(5)
%             subplot(2,1,1)
```

```
            plot(tplot,y1_st*sqrt(tplot),'--
',tplot,y1out,tplot,y2_st*sqrt(tplot),'--',tplot,y2out)
            %legend('y1 STS','y1 Asym','y2 STS','y2 Asym',-1)
            xlabel('$$Dimensionless                         Time
$$','Interpreter','Latex'),ylabel('$$Upper  and  Lower  Boundary
Position, \hat{y_1} , \hat{y_2} $$','Interpreter','Latex')
            title({['y1
small='    ,num2str(y1_st*sqrt(tplot(end))),    '             y2
small' ,num2str(y2_st*sqrt(tplot(end))),];['y1=' ,num2str(y(end
-3)),'   y2=' ,num2str(y(end-2)),];['Time = ' num2str(t) '    T
initial =' num2str(t0)]})
            grid on
            axis tight

            figure(6)
%             subplot(2,1,1)
            plot(tplot,y1_st*rt,'--',tplot,y2_st*rt,'--')
            %legend('y1 STS','y1 Asym','y2 STS','y2 Asym',-1)
            xlabel('$$Dimensionless                         Time
$$','Interpreter','Latex'),ylabel('$$Upper  and  Lower  Boundary
Position, \hat{y_1} , \hat{y_2} $$','Interpreter','Latex')
            title({['y1
small='    ,num2str(y1_st*sqrt(tplot(end))),    '             y2
small' ,num2str(y2_st*sqrt(tplot(end))),];['y1=' ,num2str(y(end
-3)),'   y2=' ,num2str(y(end-2)),];['Time = ' num2str(t) '    T
initial =' num2str(t0)]})
            grid on
            axis tight

            subplot(2,1,2)
            figure(5)
            loglog(tplot,y1_st*sqrt(tplot),'--',tplot,y1out,...
                tplot,y2_st*sqrt(tplot),'--',tplot,y2out)
            %legend('y1 STS','y1 Asym','y2 STS','y2 Asym',-1)
            xlabel('$$Dimensionless                         Time
$$','Interpreter','Latex'),ylabel('$$Upper  and  Lower  Boundary
Position, \hat{y_1} , \hat{y_2} $$','Interpreter','Latex')
            title({['y1
small='    ,num2str(y1_st*sqrt(tplot(end))),    '             y2
small' ,num2str(y2_st*sqrt(tplot(end))),];['y1=' ,num2str(y(end
-3)),'   y2=' ,num2str(y(end-2)),];['Time = ' num2str(t) '    T
initial =' num2str(t0)]})
            grid on
            axis tight
            %pause

            figure(6)
            subplot(2,2,1)
            plot(tplot,v1out,tplot,v2out)
            %legend('v1','v2',-1)
            xlabel('$$Dimensionless                         Time
$$','Interpreter','Latex'),ylabel('$$velocity,    \hat{v_1}    ,
\hat{v_2} $$','Interpreter','Latex')
            title(['v1   ='   ,num2str(y(end-1)),   '         v2
=' ,num2str(y(end))])
            grid on
            axis tight

            subplot(2,2,2)
```

```
            loglog(tplot,v1out,tplot,v2out)
            %legend('v1','v2',-1)
            xlabel('$$Dimensionless                        Time
$$','Interpreter','Latex'),ylabel('$$velocity,    \hat{v_1}    ,
\hat{v_2} $$','Interpreter','Latex')
            title(['v1   ='   ,num2str(y(end-1)),   '        v2
=' ,num2str(y(end))])
            grid on
            axis tight

            subplot(2,2,[3,4])
            plot(tplot,y2out-y1out)
            %legend('Thickness')
            xlabel('$$Dimensionless                        Time
$$','Interpreter','Latex'),ylabel('$$Thickness
$$','Interpreter','Latex')
            grid on
            axis tight

            figure(7)
            subplot(2,1,1)

plot(Y_negative+y1,y(1:N),Y_negative+y1,y((N+1):(2*N)),Y_negati
ve(2:N-1),v)
            %legend('Al       Concentration','Pressure','Marker
Velocity',-1)
            xlabel('$$Alloy                              Region
$$','Interpreter','Latex'),ylabel('$$Velocity
$$','Interpreter','Latex')
            grid on
            axis tight

            plot(tplot,y1out,tplot,Marker_Position)


figure(5),plot(tplot,y1out,tplot(2:end),Marker_Position_1+y1out
(2:end),...

tplot(2:end),Marker_Position_2+y1out(2:end),tplot(2:end),Marker
_Position_3+y1out(2:end),...

tplot(2:end),Marker_Position_4+y1out(2:end),tplot(2:end),Marker
_Position_5+y1out(2:end),...

tplot(2:end),Marker_Position_6+y1out(2:end),tplot(2:end),Marker
_Position_7+y1out(2:end),...

tplot(2:end),Marker_Position_8+y1out(2:end),tplot(2:end),Marker
_Position_9+y1out(2:end),...

tplot(2:end),Marker_Position_10+y1out(2:end))%tplot(2:end),Mark
er_Position_2,tplot(2:end),Marker_Position_3,tplot(2:end),Marke
r_Position_4)

            figure(8)
            plot(Y_negative+y1,y((N+1):(2*N)))
            legend('Pressure')
```

```
            xlabel('$$Alloy                              Region
$$','Interpreter','Latex'),ylabel('$$Pressure
$$','Interpreter','Latex')
            grid on
            axis tight

            figure(9)
            plot(Y_negative+y1,y(1:N))
            legend('Al Concentration')
            xlabel('$$Alloy                              Region
$$','Interpreter','Latex'),ylabel('$$Pressure
$$','Interpreter','Latex')
            grid on
            axis tight

            figure(10)
            plot(tplot,y2out-y1out)
            legend('Thickness')
            xlabel('$$Dimensionless                         Time
$$','Interpreter','Latex'),ylabel('$$Thickness
$$','Interpreter','Latex')
            grid on
            axis tight

            figure(11)
            plot(Y_negative(2:N-1),v)
            legend('Marker Velocity')
            xlabel('$$Dimensionless                         Time
$$','Interpreter','Latex'),ylabel('$$Thickness
$$','Interpreter','Latex')
            grid on
            axis tight
        end
    end
    dt=min(t_factor*dt,dt1);
    %save NumData2 rt_plot
end

 save NumData tplot y1out y2out c1out co1out pout v v1out v2out
vout Y_negative Y_positive y1 y2 y1_st y2_st y t

function cint = cint(s,sol,d,ci)
cint = zeros(size(s));
N = length(s);
for k = 1:N
    if s(k)>sol.x(1)
        c = deval(sol,s(k),1);
        cint(k) = 1./(c+(1-c)*d)-1/(ci+(1-ci)*d);
    end
end
```